

**BUBBLE COLUMNS AND THREE-PHASE FLUIDIZED BEDS:
FLOW REGIMES AND BUBBLE CHARACTERISTICS**

by

Junping Zhang

B. Sc., Tsinghua University, 1984

M. Sc., Tsinghua University, 1987

**A THESIS SUBMITTED IN PARTIAL FULFILLMENT OF
THE REQUIREMENTS FOR THE DEGREE OF
DOCTOR OF PHILOSOPHY**

in

THE FACULTY OF GRADUATE STUDIES

(Department of Chemical Engineering)

**We accept this thesis as conforming
to the required standard**

THE UNIVERSITY OF BRITISH COLUMBIA

May 1996

© Junping Zhang, 1996

In presenting this thesis in partial fulfillment of the requirements for an advanced degree at the University of British Columbia, I agree that the Library shall make it freely available for reference and study. I further agree that permission for extensive copying of this thesis for scholarly purposes may be granted by the head of my department or by his or her representatives. It is understood that copying or publication of this thesis for financial gain shall not be allowed without my written permission.

Department of Chemical Engineering
The University of British Columbia
2216 Main Mall
Vancouver, Canada
V6T 1Z4

Date: June 7, 1996

Abstract

Experiments were carried out in three-phase fluidized beds containing solid particles contacted by upward cocurrent flow of air and water, to study flow patterns of gas-liquid-solid systems.

The minimum fluidization velocity and the particle transport velocity in a gas-liquid-solid mixture delineate the boundaries between three types of flow systems — fixed bed, fluidized bed and transport flow. Both of these transition velocities were measured for a variety of particles. A theoretical model, the Gas-Perturbed Liquid Model, was developed to predict the minimum liquid fluidization velocity of a bed of solid particles in the presence of a fixed cocurrent superficial gas velocity. This model, together with an appropriate equation for the gas holdup on a solids-free basis, shows almost as good agreement with the present experimental data and those from the literature as the best available empirical equation for the minimum liquid fluidization velocity at low to intermediate superficial gas velocity, and has the advantage of correctly reducing to the Wen-Yu equation for minimum two-phase fluidization as the superficial gas velocity goes to zero. Two types of particle movement were observed as the superficial liquid velocity approaches the particle transport velocity. For 1.2 mm steel shot, clusters of particles were found in both liquid-solid and gas-liquid-solid systems. For 1.5 and 4.5 mm glass beads, on the other hand, no particle clusters were observed. In the latter case, a mathematical model, the Particle Transport Velocity Model, was developed to predict the superficial liquid velocity for particle transport in upward gas-liquid flow. An empirical correlation was also proposed for the transition from fluidized bed to particle transport flow. Both predictions showed good agreement with experimental data obtained in the present work and in the literature for a wide range of superficial gas velocities.

Within the fluidized bed, based on bubble characteristics, dispersed bubble flow, discrete bubble flow, coalesced bubble flow, slug flow, churn flow, bridging flow and annular flow regimes

were identified and characterized, at different combinations of gas and liquid superficial velocities. These flow regimes were also observed for two-phase air-water systems.

A comprehensive measurement method using a conductivity probe was developed to determine flow regime transitions based on bubble frequency, Sauter mean bubble chord length and the time taken by a bubble to pass a given point. Criteria for determining flow regime transitions were developed in an air-water two-phase system and then successfully applied to gas-liquid-solid three-phase fluidized beds. Flow regime maps were derived based on experimental data for three different three-phase systems. As in two-phase gas-liquid systems, churn flow, bridging flow and annular flow can be observed at high gas velocities in three-phase fluidized beds. Empirical correlations were developed to predict the flow regime boundaries in the three-phase fluidized systems investigated.

Table of Contents

Abstract	iii
List of Tables	x
List of Figures	xii
Acknowledgment	xxiii
Chapter 1 Introduction	1
1.1 Definitions of Flow Patterns.....	5
1.2 Scope of Work	9
Chapter 2 Experimental Apparatus and Measurement Methods.....	12
2.1 Apparatus.....	12
2.2 Measurement Techniques.....	15
2.2.1 Pressure Transducers	15
2.2.2 Conductivity Probe	18
2.3 Data Processing.....	22
2.3.1 Threshold.....	22
2.3.2 Signal Simplification and Bubble Frequency	24
2.3.3 Bubble Time and Local Gas Holdup	25
2.3.4 Bubble Velocity and Bubble Chord Length.....	26
2.3.5 Data Processing Procedure	29
Chapter 3 Experimental Methods.....	31
3.1 Introduction.....	31
3.2 Pressure Fluctuations.....	32
3.2.1 Previous Studies	32
3.2.1.1 Gas-liquid two-phase systems.....	32
3.2.1.2 Three-phase systems.....	34
3.2.2 Preliminary Tests	35

3.2.2.1 Effect of single bubble injection on pressure fluctuations.....	35
3.2.2.2 Effect of continuous air supply on pressure fluctuations.....	37
3.3 Local Multiphase Flow Characteristics.....	39
3.3.1 Previous Studies	39
3.3.1.1 Gas-liquid two-phase systems.....	39
3.3.1.2 Three-phase systems.....	43
3.3.2 Discussion of Existing Methods	45
3.4 Summary.....	51
Chapter 4 Experimental Criteria for Flow Regime Transitions in Gas-Liquid Systems.....	52
4.1 Introduction.....	52
4.2 Experimental Results	52
4.2.1 Raw Signals and their Statistical Results.....	52
4.2.2 Gas Holdup.....	56
4.3 Experimental Criteria for Flow Regime Transitions.....	57
4.3.1 Transition between Discrete Bubble Flow and Coalesced Bubble Flow Regimes.....	57
4.3.2 Transition between Coalesced Bubble Flow and Slug Flow Regimes	60
4.3.3 Transition between Slug Flow and Churn Flow	62
4.3.4 Transition between Churn Flow and Bridging Flow.....	63
4.3.5 Transition between Bridging Flow and Annular Flow	66
4.3.6 Transition between Discrete Bubble Flow or Coalesced Bubble Flow and Dispersed Bubble Flow.....	66
4.4 Flow Regime Transitions at Different Heights.....	67
4.4.1 Experimental Conductivity Probe Results.....	67
4.4.2 Experimental Pressure Fluctuation Results	72
4.4.3 Comparison between Conductivity Probe and Pressure Transducer Techniques.....	78

4.5 Flow Regime Map for Air-Water System.....	79
4.5.1 Experimental Results.....	79
4.5.2 Comparison	81
4.6 Summary.....	84
Chapter 5 Bubble Characteristics in Bubble Columns.....	85
5.1 Introduction.....	85
5.2 Bubble Characteristics in the Discrete and Dispersed Bubble Flow Regimes.....	85
5.2.1 Local Bubble Frequency.....	86
5.2.2 Bubble Chord Length and its Distribution.....	87
5.2.3 Average Bubble Velocity	89
5.3 Bubble Characteristics in the Slug and Churn Flow Regimes	91
5.3.1 Bubble Chord Length and its Distribution.....	92
5.3.2 Average Bubble Velocity	94
5.4 Summary	97
Chapter 6 Three-Phase Fluidization Boundaries.....	98
6.1 Minimum Liquid Fluidization Velocity at Low to Intermediate Gas Velocity.....	98
6.1.1 Introduction.....	98
6.1.2 Theoretical Models: Modifications and New Models.....	105
6.1.2.1 Modified Song model I.....	105
6.1.2.2 Modified Song model II.....	108
6.1.2.3 Pseudo-homogeneous fluid model	108
6.1.2.4 Gas-perturbed liquid model	109
6.1.2.5 Gas holdup at minimum fluidization.....	110
6.1.3 Experimental Study.....	114
6.1.3.1 Experimental procedure.....	115
6.1.3.2 Experimental results	116
6.1.4 Comparison and Discussion	118

6.1.4.1 Pressure gradient in fixed beds.....	118
6.1.4.2 Minimum fluidization velocity for liquid-solid fluidized beds.....	119
6.1.4.3 Minimum fluidization velocity for three-phase fluidized beds.....	120
6.2 Minimum Gas Fluidization Velocity at Zero or Low Liquid Velocity.....	124
6.2.1 Introduction.....	124
6.2.2 Zero Superficial Liquid Velocity	131
6.2.3 Non-Zero Superficial Liquid Velocity.....	136
6.3 Particle Transport Velocity in Gas-Liquid Mixtures	140
6.3.1 Introduction.....	140
6.3.2 Experimental Method.....	142
6.3.3 Experimental Results and Discussion.....	142
6.4 Regime Maps for Three-Phase Systems	152
6.5 Summary	154
Chapter 7 Flow Regimes in Three-Phase Fluidized Beds.....	157
7.1 Introduction.....	157
7.1.1 Visual Observations	157
7.1.2 Instrumental Measurements.....	160
7.2 Experimental Results	165
7.3 Flow Regime Transitions	169
7.3.1 Transition between Discrete (or Dispersed) and Coalesced Bubble Flow	170
7.3.2 Transition between Coalesced Bubble Flow and Slug Flow	174
7.3.3 Transition between Slug Flow and Churn Flow	176
7.3.4 Transition between Churn Flow and Bridging Flow.....	178
7.3.5 Transition between Bridging Flow and Annular Flow	180
7.3.6 Transition between Discrete (or Coalesced) and Dispersed Bubble Flow	180
7.4 Flow Regime Maps.....	183
7.4.1 Flow Regime Map for 1.5 mm Glass Beads Fluidized Bed.....	183

7.4.2 Flow Regime Map for 4.5 mm Glass Bead Fluidized Bed	184
7.4.3 Flow Regime Map for 1.2 mm Steel Shot Fluidized Bed.....	185
7.4.4 Comparison and Discussion	187
7.5 Summary	196
Chapter 8 Bubble Characteristics in Three-Phase Fluidized Beds.....	198
8.1 Introduction.....	198
8.2 Bubble Frequency.....	198
8.3 Bubble Chord Length and its Distribution	200
8.4 Average Bubble Velocity	211
8.5 Summary	219
Chapter 9 Conclusions and Recommendations	221
9.1 General Conclusions	221
9.2 Recommendations for Future Work	223
Nomenclature	225
References.....	232
 Appendix A Computer Programs for Data Acquisition and Processing	 244
Appendix B Experimental Data.....	260
Appendix C Data Validation	301

List of Tables

Table 2.1.	Properties of particles investigated.	15
Table 2.2.	Effect of probe time response on measured bubble velocity and bubble chord length.	22
Table 3.1.	Summary of some experimental methods used to delineate regime transitions in gas-liquid two-phase systems.	44
Table 3.2.	Summary of experimental methods used to delineate regime transitions in gas- liquid-solid three-phase systems.	46
Table 4.1	Flow regime transition velocities determined from the conductivity probe for air-water system at $U_\ell = 0.0184$ m/s using the criteria proposed in sections 4.3.1 to 4.3.5	72
Table 4.2.	Flow regime transition velocities determined from the standard deviation of absolute pressure fluctuations for $U_\ell = 0.0184$ m/s.....	74
Table 4.3.	Flow regime transition velocities determined from the standard deviation of differential pressure fluctuations for $U_\ell = 0.0184$ m/s.....	77
Table 4.4.	Flow regime transition velocities determined from the skewness of differential pressure fluctuations for $U_\ell = 0.0184$ m/s	77
Table 4.5.	Flow regime boundaries for air-water system at $Z = 0.65$ m and $D = 0.0826$ m....	79
Table 4.6.	Summary of some experimental regime transition measurements from the literature.....	82
Table 6.1.	Experimental conditions used in various investigations of minimum fluidization for three-phase systems (SI Units)	99
Table 6.2.	Experimental conditions used in correlations for α	112
Table 6.3.	Empirical equations for α	113

Table 6.4.	Average absolute percentage and root mean square percentage deviations between predictions from correlations for minimum fluidization velocity for three-phase fluidized beds and experimental data.....	122
Table 6.5.	Summary of experimental operating conditions for investigations of critical gas velocity.....	126
Table 6.6.	Experimental and predicted values of critical gas velocity (m/s) at zero superficial liquid velocity.....	135
Table 6.7.	Minimum fluidization velocities at low liquid velocities.....	138
Table 6.8.	Experimental results for the boundary between fluidized bed and transport flow regimes.....	143
Table 6.9.	Average absolute percentage deviation between experimental results and model predictions for particle transport velocity in gas-liquid mixture	149
Table 7.1.	Summary of previous investigations on flow regime transitions in three-phase fluidized beds.....	162
Table 7.2.	Flow regime transition velocities for air-water-1.5 mm glass bead fluidized beds.....	172
Table 7.3.	Flow regime transition velocities for air-water-4.5 mm glass bead fluidized bed ...	172
Table 7.4.	Flow regime transition velocities for air-water-1.2 mm steel shot fluidized bed	173

List of Figures

Figure 1.1. Classification of gas-liquid-solid fluidization system (from Fan, 1989).....	2
Figure 1.2. Relationship between mean bubble size and bed expansion in different flow regimes (from Matsuura and Fan, 1984).....	3
Figure 1.3. Effects of gas and liquid flow rates on axial dispersion coefficient in different flow regimes (from Muroyama et al., 1978): (a) Coalesced bubble flow (small particles). (b) Dispersed bubble flow (large particles).....	4
Figure 1.4. Schematic diagram of flow patterns.....	8
Figure 2.1. Schematic diagram of experimental apparatus.	13
Figure 2.2. Schematic diagram of three-phase separator.....	14
Figure 2.3. Typical pressure fluctuation signals in an air-water system, $Z = 1.35$ m; $\Delta Z = 0.1$ m; $U_\ell = 0.018$ m/s; $U_g = 0.041$ m/s	16
Figure 2.4. Configuration of conductivity probe.....	19
Figure 2.5. Typical raw signals of a two-element conductivity probe in an air-water system, $Z = 1.95$ m; $L = 1.1$ mm; $U_\ell = 0.018$ m/s; $U_g = 0.086$ m/s.	20
Figure 2.6. Response of conductivity probe to a gas bubble in an air-water system, $Z = 1.95$ m; $L = 1.1$ mm; $U_\ell = 0.018$ m/s; $U_g = 0.086$ m/s.....	21
Figure 2.7. Typical conductivity probe signal for steel shot three-phase system, $U_\ell = 0.036$ m/s; $U_g = 0.037$ m/s; $Z = 0.65$ m.	24
Figure 2.8. Idealized square-wave relationship between probe, bubble and simplified signal.....	25
Figure 2.9. Flow chart for data processing.	30
Figure 3.1. Schematic diagram of experimental apparatus used for preliminary pressure fluctuation tests	36
Figure 3.2. Pressure signals corresponding to single bubble formation and rise (air injector 0.25 m above the distributor).....	37

Figure 3.3. Pressure signals corresponding to continuous air supply at $U_g = 0.387$ m/s in a stagnant column containing water	38
Figure 3.4. Ideal signal for conductivity probe.	48
Figure 3.5. Relationship between gas holdup and various moment parameters of an ideal signal for conductivity probe.....	50
Figure 4.1. Typical raw signals at different superficial gas velocities from conductivity probe for air-water system at $Z = 0.65$ m, $U_\ell = 0.0184$ m/s.....	53
Figure 4.2. Probability density function of conductivity signal for air-water system at $Z = 0.65$ m, $U_\ell = 0.0184$ m/s and different gas velocities	54
Figure 4.3. Variation of moments of conductivity probe signals with superficial gas velocity for air-water system at $Z = 0.65$ m, $U_\ell = 0.0184$ m/s.....	55
Figure 4.4. Variation of moments of conductivity probe signals with gas holdup for air-water system at $Z = 0.65$ m, $U_\ell = 0.0184$ m/s.....	56
Figure 4.5. Local gas holdup at different heights for air-water system at $U_\ell = 0.0184$ m/s	57
Figure 4.6. Transition between discrete and coalesced bubble flow regimes in air-water system at different superficial liquid velocities	58
Figure 4.7. Method used to determine transition between coalesced bubble flow and slug flow in air-water system at various superficial liquid velocities	62
Figure 4.8. Plot of local bubble frequency at axis of column versus superficial gas velocity showing transition between slug flow and churn flow and the onset of annular flow in the air-water system for different superficial liquid velocities	63
Figure 4.9. Average bubble chord length and bubble time versus superficial gas velocity showing transition between churn flow and bridging flow for air-water system at $Z = 0.65$ m, $U_\ell = 0.064$ m/s.....	65

Figure 4.10. Average bubble time versus superficial gas velocity showing transition between churn flow and bridging flow in the air-water system at $Z = 0.65$ m for different superficial liquid velocities.....	65
Figure 4.11. Dimensionless standard deviation of bubble time plotted against superficial liquid velocity showing transition between discrete bubble flow and dispersed bubble flow for air-water system at $Z = 0.65$ m.....	67
Figure 4.12. Bubble frequency plotted against superficial gas velocity showing transition between discrete and coalesced bubble flow at different locations for air-water system at $U_\ell = 0.0184$ m/s	68
Figure 4.13. Sauter mean bubble chord length versus superficial gas velocity showing transition between coalesced bubble flow and slug flow at two different levels for air-water system at $U_\ell = 0.0184$ m/s.....	69
Figure 4.14. Variation of bubble frequency with gas velocity at different heights for air- water system at $U_\ell = 0.0184$ m/s.....	70
Figure 4.15. Average bubble time versus superficial gas velocity showing transition between churn flow and bridging flow at different locations for air-water system at $U_\ell = 0.0184$ m/s	71
Figure 4.16. Probability density function of absolute pressure fluctuations for air-water system at $Z = 0.65$ m and $U_\ell = 0.0184$ m/s.....	73
Figure 4.17. Standard deviation of absolute pressure fluctuations for air-water system at $U_\ell = 0.0184$ m/s.....	74
Figure 4.18. Probability density function of differential pressure fluctuations at $Z = 0.65$ m for $U_\ell = 0.0184$ m/s	76
Figure 4.19. Standard deviation of differential pressure fluctuations at different levels for $U_\ell = 0.0184$ m/s.....	76
Figure 4.20. Skewness of differential pressure fluctuations at different levels for $U_\ell =$ 0.0184 m/s.....	77

Figure 4.21. Two-phase bubble column flow regime map for air-water system with $D = 0.0826$ m and $Z = 0.65$ m. Distributor: perforated plate containing 62 2-mm circular holes	80
Figure 4.22. Comparison of flow regime maps with previous studies.	83
Figure 5.1. Linear relationship between bubble frequency and superficial gas velocity for the discrete and dispersed bubble flow regimes with air-water system at $Z = 650$ mm and $D = 82.6$ mm	86
Figure 5.2. Comparison of average bubble chord length in discrete and dispersed bubble flow regimes for air-water system at $Z = 0.65$ m and $D = 82.6$ mm.....	87
Figure 5.3. Probability density distribution of bubble chord length in discrete and dispersed bubble flow regimes for air-water system at $Z = 0.65$ m and $D = 82.6$ mm	88
Figure 5.4. Average bubble velocity at different superficial liquid velocities for air-water system at $Z = 0.65$ m and $D = 82.6$ mm.....	89
Figure 5.5. Relationship between bubble travel length and average bubble chord length for air-water system at $Z = 0.65$ m and $D = 82.6$ mm	91
Figure 5.6. Bubble chord length in slug and churn flow regimes at $Z = 0.65$ m and $D = 82.6$ mm	92
Figure 5.7. Probability density distribution of bubble chord length in the slug and churn flow regimes at $Z = 0.65$ m and $D = 82.6$ mm	93
Figure 5.8. Relationship between average bubble velocity and average bubble chord length in slug and churn flow regimes for air-water system at $Z = 0.65$ m and $D = 82.6$ mm	95
Figure 5.9. Relationship between bubble travel length and average bubble chord length in the slug and churn flow regimes for air-water system at $Z = 0.65$ m, $D = 82.6$ mm and $U_g \approx 0.002 - 6$ m/s	96

Figure 6.1. Prediction of gas holdup on solids-free basis at minimum fluidization, with properties corresponding to the experimental conditions of Begovich and Watson, 1978	114
Figure 6.2. Determination of $U_{\ell mf}$ by pressure drop and pressure gradient methods for 2.5 mm glass beads with $U_g = 0.0509$ m/s.....	115
Figure 6.3. Effect of increasing or decreasing liquid velocity on determination of $U_{\ell mf}$ for 2.5 mm glass beads with $U_g = 0.0509$ m/s.....	116
Figure 6.4. $U_{\ell mf}$ for different particle sizes and densities	117
Figure 6.5. $U_{\ell mf}$ for particles of different wettability and sphericity.....	117
Figure 6.6. Three-phase fixed and fluidized bed pressure gradient measurements compared with fixed bed prediction for 3.7 mm glass beads.	119
Figure 6.7. Comparison of minimum fluidization velocity predictions and experimental results for liquid-solid fluidized beds. Predictions are for an equation of the form $Re_{\ell mf}'' = \sqrt{a^2 + b Ar_{\ell}} - a$, with values of a and b as listed in the legend.....	120
Figure 6.8. Experimental minimum fluidization velocities for 2.5 mm glass beads compared with predictions of various empirical equations	121
Figure 6.9. Experimental minimum fluidization velocities for 2.5 mm glass beads compared with predictions of various models.....	122
Figure 6.10. Comparison of all available experimental results for $U_{\ell mf}$ with predictions of gas-perturbed liquid model, Equation (6.50)	123
Figure 6.11. Determination of critical gas velocity for full suspension of particles: $d_p = 1.5$ mm, $\rho_s = 2530$ kg/m ³ , $H_0 = 770$ mm, $U_{\ell} = 0$, $\Delta P = P_{50} - P_{650}$	132
Figure 6.12. Determination of critical gas velocity at different bed heights: $d_p = 1.5$ mm, $\rho_s = 2530$ kg/m ³ , $H_0 = 770$ mm, $U_{\ell} = 0$, $\Delta P = P_{50} - P_{650}$, $P_{50} - P_{350}$ and $P_{350} - P_{650}$	133

Figure 6.13. Effect of particle loading on critical gas velocity for complete solids suspension: $d_p = 1.5 \text{ mm}$, $\rho_s = 2530 \text{ kg/m}^3$, $H_o = 440, 770 \text{ mm}$, $U_\ell = 0$	134
Figure 6.14. Determination of critical gas velocity at zero superficial liquid velocity.....	135
Figure 6.15. Determination of critical gas velocity for three-phase system with 1.5 mm glass beads at different liquid velocities	137
Figure 6.16. Determination of critical gas velocity for three-phase system with 4.5 mm glass beads at different liquid velocities	137
Figure 6.17. Determination of critical gas velocity for three-phase system with 1.2 mm steel shot at different liquid velocities.....	138
Figure 6.18. Experimental minimum fluidization gas velocities for three-phase system at zero and low liquid superficial velocities	139
Figure 6.19. Predictions and experimental results for transition from fluidized bed to transport flow regime: air-water-1.5 mm glass beads.....	147
Figure 6.20. Predicted and experimental particle transport velocities for 4.5 mm glass beads in air-water mixture.....	147
Figure 6.21. Particle transport velocity predictions compared with experimental results of Jean and Fan (1987).....	148
Figure 6.22. Experimental data for low density ($\rho_s \leq 2876 \text{ kg/m}^3$) particle transport velocity compared with predictions of Song et al. (1989) empirical correlation and Model II.....	150
Figure 6.23. Comparison between particle transport velocity empirical correlations and experimental results for 1.2 mm steel shot.....	152
Figure 6.24. Regime map for air-water-1.5 mm glass bead three-phase system.....	153
Figure 6.25. Regime map for air-water-4.5 mm glass bead three-phase system.....	153
Figure 6.26. Regime map for air-water-1.2 mm steel shot three-phase system.....	154

Figure 7.1. Comparison of conductivity probe signals in two-phase and three-phase systems at $Z = 0.65$ m and $U_\ell = 0.0184$ m/s: (a) air-water two-phase, $U_g = 0.040$ m/s; (b) air-water-1.5 mm glass beads three-phase, $U_g = 0.039$ m/s	166
Figure 7.2. Bubble frequency in two-phase and three-phase systems for the same liquid flow rate: $Z = 0.65$ m and $U_\ell = 0.0184$ m/s	166
Figure 7.3. Average bubble chord length in two-phase and three-phase systems for the same liquid flow rate at $Z = 0.65$ m and $U_\ell = 0.0184$ m/s	167
Figure 7.4. Comparison of bubble frequency in different systems at $Z = 0.65$ m and $U_\ell = 0.0455$ m/s.....	168
Figure 7.5. Comparison of average bubble chord length in different systems at $Z = 0.65$ m and $U_\ell = 0.0455$ m/s	168
Figure 7.6. Summary of flow regime transition criteria.....	169
Figure 7.7. Transition between discrete and coalesced bubble flow regime in a three-phase fluidized bed containing 1.5 mm glass beads at different superficial liquid velocities.	171
Figure 7.8. Transition between discrete and coalesced bubble flow regime in a three-phase fluidized bed containing 4.5 mm glass beads at different superficial liquid velocities	171
Figure 7.9. Transition between discrete and coalesced bubble flow regime in a three-phase fluidized bed containing 1.2 mm steel shot at low superficial liquid velocities	173
Figure 7.10. Transition between discrete and coalesced bubble flow regimes in a three-phase fluidized bed containing 1.2 mm steel shot at high superficial liquid velocities	174
Figure 7.11. Transition between coalesced bubble flow and slug flow in a three-phase fluidized bed containing 1.5 mm glass beads at various superficial liquid velocities	175

Figure 7.12. Transition between coalesced bubble flow and slug flow in a three-phase fluidized bed containing 4.5 mm glass beads at various superficial liquid velocities	175
Figure 7.13. Transition between coalesced bubble flow and slug flow in a three-phase fluidized bed containing 1.2 mm steel shot at various superficial liquid velocities	176
Figure 7.14. Local bubble frequency at axis of column versus superficial gas velocity showing transition between slug flow and churn flow and the onset of annular flow for three-phase fluidized bed containing 1.5 mm glass beads at different superficial liquid velocities	177
Figure 7.15. Local bubble frequency at axis of column versus superficial gas velocity showing transition between slug flow and churn flow and onset of annular flow for three-phase fluidized bed containing 4.5 mm glass beads at different superficial liquid velocities	177
Figure 7.16. Plot of local bubble frequency at axis of column versus superficial gas velocity showing transition between slug flow and churn flow and the onset of annular flow for three-phase fluidized bed containing 1.2 mm steel shot at different superficial liquid velocities	178
Figure 7.17. Average bubble time versus superficial gas velocity showing transition between churn flow and bridging flow for a three-phase fluidized bed containing 1.5 mm glass beads at different superficial liquid velocities	179
Figure 7.18. Average bubble time versus superficial gas velocity showing transition between churn flow and bridging flow for a three-phase fluidized bed containing 4.5 mm glass beads at different superficial liquid velocities	179
Figure 7.19. Average bubble time versus superficial gas velocity showing transition between churn flow and bridging flow for a three-phase fluidized bed containing 1.2 mm steel shot at different superficial liquid velocities.....	180

Figure 7.20. Dimensionless standard deviation of bubble time plotted against superficial liquid velocity showing transition between coalesced bubble flow and dispersed bubble flow for 1.5 mm glass bead three-phase fluidized bed at different superficial gas velocities.....	182
Figure 7.21. Dimensionless standard deviation of bubble time plotted against superficial liquid velocity showing transition between discrete bubble flow and dispersed bubble flow for 4.5 mm glass bead three-phase fluidized bed at different superficial gas velocities.....	182
Figure 7.22. Dimensionless standard deviation of bubble time plotted against superficial liquid velocity showing transition between discrete bubble flow and dispersed bubble flow for 1.2 mm steel shot three-phase fluidized bed at different superficial gas velocities.....	183
Figure 7.23. Flow regime map for air-water-1.5 mm glass bead three-phase fluidized bed with $D = 0.0826$ m and $Z = 0.65$ m. Distributor: perforated plate containing 62 2-mm circular holes.....	184
Figure 7.24. Flow regime map for air-water-4.5 mm glass bead three-phase fluidized bed with $D = 0.0826$ m and $Z = 0.65$ m. Distributor: perforated plate containing 62 2-mm circular holes.....	185
Figure 7.25. Flow regime map for air-water-1.2 mm steel shot three-phase fluidized bed with $D = 0.0826$ m and $Z = 0.65$ m. Distributor: perforated plate containing 62 2-mm circular holes.....	186
Figure 7.26. Boundaries between various bubble flow regimes.....	187
Figure 7.27. Comparison between predictions of Equation (7.3) and experimental results	188
Figure 7.28. Comparison between predictions of Equation (7.3) and experimental data from literature.....	189
Figure 7.29. Boundaries for onset of slug flow regime	190
Figure 7.30. Comparison between predictions of Equation (7.5) and experimental data.....	191

Figure 7.31. Comparison between predictions of Equation (7.6) and experimental data.....	192
Figure 7.32. Boundaries between slug and churn flow regimes.....	193
Figure 7.33. Comparison between predictions of Equation (7.7) and experimental data.....	193
Figure 7.34. Boundaries between churn and bridging flow regimes	194
Figure 7.35. Comparison between predictions of Equation (7.8) and experimental data.....	195
Figure 7.36. Boundaries between bridging and annular flow regimes.....	196
Figure 8.1. Average bubble chord length in coalesced and dispersed bubble flow regime for air-water-1.5 mm glass bead system.....	201
Figure 8.2. Average and Sauter mean bubble chord length in slug and churn flow regime for air-water-1.5 mm glass bead system.....	201
Figure 8.3. Bubble chord length distributions in different flow regimes for air-water-1.5 mm glass bead fluidized beds	203
Figure 8.4. Average bubble chord length in discrete and dispersed bubble flow regimes for air-water-4.5 mm glass bead fluidized bed	204
Figure 8.5. Average and Sauter mean bubble chord length in different flow regimes for air-water-4.5 mm glass bead fluidized bed.....	205
Figure 8.6. Bubble chord length distributions in different flow regimes for air-water-4.5 mm glass bead fluidized bed.....	206
Figure 8.7. Average bubble chord length in discrete and dispersed bubble flow regimes for air-water-1.2 mm steel shot fluidized bed	207
Figure 8.8. Average and Sauter mean bubble chord length in different flow regimes for air-water-1.2 mm steel shot at $U_g = 0.0455$ and 0.311 m/s	208
Figure 8.9. Bubble chord length distribution in different flow regimes at low gas velocity for air-water-1.2 mm steel shot fluidized bed.....	209
Figure 8.10. Bubble chord length distribution in different flow regimes at high gas velocity for air-water-1.2 mm steel shot fluidized bed.....	210

Figure 8.11. Average bubble velocity plotted against average bubble chord length in dispersed and coalesced bubble flow regimes for air-water-1.5 mm glass bead fluidized beds, $U_g = 0.0018 - 0.145$ m/s	211
Figure 8.12. Variation of average bubble velocity plotted against average bubble chord length in slug and churn flow regimes for air-water-1.5 mm glass bead fluidized beds.....	212
Figure 8.13. Bubble travel length plotted against average bubble chord length in coalesced and dispersed bubble flow regimes for air-water-1.5 mm glass bead fluidized beds.....	213
Figure 8.14. Bubble travel length plotted against average bubble chord length in different flow regimes at low liquid velocities for air-water-1.5 mm glass bead fluidized bed	214
Figure 8.15. Bubble travel length plotted against average bubble chord length in different flow regimes at high liquid velocities for air-water-1.5 mm glass bead fluidized bed	215
Figure 8.16. Average bubble velocity in discrete and dispersed bubble flow regimes for air-water-4.5 mm glass bead fluidized bed	215
Figure 8.17. Average bubble velocity in different flow regimes for air-water-4.5 mm glass bead fluidized bed	216
Figure 8.18. Bubble travel length plotted against average bubble chord length in different flow regimes for air-water-4.5 mm glass bead fluidized bed with $U_g = 0.003$ to 4.5 m/s	217
Figure 8.19. Average bubble velocity plotted against average bubble chord length in different flow regimes for air-water-1.2 mm steel shot fluidized bed with $U_g = 0.003$ to 4.5 m/s.....	218
Figure 8.20. Bubble travel length plotted against average bubble chord length for air-water-1.2 mm steel shot fluidized bed with $U_g = 0.003$ to 4.5 m/s	219

Acknowledgment

I would like to express my sincere gratitude to Drs. N. Epstein and J. R. Grace for their guidance, support and inspiration during this work. Since the beginning, they both gave generously of their time and effort towards the creation and correction of this work. I would like to thank Dr. J.-X. Zhu for his recommendation and his co-supervision during the early stages of the project. Due to his effort I had the opportunity to be supervised by Drs. Epstein and Grace. My appreciation also goes to Dr. K.-S. Lim for his valuable comments and assistance. In addition, I would like to thank Michael Safoniuk and Dennis Pianarosa for their help and discussion, and Professors D. B. Dreisinger, S. Hatzikiriakos and P. G. Hill for acting as members of the supervisory committee. I would like to thank the Chemical Engineering workshop and stores for their cooperation and kindness during my stay in the department.

The financial support of the Natural Sciences and Engineering Research Council and of fellowships provided by the C. L. Wang Memorial Scholarship and the UBC Faculty of Graduate Studies are gratefully acknowledged.

Finally, I would like to make a special acknowledgement to my wife, Qi, for her understanding, sacrifice and support, and to my daughter, Maya, for brightening the days.

Chapter 1

Introduction

Three-phase fluidized beds have been widely used in industry for processes such as hydrotreating, Fischer-Tropsch synthesis, methanol synthesis, fermentation, and aerobic biological waste water treatment (Fan, 1989). A number of investigations have been conducted on the hydrodynamics, as well as on mass and heat transfer. Since 1968, there have been a number of review papers and books focused on this field (Ostergaard, 1968; Shah, 1979; Kolbel and Ralek, 1980; Epstein, 1981; Shah et al., 1982; Ramachandran et al., 1983; Wild et al., 1984; Darton, 1985; Muroyama and Fan, 1985; Fan, 1989).

Three-phase (gas-liquid-solid) fluidized beds can be classified into three kinds of operations, in terms of the flow directions of the two fluids, namely cocurrent, countercurrent, and stationary liquid (i.e. zero-liquid flow rate) three-phase fluidization (Epstein, 1981). A more detailed classification of three-phase fluidization, including the transport operating regime, has been presented by Fan (1989) and is shown in Figure 1.1.

Until now, most research has been devoted to cocurrent upward three-phase fluidization due to its wider application. Research topics have included incipient fluidization, bed expansion, initial bed contraction, phase holdups, bubble size, bubble size distribution, bubble wake characteristics, backmixing of all three phases, mass and heat transfer. Three flow regimes (dispersed bubble flow, coalesced bubble flow and slug flow) have been identified reflecting different flow patterns of the three phases involved. The flow pattern strongly affects the key properties of three-phase reactors. Matsuura and Fan (1984) reported that the mean bubble size is different in different flow regimes. In the dispersed bubble flow regime, a small mean bubble size is observed which increases only slowly with increasing bed expansion. In the coalesced bubble flow regime, on the other hand, a relatively large mean bubble size is observed. The mean

Expanded Bed Regime In Gas-Liquid-Solid Fluidization	Mode Designation	E-I-a-1	E-I-a-2	E-I-b	E-I-o-1	E-I-o-2	E-I-b	E-I-b	E-III-a	E-III-b
	Schematic Diagram									
	Continuous Phase	Liquid	Liquid	Gas	Liquid	Liquid	Gas	Gas	Liquid	Gas
Transport Regime In Gas-Liquid-Solid Fluidization	Flow Direction	Cocurrent Up-Flow		Cocurrent Up-Flow		Counterflow		Counterflow		Gas Up-Flow Liquid-Down-Flow
	References (Chapters)	1, 2, 3, 6, 7, 8, 10, 11, A	1, 4, 6, 7, 10, 11, A	1, 2, 11	1, 5, 6, 7, 8	5, 9, 11	1, 5, 7, 9, 11	1, 4, 7, 11	1, 5	1, 5
	Mode Designation	T-I-a-1	T-I-a-2	T-I-b	T-II-a	T-II-b	T-III-a	T-III-b	T-III-a	T-III-b
Transport Regime In Gas-Liquid-Solid Fluidization	Schematic Diagram									
	Continuous Phase	Liquid	Liquid	Gas	Liquid	Gas	Liquid	Gas	Liquid	Gas
	Flow Direction	Cocurrent Up-Flow		Cocurrent Up-Flow		Counterflow		Counterflow		Cocurrent Down-Flow
	References (Chapters)	1, 6, 7, 8, 11	1, 4, 10, 11, A	1, 6	1, 9, 11	1, 9	1, 6, 11	1, 6, 11	1, 6, 9	1, 6, 9

(S---) Independent Charge of Solids from Fluid (---S) Independent Discharge of Solids from Fluid (*S) Charge or Discharge of Solids with Fluid
A: Appendix A

Figure 1.1. Classification of gas-liquid-solid fluidization system (from Fan, 1989).

bubble size increases considerably with increasing bed expansion for the coalesced bubble flow regime, while increasing somewhat more quickly for the slug flow regime, as shown in Figure 1.2. Muroyama et al. (1978) found that in the coalesced bubble flow regime the axial dispersion coefficient of the liquid phase is significantly larger than for the dispersed bubble flow regime. Even the trends with increasing gas velocity are different, as shown in Figure 1.3. Chern et al. (1984) reported that the gas holdup in gas-liquid-solid fluidized beds varies strongly with bubble properties. Separate correlations were used to describe the variation of gas holdup in the slug flow, dispersed bubble flow and coalesced bubble flow regimes.

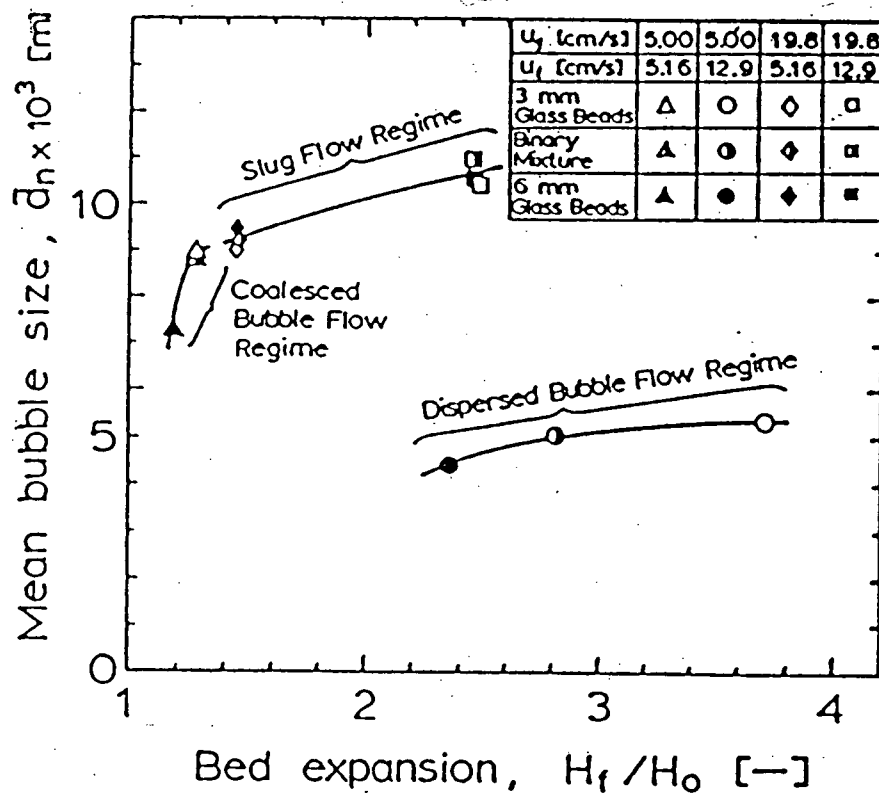


Figure 1.2. Relationship between mean bubble size and bed expansion in different flow regimes (from Matsuura and Fan, 1984).

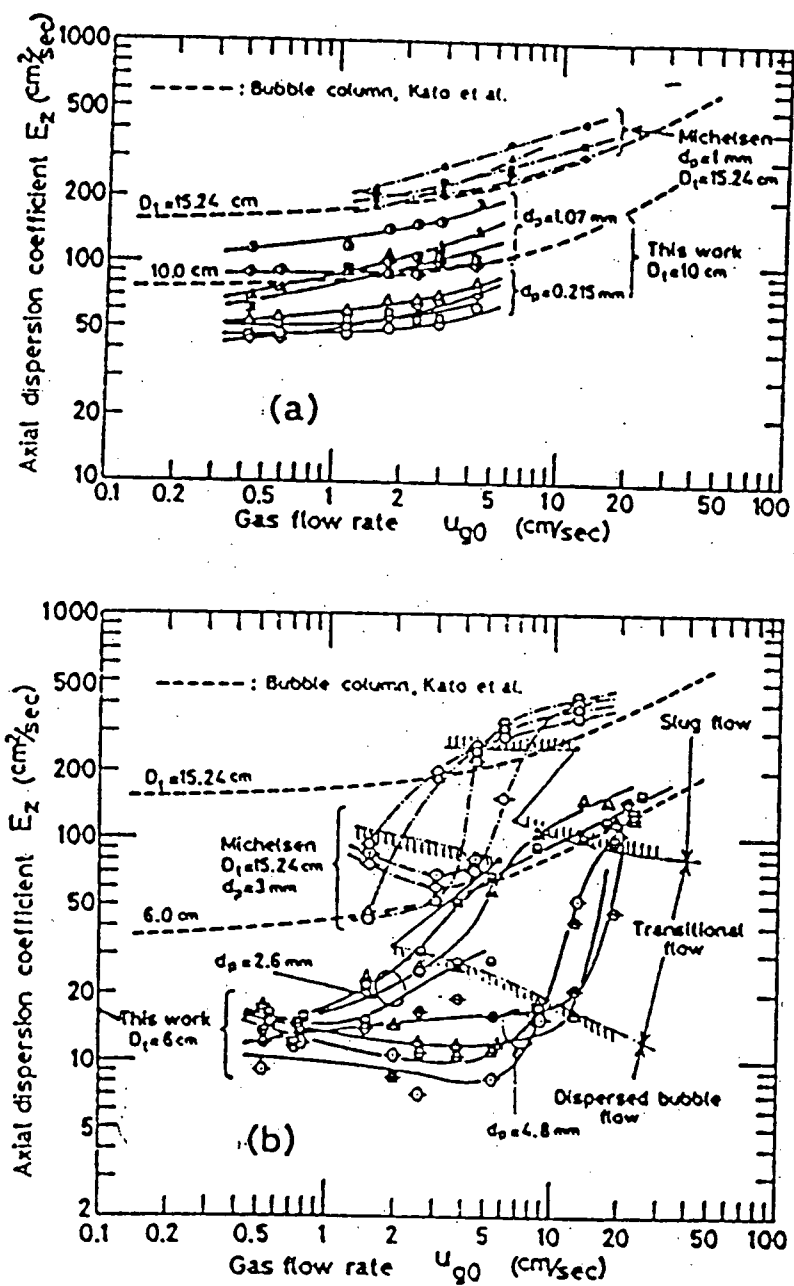


Figure 1.3. Effects of gas and liquid flow rates on axial dispersion coefficient in different flow regimes (from Muroyama et al., 1978):
 (a) Coalesced bubble flow (small particles).
 (b) Dispersed bubble flow (large particles).

With recent developments in environmental engineering, the high gas-liquid mass transfer rates of three-phase fluidized beds have been used advantageously in aerobic wastewater treatment to supply the necessary oxygen. One device used is a draft tube fluidized bed, in which a draft tube is located concentrically inside the column. Most such devices are operated at relatively high gas velocities to obtain a high oxygen concentration for microbial growth. However, the hydrodynamics of three-phase fluidized beds at such high gas velocities are still unclear. In small size columns, on increasing the gas velocity within the coalesced bubble flow regime, slug flow is encountered. There is a need for work where the gas velocity is increased further in order to fully understand the hydrodynamics of a three-phase fluidized bed. At the same time, the boundaries of any new flow regimes should be designated.

1.1 Definitions of Flow Patterns

There is still a lack of consistent definitions of flow patterns. Different terminology is often used to describe the same flow pattern by different investigators. In order to avoid confusion, the flow patterns in a bubble column and/or a three-phase fluidized bed are defined, based on characteristics of bubbles, as follows:

- 1) **Dispersed bubble flow:** The dispersed bubble flow regime predominates at high liquid velocities and at low to intermediate gas velocities. In this regime, no significant bubble coalescence occurs, even though the bubble population may be very high. The bubbles are small and of relatively uniform size. It is commonly believed that the small uniform bubbles result from turbulence of the liquid phase in gas-liquid systems (Taitel et al., 1980) and from the presence of large particles in three-phase systems (Fan, 1989).

- 2) **Discrete bubble flow:** This regime predominates at low gas and low liquid velocities. Due to the low gas velocity, the initial bubble size is small when a gas distributor with small holes is used and the bubble frequency is low, giving little chance for the bubbles to coalesce. The overall bubble characteristics are similar to those in the dispersed bubble flow regime, i.e. the bubbles are small with a narrow size distribution.
- 3) **Coalesced bubble flow:** In this regime, bubbles tend to coalesce. Both the bubble size and the bubble velocity are large and show wide distributions. Coalesced bubbles rise near the axis of the column with high velocities, causing violent agitation of the bed. Bubbles with spherical, ellipsoidal and spherical-cap shapes of various sizes are observed. This regime predominates at low liquid and intermediate gas velocities.
- 4) **Slug flow:** In this regime most of the gas phase rises as large bullet-shaped bubbles (often called Taylor bubbles or slugs) which have volume-equivalent diameters almost equal to, or greater than, the column diameter. Some small gas bubbles exist in the multiphase plugs which separate the successive large gas bubbles or slugs.
- 5) **Churn flow:** Churn flow has some similarities to slug flow, but the flow pattern is much more chaotic, frothy and disordered. The bullet-shaped bubbles become narrow, and their shapes distorted. Small bubbles in the multiphase plugs coalesce, generating new Taylor bubbles. Downward motion of the liquid phase at the walls becomes more significant as the superficial gas velocity is increased. Oscillatory longitudinal motion of the liquid in alternating directions can be observed in the multiphase regions.
- 6) **Bridging flow:** Bridging flow is a transition regime between churn flow and annular flow. Taylor bubbles are distorted and elongated in bridging flow. Multiphase plugs become very short, and finally only some multiphase layers or bridges exist between successive

Taylor bubbles. These multiphase layers are repeatedly destroyed by the high gas holdup in the core region of the column. At the same time, new multiphase layers can be observed at the bottom of the column due to downward flow of the liquid phase in the annular region. As this happens, liquid accumulates and forms new bridges which are again lifted or destroyed by the gas.

- 7) **Annular flow:** Annular flow is characterized by a continuous gas phase along the core of the column. The liquid phase moves upwards partly as a wavy annular liquid film and partly in the form of drops entrained by the gas in the core of the column.

A schematic diagram for the different flow patterns is presented in Figure 1.4. Many factors influence flow patterns and their transitions, such as physical properties of the gas and the liquid, geometry of the column and design of the gas distributor. Flow patterns and their transitions also depend on the location at which observation and measurement are carried out, as well as the distance between this location and the exit of the fluids.

For three-phase systems, the three operating regimes can be defined based on the state of particle motion. In a **fixed bed**, particles remain motionless, and the drag force on the particles induced by the flow of a gas-liquid mixture is smaller than the effective weight of the particles. In a **fluidized bed**, particles move within the system, and the drag force on the particle counterbalances the effective weight of the particles. In the **transport flow** regime, at high gas and/or liquid flow rates, solid particles are entrained from the column. If no makeup particles are added to the column, a particle-free two-phase flow then results. Within the transport flow regime, flow patterns can also be characterized as dispersed bubble flow, slug flow, churn flow, bridging flow and annular flow, depending on the gas and liquid flow rates.

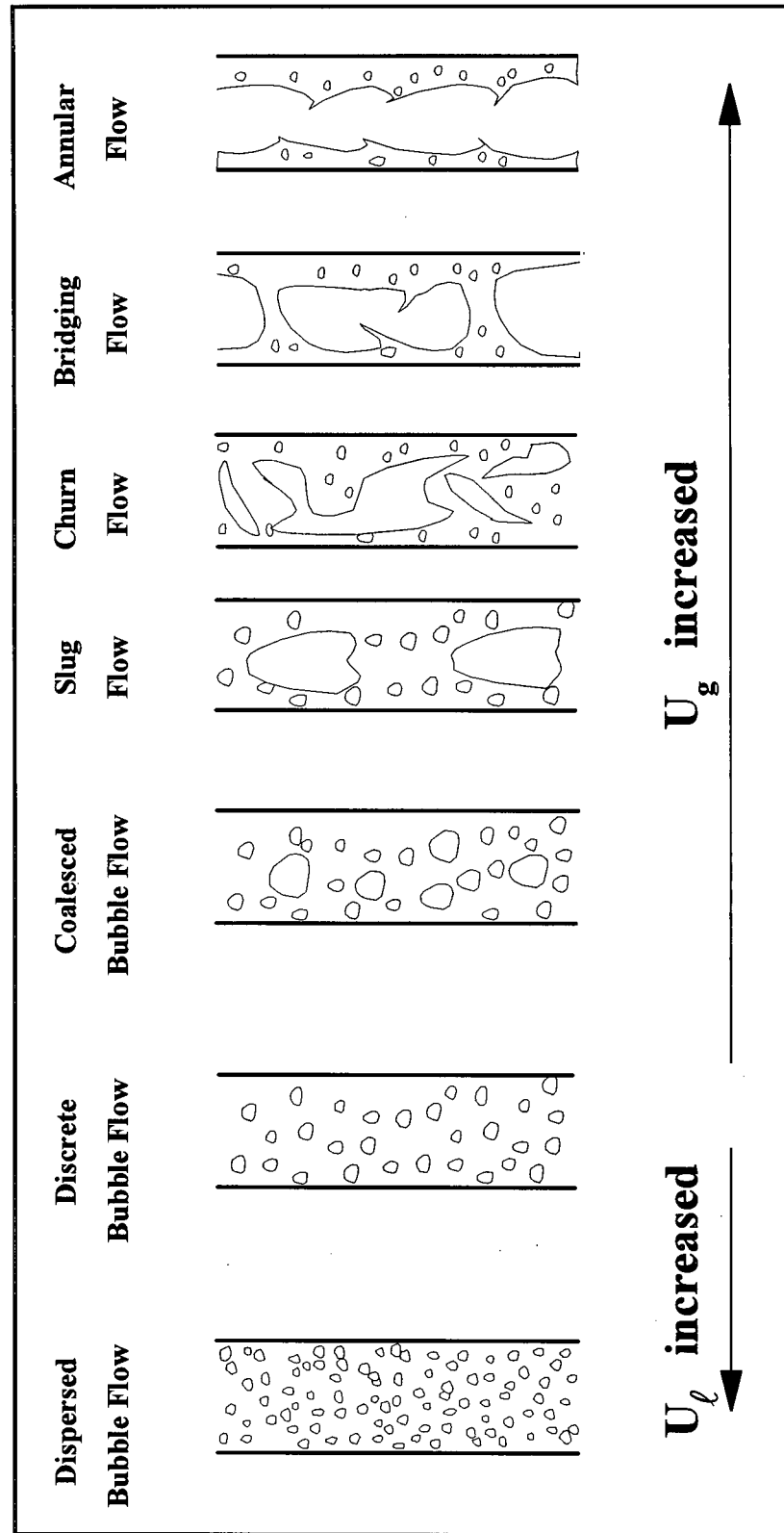


Figure 1.4. Schematic diagram of flow patterns.

1.2 Scope of Work

Since flow patterns affect transport phenomena, such as mass and heat transfer, numerous studies have been devoted to flow regime identification and flow regime transitions in cocurrent upward gas-liquid flow (Nakazatomi et al., 1992; Monji, 1993; also see Table 3.1) and in three-phase fluidization (Fan et al., 1985; Jean and Fan, 1987; Song et al., 1989; also see Table 3.2). Most studies have been based on visual observation (Griffith and Wallis, 1961; Ermakova et al., 1970; Mukherjee et al., 1974; Muroyama et al., 1978; Taitel et al., 1980; Spedding and Nguyen, 1980; Weisman and Kang, 1981; Fernandes et al., 1983; Fan et al., 1984; Matsuura and Fan, 1984; Fan et al., 1985; Fan et al., 1986; Hasan and Kabir, 1992). However, due to the rapid and chaotic nature of multiphase flow, visualization may not be a reliable method of distinguishing flow regimes. This method is also unsuitable for non-transparent columns, such as three-phase fluidized beds in commercial units.

The objectives of this work are: (1) to develop a measurement technique that can be used to determine gas-liquid and gas-liquid-solid flow regime transitions objectively, explore new flow regimes at higher superficial gas velocities and delineate the boundaries between each flow regime, and (2) to delineate the boundaries between fixed bed, fluidized bed and particle transport flow.

Since the definitions of most flow patterns are based on bubble characteristics, the criteria for flow regime transitions should be based on these characteristics. An electrical conductivity probe has been used to measure bubble characteristics. The configuration of the probe, as well as data acquisition and data processing techniques, are described in Chapter 2.

Aside from visual observations, other instrument methods for distinguishing flow regimes have been reported based on pressure transducers, conductivity probes and X-ray measurement systems (Vince and Lahey, Jr., 1982; Kitano and Ikeda, 1988; Mao and Dukler, 1989; Lee et al., 1990; Han and Kim, 1990; Franca et al., 1991; Soria and de Lasa, 1992). Chapter 3 summarizes alternative measurement techniques and criteria for flow regime transitions. Some preliminary tests carried out to investigate the different techniques and criteria are then presented.

In Chapter 4 the criteria for flow regime transitions are proposed for two-phase (gas-liquid) systems based on experimental results of bubble characteristics. These gas-liquid results and criteria serve as a basis for the subsequent investigation of gas-liquid-solid systems in later chapters. A flow regime map for the gas-liquid (air-water) system is also presented in Chapter 4.

Chapter 5 presents detailed bubble characteristics, such as bubble frequency, bubble chord length and its distribution as well as bubble rising velocity in different gas-liquid flow patterns. The variation of the bubble characteristics with operating conditions in an air-water system is also presented in this chapter.

On adding solid particles to a gas-liquid system, the first issue which might arise is the transition between a fixed bed and a fluidized bed, i.e., determination of the incipient fluidization velocity. Chapter 6 presents experimental results and theoretical models for minimum fluidization velocity in three-phase fluidized beds. Seven different kinds of particles were tested in this study. A successful new model is proposed based on this work. Another issue is the boundary between a fluidized bed and a solids transport flow regime, i.e., the particle transport velocity in a cocurrent gas-liquid flow. A theoretical model and an empirical correlation are proposed, based on experiments with three different types of particles and data available from the literature.

An experimental study of flow regime transitions in a three-phase fluidized bed is presented in Chapter 7. The measurement technique and the criteria for flow regime transitions are identical to those already described for the two-phase gas-liquid system. Three kinds of solid particles are used to demonstrate the effect of particle size and particle density on flow regime transitions. Five empirical correlations for the boundaries between the flow regimes in three-phase fluidized beds are proposed, based on the present study. These correlations are then compared with data from the literature. Reasonable agreement is found between the predictions and the literature data.

Bubble characteristics for a three-phase fluidized bed are presented in Chapter 8. Bubble frequency, chord length and its distribution, as well as rise velocity in different flow regimes are discussed in this chapter. Conclusions of this study and recommendations for future work are provided in Chapter 9.

Chapter 2

Experimental Apparatus and Measurement Methods

A 2D Plexiglas column, of rectangular cross-section 300 mm by 13 mm and 2.0 m high, was used in this work to qualitatively observe the flow patterns at different operating conditions and the interaction between a conductivity probe and bubbles. However, all quantitative experiments in this work were carried out in a 3D Plexiglas column, of circular cross-section 82.6 mm in diameter, as described below. Both columns and their auxiliaries were designed, constructed and assembled for the present project.

2.1 Apparatus

The main component of the experimental apparatus consisted of a 0.0826 m diameter by 2 m high Plexiglas column with a perforated gas-liquid distributor plate containing 62 2-mm circular holes (covered by a stainless steel screen). The region below the distributor plate was a 0.5 m long gas-liquid calming section packed with 1/2 inch (13 mm) ceramic intalox saddles as shown in Figure 2.1.

A three-phase separator was designed, built and attached to the top of the column. A schematic diagram (proportionally scaled) of this separator is shown in Figure 2.2. The three-phase mixture rising from the main column entered the separator from its bottom. The gas phase was led to a draft tube with a conical lower section (1) and then ventilated by a gas vent cylinder (2). The liquid-solid mixture was forced into the liquid-solid region (III) from the lower end of the gas vent cylinder (2) by the static head of the three-phase mixture inside the cylinder. In the liquid-solid region, a liquid-solid fixed/fluidized bed was formed which provided a clear bed surface allowing pure liquid to overflow into the outer liquid channel (IV) from where it passed to the drain. A successful design should prevent the gas phase from reaching the liquid-solid region,

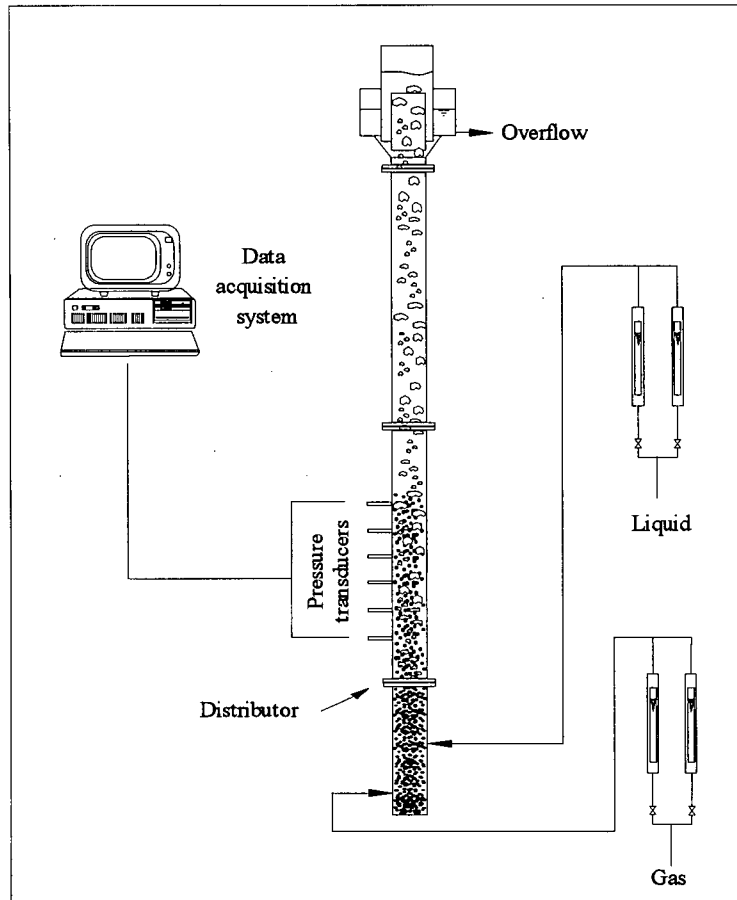


Figure 2.1. Schematic diagram of experimental apparatus.

since in a three-phase system entrainment of solid particles is mainly caused by bubble wakes (Dayan and Zalmanovich, 1982; El-Temtamy and Epstein, 1989; Page and Harrison, 1974). This was achieved with the aid of the draft tube (1). The apparent density in the draft tube is significantly lower than in region II due to the presence of gas phase in region I. Hence, a circulation is created between regions I and II. This circulation prevents gas bubbles from entering region III, while, at the same time, causing the particles to return to the main column near the lower end of the draft tube (1).

This separator allowed experiments to be carried out for a very wide range of operating conditions. At high gas and liquid flow rates, most particles were carried over into the separator

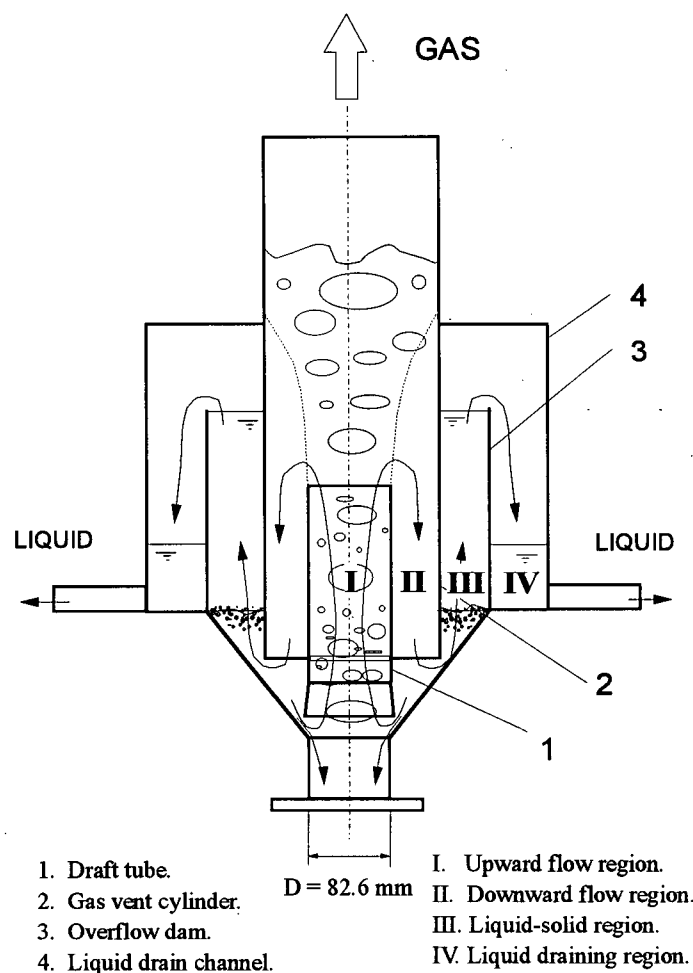


Figure 2.2. Schematic diagram of three-phase separator.

where they spent considerable time in the liquid-solid region (III). Even under solid transport flow conditions, no particles were carried out of the separator with the liquid or gas stream. A top-dense bottom-dilute solid concentration profile was observed in the main column at very high gas and liquid velocities due to the build-up of particles in the separator at the top of the column.

Air and tap water were used as the gas and liquid phases respectively throughout the work described in this thesis. The water temperature was measured at the outlet to determine the liquid viscosity and density, while gas and liquid flow rates were measured by inlet rotameters. The gas velocity was corrected for the pressure difference between the rotameters and the bottom of the

Table 2.1. Properties of particles investigated.

Type of particles	d_p , mm	ρ_s , kg / m ³	ϵ_o , —	ϕ , —
Glass beads	1.5	2530	0.39	1.0
	2.5	2520	0.39	1.0
	3.7	2510	0.38	1.0
	4.5	2490	0.37	1.0
Glass beads coated with TFE	2.5	2520	0.39	1.0
Sand	2.4	2610	0.39	0.8
Steel shot	1.2	7510	0.41	1.0

column. The superficial gas velocities ranged from 0 to 6.9 m/s, while the superficial liquid velocity was varied from 0 to 0.4 m/s in this study. Seven different particle types with measured properties as given in Table 2.1 were used in the investigation of incipient fluidization at low to intermediate gas velocity (Chapter 6). The particle diameter was measured by a vernier caliper based on one hundred particles. The particle density and the static bed voidage were determined by pouring a known weight of particles into a cylinder containing water, measuring both the water level increase and the bed volume. Three of these types of particles, glass beads of diameters 1.5 and 4.5 mm as well as steel shot of diameter 1.2 mm, were also chosen for the investigation of incipient fluidization at high gas velocity, transition from fluidized bed to transport flow regimes (Chapter 6) and bubble-characteristic flow regime transitions within fluidized beds (Chapter 7). Except for the sand ($\phi \approx 0.8$), sphericities were all very nearly unity. Glass beads coated with TFE (Teflon) were used to investigate the effect of wettability on minimum fluidization velocity, while the steel shot allowed study of the effect of particle density.

2.2 Measurement Techniques

In order to study the flow regime transitions objectively, quantitative measurements were required. In this study, pressure transducers and a conductivity probe were utilized for this

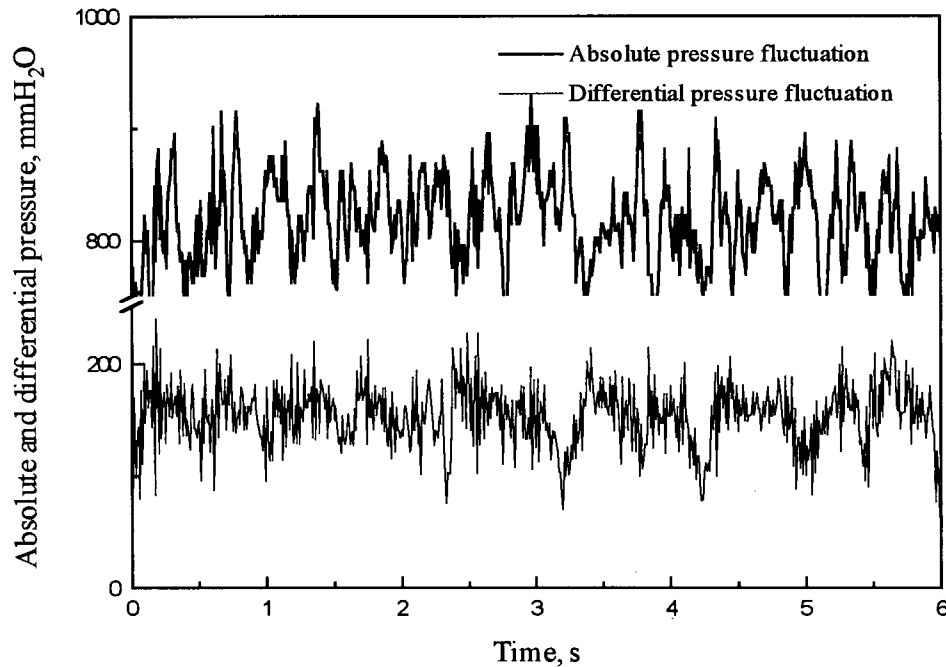


Figure 2.3. Typical pressure fluctuation signals in an air-water system, $Z = 1.35$ m; $\Delta Z = 0.1$ m; $U_\ell = 0.018$ m/s; $U_g = 0.041$ m/s.

purpose. A personal computer (IBM 486-DX2) with a data acquisition board (Keithley DAS-1202) was used for data logging and data analysis.

2.2.1 Pressure Transducers

Several pressure transducers (Omega PX603) were employed to determine pressure gradients along the column, absolute pressure fluctuations and differential pressure fluctuations. Since the dominant frequency of the pressure fluctuations was around 10 Hz (Tutu, 1982; Matsui, 1984, 1986; Fan et al., 1986; Nishiyama et al., 1989; Franca et al., 1991; Spedding and Spence, 1993; Kwon et al., 1994), the data logging sampling rate was set at 100 Hz (an order of magnitude greater than the dominant frequency).

Typical absolute and differential pressure fluctuation raw signals are shown in Figure 2.3. The probability density distribution, mean value, standard deviation, skewness and kurtosis of the signals were calculated based on the definitions given by Snedecor and Cochran (1989).

Consider a voltage-time trace signal $V(t)$, where the voltage scale is divided into equal increments of width ΔV and the time scale into Δt equal increments. If, during the observation period t , the voltage is within the range $(V_i - \Delta V/2, V_i + \Delta V/2)$ for a total of n_i times, then the Probability Density Distribution Function (PDF), $p(V_i)$, is defined as:

$$p(V_i) = \lim_{\Delta V \rightarrow 0} \frac{P(V_i, \Delta V)}{\Delta V} = \lim_{\Delta V \rightarrow 0} \frac{1}{\Delta V} \left(\lim_{t \rightarrow 0} \frac{n_i \Delta t}{t} \right) \quad (2.1)$$

where $P(V_i, \Delta V)$ is the probability distribution function and $\sum_{i=1}^N P(V_i, \Delta V) = 1$, $N = \frac{V_1 - V_0}{\Delta V}$.

The Mean value of $V(t)$ is given by

$$\bar{V} = \sum_{i=1}^N V_i P(V_i, \Delta V) \quad (2.2)$$

The Variance and the Standard Deviation (σ_v) of $V(t)$ are given respectively by

$$\text{Var} = \sum_{i=1}^N (V_i - \bar{V})^2 P(V_i, \Delta V) \quad (2.3)$$

and

$$\sigma_v = \sqrt{\text{Var}} \quad (2.4)$$

Similarly, the Skewness (M_3) and Kurtosis (M_4) of $V(t)$ are defined respectively as

$$M_3 = \sum_{i=1}^N (V_i - \bar{V})^3 P(V_i, \Delta V) \quad (2.5)$$

and

$$M_4 = \sum_{i=1}^N (V_i - \bar{V})^4 P(V_i, \Delta V) \quad (2.6)$$

The physical meaning of each of these moments can be explained as follows: The mean is the average value of a distribution. The variance is a measure of the distribution about the mean. The skewness is a measure of the asymmetry of a distribution. A symmetric distribution, such as a normal distribution, has zero skewness since the mean and the median coincide. A unimodal distribution, which has a median to the left of the mean, i.e. it is skewed to the left, has negative skewness. If the distribution is skewed to the right, it has a positive skewness. The kurtosis (flatness) is a measure of the distribution's peakedness.

2.2.2 Conductivity Probe

A conductivity probe was used to measure local bubble characteristics, such as bubble frequency, bubble volume fraction, bubble time (defined later), bubble velocity and bubble chord length.

Numerous methods have been reported for obtaining information on bubble characteristics. Three kinds of methods have primarily been employed for observing the behavior of bubbles in fluidized beds: a) photographic methods with a "two-dimensional" column, b) non-invasive methods and c) intrusive probe techniques. The most common method to obtain information on bubble characteristics in fully three-dimensional columns is the intrusive probe technique. Several kinds of probes have been utilized including: capacitance probes (e.g. Geldart and Kelsey, 1972; Werther, 1974; Wittmann et al., 1981; Gunn and Al-Doori, 1985), electro-resistivity or conductivity probes (Park et al., 1969; Rigby et al., 1970; Ueyama et al., 1980; Burgess et al., 1981; Matsuura and Fan, 1984; Choi et al., 1988) and optical fiber probes (de Lasa

et al., 1984; Hatano et al., 1986; Glicksman et al., 1987; Lee and de Lasa, 1987,1988; Yu and Kim, 1988; Han and Kim, 1990, 1993; Lee et al., 1990).

Since conductivity probes (or electrical impedance probes) are easy to manufacture, and due to their economy and rapid response, this type of probe was chosen in this study. The simplicity, convenience and low-cost are the major advantages of electro-resistivity or conductivity probes. However, if the continuous phase were not conductive, an electro-resistivity probe might be unsuitable. Another problem can occur when bubbles strike the probe; slow drainage of a liquid film surrounding the probe can cause a delay in the signal response (Hewitt, 1978; Burgess et al., 1981). These problems were overcome in this study by using a conductive liquid (water in this work) and reducing the exposure area of the conductivity probe.

The configuration of the two-element conductivity probe is shown in Figure 2.4. Two 0.31 mm diameter wires are used as electrodes, with only their ends electrically exposed to the

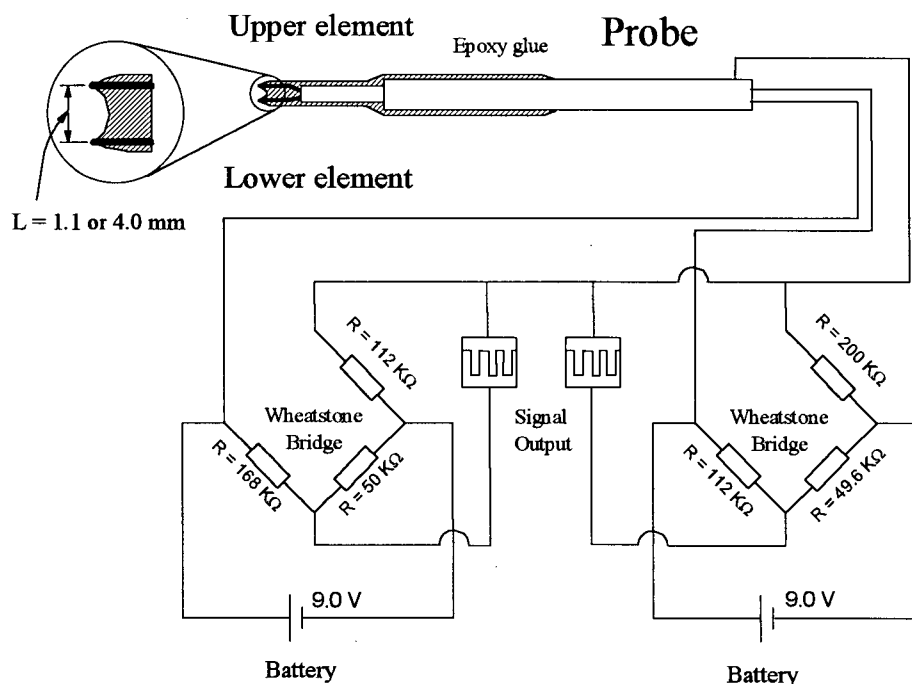


Figure 2.4. Configuration of conductivity probe.

multiphase mixture. This design minimized the film effect of the probe. A stainless steel tube of 5.0 mm outer diameter serves as the common ground electrode for both wires. Two Wheatstone bridges are connected with this probe to obtain electrical voltage signals. This probe was developed in a semi-circular cross-section bubble column and the interaction between the probe and bubbles was observed in the 2D column, before it was used in the 3D column.

Two probes of different wire spacing (see enlarged view in Figure 2.4, $L = 1.1$ and 4.0 mm) were used in this study. The one with the smaller wire interval was used to measure small bubbles at low gas velocities, while the other was utilized for large bubbles at high gas velocities. Each of these probes was inserted into the column horizontally so that the ends of these two wires were aligned vertically at the axis of the column.

A typical raw signal is presented in Figure 2.5. The high voltage output corresponds to the

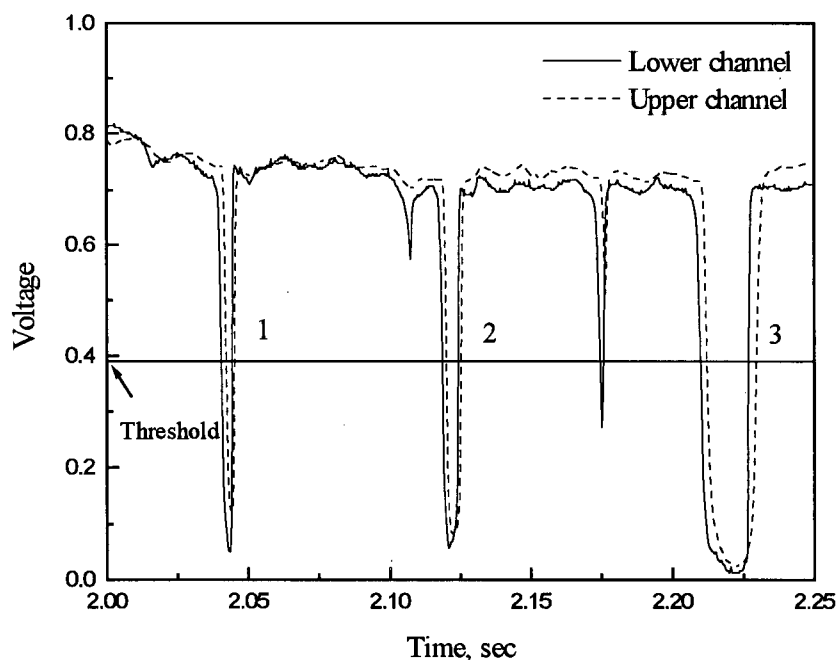


Figure 2.5. Typical raw signals of a two-element conductivity probe in an air-water system, $Z = 1.95$ m; $L = 1.1$ mm; $U_\ell = 0.018$ m/s; $U_g = 0.086$ m/s.

liquid phase, and the low peaks to the gas phase. When bubbles strike the probe, pulses can be read from the signal output. For this particular example, four bubbles are detected by the lower element of the probe, while three by the upper element. It can be seen that there is a time shift between lower and upper element outputs. A threshold can be set between the low and high voltage output to distinguish gas bubbles and allow bubble characteristics to be computed. Detailed data processing techniques are discussed further below.

Probe response time can be estimated from raw signals (Burgess and Calderbank, 1975; Burgess et al., 1981). Figure 2.6 shows detailed information on the first bubble in Figure 2.5. The probe response time, Δt , for the lower element is 1.2 ms. The time shift between the two elements, τ_1 , is 1.6 ms. The time during which the lower element is enveloped by the bubble, called the bubble time t_i , is 4.0 ms. By setting a threshold, the bubble velocity, U_b , and the bubble

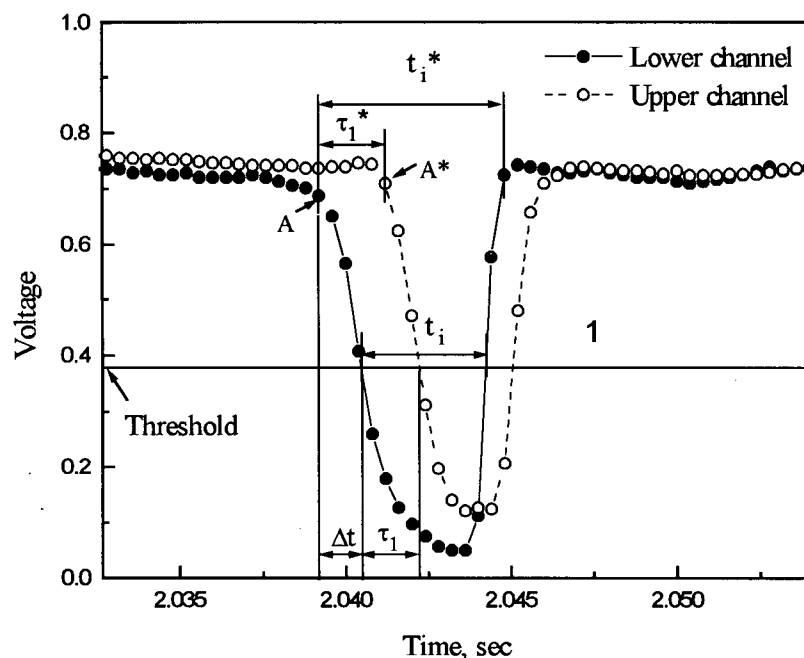


Figure 2.6. Response of conductivity probe to a gas bubble in an air-water system, $Z = 1.95$ m; $L = 1.1$ mm; $U_l = 0.018$ m/s; $U_g = 0.086$ m/s.

Table 2.2. Effect of probe time response on measured bubble velocity and bubble chord length.

Bubble No. in Fig. 2.5	Δt , ms	U_b , m/s $= L/\tau_1$	U_b^* , m/s $= L/\tau_1^*$	Relative % difference between U_b^* and U_b	ℓ_b , mm $= t_i U_b$	ℓ_b^* , mm $= t_i^* U_b^*$	Relative % difference between ℓ_b^* and ℓ_b
1	1.20	0.69	0.55	25.5	5.8	8.1	-28.4
2	1.20	0.69	0.69	0.0	8.1	10.0	-19.0
3	1.60	0.46	0.39	17.9	37.5	43.6	-14.0

chord length, ℓ_b , can be calculated, based on τ_1 and t_i . An alternative method to calculate U_b and ℓ_b is based on τ_1^* and t_i^* , which may avoid the effect of probe response time. However, the latter causes difficulty in searching positions A and A* (see Figure 2.6) and also takes too much time for data processing. The results for all three bubbles which pass the threshold for both channels in Figure 2.5 are summarized in Table 2.2.

It is seen that the probe response time is of the order of ms and the difference between the results with and without consideration of probe response time is 0 to 26% and -14 to -29% for the bubble velocity and the bubble chord length, respectively. It also can be seen that without taking into account the probe response time, the measured bubble chord length may be underestimated. However, this is generally acceptable from an engineering point of view, especially when discrimination logic (described below) is applied to the signal analysis to screen out obliquely rising gas bubbles for the calculation of bubble velocities and chord lengths.

2.3 Data Processing

For the conductivity probe, the data processing included data logging and data analysis. In order to obtain enough signal resolution for calculating bubble velocity and bubble chord length, the data logging sampling rate had to be 2500 Hz or higher. This reduced the total test time (due to the limitation of computer memory) and generated large size data files. Hence a computer

program which can log the original signal, extract all useful information and then discard the original data had to be developed.

2.3.1 Threshold

When a bubble strikes the probe, a pulse can be read from the signal output. As shown in Figure 2.5, the original signal is not a perfect square wave, due to high frequency noise and the time response of the probe. A threshold was set to distinguish whether a probe was surrounded by a gas bubble or by a liquid-solid mixture. This is a critical value which affects the calculated results of bubble chord length and local gas holdup. Depending on the probe response time, the amplitude of noise and any fluctuation in the conductivity of the liquid-solid mixture, the threshold value has been set differently by different investigators. Matsuura and Fan (1984) and Rigby et al. (1970) set the threshold at 80% of the high level of the amplified signal intensity; Werther (1974) set it at 50%. Gunn and Al-Doorri (1985) found that setting the threshold voltage in the range of -12 to -25 mV could yield an accurate result when the voltage amplitude was -2V for their measurement system.

Since the output voltage of the conductivity probe fluctuated for the probe within the liquid phase (see Figure 2.5), the threshold in this study was set based on the Probability Density Distribution Function, PDF, rather than basing it on the mid-point between the minimum and maximum values of the raw signal. For a bimodal distribution of the PDF, it was set at the average of these two peak locations (i.e., half way between the two peak locations). For a single peak, it was set mid-way between peak location and the minimum or maximum of the signal voltage, depending on the skewness of the signal. Several different thresholds have been set to check the effect of the threshold on the experimental results. It was found that when the threshold was in the range from 25% to 75% of the PDF peak locations, the results did not vary significantly, especially when using the results to determine flow regime transitions.

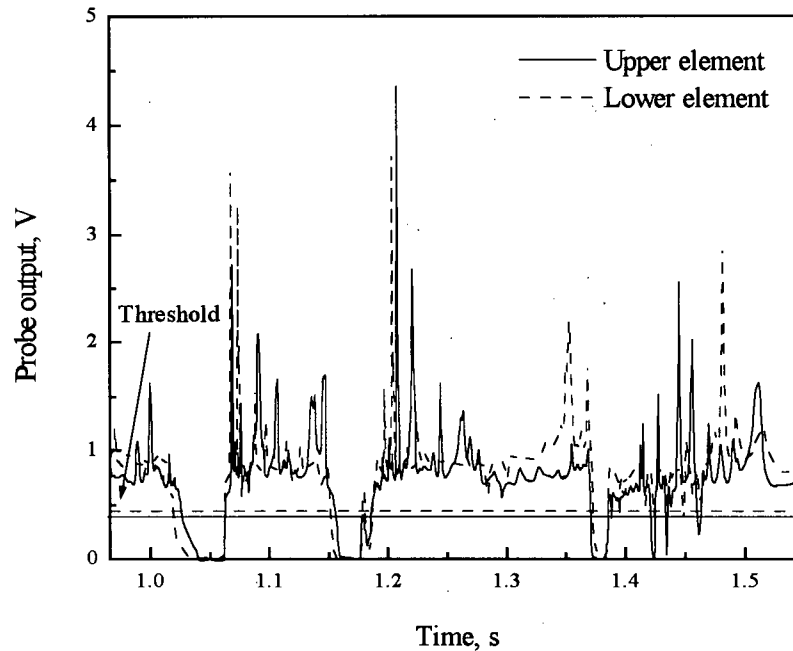


Figure 2.7. Typical conductivity probe signal for steel shot three-phase system,

$$U_{\ell} = 0.036 \text{ m/s}; U_g = 0.037 \text{ m/s}; Z = 0.65 \text{ m}.$$

When steel shot was used in a three-phase system, the electrical conductivity of the solid particles affected the probe output. Figure 2.7 shows a typical result for a steel shot/air/water system. When a particle hits the end of the probe, an upward spike appears on the trace. This is probably due to the effect of particle surface, which increases the contact area of the probe when the particle makes contact with it. The threshold was set half way between the liquid and the gas output voltages as shown in Figure 2.7.

2.3.2 Signal Simplification and Bubble Frequency

Since the sampling rate and the test time are high, it is impossible and unnecessary to store all the original data. Once the threshold is set, the original signal can be simplified into a square wave form as shown in Figure 2.8. In this study, the time when a bubble struck the probe and the

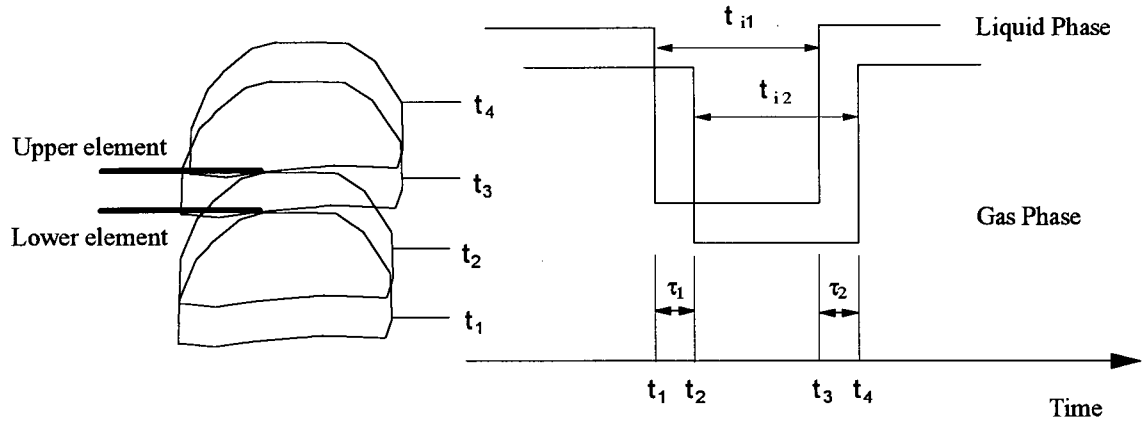


Figure 2.8. Idealized square-wave relationship between probe, bubble and simplified signal.

time when this bubble left the probe were recorded. Thus, the size of the data file was reduced significantly, without losing the essential information for the purpose of calculating bubble properties.

The bubble frequency, f , was obtained by counting the number of pulses within the test time, i.e.

$$f = \frac{M}{t_{\text{tot}}} \quad (2.7)$$

where M is the total number of bubbles detected and t_{tot} is the total test time.

2.3.3 Bubble Time and Local Gas Holdup

The bubble time, t_i , is defined as the width (i.e. duration) of the pulse as indicated in Figure 2.8. It represents the duration of the probe being immersed in the bubble. This parameter is a function of the bubble size, bubble velocity, bubble shape, position where the probe pierces the bubble, and the angle with which the bubble travels relative to the vertical direction. Here t_i was calculated from (see Figure 2.8):

$$t_{i1} = t_3 - t_1 \quad \text{or} \quad t_{i2} = t_4 - t_2 \quad (2.8)$$

The time average local gas holdup, ε_g , was calculated from:

$$\varepsilon_g = \frac{1}{t_{\text{tot}}} \sum_{i=1}^M t_i \quad (2.9)$$

The bubble time is related to both the bubble frequency and local gas holdup, i.e.

$$t_i = \frac{\ell_{bi}}{U_{bi}} \quad (2.10)$$

where U_{bi} and ℓ_{bi} are the velocity and the chord length of an individual bubble, respectively, providing the bubble rises vertically. The average value of t_i is defined as:

$$\bar{t}_i = \frac{1}{M} \sum_{i=1}^M t_i \quad (2.11)$$

Combining Eqs. (2.7), (2.9) and (2.11) leads to:

$$\bar{t}_i = \frac{\varepsilon_g}{f} \quad (2.12)$$

In other words the average bubble time is the ratio of the gas holdup to the bubble frequency.

2.3.4 Bubble Velocity and Bubble Chord Length

A number of investigators have utilized two-element probes to detect bubble velocity and chord length (e.g. Rigby et al., 1970; Tutsui and Miyauchi, 1980; Ueyama et al., 1980; Wittmann et al., 1981; Lee and de Lasa, 1988; Yu and Kim, 1988; Lee et al., 1990; Han and Kim, 1993). Although some of these studies used an optical fiber probe instead of a conductivity probe or an impedance probe, the principle was the same.

With a two-element probe, the bubble velocity, U_b , and bubble chord length, ℓ_b , can be computed if the vertical distance, L , between the two elements is known, providing all bubbles rise vertically, i.e.

$$U_b = \frac{L}{\tau_1} \quad \text{or} \quad U_b = \frac{L}{\tau_2} \quad (2.13)$$

$$\ell_b = U_b \times t_{i1} \quad \text{or} \quad \ell_b = U_b \times t_{i2} \quad (2.14)$$

In practice, after an original signal has been simplified to a square wave, a logic circuit is needed to select signals created by bubbles which are travelling upwards. This is because: (1) a bubble detected by the lower element may be deflected and never contact the upper element; (2) one bubble may be detected by the lower element while another bubble reaches the upper element at almost the same time; (3) if a bubble rises obliquely, the effect of bubble shape may cause significant error in U_b and ℓ_b when equations (2.13) and (2.14) are used.

Matsuura and Fan(1984) set their logic circuit as follows (see Figure 2.8):

(1). The signal for the upstream element is used as a trigger signal.

(2). They required $t_1 < t_2$ and $t_3 < t_4$.

(3). They further required $0.9 < \frac{\tau_1}{0.5(\tau_1 + \tau_2)} < 1.1$

They claimed that 50% or fewer of the signal pairs detected by their probe were ignored for typical dispersed bubble flow, whereas about 65% or fewer were neglected for the coalesced bubble flow regime and 80% or fewer for the slug flow regime.

It should be noted that without the logic circuit to select the signal, there is a significant error when U_b and ℓ_b are calculated. For example, the apparent bubble chord length could have been greater than the column diameter when the column was operated in the discrete bubble flow

regime or the coalesced bubble flow regime. A recent study (Lim and Agarwal, 1992) revealed that the principal error results from bubbles with non-vertical rise.

The logic circuit in this study required for acceptance the following criteria (see Figure 2.8):

1. $t_1 < t_2 < t_3 < t_4$
2. $0.9 < \frac{t_{i1}}{0.5(t_{i1} + t_{i2})} < 1.1$

The first criterion screens out signals created by different bubbles. Only those bubbles which contacted the lower element first and then the upper element were considered for computing the bubble velocity and the bubble chord length. The second criterion screened out signals created by bubbles with a significant non-vertical component of rise velocity. Although this logic circuit did not guarantee that all bubbles selected were rising vertically, it helped reduce the error from the two-element probe.

Almost all investigators have recognized that the measured bubble chord length distribution is not equal to the real bubble size distribution. There is a relationship between these two parameters which depends strongly on the bubble shape. If the measured bubble length distribution and the bubble size distribution at the measuring period are $Z(\ell_b)$ and $R(d_b)$, respectively, then:

$$Z(\ell_b) = \int_{\ell_b}^{\infty} p(d_b, \ell_b) R(d_b) d(d_b) \quad (2.15)$$

where $p(d_b, \ell_b)$ is the probability density function of measured chord length, ℓ_b , when the bubble diameter is d_b . For spherical bubbles, $p(d_b, \ell_b)$ can be expressed (e.g. Werther, 1974; Tutsui and Miyauchi, 1980; Matsuura and Fan, 1984; Clark and Turton, 1988; Han and Kim, 1993) by:

$$p(d_b, \ell_b) = \begin{cases} \frac{2 \ell_b}{d_b^2} & \text{for } d_b > \ell_b \\ 0 & \text{for } d_b < \ell_b \end{cases} \quad (2.16)$$

For bubbles of other shapes, expressions for $p(d_b, \ell_b)$ are given by Clark and Turbva (1988).

2.3.5 Data Processing Procedure

A computer program was developed to perform data acquisition and data processing. The flow chart of the program is shown in Figure 2.9. The sampling rate was 2500 s^{-1} . In principle, the higher the sampling rate the better. However, the higher sampling rate reduces the sampling time due to the finite computer memory. With the sampling rate of 2500 s^{-1} , 3 s bursts could be handled.

For each 3 s sub-sample, the probability distribution function, $P\{V/V_{\max}, \Delta(V/V_{\max})\}$ was calculated, where $\Delta(V/V_{\max}) = 0.01$ in this study. The reason for using V/V_{\max} is to overcome the shift of the signal; also it is dimensionless. The threshold was based on the Probability Distribution Function. Then the original signal was simplified and the condensed information stored.

Data logging was terminated when 500 bubbles had been detected or the total sampling time reached 120 seconds (i.e., 40 sub-samples, each of 3 s duration). The bubble frequency, local gas holdup and bubble time were computed for each element, using Equations (2.7), (2.9) and (2.8), respectively. The bubble velocity and the bubble chord length were then calculated after false signals and non-vertical rise bubble signals had been screened out by the logic circuit. The PDF and key moments of the bubble time, the bubble velocity and the bubble chord length were also obtained using Equations (2.1), (2.2) and (2.4), respectively. All computer programs are given in Appendix A.

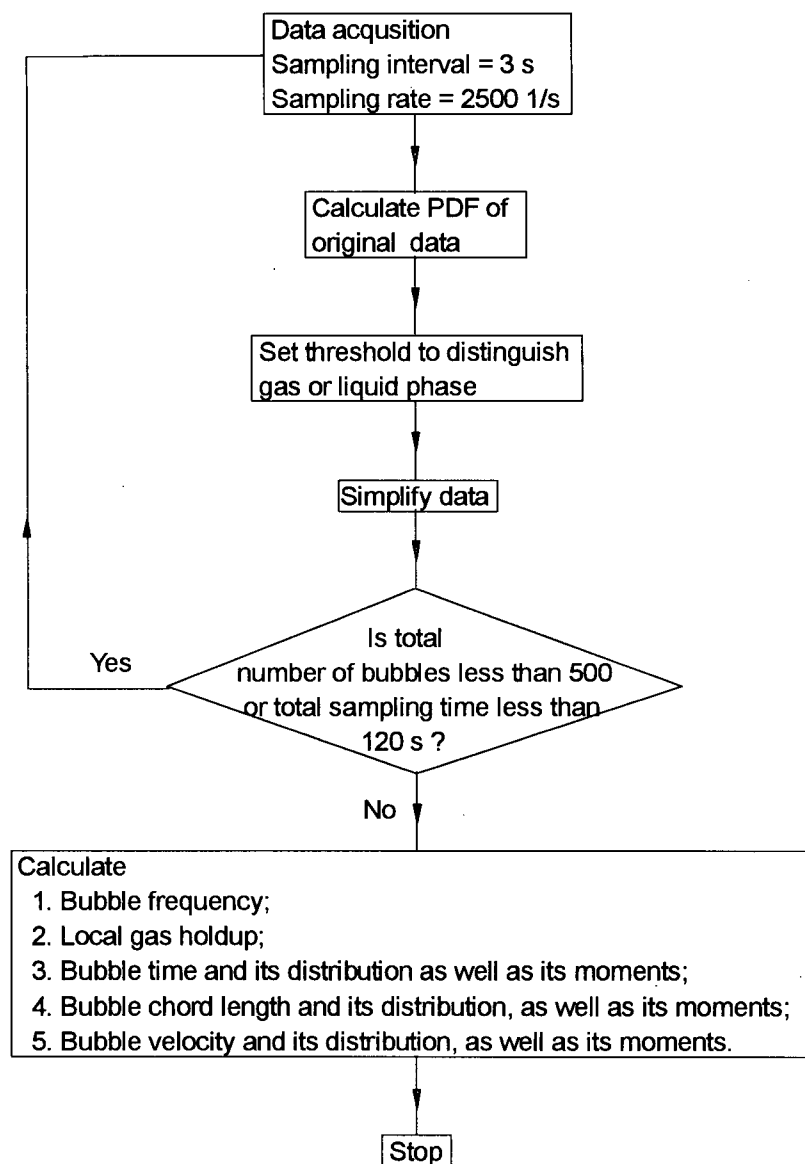


Figure 2.9. Flow chart for data processing.

Chapter 3

Experimental Methods

3.1 Introduction

Flow regimes and their transitions can be determined by visual observation and instrument measurement. Most previous studies have been based on visual observation (e.g., in gas-liquid systems: Griffith and Wallis, 1961; Spedding and Nguyen, 1980; Taitel et al., 1980; Weisman and Kang, 1981; Fernandes et al., 1983; Hasan and Kabir, 1992; in gas-liquid-solid systems: Ermakova et al., 1970; Mukherjee et al., 1974; Muroyama et al., 1978; Fan et al., 1984; Matsuura and Fan, 1984; Fan et al., 1985; Hu et al., 1985; Fan et al., 1986; Song et al., 1989; Nacef et al., 1992, 1995). Others have determined flow regimes with the aid of instruments, e.g., pressure transducers, conductivity probes and X-ray measurements (in gas-liquid two-phase systems: Vince and Lahey, 1982; Mao and Dukler, 1989; Franca et al., 1991; in three-phase systems: Kitano and Ikeda, 1988; Han and Kim, 1990; Lee et al., 1990; Soria and de Lasa, 1992).

Although visual observation provides direct information on the flow patterns, some difficulties occur due to the rapid and chaotic nature of multiphase flow. It is often difficult to identify the transition of flow patterns without quantitative means. Alternatively, various statistical measures, such as standard deviations, skewness, kurtosis, probability density functions or power spectrum functions, can be calculated from the signals obtained by the instruments. Criteria for flow transitions can then be set by analyzing these quantities. However, the results can differ significantly depending on the parameters measured and the criteria adopted. This chapter discusses existing instrumental methods for determining flow regime transitions.

3.2 Pressure Fluctuations

Absolute and differential pressure fluctuations reflect some characteristics of multiphase systems and can be detected readily using pressure transducers. Many investigators have used pressure fluctuations to study flow regime transitions. Standard deviations (SD), probability density functions (PDF) and power spectrum functions (PSF) of the pressure fluctuations have been calculated, and criteria for distinguishing flow regimes have been defined accordingly.

3.2.1 Previous Studies

3.2.1.1 Gas-liquid two-phase systems

Absolute pressure fluctuations were initially used by Tutu (1982) who found that the root mean square of the pressure fluctuations was much smaller in annular flow than in churn flow. Subsequently, Tutu (1984) reported that it is better to use differential pressure (ΔP) fluctuations to distinguish flow regimes. Two pressure transducers, vertically separated by a distance of $D/2$, were used to obtain the differential pressure fluctuations. It was found that the PDF of the ΔP fluctuations could be used as a criterion for bubble-slug transition. In bubble flow, a single peak near the value corresponding to the static head of the liquid phase was observed in the PDF plot. In annular flow, the PDF plot showed a single peak located at $\Delta P = 0$, corresponding to the gas phase. In slug and churn flows, a bimodal distribution was observed in the PDF plot. Hence, the PDF curve was divided into two parts at the minimum PDF value. The areas under the PDF curve for these two parts were calculated, one, A_g , corresponding to Taylor bubbles and the other, A_ℓ , to the liquid phase. When the fraction of the area, $A_g/(A_g + A_\ell)$, reached a minimum with respect to $\beta Fr_\ell^{-0.0375} - Fr_\ell^{-0.075}$, the transition from bubble to slug flow was assumed to occur, where $\beta = U_g/(U_g + U_\ell)$ and $Fr_\ell = U_\ell^2/(gD)$. An alternative method was suggested based on the standard

deviation (SD) of the ΔP fluctuations. The bubble/slug flow transition was claimed to occur at the inflection point in a plot of the standard deviation of the ΔP fluctuations vs. $\beta Fr_\ell^{0.31}$.

Matsui (1984, 1986) analyzed the differential pressure fluctuations of two differential pressure transducers. One, with a separation of $D/2$, was called the short-scale ΔP fluctuation probe; the other, with an interval of $10D$, was called the long-scale ΔP fluctuation probe. The PDFs of these two probes were used to determine various flow regimes. It was found that with the short-scale probe, bubble, annular and mist flow exhibited a single peak in the PDF plots, while bimodal PDFs corresponded to slug-like flow. With the long-scale probe, dispersed bubble, slug, annular and mist flow exhibited single-peaked PDFs too; however, twin-peaked PDFs appeared in churn flow. The moments (mean, standard deviation, skewness and kurtosis) of both short-scale and long-scale ΔP fluctuations showed different values in different flow regimes. The author proposed a flow chart to identify the respective flow regimes by using these parameters combined with 13 transition criteria, one for each of the parameters.

Franca et al. (1991) calculated the PDF and the power spectral density function (PSF) of ΔP fluctuations in a gas-liquid horizontal flow system. Although different shapes of the PDF resulted from various flow regimes, the authors claimed that these shapes were not explicit enough to be used to distinguish flow regimes. For the PSF, they claimed that a relatively continuous frequency range characterized wavy and annular flows, while a multi-peaked spectrum was associated with plug and slug flow. The authors also used fractal techniques to analyze the ΔP fluctuations. However, they asserted that neither the PSF nor the fractal technique could easily provide numerical criteria for flow regime identification.

3.2.1.2 Three-phase systems

Fan et al. (1986) determined flow regimes by analyzing the statistical properties of wall pressure fluctuations in a 0.102 m ID column. It was observed that the root mean square (RMS) of the pressure fluctuations decreased nearly linearly with U_ℓ in the coalesced bubble flow regime, while it remained constant or decreased slightly with U_ℓ in the dispersed bubble flow regime. On the other hand, the RMS of the pressure fluctuations increased linearly in the coalesced bubble flow regime and remained steady or increased slightly in slug flow. It was also observed that the power spectral density of the pressure fluctuations exhibited different shapes with different dominant frequencies in these three flow regimes. Although pressure transducers were used to collect information on absolute pressure fluctuations, the flow regime boundaries were determined by visual observation.

Kitano and Ikeda (1988) used pressure transducers to study the transition between dispersed bubble flow and the coalesced bubble flow regime. The integral of the power spectral density function of the pressure fluctuations between 0 and 10 Hz was used to detect the flow regime transition. For the dispersed bubble flow regime, this integral increased linearly with decreasing liquid velocity at a given gas flow rate. The transition from dispersed bubble flow to coalesced bubble flow was assumed to take place when the values began to deviate from this linear relationship. It was also found that there was a transitional regime between the dispersed bubble flow and the coalesced bubble flow regimes.

Absolute pressure fluctuations have also been used to determine the flow regimes for other three-phase reactors (Zheng et al., 1988; Chen et al., 1995).

3.2.2 Preliminary Tests

Pressure transducers are simple devices able to determine absolute pressure and/or differential pressure fluctuations in a multiphase flow system. In reviewing the definitions of the flow regimes, it can be seen that these definitions are based on multiphase flow characteristics such as bubble size, bubble shape, liquid motion and liquid film properties. There is a relationship between the flow characteristics and the pressure fluctuations. For example, when a single bubble rises in a stagnant liquid column, the pressure along the bubble centerline exhibits a significant fluctuation. But far away from the bubble centerline, this fluctuation becomes smaller, and finally vanishes. Another example: when bubbles are formed at an air injector, the injection of the bubbles causes a pressure disturbance; this disturbance can propagate throughout the whole column and can be registered by pressure transducers.

In order to clarify the relationship between the multiphase flow characteristics (or flow structure) and the pressure fluctuations, some simple experiments were performed.

3.2.2.1 Effect of single bubble injection on pressure fluctuations

In this test, four absolute pressure transducers (P1 to P4) were mounted 50, 150, 650 and 750 mm above the distributor of the 82.6 mm I.D. column. The total stagnant height of the water was 1.27 m. An air injector was located 250 mm above the distributor. The schematic diagram of the apparatus for this test is shown in Figure 3.1 (a).

Quickly opening and closing the gas valve of the injector was used to create a large bubble of the same diameter as that of the column. Several experiments were carried out to check the reproducibility. A set of typical results is shown in Figure 3.2. When the bubble was introduced into the column, a pressure disturbance could be observed immediately. This pressure disturbance

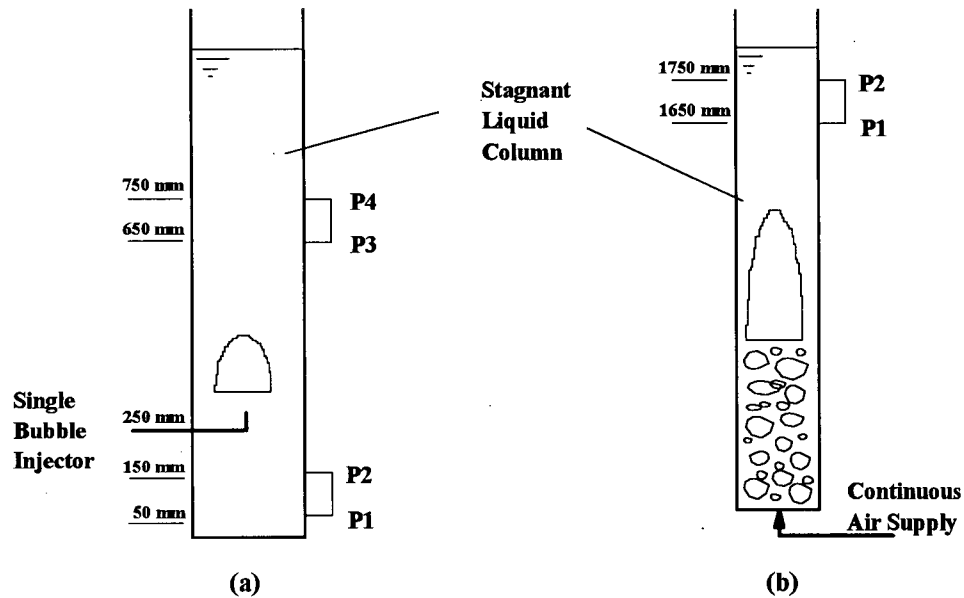


Figure 3.1. Schematic diagram of experimental apparatus used for preliminary pressure fluctuation tests.

could travel upwards to P3, located above the air injector, or downwards to P1, located below the injector, as shown in Figures 3.2 (a) and (b). Since P1 was closer to the air injector, the amplitude of the signal from P1 was greater than that from P3. After the air bubble was injected, the mean pressure at P3 increased due to the increase of static head at this point. When this bubble passed P3, a fluctuation could be observed due to the effect of the bubble and its wake.

Figures 3.2 (c) and (d) show the differential pressure fluctuations when a bubble was injected into the column. It is clear that the pressure disturbance caused by the bubble injection could be registered by both differential pressure transducers (P3 - P4) located above the injector, and (P1 - P2) below the injector. When the bubble passed the transducers at P3 and P4, a pressure fluctuation could be observed too (Figure 3.2 (c)). Comparing Figure 3.2 (a) and 3.2 (c), it can be seen that the absolute pressure fluctuation caused by the air injection was stronger than that caused by the bubble itself, whereas the differential pressure fluctuation caused by the air injection

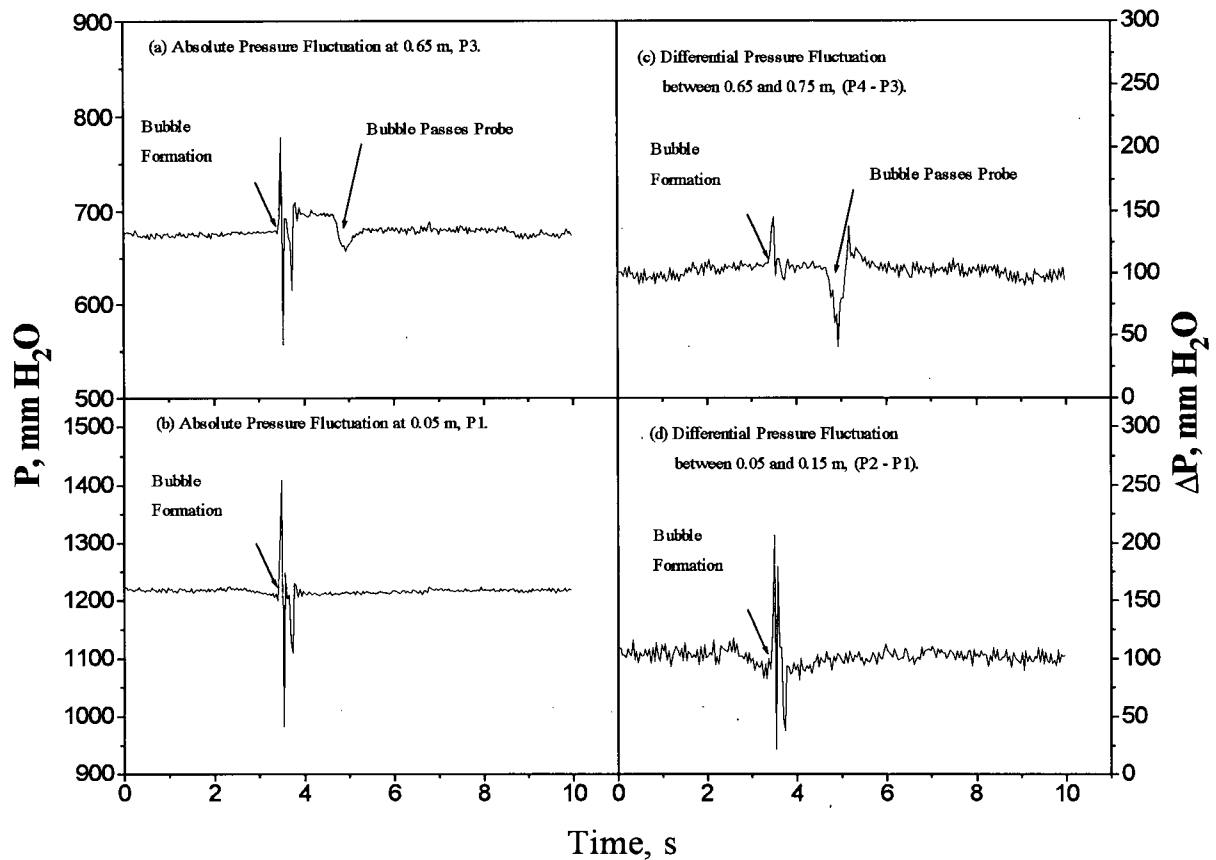


Figure 3.2. Pressure signals corresponding to single bubble formation and rise (air injector 0.25 m above the distributor).

and the bubble itself were of same order. This implies that a differential pressure transducer can reduce, but not eliminate, the effect of bubble injection.

3.2.2.2 Effect of continuous air supply on pressure fluctuations

The purpose of this test was to check the effect of continuous air supply on pressure fluctuations. Two absolute pressure transducers were mounted 1.65 and 1.75 m above the air distributor. The column was filled with stagnant water to a height of 1.85 m height as shown in Figure 3.1 (b). The pressure fluctuations were then recorded when the air valve was quickly opened. Typical results are shown in Figure 3.3. At around 2 s, the air valve was quickly opened.

First a very large bubble was created by the sudden release of pressure in the air pipe. Then small bubbles as well as some Taylor bubbles followed the large bubble, since the air valve remained open. Thus the mean pressure at 1.75 m increased before the first big bubble arrived, which happened at around 4 s. From 4 to 5 s, this bubble covered both transducers, so that ΔP almost reached zero in this period of time. At the same time, the mean pressure at 1.75 m dropped. Although no bubble passed the transducers before 4 s, both the absolute pressure and the differential pressure fluctuated significantly due to the air injection and other sources of pressure disturbance. Note that the amplitude of the fluctuations caused by the air injection is of the same magnitude as that after the first bubble passed the transducers.

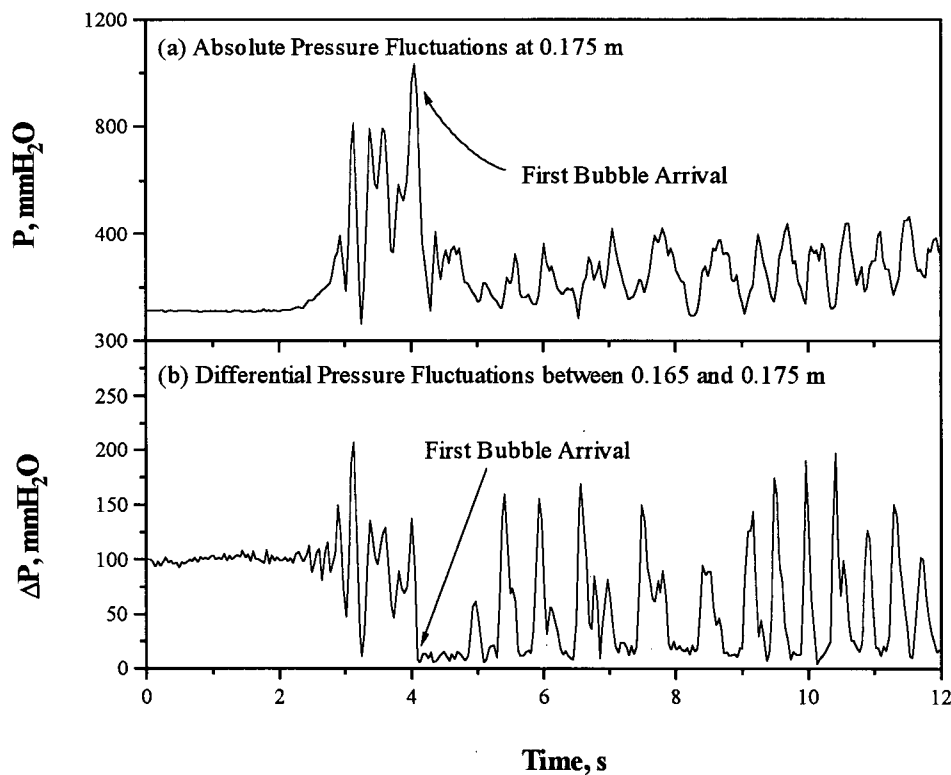


Figure 3.3. Pressure signals corresponding to continuous air supply at $U_g = 0.387$ m/s in a stagnant column containing water.

Both tests show that the absolute pressure and the differential pressure fluctuations include information not only from bubbles passing the pressure transducers, but also from other sources throughout the column, e.g. pressure disturbances caused by bubble formation. Hence, caution should be exercised when absolute and differential pressure fluctuations are used to distinguish flow regimes. This is especially true if the standard deviation of the fluctuations is adopted as the criterion for flow regime transitions, since the component of the pressure fluctuations caused by other disturbances may then contribute significantly and randomly to the total standard deviation.

3.3 Local Multiphase Flow Characteristics

Local multiphase characteristics can be used to determine the flow regime transitions. Different measurement techniques (e.g., conductivity probe and X-ray measurement systems) have been used to determine the local characteristics and flow structure of multiphase systems. Most investigators have based the transition criteria on statistical information from the original signals. However, due to the intrinsic attributes of the original signals, this method has its own shortcomings.

3.3.1 Previous Studies

3.3.1.1 Gas-liquid two-phase systems

Since the electrical conductivities of the liquid and gas differ, it is possible to detect the presence of liquid or gas at a certain location using a pair of electrodes. This method has been used by many investigators (Barnea et al., 1980; Matuszkiewicz et al., 1987; Kelessidis and Dukler, 1989; Mao and Dukler, 1989; Nakazatomi et al., 1992; Soria and de Lasa, 1992; Das and

Pattanayak, 1993, 1994; Monji, 1993). Different probe configurations have been employed by different authors, so that the results are quite different.

Barnea et al. (1980) determined flow regimes with two conductance probes, one located on the wall of the pipe, the other at the centerline. These probes shared a common ground and with only the tip of each probe was electrically exposed to the two-phase mixture. The voltage-time traces of the probes were used to identify flow regimes. In annular flow, the trace of the probe at the axis exhibited a zero output. In slug flow, periods of zero output, representing Taylor bubbles, and periods of high voltage with some downward spikes, representing small bubbles within a liquid plug, could be observed in the trace. In churn flow, near the transition to annular flow, the trace output was almost zero except for some small upward spikes; near the transition from slug flow, a group of spikes, sometimes in a form similar to a group of small bubbles, appeared in the trace. Flow transitions were adjudged based on the probe outputs.

The same phenomena were observed by Mao and Dukler (1989) with a radio-frequency (RF) probe. This probe was designed to detect the local presence of either air or water. The characteristics of this probe were similar to those of a high-frequency impedance probe according to the authors. Flow patterns were discerned from visual observation of the time trace of the RF probe.

Several pairs of square electrodes mounted at different heights along the column were used as conductivity probes by Matuszkiewicz et al. (1987). The Power spectrum distribution functions (PSF) of the probes presented some very sharp peaks at frequencies of $f_s = 1.0$ and $f_s = 1.2$ Hz in slug flow. However, only one smooth peak appeared in the PSD function for bubble flow and for the transition regime between bubble flow and slug flow. The standard deviation of each probe output went through a maximum as the gas void fraction increased. This maximum appeared at the middle of the transition between bubble flow and slug flow. Other parameters

were also calculated, e.g., a system phase factor, system gain factor and coherence function for each successive probe. The authors suggested that the actual bubble-slug transition might be characterized by a sudden increase in the coherence function of natural fluctuations at two successive probes for some "sensitive" frequencies (e.g., $f_s = 1.0$ or $f_s = 1.2$ Hz).

Das and Pattanayak (1993, 1994) used two electrical impedance probes to identify flow patterns. One was called a wide-gap probe with two electrodes separated by a distance of $D/2$, while the other was a narrow-gap probe with a pair of electrodes separated by 1.6 mm. The outputs of the probes were converted by a complicated measuring circuit to create a digital equivalent of mixture resistance (DEMR) reading. The DEMR reading was preset to vary from 0 to 100, corresponding to 0% to 100% gas holdup. It was found that when the DEMR started to show values above 32, slug flow was observed. The criterion was adopted that if within 5 s, ten or more DEMR readings exceeded 32, the bubble-slug transition had occurred. When these two probes were separated by $8D$, the number of liquid plugs longer than $8D$ could be counted. The criterion for the slug-churn transition was that if fewer than 10 liquid plugs (of length $\geq 8D$) were found within 5 s duration, then steady churn flow existed. Beyond the churn-annular transition, the gas core was occasionally bridged by the liquid. In a period of 5 s the number of bridgings had to be less than ten to establish annular flow.

A conductance probe of the same configuration as that proposed by Barnea et al. (1980) was used by Kelessidis and Dukler (1989) in vertical concentric and eccentric annuli to detect flow patterns. The PDF of the probe output was used to set the criteria for flow regime transitions. The PDFs exhibited different shapes in various flow regimes. Bubble flow was characterized by a single peak of the PDF at V/V_{\max} near 1.0 such that the integral of the PDF with V/V_{\max} ranging from 0.75 to 1.0 should equal unity. Slug flow was characterized by two well-defined peaks in the PDF plot. Since the peak at low voltage corresponded to Taylor bubbles, slug flow was assumed to occur when the integral of the PDF with V/V_{\max} ranging from

0 to 0.25 was greater than 0.2. The slug-churn transition took place when the integral of the PDF with V/V_{\max} ranging from 0.75 to 1.0 was less than 0.2. Annular flow was characterized by a single narrow peak located at low V/V_{\max} in the PDF plot.

Vince and Lahey (1982) used an X-ray measurement system to measure void fraction fluctuations at different chord positions. PDFs and PSFs, as well as their moments, were calculated. It was found that the variance of the output could be used as a flow regime indicator. In the slug and churn flow regimes, the variance was greater than 0.04 (i.e. standard deviation > 0.2). They also found that significant differences existed in the band width and the amplitude of the PSF for various flow regimes. However, both the shape of the PSF curve and its moments could not be used as criteria for flow regime transitions.

Jones and Zuber (1975) used an X-ray beam as a local probe in a 2D column. The PDF of the probe output was used to distinguish flow regimes. In bubble flow, a single-peaked PDF at low void fraction was found; in slug and churn flow, the PDF was twin-peaked; in annular flow, there was a single-peaked PDF at high void fraction. They found that the bubble-slug transition took place at $\epsilon_g = 0.2$ and the slug-annular transition at $\epsilon_g = 0.8$.

Govier et al. (1957, 1958) studied the pressure gradient and the void fraction of two-phase systems. With increasing gas velocity, the pressure gradient decreased first and then increased to a maximum. After that it decreased again and reached a second minimum, then went up again. Flow regimes were determined based on the inflection points of the void fraction curves and at the minima in the pressure gradient curves.

Based on a plot of pressure gradient vs. superficial gas velocity, Jayanti and Hewitt (1992) found that in bubble flow the pressure gradient decreased sharply with increasing gas velocity. It decreased more gradually in slug flow. At the slug/churn transition point, the pressure gradient

increased suddenly. They claimed that this transition point was quite consistent with visualization results.

Table 3.1 summarizes measurement methods used for flow regime identification in gas-liquid two-phase systems.

3.3.1.2 Three-phase systems

Soria and de Lasa (1992) measured the liquid volume fraction, using a set of electrical conductivity sensors in a bubble column. The sensors were composed of several pairs of square electrodes and were used to measure the conductivity of a three-phase mixture. The transition between the homogeneous bubbling regime and the churn-turbulent regime could be characterized by observing the asymptotic change in the slope of ε_ℓ vs. U_g plots. The homogeneous bubbling regime was observed at low superficial gas velocities. The spectrum of liquid volume fraction signals showed a dominant frequency peak below 1.0 Hz in the homogeneous bubbling flow regime. A further increase in superficial gas velocity produced a vigorously turbulent regime with fingered (multi-peak) spectra showing characteristic frequencies below 10 Hz. In a three-phase fluidized bed, it was found that the transition between dispersed bubble flow and coalesced bubble flow was governed by the superficial liquid velocity. In a plot of ε_ℓ vs. U_ℓ , a common crossover point was found for three sets of experiments carried out at different constant U_g values. This crossover point was hypothesized to be the transition between the coalesced bubble flow and the dispersed bubble flow regimes.

Table 3.1. Summary of some experimental methods used to delineate regime transitions in gas-liquid two-phase systems.

Measurement Method	Reference	Parameter used to set criteria	Comments
Visual observation	Griffith and Wallis (1961) Taitel et al. (1980) Spedding and Nguyen (1980) Weisman and Kang (1981) Fernandes et al. (1983) Hasan and Kabir (1992)	Visual appearance.	Subjective.
Pressure gradient	Govier et al. (1957, 1958) Jayanti and Hewitt (1992) Spedding and Spence (1993)	Inflection points of void fraction curves and minima of pressure gradient curves.	Inflection points are not very clear.
Pressure transducer	Tutu (1982, 1984) Matsui (1984, 1986) Lin and Hanratty (1987) France et al. (1991)	Original signal. Shape of PDF curve and its moments. Shape of PSF curve. Parameters from fractal techniques.	Pressure fluctuation contains other pressure disturbances. Shape — still subjective.
Electrical impedance, conductivity and radio-frequency probe	Barnea et al. (1980) Matuszkiewicz et al. (1987) Kelessidis and Dukler (1989) Mao and Dukler (1989) Das and Pattanayak (1993, 1994)	Original signal. Shape of PDF curve. Integral of part of PDF curve. SD, PSF and coherence function at certain frequencies.	Raw signals, shape — still subjective. SD — directly related to void fraction.
X-rays	Jones and Zuber (1975) Vince and Lahey (1982)	Shape of PDF curve and SD of raw signal.	Shape — still subjective. SD — directly related to void fraction.

Abbreviations: PDF: Probability Density Function. PSF: Power Spectrum Function. SD: Standard Deviation.

Han and Kim (1990) proposed a flow regime map using coordinates of gas holdup fraction over bed porosity, $\alpha (= \frac{\epsilon_g}{\epsilon_g + \epsilon_\ell})$, and gas-liquid slip velocity, $U_s (= \frac{U_g}{\epsilon_g} - \frac{U_\ell}{\epsilon_\ell})$, on the basis that the previous flow regime maps did not account for particle size and liquid properties. The dispersed bubble flow regime was characterized by relatively low gas-liquid slip velocities (0.4 - 0.5 m/s) with α in the range of 0 to 0.4. The coalesced bubble flow regime was characterized by higher slip velocities (0.4 to 0.8 m/s), with $0 \leq \alpha \leq 0.2$. The slug flow regime was characterized by high slip velocities with α from 0.2 to 0.4.

Lee et al. (1990) determined flow regimes based on mean bubble sizes throughout a fluidized bed fitted with a single pipe gas distributor. A progressive increase in mean bubble length with height was indicative of coalesced bubble flow. A decrease in mean bubble length with height implied dispersed bubble flow. Based on four experimental runs and literature data, a flow regime map was proposed using particle diameter and superficial liquid velocity as coordinates. The fixed bed, coalesced bubble flow, dispersed bubble flow and transport regimes were presented on this map. Table 3.2 summarizes the measurement methods used for flow regime identification in gas-liquid-solid three-phase systems.

3.3.2 Discussion of Existing Methods

X-ray measurement systems, conductivity probes and electrical impedance probes are usually designed to detect the presence of either gas or liquid. These methods offer a more direct way of investigating flow regime transitions than those based on P and ΔP fluctuations.

Table 3.2. Summary of experimental methods used to delineate regime transitions in gas-liquid-solid three-phase systems.

Measurement Method	Reference	Parameter used to set criteria	Comments
Visual observation	Ernakova et al. (1970) Mukherjee et al. (1974) Darton and Harrison (1975) Muroyama et al. (1978) Beaver and Fan (1984) Fan et al. (1984) Matsuura and Fan (1984) Hu et al. (1985) Lee et al. (1990) Nacef et al. (1992, 1995)	Visual appearance.	Subjective.
Pressure transducer	Kitano and Ikeda (1988) Zheng et al. (1988) Chen et al. (1995)	Integral of part of the PSF. PSF curve.	Pressure fluctuations contain other pressure disturbances.
Visual observation, while other methods were suggested	Fan et al. (1986) Han and Kim (1990)	Root mean square of pressure fluctuation. Fraction of gas holdup and relative bubble velocity.	Flow regime map was obtained visually.
Electrical impedance probe	Soria and de Lasa (1992)	Liquid volume fraction.	Transition point was not obvious enough.

Except for Das and Pattanayak (1993, 1994) in a two-phase system and Lee et al. (1990) in a three-phase system, most investigators used the original signals or statistical parameters derived from the original signals, instead of the bubble characteristics, to determine flow regime transitions. Barnea et al. (1980) and Mao and Dukler (1989) used the raw signals of a conductivity probe and a RF probe respectively, to distinguish flow regimes. These are somewhat more objective than visual observation. With the X-ray technique, Vince and Lahey (1982) and Jones and Zuber (1975) calculated the PDF of the measurement system output. Both reported that the shape of the PDF was different in each flow regime. This was confirmed by Kelessidis and Dukler (1989) with a conductance probe. The variance of the probe output was used as an indicator by Vince and Lahey (1982). The shape of the PDF was used by Jones and Zuber (1975), while the integration of the PDF within a certain range was used by Kelessidis and Dukler (1989) to distinguish flow regimes.

The output of an X-ray measurement system, a conductivity probe or an electrical impedance probe varies from a low voltage to a high voltage corresponding to the presence of gas and liquid respectively. The values of the low and high voltage depend on power supply, liquid properties and the probe configuration. Instead of using V directly, the outputs were normalized (as V/V_{\max}) such that the values would only vary from 0 to 1.0. In such a case, the PDF and its moments of the signal are related to the gas holdup.

Consider an ideal voltage-time trace signal as shown in Figure 3.4. V_0 and V_1 correspond to gas phase and liquid phase respectively and appear alternately. According to the definitions of PDF, average, standard deviation and other moments in Equations (2.1) to (2.6), the statistical parameters of this ideal trace are as follows:

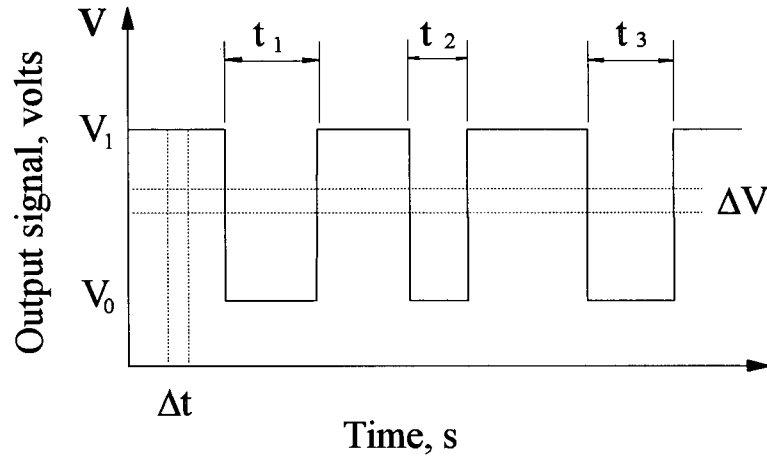


Figure 3.4. Ideal signal for conductivity probe.

Probability of the signal having value V_0 :

$$P(V_0, \Delta V) = \frac{1}{t_{\text{tot}}} \sum_{i=1}^3 t_i = p_0 \quad (3.1)$$

Probability of the signal having value V_1 :

$$P(V_1, \Delta V) = 1 - \frac{1}{t_{\text{tot}}} \sum_{i=1}^3 t_i = p_1 \quad (3.2)$$

The mean, variance, skewness and kurtosis of $V(t)$ can be expressed by:

$$\bar{V} = \sum_{i=0}^1 V_i P(V_i, \Delta V) = V_0 p_0 + V_1 p_1 \quad (3.3)$$

$$\text{Var} = \sum_{i=0}^1 (V_i - \bar{V})^2 P(V_i, \Delta V) = V_0^2 p_0 + V_1^2 p_1 - \bar{V}^2 \quad (3.4)$$

$$M_3 = \sum_{i=0}^1 (V_i - \bar{V})^3 P(V_i, \Delta V) = V_0^3 p_0 + V_1^3 p_1 - 3\bar{V} \text{Var} - \bar{V}^3 \quad (3.5)$$

$$M_4 = \sum_{i=0}^1 (V_i - \bar{V})^4 P(V_i, \Delta V) = V_0^4 p_0 + V_1^4 p_1 - 4\bar{V} M_3 - 6\bar{V}^2 \text{Var} - \bar{V}^4 \quad (3.6)$$

Assuming $V_0 = 0$ and $V_1 = 1$ volt, then

$$\bar{V} = p_1 \quad (3.7)$$

$$\text{Var} = \sigma_v^2 = p_0 p_1 \quad (3.8)$$

$$M_3 = p_0 p_1 (1 - 2 p_1) \quad (3.9)$$

$$M_4 = p_0 p_1 (1 - 3 p_0 p_1) \quad (3.10)$$

On the other hand, a conductivity probe can be used to measure local gas holdup. The time average gas holdup can be calculated by Equation (2.9). For the case in Figure 3.4,

$$\epsilon_g = \frac{1}{t_{\text{tot}}} \sum_{i=1}^3 t_i \quad (3.11)$$

Comparing this equation with Equation (3.1) we can see that

$$\epsilon_g = p_0 \quad \text{for } V_0 = 0 \text{ and } V_1 = 1 \quad (3.12)$$

Hence the integral of the PDF with $V(t)$ ranging from 0 to 0.25 volts (after Kelessidis and Dukler, 1989) is:

$$\int_0^{0.25} \frac{P(V_i, \Delta V)}{\Delta V} dV = \int_0^{0.25} \frac{P(V_0, \Delta V)}{\Delta V} dV = p_0 = \epsilon_g \quad (3.13a)$$

and the integral of the PDF with $V(t)$ ranging from 0.75 to 1 volt is:

$$\int_{0.75}^1 \frac{P(V_i, \Delta V)}{\Delta V} dV = \int_{0.75}^1 \frac{P(V_1, \Delta V)}{\Delta V} dV = p_1 = 1 - \epsilon_g \quad (3.13b)$$

The moments of the signal can also be expressed in terms of the gas holdup of the multiphase mixture:

$$\bar{V} = 1 - \epsilon_g \quad (3.14)$$

$$\text{Var} = \epsilon_g (1 - \epsilon_g) \quad (3.15)$$

$$M_3 = \epsilon_g (1 - \epsilon_g) (2\epsilon_g - 1) \quad (3.16)$$

$$M_4 = \epsilon_g (1 - \epsilon_g) [1 - 3\epsilon_g (1 - \epsilon_g)] \quad (3.17)$$

Figure 3.5 shows the variation of the moments with the gas holdup. Several loci can be found in the figure. At $\varepsilon_g = 0.5$, the variance reaches its maximum, and the skewness equals zero. At $\varepsilon_g = 0.21$ and $\varepsilon_g = 0.79$, the skewness reaches its minimum and maximum, respectively. If these loci were used to determine flow regime transitions, that would not be different from using the gas holdup itself. For example, the assumption that the maximum point of the standard deviation for the variation of the signal is a flow regime transition point is the same as the assumption that the flow regime transition occurs when the measured gas holdup is equal to 0.5. It is well known that, the gas holdup increases with gas velocity at constant liquid velocity. There is, however, no dramatic change which reflects the flow regime transition in a plot of the gas holdup vs. superficial gas velocity, as shown in section 4.2.2.

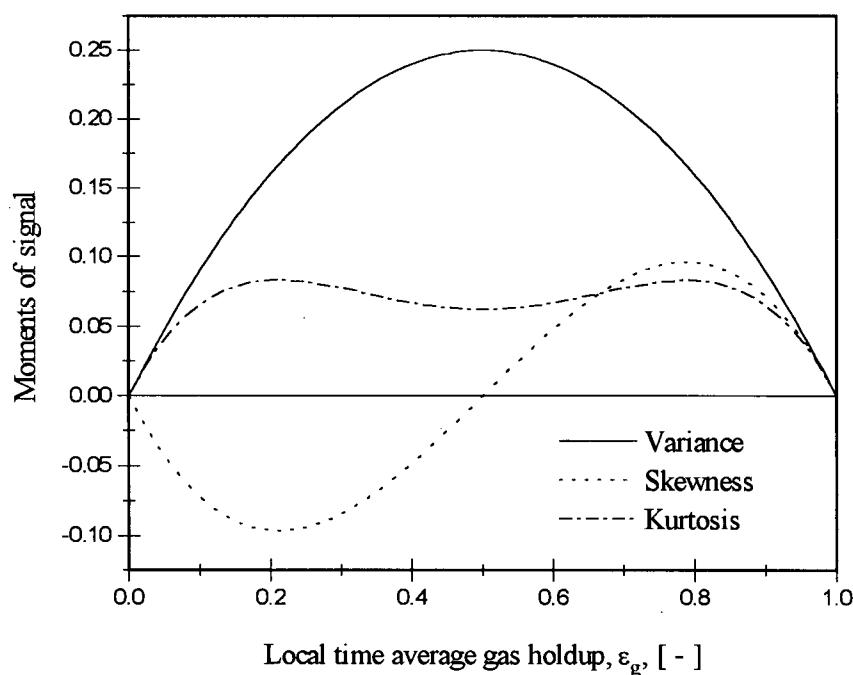


Figure 3.5. Relationship between gas holdup and various moment parameters of an ideal signal for conductivity probe.

3.4 Summary

Aside from visual observation, absolute and differential pressure fluctuations and local multiphase characteristics have been used to determine the flow regime transitions. However, pressure fluctuations include information on local flow structures as well as pressure disturbances caused by other remote sources (e.g., due to air injection). When the statistical parameters of the pressure fluctuations are used as the flow regime transition criteria, these pressure disturbances may affect the results significantly and randomly. Although differential pressure measurements can reduce the amplitude of pressure disturbances, they do not totally eliminate their influence. Thus, both absolute and differential pressure fluctuation methods appear to be unsuitable for flow regime determination in multiphase systems.

An objective measurement method for flow regime transitions should be based on the multiphase characteristics of the system. Many investigators have attempted to achieve this goal using techniques which detect bubble characteristics. However, most such methods have used statistical parameters of the original signals from instruments, instead of the more direct manifestations of the bubble characteristics, to determine the flow regimes. Due to the intrinsic attributes of the measurement techniques, these statistical parameters are directly related to the local time-average gas holdup at the measurement location. However, information on gas holdup is not enough for determining the flow regime transitions in a multiphase system. A new method is needed and is presented in the next chapter.

Chapter 4

Experimental Criteria for Flow Regime Transitions in Gas-Liquid Systems

4.1 Introduction

This chapter presents experimental results on tests where bubble characteristics were investigated under operating conditions which span all flow regimes in order to establish criteria for the flow regime transitions. The bubble characteristics measured in this work were bubble frequency, gas holdup, bubble velocity, bubble chord length and their distributions. The flow regimes investigated are discrete bubble flow, dispersed bubble flow, coalesced bubble flow, slug flow, churn flow, bridging flow and annular flow.

4.2 Experimental Results

The experimental set-up and the conductivity probe used in this work are described in Chapter 2. The probe was installed horizontally at several heights above the distributor, always at the axis of the column of inside diameter 82.6 mm.

4.2.1 Raw Signals and their Statistical Results

Some typical raw signals from the conductivity probe are shown in Figure 4.1. At the lowest gas velocity ($U_g = 0.0099$ m/s), discrete bubble flow was encountered. In the time trace of the conductivity probe, some downward spikes were observed, corresponding to small bubbles striking the probe. As the gas velocity was increased, a few large bubbles appeared in the column. At a gas velocity of 0.041 m/s, near the transition velocity to slug flow, longer periods of zero output were observed corresponding to large gas bubbles.

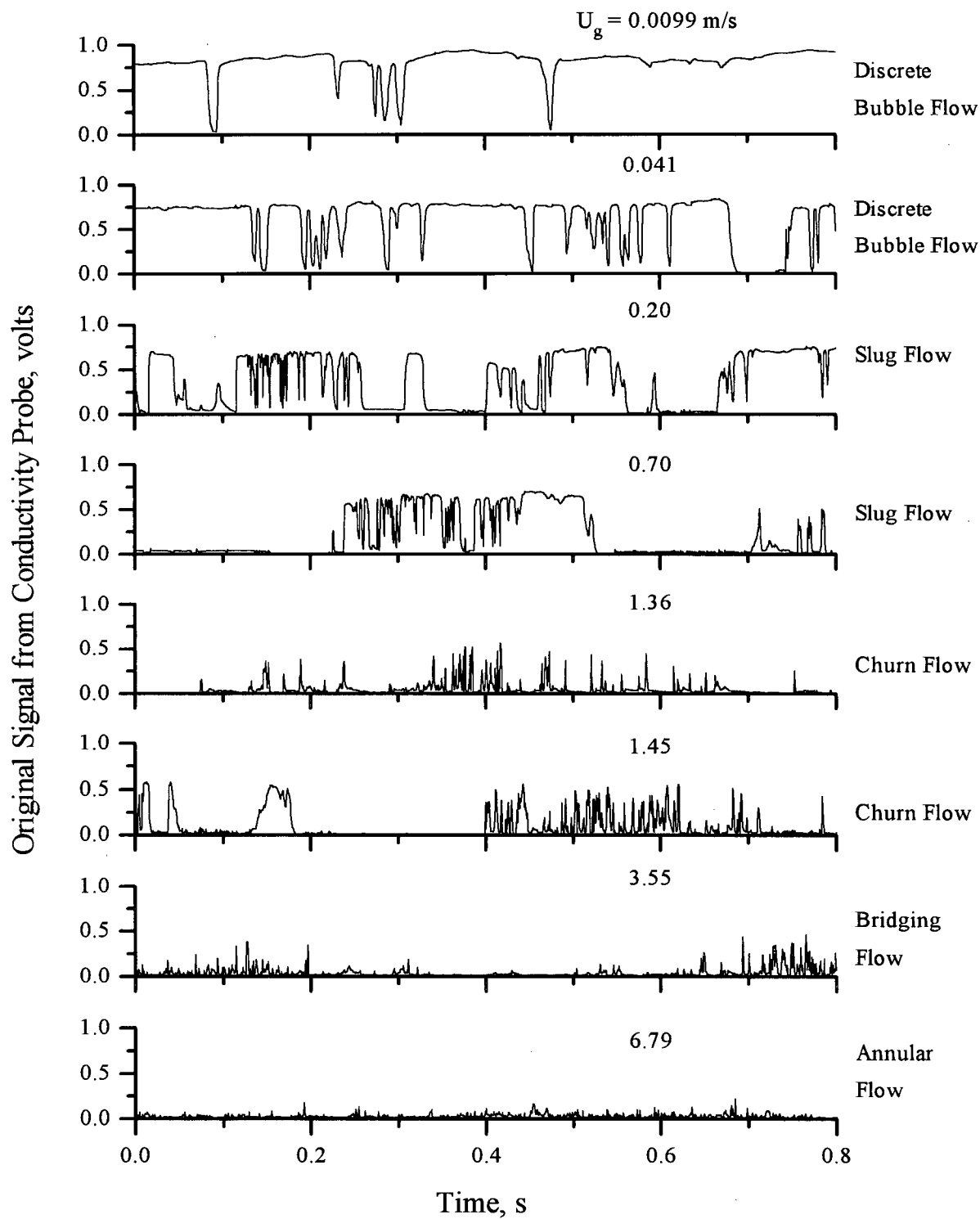


Figure 4.1. Typical raw signals at different superficial gas velocities from conductivity probe for air-water system at $Z = 0.65 \text{ m}$, $U_l = 0.0184 \text{ m/s}$.

A further increase in gas velocity to $U_g = 0.20$ m/s resulted in a transition to slug flow. In this regime periods of zero output corresponding to Taylor bubbles are interspersed with periods of high voltage with some downward spikes, corresponding to small bubbles in gas-liquid plugs. In the churn flow and bridging flow regimes, upward spikes corresponding to liquid bridging were observed in the original signals. For annular flow ($U_g = 6.79$ m/s), the output of the probe was always close to zero, indicating that the probe was always in the gas phase.

The probability density functions (PDFs) of the signals are shown in Figure 4.2. Bimodal distributions are seen at low gas velocities corresponding to discrete bubble flow and slug flow. Single peak distribution of the PDFs are observed at high gas velocities, which correspond to churn flow, bridging flow and annular flow. However, it is probably impossible to determine the flow regime transitions based on the shape of the PDF curves.

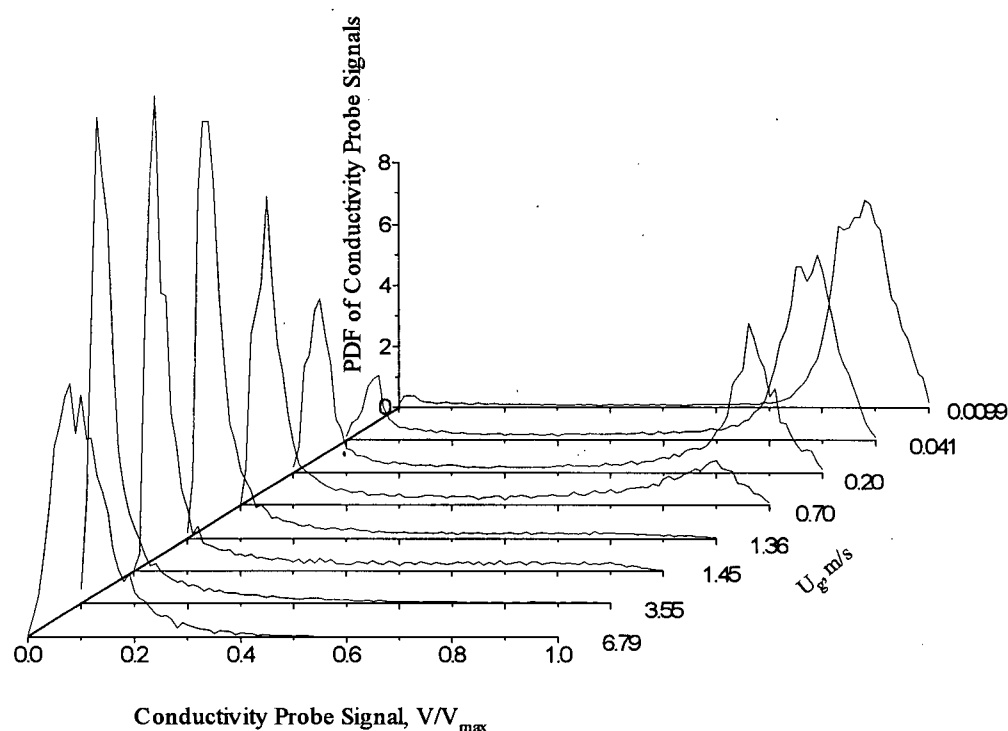


Figure 4.2. Probability density function of conductivity signal for air-water system at $Z = 0.65$ m, $U_l = 0.0184$ m/s and different gas velocities.

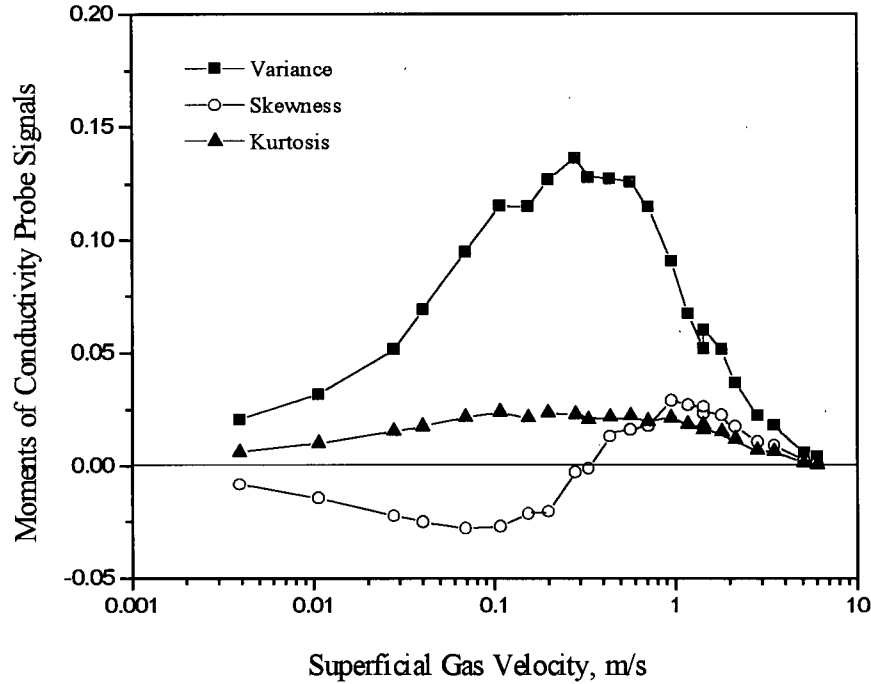


Figure 4.3. Variation of moments of conductivity probe signals with superficial gas velocity for air-water system at $Z = 0.65$ m, $U_l = 0.0184$ m/s.

Figure 4.3 shows the variation of the moments of the original signals with respect to the gas velocity. The variance of the signals increases with the gas velocity and reaches a maximum at $U_g \approx 0.34$ m/s. It approaches zero at high gas velocities in the annular flow regime. The skewness of the signals decreases with increasing gas velocity at low gas velocities and reaches a minimum value at $U_g \approx 0.08$ m/s. Then it increases, passing through zero at $U_g = 0.34$ m/s and reaching a maximum value at $U_g \approx 1.0$ m/s, before approaching zero again at high gas velocities corresponding to annular flow. The kurtosis of the signals increases first and then levels off at $U_g \approx 0.08$ m/s. It begins to decrease at $U_g \approx 1.0$ m/s and approaches zero at high gas velocities.

Several characteristic features are seen in Figure 4.3. These features, however, are directly related to gas holdup as shown in Figure 4.4. The maximum variance of the signals appears at $\epsilon_g \approx$

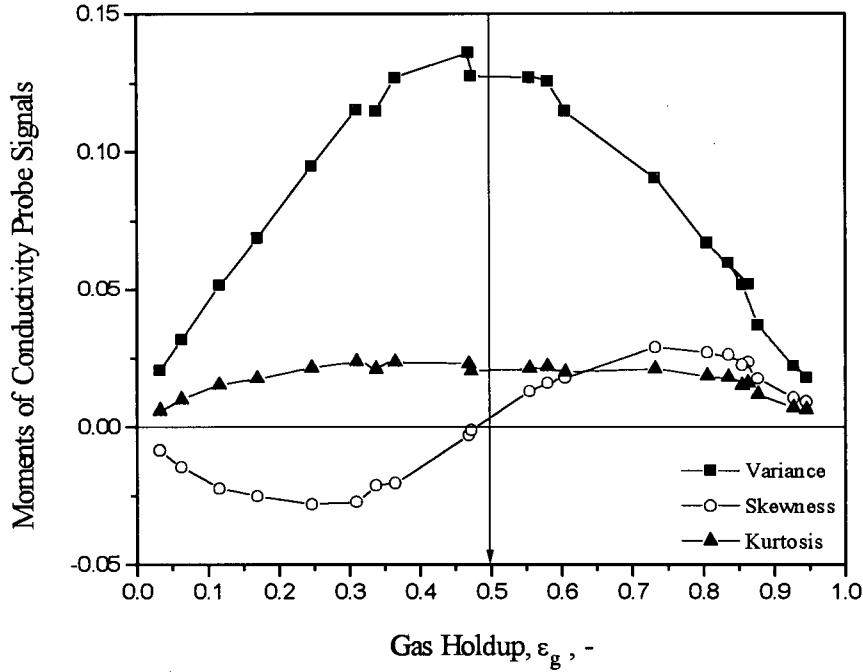


Figure 4.4. Variation of moments of conductivity probe signals with gas holdup for air-water system at $Z = 0.65$ m, $U_\ell = 0.0184$ m/s.

0.5, while the minimum value, the zero point and the maximum value of the skewness appear at $\epsilon_g \approx 0.25$, 0.5 and 0.75, respectively. Using these moments to determine the flow regime transitions is equivalent to basing the transitions on the gas holdup.

4.2.2 Gas Holdup

The variation of time-average gas holdup at the centre of the column with respect to the gas velocity is shown in Figure 4.5 at four different heights. It can be seen that gas holdup, ϵ_g , increases with gas velocity monotonically for all four levels. There are no obvious turning points indicating flow regime transitions.

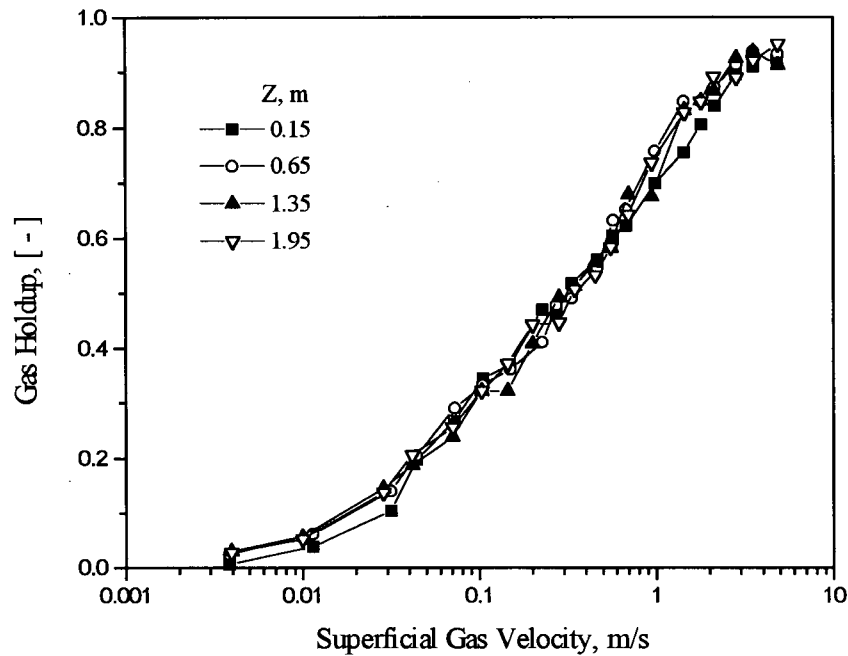


Figure 4.5. Local gas holdup at different heights for air-water system at $U_l = 0.0184$ m/s.

4.3 Experimental Criteria for Flow Regime Transitions

In addition to the statistical properties of the original signals and gas holdup, bubble characteristics can be obtained from the conductivity probe signals. For this section, the measurement location was always on the axis of the column 0.65 m above the distributor.

4.3.1 Transition between Discrete Bubble Flow and Coalesced Bubble Flow Regimes

At low liquid flow rates, when small amounts of gas are introduced into the column, small bubbles appear. The bubble size distribution is narrow and strongly dependent on the gas distributor. The number of bubbles and the gas holdup are also small. Bubbles do not have sufficient time to coalesce since the distance between individual bubbles is large compared to the

sizes of the bubbles. Hence, the overall behavior of the gas bubbles may be characterized as homogeneous.

With increasing gas velocity, larger bubbles of wider size distribution are encountered. The population of bubbles increases, while the distance between individual bubbles decreases. Some bubbles coalesce as they ascend. The overall behavior of the multi-phase mixture is categorized as coalesced bubble flow or as heterogeneous.

In this study, it was found that the relationship between bubble frequency and superficial gas velocity is different in the discrete and coalesced bubble flow regimes. In the discrete bubble flow regime, bubble frequency increases linearly with gas velocity, with a proportionality constant of 545 m^{-1} . On further increasing the gas velocity, the bubble frequency deviates from this linear relationship when the transition to coalesced bubble flow takes place. Hence, the

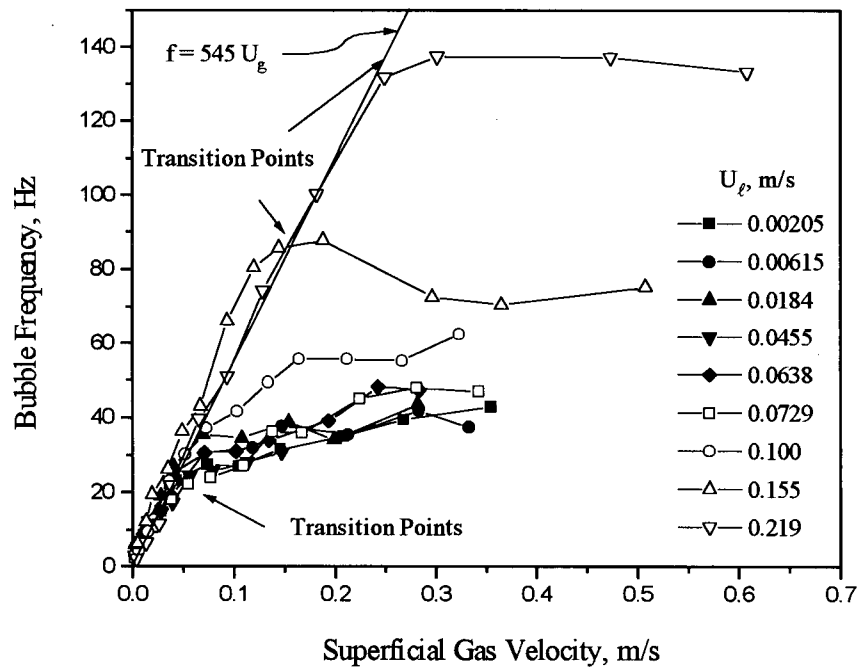


Figure 4.6. Transition between discrete and coalesced bubble flow regimes in air-water system at different superficial liquid velocities.

discrete/coalesced bubble flow transition can be obtained from a plot of bubble frequency versus superficial gas velocity, corresponding to the point where the bubble frequency deviates significantly from a linear relationship. Figure 4.6 displays some typical results showing this transition.

In discrete bubble flow, assuming all small bubbles are spherical and of uniform size, distributed uniformly across the column, then

$$\frac{\text{bubble detection area}}{\text{column cross-sectional area}} = \frac{\text{No. of bubbles passing detection area}}{\text{No. of bubbles passing cross-sectional area}}$$

The detection area is dependent on the bubble size. A bubble of diameter d_{vs} can be detected only when the distance between the probe and the center of the bubble is less than $d_{vs}/2$. Therefore, The equation above can be written as:

$$\frac{\frac{\pi}{4} d_{vs}^2}{A_c} = \frac{f t}{\frac{\pi}{6} d_{vs}^3 A_c U_g t}$$

where f is the measured local bubble frequency and A_c is the cross-sectional area of the column. Rearranging this equation, the local or point bubble frequency can be expressed by:

$$f = \frac{1.5}{d_{vs}} U_g \quad (4.1)$$

where d_{vs} is the bubble diameter, which is a function of the diameter of the holes in the distributor, and of the gas and liquid flowrates and physical properties. For stagnant liquid columns, Kumar et al. (1976) correlated the bubble diameter by:

$$d_{vs} = \begin{cases} 1.56 \text{ Re}_N^{0.058} \left(\frac{\gamma d_N^2}{(\rho_\ell - \rho_g)g} \right)^{1/4} & \text{for } 1 < \text{Re}_N \leq 100 \\ 0.32 \text{ Re}_N^{0.425} \left(\frac{\gamma d_N^2}{(\rho_\ell - \rho_g)g} \right)^{1/4} & \text{for } 100 < \text{Re}_N < 2100 \end{cases} \quad (4.2)$$

In the present study, when U_g was varied from 0.004 to 0.1 m/s, Re_N in Equation (4.2) changed from 15.5 to 388. The bubble size, d_{vs} , predicted by Equation (4.2), varied from 4.2 to 9.3 mm. Taking an average bubble diameter, $d_{vs} = 6.8$ mm, and since the bubble frequency is proportional to the gas velocity, by Equation (4.1) the linear constant relating them is $1.5/0.0068$ or 221 m^{-1} . This value is of the same order as 545 m^{-1} (see Figure 4.6). Since Equation (4.2) was obtained for a stagnant liquid column, the predicted bubble diameter may be overestimated and the corresponding linear constant underestimated.

The discrete/coalesced flow transition criterion can also be applied to flow regime transitions at high U_ℓ , i.e. the transition between dispersed bubble flow and coalesced bubble flow or, if the coalesced bubble flow regime is absent, between dispersed bubble flow and slug flow. However, this transition criterion may be difficult to apply when discrete bubble flow exists only within a small gas velocity range.

4.3.2 Transition between Coalesced Bubble Flow and Slug Flow Regimes

As the gas velocity is increased further, bubbles become larger and more elongated, and some bubble cross-sectional dimensions approach the diameter of the column. The appearance of

Taylor bubbles indicates that the flow pattern has changed to slug flow. In the slug flow regime, many small bubbles with diameter approximately equal to 4 mm are observed in the liquid plugs which follow the Taylor bubbles. Both the Taylor bubbles and the small bubbles are detected by the conductivity probe. These small bubbles result in a small value of the arithmetic mean bubble chord length, when few Taylor bubbles are present in the column. In order to detect the point at which Taylor bubbles begin to appear in the column, the Sauter mean bubble chord length,

$$\ell_{b,sv} = \frac{\sum_{i=1}^M \ell_{bi}^3}{\sum_{i=1}^M \ell_{bi}^2} \quad (4.3)$$

is used as the parameter to set the criterion in this study,

This parameter gives more weight to large bubbles than small ones. A sample calculation may be useful to exhibit this. Consider 10 bubbles, one of which has a chord length of 10 mm while the rest all have a chord length of 1 mm. The Sauter mean chord length is then 9.26 mm, while the arithmetic average chord length is only 1.9 mm.

The appearance of bullet-shaped or Taylor bubbles marks the transition between coalesced bubble flow and slug flow. In the air-water system, the bubble chord length at the center of a Taylor bubble is usually equal to or greater than the diameter of the bubble. Hence, the criterion for the transition between coalesced bubble flow and slug flow is set as the point at which the Sauter mean bubble chord length, $\ell_{b,vs}$, measured at the center of the column, reaches the column diameter, D , 0.0826 m in this study. Figure 4.7 shows the experimental results identifying this transition.

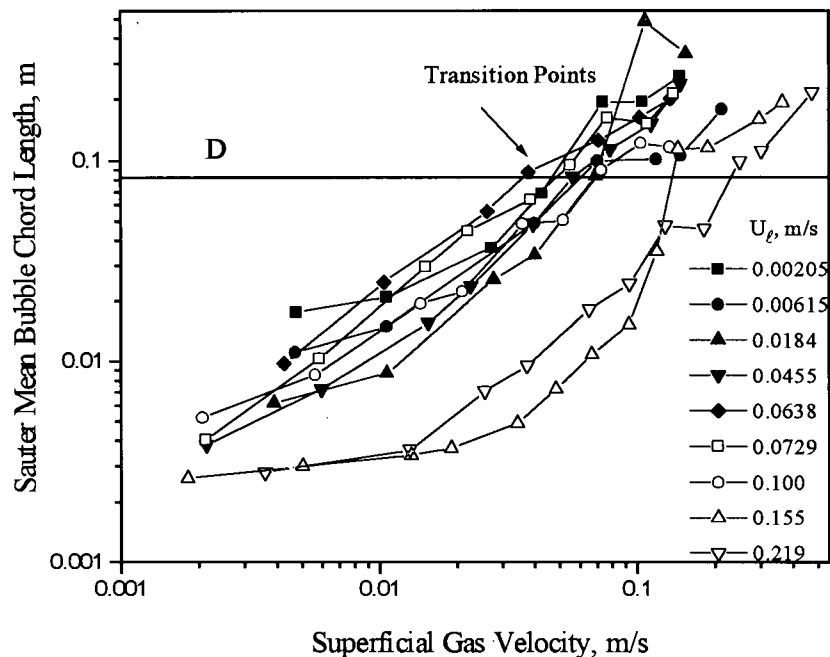


Figure 4.7. Method used to determine transition between coalesced bubble flow and slug flow in air-water system at various superficial liquid velocities.

4.3.3 Transition between Slug Flow and Churn Flow

The transition between slug and churn flow can be taken to occur when the gas holdup within the liquid plugs corresponds to a maximum volumetric packing of bubbles (Brauner and Barnea, 1986; Mao and Dukler, 1989). Beyond this point, the bubble frequency decreases with increasing gas velocity due to coalescence of the small bubbles within the liquid plugs. Hence, the maximum bubble frequency in a plot of bubble frequency vs. superficial gas velocity can be used to distinguish between slug flow and churn flow. Figure 4.8 shows experimental results for this transition.

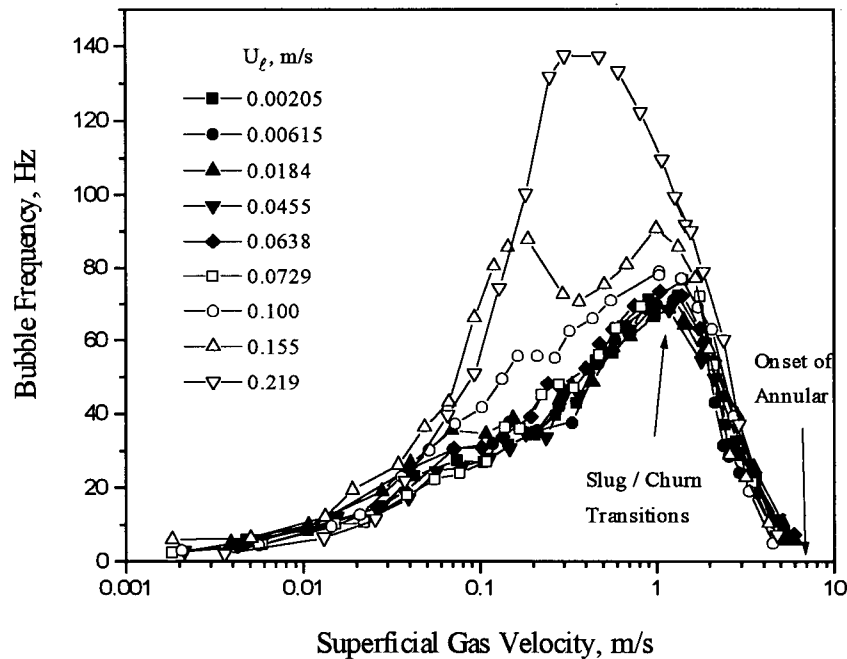


Figure 4.8. Plot of local bubble frequency at axis of column versus superficial gas velocity showing transition between slug flow and churn flow and the onset of annular flow in the air-water system for different superficial liquid velocities.

Note that Figure 4.8 is plotted on semi-log coordinates, while Figure 4.6 is on a linear scale. This causes the shapes of the bubble frequency curves in Figure 4.8 to differ from those in Figure 4.6.

4.3.4 Transition between Churn Flow and Bridging Flow

Bridging flow occurs when there are liquid bridges spanning the core region of the column linking the liquid film occupying the annular region of the column in any cross-section. In churn flow, some distorted Taylor bubbles were observed. As the gas velocity was increased, the distorted Taylor bubbles became elongated. Some successive Taylor bubbles coalesced forming larger bubbles, while the liquid plugs between successive Taylor bubbles became thinner. The

measured bubble frequency continued to decrease (as shown in Figure 4.8), and the average bubble chord length showed a sharp increase with respect to the gas velocity, as illustrated in Figure 4.9. The abrupt change in slope in Figure 4.9 can be taken to denote the onset of bridging flow.

Figure 4.9 also shows the variation of the average bubble time (defined in section 2.3.3, Chapter 2) with the gas velocity under the same conditions. The average bubble chord length shows the same tendency as the average bubble time. This is because the average bubble chord length is related to the average bubble time. The definition of the average bubble chord length is:

$$\bar{\ell}_b = \frac{1}{M} \sum_{i=1}^M (t_i U_{bi}) \quad (4.4)$$

If U_{bi} is a constant, then from Equation (2.11), one can write Equation (4.4) as:

$$\bar{\ell}_b = U_b \bar{t}_i \quad (4.5)$$

Equation (4.5) indicates that the average bubble chord length is proportional to the average bubble time, providing that the bubble velocities are the same. Because the measurement of ℓ_b requires a two-element probe, while \bar{t}_i requires only a single element, the average bubble time was used to determine the transition between churn flow and bridging flow throughout this work. This avoids several problems which might be associated with a two-element probe, such as the measurement error resulting from bubbles with a significant non-vertical component of rise velocity. As illustrated in Figure 4.9, this method does not cause a significant error in determining the flow regime transition, and it also simplifies the measurement system. Figure 4.10 shows the variation of the average bubble time with respect to U_g for other operating conditions.

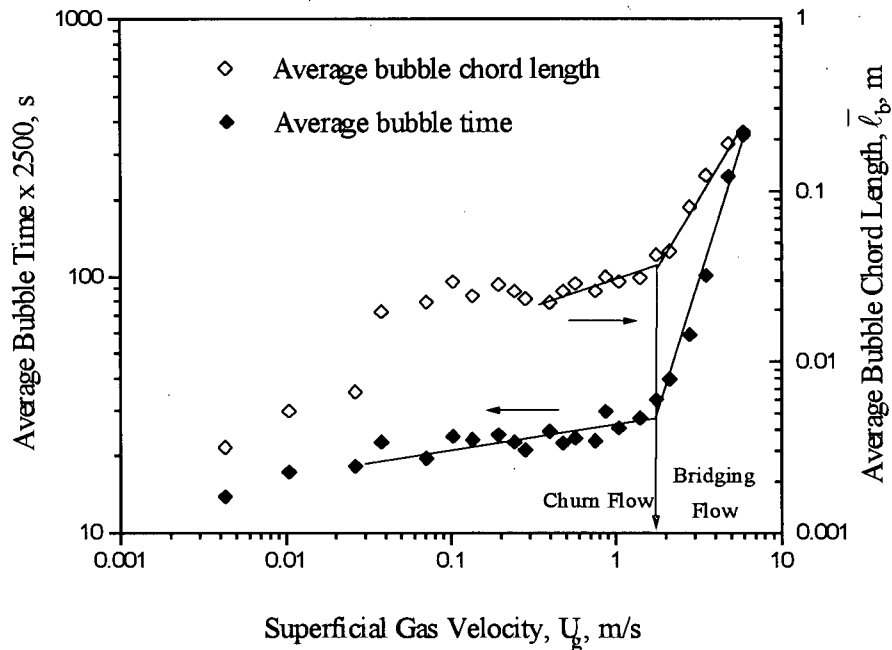


Figure 4.9. Average bubble chord length and bubble time versus superficial gas velocity showing transition between churn flow and bridging flow for air-water system at $Z = 0.65$ m, $U_\ell = 0.064$ m/s.

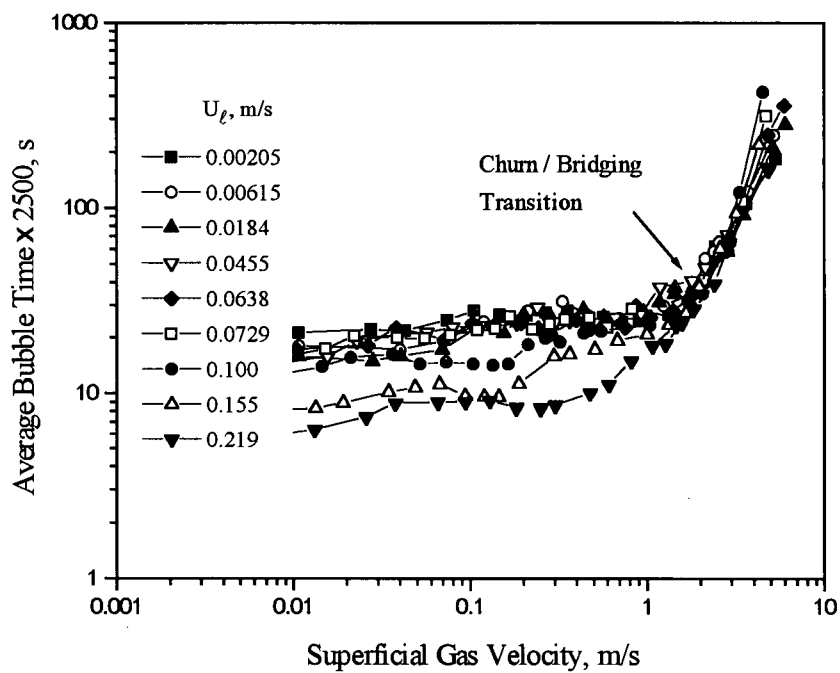


Figure 4.10. Average bubble time versus superficial gas velocity showing transition between churn flow and bridging flow in the air-water system at $Z = 0.65$ m for different superficial liquid velocities.

4.3.5 Transition between Bridging Flow and Annular Flow

Annular flow is characterized by a continuous gas region at the core and a continuous liquid region at the wall. In some cases, small bubbles were found in the liquid annular region. At the center of the column, in the annular flow regime, bubble frequency or liquid bridge frequency should be zero, and measured bubble chord length, infinite. This is used to determine the onset of annular flow. In this work, since the probe was always on the axis of the column, by extrapolating the measured bubble frequency to zero in a plot of f vs. U_g , the transition velocity between bridging flow and annular flow can be obtained experimentally as shown in Figure 4.8.

4.3.6 Transition between Discrete Bubble Flow or Coalesced Bubble Flow and Dispersed Bubble Flow

At a constant low gas flow rate, as liquid flow is increased, bubbles become smaller and their size distributions become narrower. This regime is the dispersed bubble flow regime. The bubble behavior in this regime is relatively independent of the gas distributor.

In this study, it was found that both the average and standard deviation of ℓ_b (or t_i) decreased in the discrete and dispersed bubble flow regimes. (Bubble characteristics for different flow regimes in the air-water system are presented in the next chapter.) However, the ratio of standard deviation of t_i to average t_i , σ_t / \bar{t}_i , increased for either discrete or coalesced bubble flow, but decreased for dispersed bubble flow. The transition from the discrete (or coalesced bubble flow regime when the discrete regime does not exist) to the dispersed bubble flow regime was assumed to correspond to the maximum value of σ_t / \bar{t}_i . This parameter is equal to $\sigma_\ell / \bar{\ell}_b$, providing that the velocities of all bubbles are the same. Figure 4.11 shows the variation of σ_t / \bar{t}_i with respect to the superficial liquid velocity.

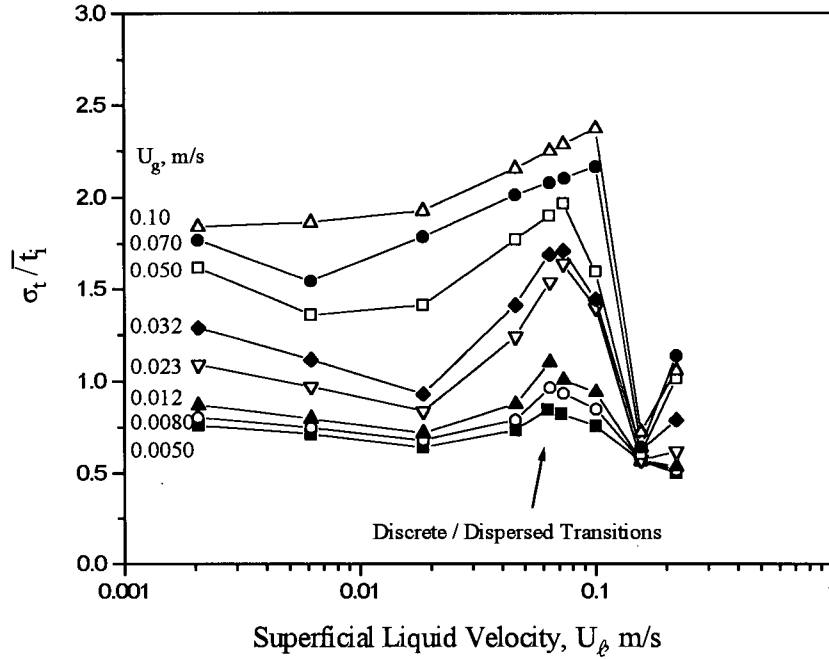


Figure 4.11. Dimensionless standard deviation of bubble time plotted against superficial liquid velocity showing transition between discrete bubble flow and dispersed bubble flow for air-water system at $Z = 0.65$ m.

4.4 Flow Regime Transitions at Different Heights

4.4.1 Experimental Conductivity Probe Results

In order to compare the results with those from pressure signals, the conductivity probe was installed at the same positions as the pressure transducers. The same criteria as described previously in section 4.3 were used to determine the flow regime transitions experimentally. The raw signals and the corresponding PDFs of the signals for the conductivity probe at different locations were similar to those shown in Figures 4.1 and 4.2.

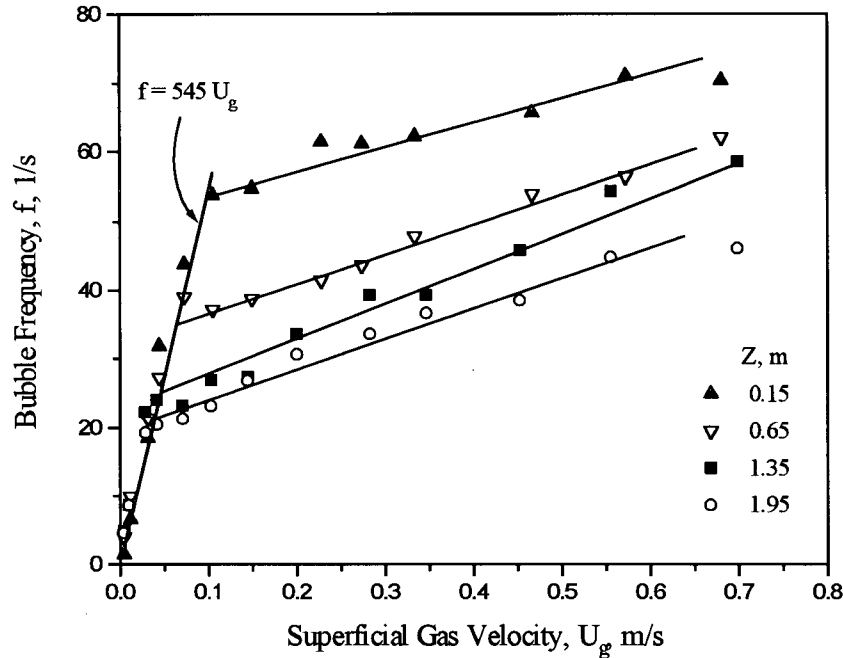


Figure 4.12. Bubble frequency plotted against superficial gas velocity showing transition between discrete and coalesced bubble flow at different locations for air-water system at $U_\ell = 0.0184$ m/s.

Figure 4.12 presents the bubble frequency at several different levels in the column. The bubble frequency increases linearly with gas velocity in the discrete bubble flow regime. At a certain gas velocity, depending on the measurement location, the bubble frequency deviates abruptly from this line; at this point coalesced bubble flow is encountered. It would appear that coalescence begins at the top of the column and develops downward from the top to the bottom of the column. The transition gas velocity is smallest at $Z = 1.95$ m and highest at 0.15 m.

As proposed in section 4.3.2 above, the transition from coalesced bubble flow to slug flow occurs when the Sauter mean bubble chord length equals the diameter of the column. Figure 4.13 shows the variation of the Sauter mean bubble chord length with respect to the superficial gas velocity. It can be seen that the Sauter mean bubble chord length reaches the column diameter at a

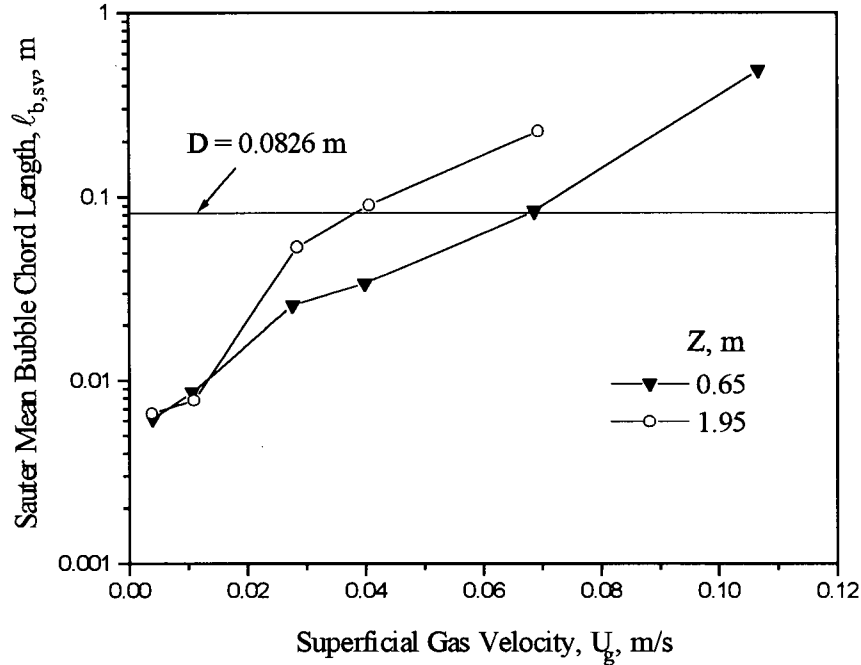


Figure 4.13. Sauter mean bubble chord length versus superficial gas velocity showing transition between coalesced bubble flow and slug flow at two different levels for air-water system at $U_\ell = 0.0184$ m/s.

lower U_g for $Z = 1.95$ m than for $Z = 0.65$ m. This indicates that bubbles continue to coalesce as they rise from $Z = 0.65$ m to 1.95 m. Thus, slug flow is encountered at the top of the column first, leading to a lower gas velocity for this transition. The results are in good agreement with visual observations.

When the gas velocity is increased further, the bubble frequency as shown in Figure 4.14 reaches a maximum corresponding to the transition from slug flow to churn flow. It is seen that the transition gas velocities, determined as proposed in section 4.3.3, do not vary significantly with respect to the measurement level. Once U_g is great enough, the transition from slug flow to churn flow occurs throughout the column. This implies that churn flow may not be the result of an entrainment effect as claimed by Taitel et al. (1980).

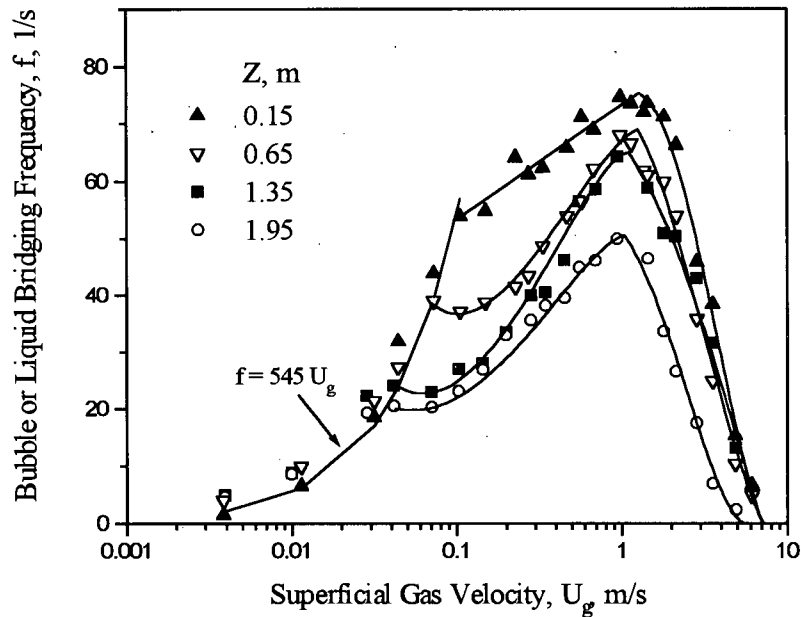


Figure 4.14. Variation of bubble frequency with gas velocity at different heights for air-water system at $U_l = 0.0184$ m/s.

The onset gas velocities for annular flow at different locations can also be determined from Figure 4.14 by extrapolating the bubble frequency curves to $f = 0$. It can be seen that the onset gas velocities for $Z = 0.15$, 0.65 and 1.35 m are essentially the same. However, the onset velocity for $Z = 1.95$ m is significantly lower than those at the other three levels. This could be an exit effect since $Z = 1.95$ m is very close to the top of the column. (The column height is 2.1 m, including a section in the separator.)

Consistent with section 4.3.4 above, the transition from churn flow to bridging flow can be determined from the plot of average bubble time vs. gas velocity, and this is shown in Figure 4.15. It is seen that the transition gas velocity at 1.95 m is lower than for the other heights. As the gas velocity is increased, bridging flow can be observed at 1.35 m, 0.65 m, and even near the bottom of the column, at $Z = 0.15$ m.

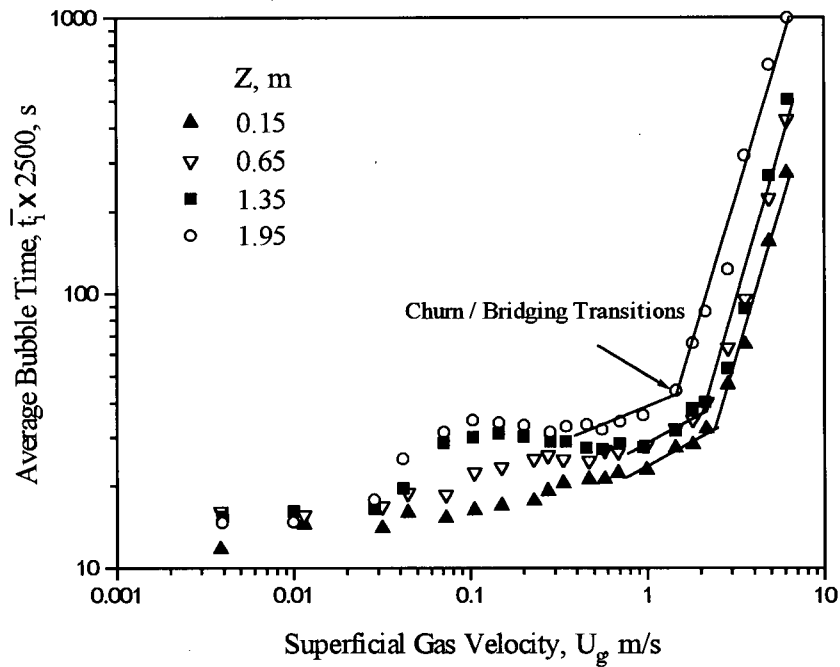


Figure 4.15. Average bubble time versus superficial gas velocity showing transition between churn flow and bridging flow at different locations for air-water system at $U_l = 0.0184$ m/s.

The experimental flow regime transitions determined with the conductivity probe at different locations are summarized in Table 4.1. It can be seen that the transition gas velocities for the discrete/coalesced bubble flow and the coalesced bubble/slug flow regimes are almost the same. This implies that the coalesced bubble flow regime exists only over a narrow range of gas velocity for the experimental system used. Since the column diameter is small (82.6 mm), once the bubbles coalesce, Taylor bubbles can be observed almost immediately and slug flow is encountered.

Table 4.1 Flow regime transition velocities determined from the conductivity probe for air-water system at $U_\ell = 0.0184$ m/s using the criteria proposed in sections 4.3.1 to 4.3.5.

Probe locations, Z, m	Superficial gas velocity corresponding to flow regime transition, m/s				
	Discrete/Coalesced	Coalesced/Slug	Slug/Churn	Churn/Bridging	Bridging/Annular
0.15	0.10	not measured	1.3	2.4	7
0.65	0.066	0.068	1.2	2.0	7
1.35	0.047	not measured	1.1	2.0	7
1.95	0.038	0.038	1.0	1.4	5.3

4.4.2 Experimental Pressure Fluctuation Results

As discussed in section 3.2.2, a pressure transducer registers not only pressure fluctuations caused by bubbles passing the probe, but also pressure waves caused by other disturbance sources. Nevertheless, some experiments were carried out since this is the simplest among all instrument methods. Four pressure transducers were mounted on the column wall, 0.15, 0.65, 1.35 and 1.95 m above the distributor. For periods of 20 s these pressure fluctuation signals were acquired by a computer at a sampling rate of 100 s^{-1} . While the superficial liquid velocity was maintained constant at $U_\ell = 0.0184$ m/s, the gas velocity was varied from 0.0035 to 6.2 m/s, spanning discrete bubble, slug and churn flow regimes and coming very close to annular flow.

The probability density distribution functions of the absolute pressure fluctuations at 0.65 m are shown in Figure 4.16. The results show that with an increase in superficial gas velocity, the mean pressure at this height decreases. The fluctuations in pressure first increase to a maximum, then decrease. It can also be noted that the peak of the PDF shifts to the left with increasing U_g . These characteristics are reflected in the standard deviation and the skewness of the signal. Figure 4.17 presents the variation of the standard deviation of the absolute pressure fluctuations at different levels. It can be seen that there is not much difference among the results at these

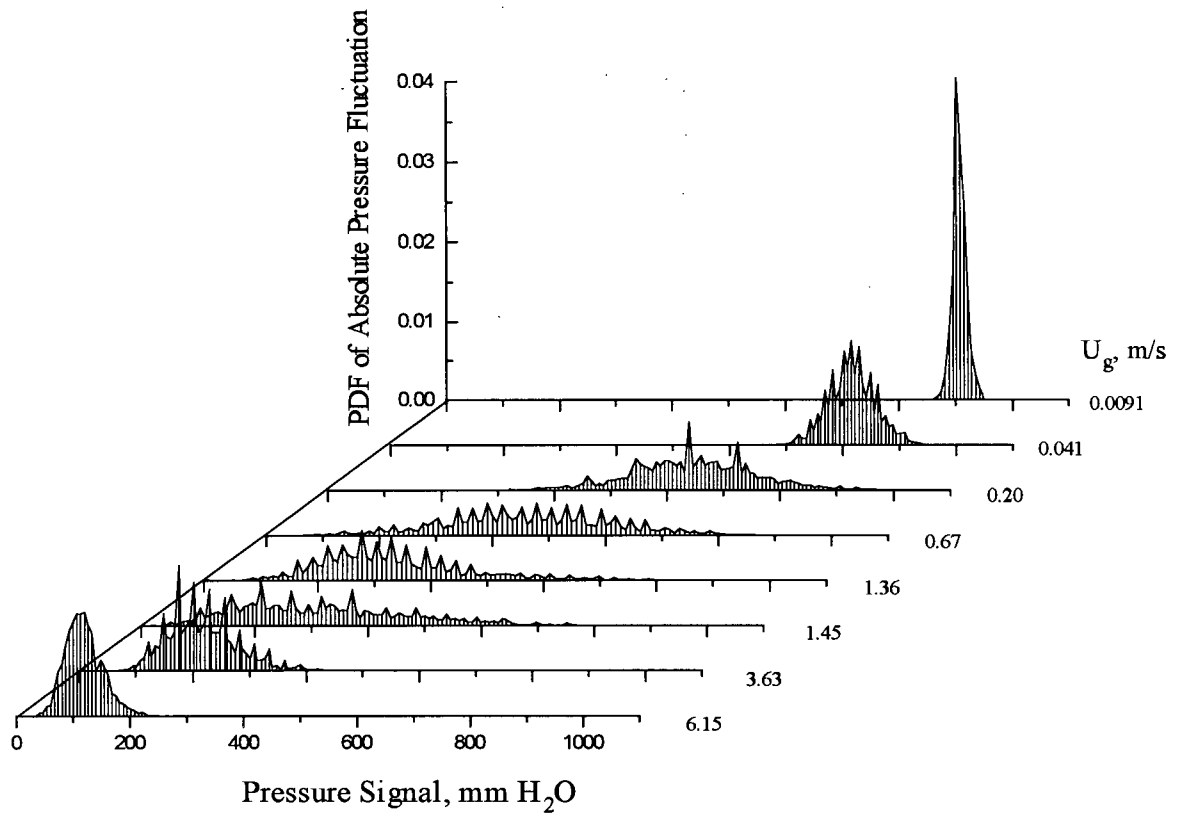


Figure 4.16. Probability density function of the absolute pressure fluctuations for air-water system at $Z = 0.65$ m and $U_\ell = 0.0184$ m/s.

locations except for $Z = 1.95$ m. As this location is close to the exit, this could be due to an exit effect. The first turning point is at $U_g = 0.026$ m/s. This could correspond to the first bubble/slug transition. From visual observations and Figure 4.13, Taylor bubbles develop first at the top of the column. With increasing gas velocity, Taylor bubbles can be observed near the distributor. This phenomenon, however, is not manifested by the pressure fluctuations since the pressure transducer registers pressure waves from within the entire column.

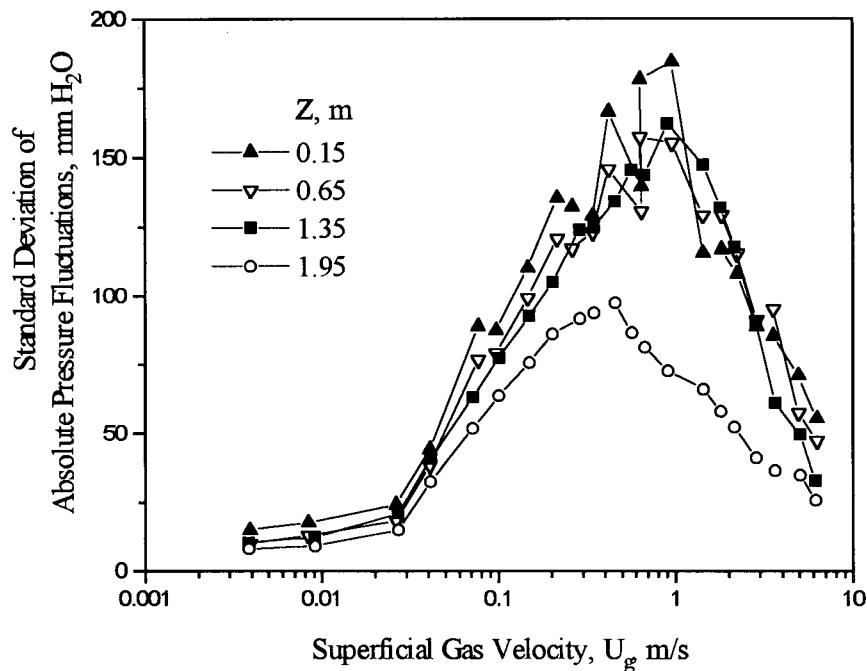


Figure 4.17. Standard deviation of absolute pressure fluctuations for air-water system at $U_\ell = 0.0184$ m/s.

The slug/churn flow transition could take place at the maximum of the standard deviation in Figure 4.17. The transition velocities which can be determined from pressure fluctuation signals are summarized in Table 4.2. Pressure fluctuation signals are not helpful in delineating higher gas velocity transitions.

Table 4.2. Flow regime transition velocities determined from the standard deviation of absolute pressure fluctuations for $U_\ell = 0.0184$ m/s.

Probe location, m	Superficial gas velocity corresponding to flow regime transition, m/s	
	Bubble/Slug	Slug/Churn
0.15	0.026	0.90
0.65	0.026	0.80
1.35	0.026	0.90
1.95	0.026	0.43

Some experiments were also performed to determine differential pressure fluctuations. The vertical distance between the two pressure transducer ports was 100 mm. The differential pressure was zero when a Taylor bubble passed the transducers. The PDFs of the differential pressure fluctuations are presented in Figure 4.18. It can be seen that, with increasing superficial gas velocity, the mean value of ΔP decreases. The corresponding fluctuations of ΔP increase first, then decrease. This phenomenon is related to the standard deviation of the signal as shown in Figure 4.19. It can also be seen in Figure 4.18 that at a certain gas velocity, a peak becomes evident near $\Delta P = 0$, causing asymmetry of the PDF curves. However, at high gas velocities, the PDF curves become symmetric again. This phenomenon is reflected in the skewness as shown in Figure 4.20.

In Figure 4.19, two characteristic features can be seen. One is the sharp increase in the standard deviation at $U_g \approx 0.026$ m/s. The other is the maximum value of the standard deviation. If we assume that the bubble/slug flow transition occurs where the standard deviation of the ΔP fluctuations increases sharply, while the slug/churn flow transition takes place where the standard deviation reaches its maximum, then the flow regime transition velocities can be summarized in Table 4.3. With the same assumptions, but using the skewness as the indicator instead of the standard deviation, the transition velocities can also be obtained from Figure 4.20. In addition, if we assume that annular flow takes place where the skewness returns to zero, by extrapolating the skewness curves in Figure 4.20, the transition velocity for annular flow can also be estimated. The results are summarized in Table 4.4.

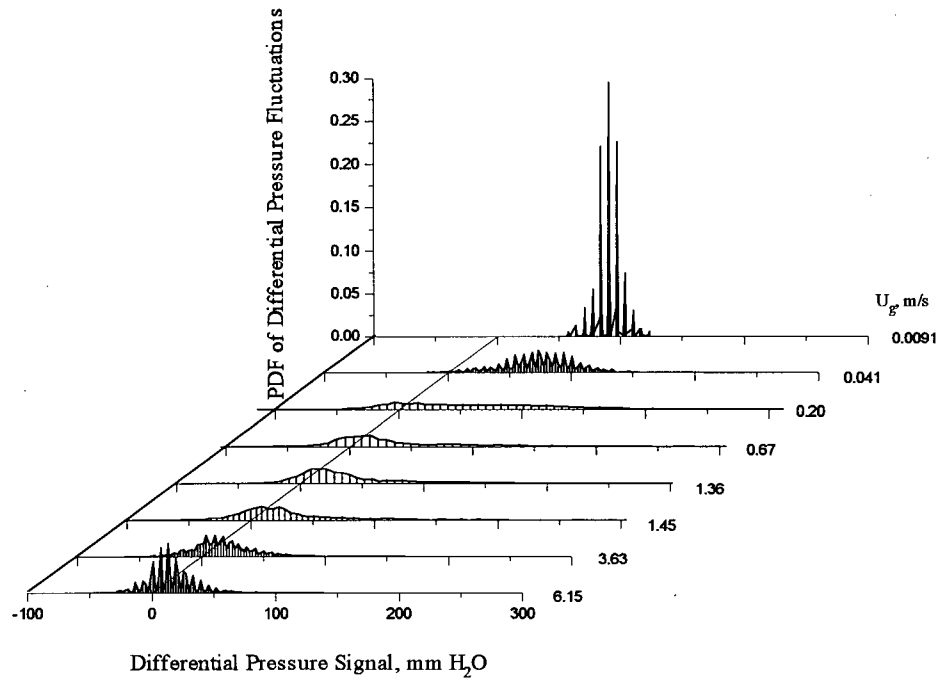


Figure 4.18. Probability density function of differential pressure fluctuations at $Z = 0.65$ m for $U_\ell = 0.0184$ m/s.

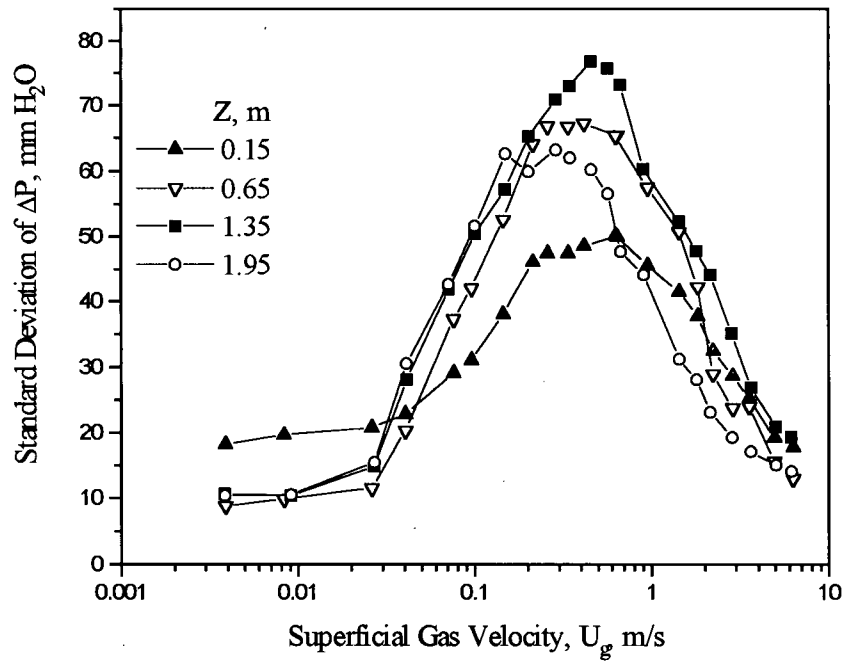


Figure 4.19. Standard deviation of differential pressure fluctuations at different levels for $U_\ell = 0.0184$ m/s.

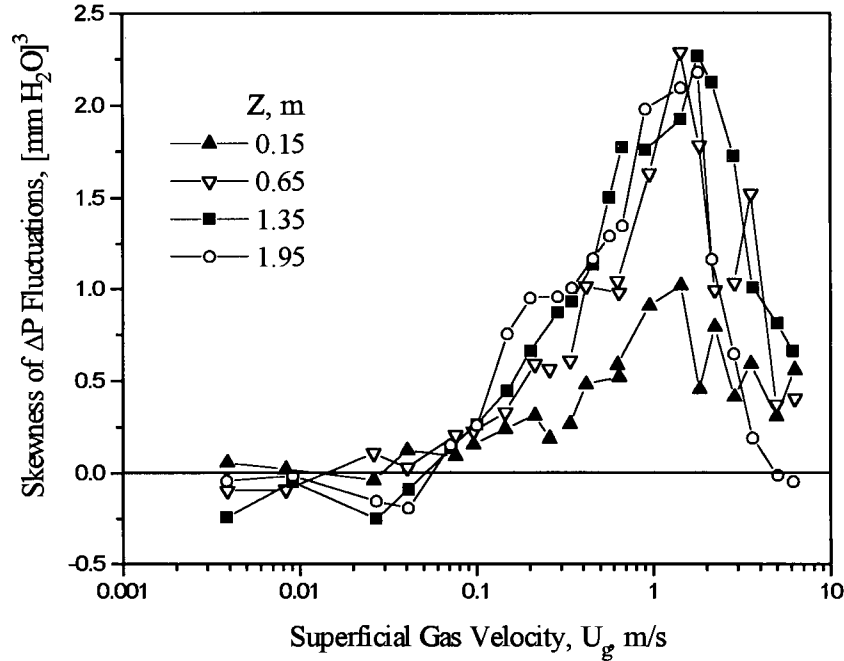


Figure 4.20. Skewness of differential pressure fluctuations at different levels for $U_\ell = 0.0184$ m/s.

Table 4.3. Flow regime transition velocities determined from the standard deviation of differential pressure fluctuations for $U_\ell = 0.0184$ m/s.

Probe location, m	Superficial gas velocity corresponding to flow regime transition, m/s	
	Bubble/Slug	Slug/Churn
0.15	0.059	0.65
0.65	0.026	0.41
1.35	0.026	0.46
1.95	0.026	0.28

Table 4.4. Flow regime transition velocities determined from the skewness of differential pressure fluctuations for $U_\ell = 0.0184$ m/s.

Probe location, m	Superficial gas velocity corresponding to flow regime transition, m/s		
	Bubble/Slug	Slug/Churn	Bridging/Annular
0.15	0.075	1.4	20
0.65	0.043	1.4	6.9
1.35	0.052	1.8	8.5
1.95	0.052	1.8	5.0

4.4.3 Comparison between Conductivity Probe and Pressure Transducer Techniques

Tables 4.1 to 4.4 summarize the experimental results at different heights from the conductivity probe and pressure transducer techniques using different criteria. For the conductivity probe, the results are in good agreement with the visual observations. They also reflect the development of each flow pattern along the column. All flow regime transitions can be determined by the two-element probe using the criteria proposed in section 4.3. For the pressure transducers, however, only some transitions can be detected.

It can be seen that for the bubble/slug transition, the results from the standard deviation of absolute pressure fluctuations (in Table 4.2) are close to those from the standard deviation of differential pressure fluctuations (in Table 4.3). Since the standard deviation is a measure of the distribution about the mean, the pressure disturbance caused by air injection and/or other pressure disturbances could enhance the value of the standard deviation in the same ways for both P and ΔP . The results also indicate that even with a differential pressure transducer, the effect of air injection and other pressure disturbances cannot be totally eliminated. Comparing with the results from the conductivity probe, we see that the techniques based on standard deviations of absolute and differential pressure fluctuations underestimate the gas velocities corresponding to the bubble/slug transition. However, the results from the skewness of the different pressure fluctuations are comparable to those from the conductivity probe; since the skewness is a measure of the asymmetry of a distribution, the effect of the air injection and other pressure disturbances may be small.

For the slug/churn transitions, the technique using the standard deviation of differential pressure fluctuations underestimates the transition gas velocities significantly, compared with the results from the conductivity probe. However, the results from the standard deviation of absolute

pressure and from the skewness of differential pressure fluctuations are comparable to those from the conductivity probe.

Tables 4.3 and 4.4 demonstrate that, with the same measurement technique, different parameters used as transition criteria provide different results.

4.5 Flow Regime Map for Air-Water System

4.5.1 Experimental Results

The flow regime boundaries based on conductivity measurements as derived from Figures 4.6, 4.7, 4.8, 4.10 and 4.11 are summarized in Table 4.5. They are also plotted in Figure 4.21. It can be seen that the discrete bubble flow regime predominates at low gas and liquid velocities, while the dispersed bubble flow regime is encountered at higher liquid velocities. Both discrete and dispersed bubble flow regimes are characterized by small bubbles with relatively uniform size distributions. The bubbles in the dispersed bubble flow regime, however, are smaller and more

Table 4.5. Flow regime boundaries for air-water system for $Z = 0.65$ m and $D = 0.0826$ m.

Discrete / Dispersed			Discrete / Coalesced	Coalesced / Slug	Slug / Churn	Churn / Bridging	Bridging / annular
U_ℓ , m/s	U_g , m/s	U_ℓ , m/s	U_g , m/s				
0.064	0.0050	0.00205	0.047	0.047	1.3	1.77	6.3
0.064	0.0080	0.00615	0.052	0.061	1.3	1.77	6.7
0.064	0.012	0.0184	0.061	0.068	1.2	1.72	6.7
0.073	0.023	0.0455	0.048	0.056	1.1	1.72	6.7
0.073	0.032	0.0638	0.036	0.048	1.3	1.77	6.7
0.073	0.050	0.0729	0.040	0.048	1.4	1.77	5.7
0.10	0.070	0.100	0.062	0.069	1.1	1.85	5.1
0.10	0.10	0.155	0.13	0.13	0.99	1.72	5.2
		0.219	0.26	0.23	0.36	1.85	5.2

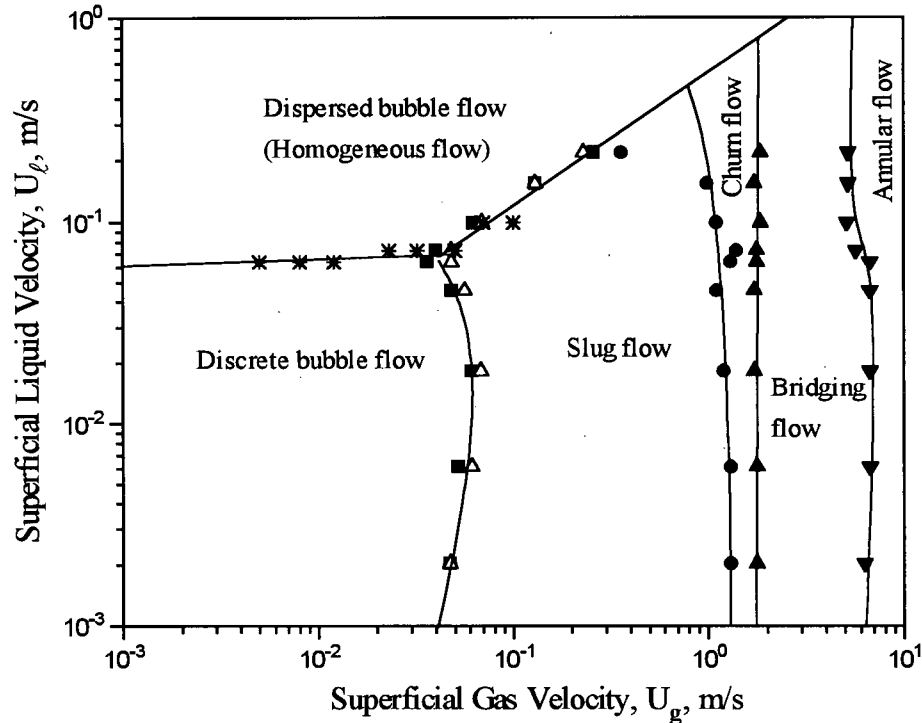


Figure 4.21. Two-phase bubble column flow regime map for air-water system with $D = 0.0826$ m and $Z = 0.65$ m. Distributor: perforated plate containing 62 2-mm circular holes.

uniform resulting from the turbulence of the liquid, while the bubble size and distribution in the discrete bubble flow regime could be a function of the gas distributor. The coalesced bubble flow regime in Figure 4.21 appears in a very narrow gas velocity range between the discrete bubble flow regime and slug flow regime due to the small column used in this study.

The slug flow regime spans a wide range of gas velocities. At low liquid velocities, the onset of slug flow is almost independent of the superficial liquid velocity while at high liquid velocities the transition from dispersed bubble flow to slug flow is a function of the liquid velocity. With increasing superficial liquid velocity, the transition gas velocity from dispersed bubble flow to slug flow increases.

The transitions among the slug, churn, bridging and annular flow regimes are nearly independent of the superficial liquid velocity. For the conditions studied in this work, the churn flow regime only exists within a small range of gas velocity.

4.5.2 Comparison

Many investigators have studied flow regime transitions experimentally. Some earlier studies have been based on visualization. Others determined the flow regime with the aid of instruments, e.g., pressure transducer, conductivity probe and X-ray measurement systems. Table 4.6 summarizes some previous studies in vertical gas-liquid two-phase flow. In comparison with this study, it should be mentioned that none of them used a gas distributor. In addition, the column diameter used in most previous studies was much smaller, usually 25 or 51 mm, and the measurement locations were several meters above the gas injector. This makes comparison difficult. Nevertheless, a comparison between this study and some previous studies is shown in Figure 4.22. It can be seen that there is a wide discrepancy among results in the literature, and that the results obtained in this work are similarly discrepant.

Table 4.6. Summary of some experimental regime transition measurements from the literature.

Reference	Measurement Method	Flow Regime Map	Experimental conditions			
			Gas / liquid	Column diameter, mm	Column height, m	Measurement height, m
Griffith and Wallis (1961)	Visual observation	$Q_g/(Q_g+Q_l)$ vs. Fr_m	air/water	12, 19 and 25	5.5	
Spedding and Nguyen (1980)	Visual observation	$(Fr_m)^{1/2}$ vs. Q_l/Q_g	air/water	45.5		
Taitel et al. (1980)	Visual observation	U_l vs. U_g	air/water	25 and 51		
Weisman and Kang (1981)	Visual observation	Gas flow rate vs. liquid flow rate	air/water air/glycerol Freon-113 vapor /Freon-113 liquid	12, 25 and 51	6.1	
Fernandes et al. (1983)	Visual observation	U_l vs. U_g	air/water	50.7	11.1	
Tutu (1982, 1984)	Pressure transducer	N/A	air/water	52.2	4	2.13
Annunziato and Girardi (1985)	Differential pressure transducer	U_l vs. U_g	air/water	92	3.7	2.19 and 3.0
Matsui (1984, 1986)	Differential pressure transducer	N/A	nitrogen/water	22	2.3	1.1 and 1.4
Barnea et al. (1980)	Conductance probe	N/A	air/water	25		
Matuszkiewicz et al. (1987)	Conductivity probe (square probe)	N/A	air/water	20 × 20 mm	1.75	0.15, 0.30, 0.45, 0.60, etc.
Das and Pattanayak (1993, 1994)	Electrical impedance probe	N/A	air/water	11	2.9	2.4
Mao and Dukler (1989)	Radio-frequency probe	N/A	air/electrolytic solution	50.8	12.0	3.3, 4.2, 5.5, 6.7 and 8.9
Vince and Lahey, Jr. (1982)	X-rays	U_l vs. U_g	air/water	25.4		
Jones, Jr. and Zuber (1975)	X-rays	U_l vs. ϵ_g	air/water	5 × 63.5 (2D)	3.05	
Govier et al. (1957, 1958)	Pressure gradient	U_l vs. U_g/U_l	air/water	16, 26, 38 and 64	7	
Jayanti and Hewitt (1992)	Pressure gradient	N/A	air/water	31.8	20	

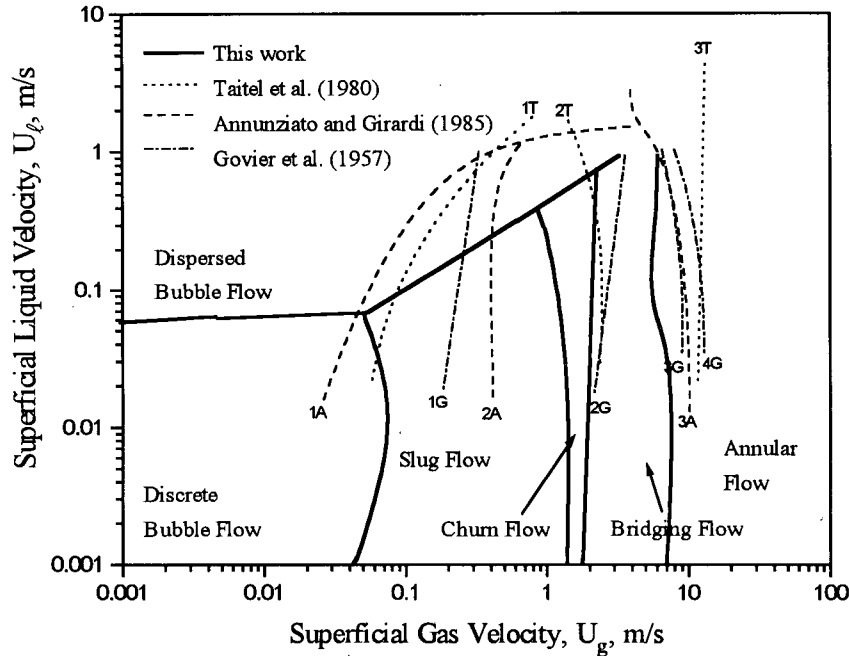


Figure 4.22. Comparison of flow regime maps with previous studies.

- 1A: Bubble/Slug Flow Transition, Annunziato and Girardi (1985)
- 2A: Slug/Churn Flow Transition, Annunziato and Girardi (1985)
- 3A: Churn/Annular Flow Transition, Annunziato and Girardi (1985)
- 1G: Bubble/Slug Flow Transition, Govier et al. (1957)
- 2G: Slug/Froth Flow Transition, Govier et al. (1957)
- 3G: Froth/Ripple Flow Transition, Govier et al. (1957)
- 4G: Ripple/Film Flow Transition, Govier et al. (1957)
- 1T: Bubble/Slug Flow Transition, Taitel et al. (1980)
- 2T: Slug/Churn Flow Transition, Taitel et al. (1980)
- 3T: Churn/Annular Flow Transition, Taitel et al. (1980)

4.6 Summary

A conductivity probe directly reflects the behavior of a two-phase mixture. By measuring bubble frequency, Sauter mean bubble chord length and either average bubble length or average bubble time, flow pattern transitions can be determined. Methods for delineating these transitions are given in this chapter, and experimental results are presented for air-water in a column of diameter 82.6 mm.

A pressure transducer registers all pressure fluctuation information including the pressure fluctuations caused by bubbles passing the probe and the pressure disturbances caused by other sources (e.g., air injection). Although a differential pressure transducer may give more weight to the signals which relate to local bubble characteristics by reducing the amplitude of disturbances from outside the interval of interest, it does not totally eliminate the effect of other pressure disturbance sources. Both methods do not appear to be suitable for flow regime determination in gas-liquid systems.

Measurement location plays an important role on flow regime transitions, especially at low gas velocities, since bubbles grow as they ascend in coalesced bubble flow. A flow regime map for the air-water system, determined at 0.65 m above the distributor, is obtained. This is in reasonable agreement with previous studies considering the differences in the experimental conditions. This map and the techniques developed for distinguishing flow regime transitions serve as the basis for further investigation on flow regime transitions in three-phase systems, as discussed in later chapters.

Chapter 5

Bubble Characteristics in Bubble Columns

5.1 Introduction

As described in the previous chapter, several flow regimes were observed in a bubble column: discrete bubble flow, dispersed bubble flow, slug flow, churn flow, bridging flow and annular flow. This chapter presents experimental results to demonstrate bubble characteristics in these flow regimes. The bubble properties measured in the present work are bubble frequency, gas holdup, bubble velocity, bubble chord length and the chord length distribution. Some results have already been presented in Chapter 4 for the purpose of establishing criteria for flow regime transitions.

The experimental apparatus and conductivity probe used in this work to measure the bubble characteristics are presented in Chapter 2. The probe was inserted horizontally 650 mm above the gas-liquid distributor with the end of the probe on the axis of the column of inside diameter 82.6 mm. A perforated plate with 62 orifices of diameter 2.0 mm served as the air distributor.

5.2 Bubble Characteristics in the Discrete and Dispersed Bubble Flow Regimes

The discrete and dispersed bubble flow regimes are both characterized by small bubbles and narrow size distributions as noted in Chapter 1. The difference between these two flow patterns is that the uniform small size bubbles in the dispersed bubble flow regime result from turbulence of the liquid phase, while in the discrete bubble flow regime, small bubbles are generated mainly by the gas distributor at low gas and liquid velocities. These two regimes can be distinguished from each other by the ratio of the standard deviation of bubble time to the average bubble time, as described in Chapter 4. The discrete bubble flow regime was observed for liquid

velocities between 0 and approximately 0.07 m/s and gas velocities from 0.00205 to approximately 0.05 m/s. The dispersed bubble flow regime was found at higher liquid velocities in the air-water system, as shown in Figure 4.21.

5.2.1 Local Bubble Frequency

The local bubble frequency in these two regimes is plotted against the superficial gas velocity in Figure 5.1. A linear relationship between the bubble frequency and the superficial gas velocity is found in both the discrete and dispersed bubble flow regimes. The superficial liquid velocity is found in both the discrete and dispersed bubble flow regimes. The superficial liquid velocity does not significantly affect this linear relationship. As discussed in Chapter 4, the local bubble frequency can be expressed by Equation (4.1), assuming that all small bubbles are spherical and of uniform size, distributed uniformly across the column. The linear constant for the bubble frequency and the superficial gas velocity is $545 \pm 80 \text{ m}^{-1}$.

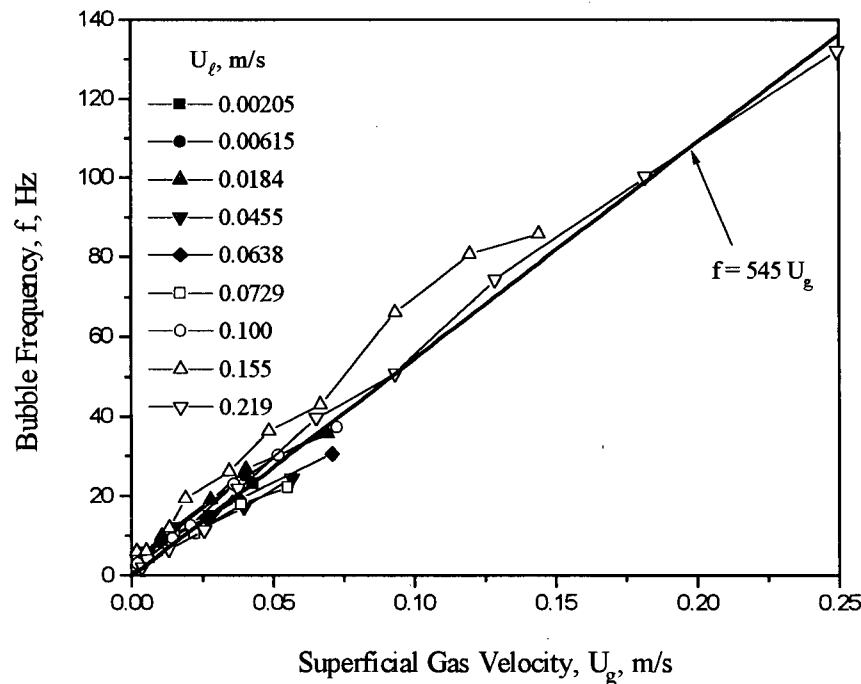


Figure 5.1. Linear relationship between bubble frequency and superficial gas velocity for the discrete and dispersed bubble flow regimes: air-water system at $Z = 650 \text{ mm}$ and $D = 82.6 \text{ mm}$.

5.2.2 Bubble Chord Length and its Distribution

Figure 5.2 presents experimental results for the average bubble chord length as a function of the superficial gas and liquid velocities. The average bubble chord length increases with increasing gas velocity. It can be seen that the average bubble chord length decreases with increasing liquid velocity. As the liquid velocity is increased, a gradual transition takes place between discrete and dispersed bubble flow.

Some typical distributions of bubble chord length in the discrete and the dispersed bubble flow regimes are presented in Figure 5.3. The four left-hand plots are for the discrete bubble flow regime at $U_\ell = 0.0184$ m/s, while the four right-hand plots correspond to the dispersed bubble flow regime at $U_\ell = 0.155$ m/s. The standard deviation of the bubble chord length for each

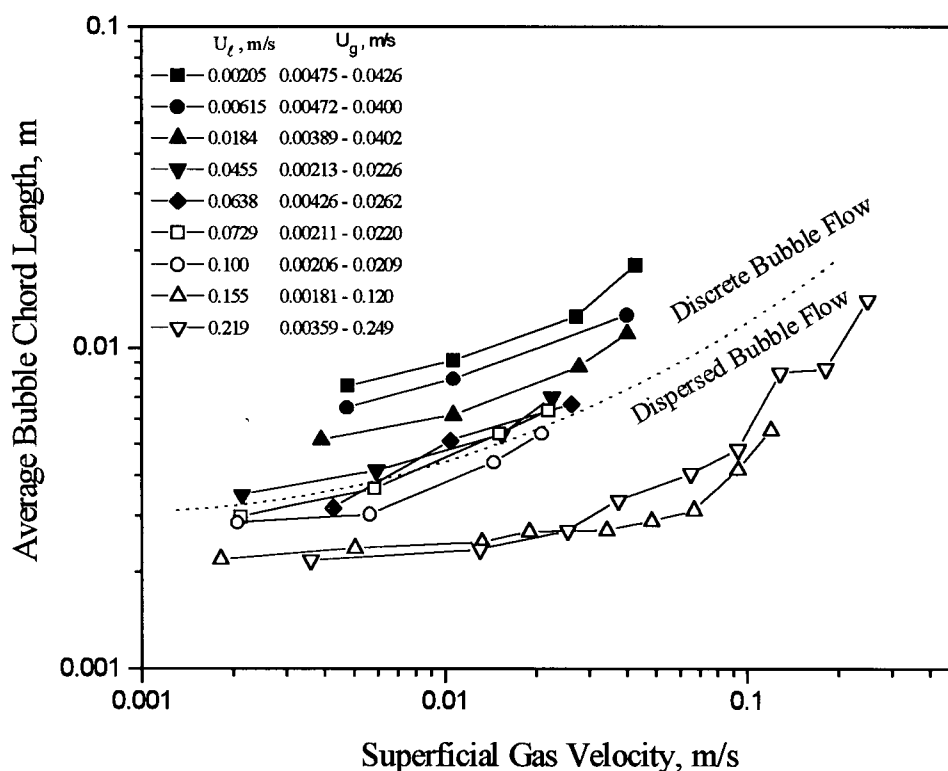


Figure 5.2. Comparison of average bubble chord length in discrete and dispersed bubble flow regimes for air-water system at $Z = 0.65$ m.

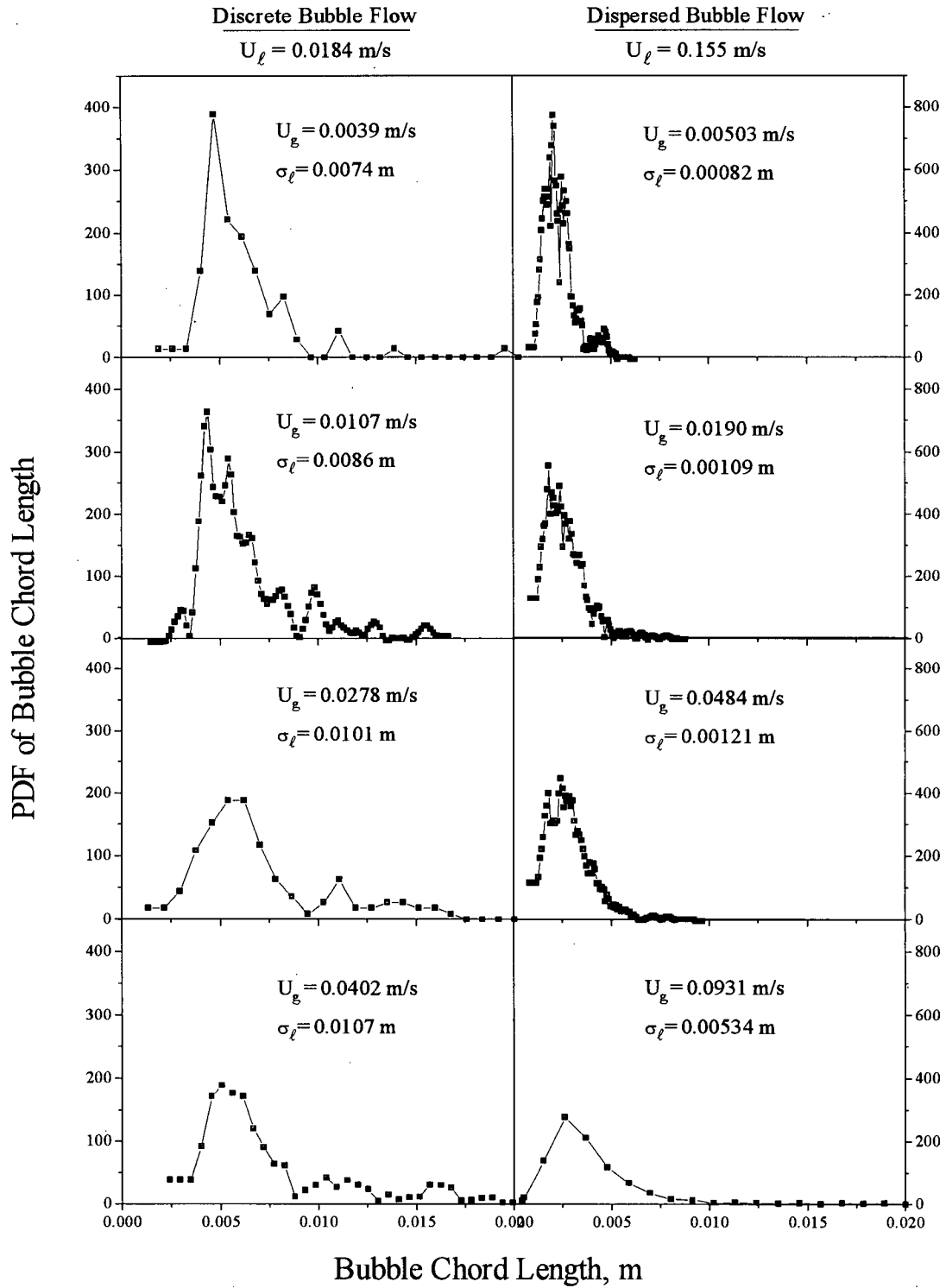


Figure 5.3. Probability density distribution of bubble chord length in discrete and dispersed bubble flow regimes for air-water system at $Z = 0.65$ m.

operating condition is also given in the figure. It can be seen that the peak values of the PDF curves appear at an average bubble chord length of approximately 5 mm for the discrete bubble flow and 2.5 mm for the dispersed bubble flow, indicating that smaller bubbles were detected in the dispersed bubble regime. The standard deviation of the bubble chord length distribution increases with the gas velocity in both flow regimes. However, the standard deviation of the bubble chord length distribution in the dispersed bubble flow regime is smaller than in the discrete bubble flow regime, indicating a narrower distribution in the dispersed bubble flow regime.

5.2.3 Average Bubble Velocity

The experimental results for the average bubble velocities in the discrete and dispersed bubble flow regimes are plotted against average bubble chord length in Figure 5.4. It is seen that the average bubble velocity increases with increasing chord length. The bubble velocities at high

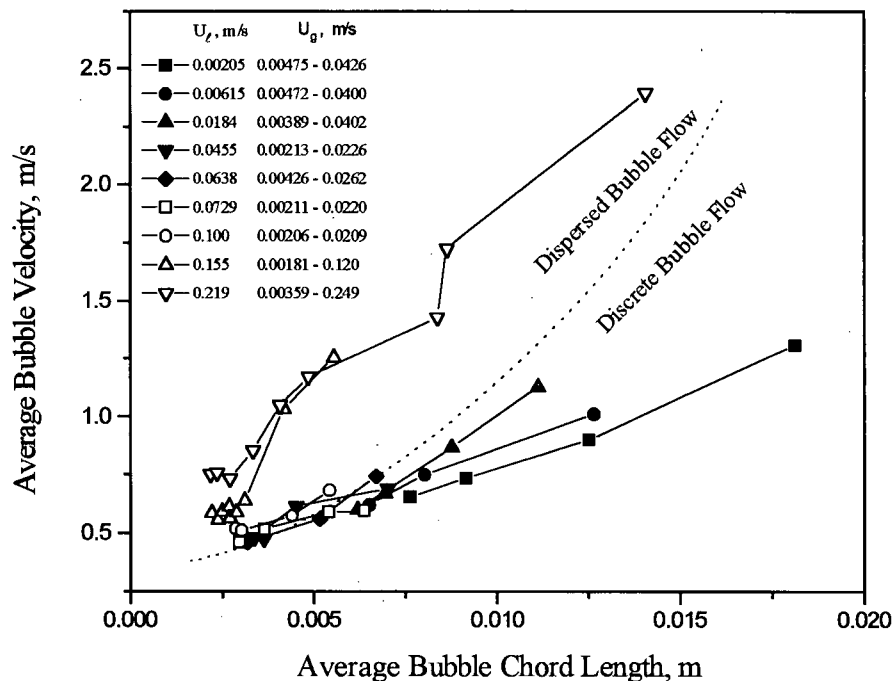


Figure 5.4. Average bubble velocity at different superficial liquid velocities for air-water system at $Z = 0.65$ m.

liquid superficial velocities are greater than at low liquid velocities.

The bubble velocity and the bubble chord length can be correlated in an alternative way. Consider a system with uniform spherical bubbles of diameter d_b , during a period of time t ; the local gas holdup measured by a conductivity probe can then be expressed by:

$$\epsilon_g = \frac{f \left(\frac{\pi}{6} d_b^3 \right)}{U_b \left(\frac{\pi}{4} d_b^2 \right)} \quad (5.1)$$

Rearrangement of Equation (5.1) yields:

$$\frac{\epsilon_g}{f} U_b = \frac{2}{3} d_b \quad (5.2)$$

The left-hand side of the above equation, defined here as bubble travel length, $\frac{\epsilon_g}{f} U_b$, is plotted against the average bubble chord length in Figure 5.5 for the discrete and the dispersed bubble flow regimes. A non-linear relationship between the bubble travel length and the average bubble chord length is observed. This could be due to the difference between the bubble chord length and the bubble diameter and the difference between the model assumptions and the real situation. The following empirical correlation can be used to describe the relationship between the bubble travel length and the average bubble chord length for the discrete and the dispersed bubble flow regimes:

$$\frac{\epsilon_g}{f} U_b = 0.00730 \log \bar{\ell}_b + 0.0211 \quad (\text{SI units}) \quad (5.3)$$

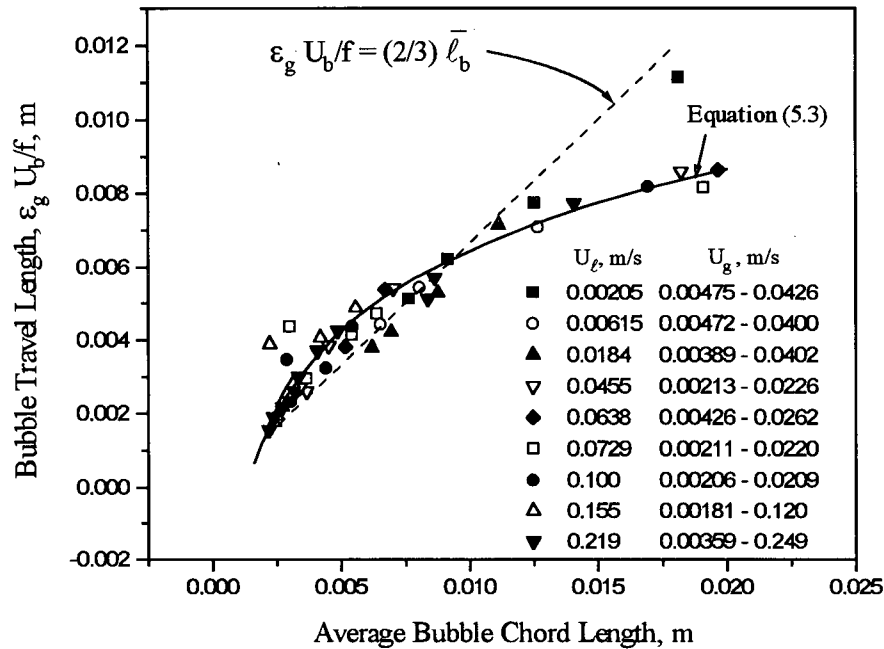


Figure 5.5. Relationship between bubble travel length and average bubble chord length for air-water system at $Z = 0.65$ m and $D = 82.6$ mm.

5.3 Bubble Characteristics in the Slug and Churn Flow Regimes

The slug and the churn flow regimes are defined in Chapter 1. In the slug flow regime, one can observe bullet-shaped bubbles and small bubbles in the liquid plugs separating them. In the churn flow regime, the bullet-shaped bubbles become narrow and their shapes are distorted. Small bubbles in the liquid plugs coalesce and generate new bullet-shaped bubbles. The overall bubble frequency then increases with the gas velocity in the slug flow regime and decreases with the gas velocity in churn flow. This difference in trends can be used to determine the transition from slug to churn flow as shown in Figure 4.9. In Chapter 4, the slug flow regime was observed when the gas velocity varied from approximately 0.05 to 1 m/s, while the churn flow regime was found at higher gas velocities, 1 to 2 m/s, in the air-water system with $D = 0.0826$ m, as shown in Figure 4.23.

5.3.1 Bubble Chord Length and its Distribution

As discussed in Chapter 4, the onset of the slug flow regime was determined by the Sauter mean bubble chord length since this parameter gives added weight to large bubbles. Figure 5.6 plots the Sauter mean bubble chord length and the average bubble chord length against the superficial gas velocity. It is seen that the Sauter mean bubble chord length is always greater than the average bubble chord length at the same gas velocity. The average bubble chord length is always less than the column diameter in the slug and the churn flow regimes due to the large number of small bubbles in the system. Both the Sauter mean bubble chord length and the average bubble chord length increase slightly with U_g in the slug flow regime. The bubble chord length distributions in the slug and churn flow regimes are presented in Figure 5.7.

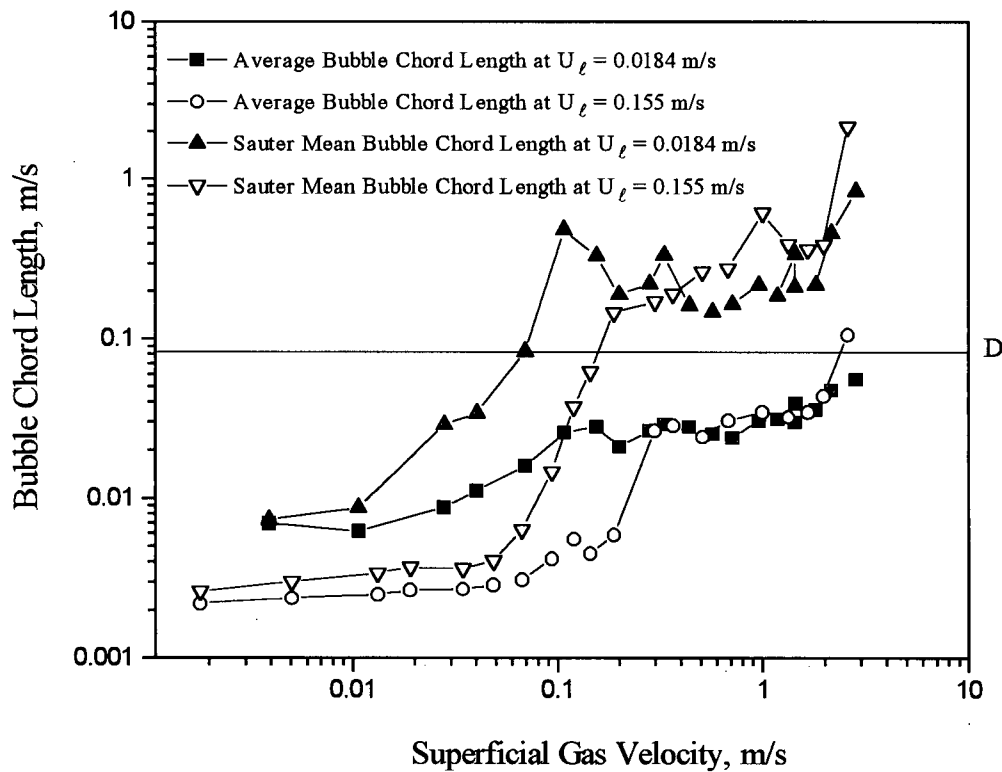


Figure 5.6. Bubble chord length in slug and churn flow regimes at $Z = 0.65$ m and $D = 82.6$ mm.

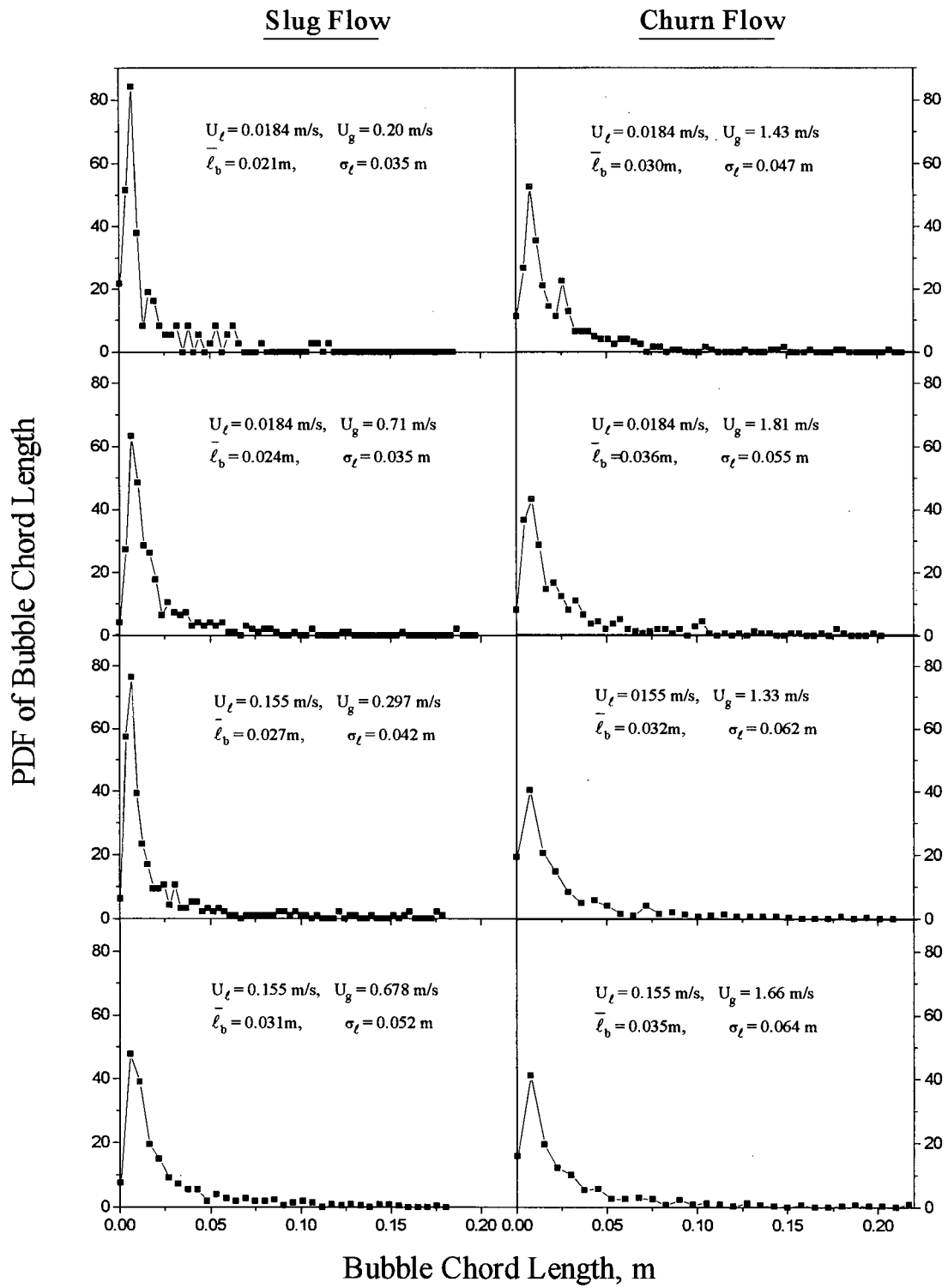


Figure 5.7. Probability density distribution of bubble chord length in the slug and churn flow regimes at $Z = 0.65 \text{ m}$ and $D = 82.6 \text{ mm}$.

It is seen that the average bubble chord length and the standard deviation for slug flow (left-hand side of Figure 5.7) under different operating conditions vary from 21 to 31 mm and from 35 to 52 mm, respectively, while the peaks of the PDF of the bubble chord length appear at a bubble chord length of 6 to 7 mm. This indicates that there are many small bubbles in the slug flow regime. In the churn flow regime (right-hand side of Figure 5.7), both the average and the standard deviation of the bubble chord length are higher than in the slug flow regime. However, the peak values of the PDF curves at low bubble chord length decrease and the PDF curves become wider, indicating that the population of small bubbles in the churn flow regime decreases while the population of large bubbles increases, due to coalescence of small bubbles.

5.3.2 Average Bubble Velocity

The difference between the slug and the churn flow regimes can also be seen from a plot of the average bubble velocity versus the average bubble chord length, as shown in Figure 5.8. The dashed line in the figure corresponds to the flow regime boundary in Figure 4.21 of Chapter 4. It is seen that the average bubble velocity increases sharply as the average bubble chord length varies from approximately 0.02 to 0.03 m in the slug flow regime. The reason could be the following: in the slug flow regime, the average bubble velocity is not only dependent on the average bubble chord length, but also on the superficial gas velocity. As discussed in the previous section, the average bubble chord length does not change significantly as the superficial gas velocity varies from approximately 0.05 to 1 m/s, due to the large number of small bubbles in the slug flow regime. Hence, a small increase in the average bubble chord length requires a large increase in superficial gas velocity, which increases the average bubble velocity significantly. In the churn flow regime, the average bubble chord length increases with gas velocity, by reducing the population of small bubbles and increasing the number of large bubbles. The average bubble velocity, however, increases only slightly in the churn flow regime, probably due to the relatively

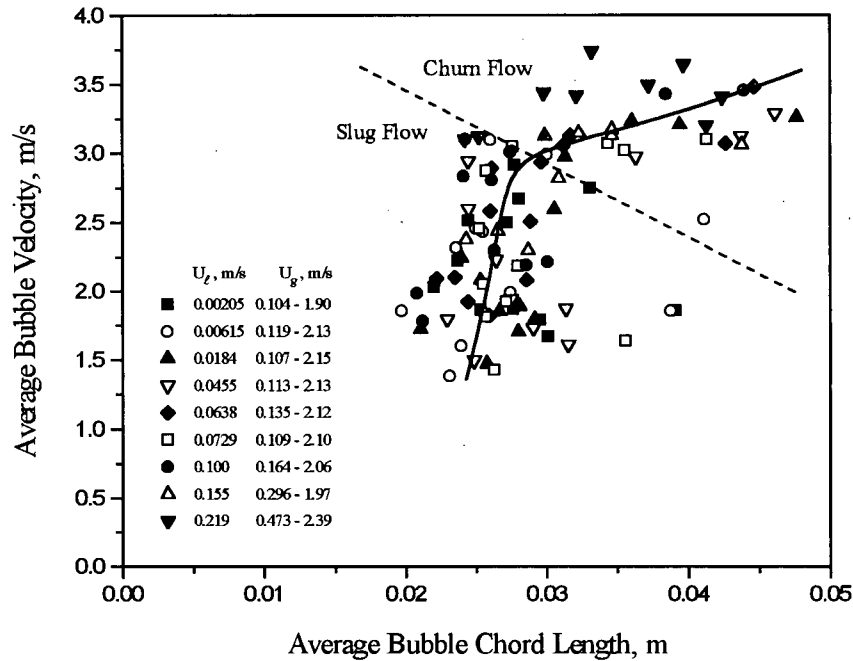


Figure 5.8. Relationship between average bubble velocity and average bubble chord length in slug and churn flow regimes for air-water system at $Z = 0.65$ m and $D = 82.6$ mm.

small change in the gas velocity, as the average bubble chord length increases from approximately 0.03 to 0.045 m.

The relationship between the bubble characteristics can be correlated by the bubble travel length and the average bubble length. Figure 5.9 presents the experimental results for the bubble travel length with respect to the average bubble chord length. Three distinctive regions corresponding to different flow regimes determined by the methods described in Chapter 4 can be found in this figure. At lower average bubble chord length, corresponding to the discrete and dispersed bubble flow regimes, the relationship between the bubble travel length and the average bubble chord length can be correlated by Equation (5.3). At intermediate average bubble chord length, corresponding to the slug and churn flow regimes, the relationship between the bubble travel length and the average bubble chord length can be expressed by another empirical correlation,

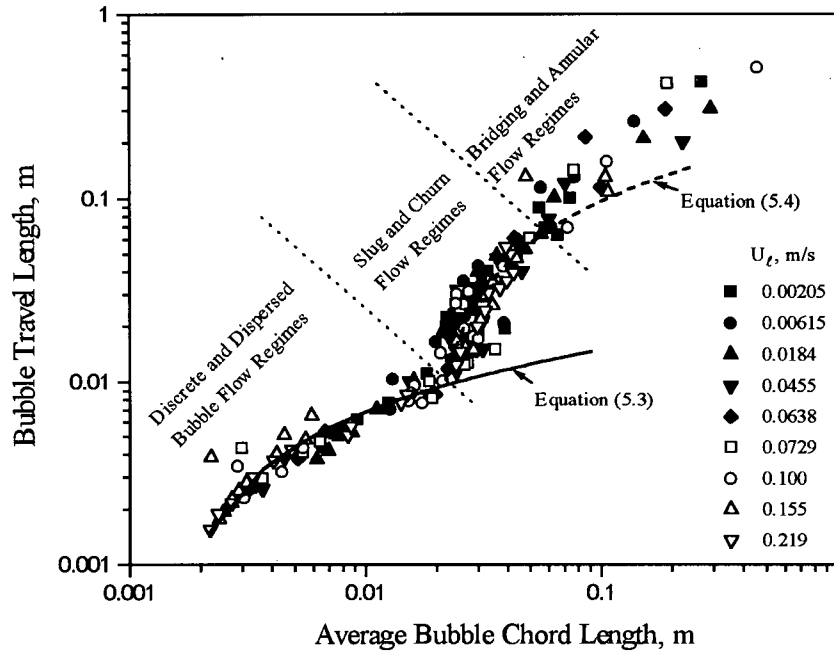


Figure 5.9. Relationship between bubble travel length and average bubble chord length in the slug and churn flow regimes for air-water system at $Z = 0.65$ m, $D = 82.6$ mm and $U_g \approx 0.002 - 6$ m/s.

$$\frac{\epsilon_g}{f} U_b = 0.1312 \log \bar{\ell}_b + 0.2276 \quad (5.4)$$

as shown in Figure 5.9.

It is also seen in Figure 5.9 that at high average bubble chord length, corresponding to the bridging and the annular flow regimes, the experimental data for the bubble travel length are significantly greater than predicted by Equation (5.4). The relationship between the bubble travel length and the average bubble chord length can also be used as an alternative method to determine the flow regimes in gas-liquid cocurrent upward systems. By measuring the bubble/void characteristics with a two-element conductivity probe, if the measured bubble velocity, gas

holdup, bubble frequency and average bubble chord length satisfy Equation (5.3), then the flow pattern corresponds to the discrete or dispersed bubble flow. If the measured bubble characteristics satisfy Equation (5.4), then we have slug or churn flow. If the bubble travel length is significantly greater than predicted by either Equation (5.3) or Equation (5.4), then the flow pattern is either bridging or annular flow.

5.4 Summary

Bubble characteristics in the different flow regimes exhibit different variation with respect to the gas and the liquid flowrates. Bubble frequency increases linearly with superficial gas velocity in the discrete and dispersed bubble flow regimes. Bubble frequency also increases with gas velocity in the slug flow regime but decreases in the churn flow, bridging flow and annular flow regimes. Bubble chord length and its distribution in the dispersed bubble flow regime are smaller and narrower than in the discrete bubble flow regime. Both the average and the standard deviation of the bubble chord length increase with increasing superficial gas velocity in the discrete, dispersed and churn flow regimes. However, the average bubble chord length does not change significantly in the slug flow regime due to the high population of small bubbles in the liquid plugs which separate successive Taylor bubbles.

The bubble travel length, defined as $(\epsilon_g U_b)/f$, can be used to correlate the bubble characteristics. The relationship between the bubble travel length and the average bubble chord length can be expressed by Equation (5.3) for the discrete and dispersed bubble flow regimes and by Equation (5.4) for the slug and the churn flow regimes. These two equations provide an alternative method to determine the flow regimes. Further study is needed to extend this new method.

Chapter 6

Three-Phase Fluidization Boundaries

6.1 Minimum Liquid Fluidization Velocity at Low to Intermediate Gas Velocity

6.1.1 Introduction

Three-phase fluidized beds, containing solid particles fluidized by upward cocurrent flow of liquid and gas, have important applications in hydrocarbon and coal processing and in some biological reactors. Accurate design of such reactors is complicated by many factors, such as lack of knowledge of the minimum gas and liquid velocities required to achieve fluidization, although considerable research, mostly experimental, has been devoted to this subject.

Begovich and Watson (1978) studied the minimum fluidization velocity in columns of 76.2 and 152 mm diameter with air and water as the gas and the liquid, respectively. Various types of particles were used as the solid phase. The experimental conditions are listed in Table 6.1. Since fluidization is achieved when the upward drag force exerted on the particles by the fluid matches the buoyant weight of the bed, neither the column diameter nor the mass (as opposed to density) of solids in the column have any significant effect upon the minimum fluidization velocities. As the gas velocity is increased, the minimum liquid velocity required to achieve fluidization in each system studied decreases. The magnitude of this decrease differs considerably for different particles. At the same gas velocity, the liquid velocity required to achieve fluidization for large/heavy particles is greater than for small/light particles. An empirical correlation was obtained by Begovich and Watson (1978) for the minimum liquid fluidization velocity at a fixed cocurrent gas velocity:

$$\text{Re}_{\ell\text{mf}} = 5.121 \times 10^{-3} \text{Ar}_t^{0.662} \text{Fr}_g^{-0.118} \quad (6.1)$$

Table 6.1. Experimental conditions used in various investigations of minimum fluidization for three-phase systems (SI Units).

Authors	Type of articles	d_p	ρ_s	ϕ	ε_o	ρ_t	μ_t	D	H_o	U_g	U_t
Begovich (1978)	Glass beads	0.0019	1720	1	--	995	0.001	0.0762 and 0.152	0.22 to 0.453	0.0 to 0.18	0.0 to 0.060
		0.0032	2240								
		0.0046	2240								
		0.0062	2200								
Bloxm et al. (1975)	Alumina	0.0062	1990	1	--	995 to 1160	0.001 to 0.0112	0.0762	--	0.15	0.05
	Plexiglas	0.0063	1170								
	Glass beads	0.0046	2240								
Ernakova et al. (1970)	Glass beads	0.0012	2450	1	--	998	0.001	0.10	--	0.06	0.03
Lee and Al-Dabbagh (1978)	Glass beads	0.002	2450	1	--	998	0.001	0.0712	--	0.02	0.08
		0.00403	2560								
		0.00608	2590								
Fan et al. (1985)	Glass beads	0.00304	2520	1	--	998	0.001	0.0762	--	0.2	0.08
		0.00399	2530								
		0.00611	2200								
		0.0055	3690								
Fan et al. (1987)	Glass beads	0.00046	2500	1	--	998	0.001	0.0762	--	0.0519	0.07
		0.00078	2472								
		0.001	2876								
		0.00304	2525								
		0.00399	2470								
		0.00611	2200								
Song et al. (1989)	Cylindrical catalyst	0.00151	1890	0.75	--	997	0.00089	0.0762	--	0.06	0.06
		0.0019	2000	0.68							
		0.00078	2472	1							
This work	Glass beads	0.004	2470	1	0.39	1000	0.00135 to 0.00143	0.0826	0.60 to 0.69	0.152	0.06
		0.0015	2530		0.39						
		0.0025	2520		0.39						
		0.0037	2510		0.38						
	Glass beads coated with TFE	0.0045	2490	1	0.37						
		0.0025	2520		0.39						
		0.0024	2610	~ 0.8	0.39						
	Steel shot	0.0012	7510	1	0.41						

Clearly Equation (6.1) is not valid for zero gas flow rate. To produce a three-phase correlation that reduces to an acceptable two-phase correlation as the gas flow rate goes to zero, they proposed another correlation (SI units):

$$\frac{U_{\ell mf}}{U''_{\ell mf}} = 1 - 1622 U_g^{0.436} \mu_\ell^{0.227} d_p^{0.598} (\rho_s - \rho_\ell)^{-0.305} \quad (6.2)$$

Costa et al. (1986) proposed that the well-known drift flux model could be used for three-phase systems. Liquid and gas were considered to form a homogeneous combined fluid. A constant ratio $\varepsilon_\ell/\varepsilon$ was assumed for the whole bed. The superficial velocity and properties of the pseudo-homogeneous fluid were described by:

$$U_H = U_\ell + U_g \quad (6.3)$$

$$\rho_H = \frac{\varepsilon_\ell}{\varepsilon} \rho_\ell + \frac{\varepsilon_g}{\varepsilon} \rho_g \approx \frac{\varepsilon_\ell}{\varepsilon} \rho_\ell \quad (6.4)$$

$$\mu_H = \mu_\ell \quad (6.5)$$

The homogeneous fluid and the solids were treated as if they constituted a two-phase flow using the drift flux model proposed by Wallis (1969). According to this model the frictional pressure gradient is given by a Fanning-type equation:

$$\left(-\frac{dP}{dz} \right)_f = (1 - \varepsilon) C_D A_p \left(\frac{1}{2} \rho_H U_H^2 \right) \quad (6.6)$$

where C_D is the drag coefficient for a given bed porosity and A_p is the projected surface area of the particles per unit volume in the flow direction. For non-spherical particles of volume-equivalent-sphere diameter d_p ,

$$A_p = \frac{3}{2d_p \phi} \quad (6.7)$$

According to Wen and Yu (1966), for a system consisting of a single fluid and solid particles,

$$\frac{C_{D\infty}}{C_D} = \varepsilon^n \quad (6.8)$$

where $C_{D\infty}$ is the drag coefficient for individual particles as the solids concentration approaches zero. By substituting Equations (6.4), (6.7) and (6.8) into Equation (6.6), we can express the frictional pressure drop along a three-phase bed by:

$$\left(- \frac{\Delta P}{\Delta Z} \right)_f = \frac{3(1-\varepsilon) C_{D\infty} (1-\alpha) \rho_\ell (U_\ell + U_g)^2}{4 \phi d_p \varepsilon^n} \quad (6.9)$$

where $\alpha = \varepsilon_g / \varepsilon$. When particles are fluidized, the buoyed weight of the solid particles is supported by drag from the upward homogeneous fluid so that

$$\left(- \frac{\Delta P}{\Delta Z} \right)_f = g(1-\varepsilon)(\rho_s - \rho_H) \quad (6.10)$$

Combining Equations (6.4), (6.9) and (6.10) leads to

$$U_{\ell mf} = \left\{ \frac{\varepsilon^n 4 \phi d_p g [\rho_s - (1-\alpha_{mf}) \rho_\ell]}{3 C_{D\infty} (1-\alpha_{mf}) \rho_\ell} \right\}^{1/2} - U_g \quad (6.11)$$

with

$$n = 5.7 - 8 U_g \quad (6.12)$$

$$C_{D\infty} = \frac{24}{Re_\infty} (1 + 0.15 Re_\infty^{0.687}) \quad (Re_\infty \leq 10^3) \quad (6.13)$$

$$C_{D\infty} = 0.44 \quad (10^3 < Re_{\infty} \leq 10^5) \quad (6.14)$$

$$\text{where } Re_{\infty} = \frac{U_{\infty} d_p (1 - \alpha_{mf}) \rho_{\ell}}{\mu_{\ell}} \quad (6.15)$$

$$U_{\infty} = \left\{ \frac{4}{3} \phi d_p \frac{g}{C_{D\infty}} \left[\frac{\rho_s}{(1 - \alpha_{mf}) \rho_{\ell}} - 1 \right] \right\}^{\frac{1}{2}} \quad (6.16)$$

$$\alpha_{mf} = 3.464 \times 10^{-9} \frac{U_{\ell mf}^{-0.66} (\phi d_p)^{0.5} \rho_s^{2.3}}{1 + 1.74 \left(\frac{U_{\ell mf}}{U_{\ell mf} + U_g} \right)^{3.74} H_o^{0.43} (\rho_{\ell} - \rho_g)^{0.06} D_T^{0.23} \mu_{\ell}^{0.08}} \quad (6.17)$$

Equation (6.17) is the particular case at minimum fluidization (for which $U_{\ell} = U_{\ell mf}$ and $\alpha = \alpha_{mf}$) of three-phase fluidized beds. Values of $U_{\ell mf}$ calculated by this method were usually higher than experimental values. Costa et al. (1986) claimed that this was due to underestimation of α as minimum fluidization is approached. They therefore proposed an alternate empirical correlation for $U_{\ell mf}$:

$$U_{\ell mf} = 6.969 \times 10^{-4} U_g^{-0.328} (\phi d_p)^{1.086} (\rho_s - \rho_{\ell})^{0.865} D_T^{0.042} \mu_{\ell}^{-0.355} \quad (6.18)$$

which is again invalid for $U_g = 0$.

Song et al. (1989) considered the gas and liquid to be separated and assumed that solid particles are completely wetted by the liquid so that there is no direct contact between the gas and solids. Under such conditions, the system is viewed as three distinct phases. The equivalent diameter, D_e , of the liquid channels was expressed by:

$$D_e = \frac{2(1-\epsilon_s)}{3\epsilon_s} [1-\sqrt{\alpha}] \phi d_p \quad (6.19)$$

The pressure gradient along the three-phase fixed packed bed was written as

$$\left(-\frac{dP}{dz}\right) = (1-\alpha)\rho_\ell g + \alpha\rho_g g + (1-\alpha)\left(-\frac{dP}{dz}\right)_f^{\ell-s} \quad (6.20)$$

The final term includes the frictional pressure gradient between the liquid and the solid phase which was expressed by Fanning's equation as

$$\left(-\frac{dP}{dz}\right)^{\ell-s} = 4f_c \left(\frac{1}{D_e}\right) \left[\frac{1}{2}\rho_\ell \left(\frac{U_\ell}{\epsilon_\ell}\right)^2\right] \quad (6.21)$$

Here f_c can be correlated empirically as a function of the modified Reynolds number and gas particle Froude number:

$$f_c = \begin{cases} f_{\ell-s} (1 - 0.572 Fr_g^{1.38}) & (Re'_\ell \leq 10) \\ f_{\ell-s} (1 + 2.29 Fr_g^{0.0755}) & (Re'_\ell > 10) \end{cases} \quad (6.22)$$

where $f_{\ell-s}$ is calculated from the Ergun equation (1952) and can be expressed by

$$f_{\ell-s} = 0.583 + \frac{33.3}{Re'_\ell} \quad (6.23)$$

$$\text{with } Re'_\ell = \frac{D_e \rho_\ell U_\ell}{\mu_\ell \epsilon_\ell}$$

At minimum fluidization conditions, the pressure gradient is given for small ρ_g by

$$\left(-\frac{dP}{dz}\right) = (\epsilon_\ell \rho_\ell + \epsilon_s \rho_s) g \quad (6.24)$$

Combining Equations (6.20), (6.21), and (6.24), one can obtain an equation which allows the minimum liquid fluidization velocity to be calculated, i.e.

$$\begin{aligned} (1 - \alpha_{mf}) \left\{ 4f_c \left(\frac{1}{D_e} \right) \left[\frac{1}{2} \rho_\ell \left(\frac{U_{lmf}}{(1 - \alpha_{mf}) \epsilon_{mf}} \right)^2 \right] \right\} + (1 - \alpha_{mf}) \rho_\ell g \\ = [(1 - \alpha_{mf}) \epsilon_{mf} \rho_\ell + (1 - \epsilon_{mf}) \rho_s] g \end{aligned} \quad (6.25)$$

where empirically, Song et al. wrote:

$$(1 - \alpha_{mf}) = \begin{cases} 1 - 0.531 U_{lmf}^{-0.350} U_g^{0.977} & (d_p > 3 \text{ mm}) \\ 1 - 1.69 U_{lmf}^{-0.0902} U_g^{0.955} & (d_p \leq 3 \text{ mm}) \end{cases} \quad (6.26)$$

and ϵ_{mf} for particles of known ϕ was estimated (Wen and Yu, 1966) from Equation (6.39) below.

U_{lmf} can then be obtained iteratively from Equations (6.22), (6.23), (6.25) and (6.26).

Song et al. (1989) also suggested an alternate empirical correlation for U_{lmf} :

$$\frac{U_{lmf}}{U''_{lmf}} = 1 - 376 U_g^{0.327} \mu_\ell^{0.227} d_p^{0.213} (\rho_s - \rho_\ell)^{-0.423} \quad (\text{SI Units}) \quad (6.27)$$

Ermakova et al. (1970) proposed a simple empirical equation,

$$\frac{U_{lmf}}{U''_{lmf}} = 1 - \epsilon_g - 0.5 U_g^{0.075} \quad (\text{SI Units}) \quad (6.28)$$

Lee and Al-Dabbagh (1978) measured the pressure drop and the phase holdup in both packed and fluidized beds of 4.03 mm and 6.08 mm glass beads. Initially, at constant gas velocity, pressure drop and liquid phase holdup both increased with increasing liquid velocity. Prior to fluidization, however, a particle jumping movement was observed which led to a measurable decrease of both bed porosity and pressure drop. Fluidization occurred at a lower liquid flow rate than in the absence of gas.

6.1.2 Theoretical Models: Modifications and New Models

6.1.2.1 Modified Song model I

Starting from the Song et al. (1989) model and rearranging Equation (6.25), one can obtain the following equation at incipient fluidization:

$$4f_c \left(\frac{1}{D_e} \right) \left[\frac{1}{2} \rho_\ell \left(\frac{U_{\ell mf}}{(1 - \alpha_{mf}) \epsilon_{mf}} \right)^2 \right] = (1 - \epsilon_{mf}) \left[\frac{\rho_s}{(1 - \alpha_{mf})} - \rho_\ell \right] g \quad (6.29)$$

From Equations (6.22) and (6.23),

$$f_c = K \left(0.583 + \frac{33.3}{\frac{D_e \rho_\ell U_{\ell mf}}{\mu_\ell \epsilon_\ell}} \right) \quad (6.30)$$

where

$$K = \begin{cases} 1 - 0.572 Fr_g^{1.38} & (Re'_\ell \leq 10) \\ 1 + 2.29 Fr_g^{0.0755} & (Re'_\ell > 10) \end{cases} \quad (6.31)$$

Combining Equations (6.29) and (6.30), we find that:

$$\frac{2K}{D_e \varepsilon_\ell^2} \left(0.583 + \frac{33.3}{\frac{D_e}{d_p \varepsilon_\ell} \left(\frac{d_p \rho_\ell U_{\ell mf}}{\mu_\ell} \right)} \right) \rho_\ell U_{\ell mf}^2 = (1 - \varepsilon_{mf}) \left[\frac{\rho_s}{(1 - \alpha_{mf})} - \rho_\ell \right] g \quad (6.32)$$

Multiplying by $\rho_\ell d_p^2 / \mu_\ell^2$ and rearranging, one can obtain:

$$\frac{1.166 K}{D_e \varepsilon_\ell^2} \text{Re}_{\ell mf}^2 + \frac{66.6 d_p K}{D_e^2 \varepsilon_\ell} \text{Re}_{\ell mf} = (1 - \varepsilon_{mf}) \frac{\frac{\rho_s}{(1 - \alpha_{mf})} - \rho_\ell}{d_p (\rho_s - \rho_\ell)} \text{Ar}_\ell \quad (6.33)$$

Solution of this quadratic equation gives

$$\text{Re}_{\ell mf} = \frac{d_p \rho_\ell U_{\ell mf}}{\mu_\ell} = \sqrt{a^2 + b \text{Ar}_\ell} - a \quad (6.34)$$

with

$$a = \frac{33.3}{1.166} \frac{d_p \varepsilon_\ell}{D_e} \quad (6.35a)$$

$$b = \frac{1}{1.166} \left[\frac{\frac{\rho_s}{(1 - \alpha_{mf})} - \rho_\ell}{\rho_s - \rho_\ell} \right] \frac{D_e \varepsilon_\ell^2 (1 - \varepsilon_{mf})}{d_p K} \quad (6.35b)$$

and $\text{Ar}_\ell = \rho_\ell (\rho_s - \rho_\ell) g d_p^3 / \mu_\ell^2$. Note that Equation (6.34) has the same form as that often used for two-phase fluidized beds.

In the Song et al. model, the equivalent diameter of liquid channel, D_e , was defined by Equation (6.19), obtained from the separated flow model of Chern et al. (1983) by erroneously

adding the gas-liquid interfacial perimeter to the liquid-solid interfacial perimeter in their expression for solid-wetted perimeter. A general definition of the equivalent diameter of liquid channels in a bed of particles is more reasonable, i.e.

$$D'_e = \frac{4 \times \text{liquid volume}}{\text{wetted particle surface}} = \frac{2}{3} \frac{(1 - \epsilon_s)}{\epsilon_s} (1 - \alpha) \phi d_p \quad (6.36)$$

a result also obtainable from the separated flow model of Chern et al. (1983) if one excludes the gas-liquid interface in the calculation of wetted perimeter. Replacing D_e in Equation (6.35) by D'_e from (6.36) and rearranging, with $\epsilon_\ell = \epsilon_{mf} - \epsilon_g = \epsilon_{mf} (1 - \alpha_{mf})$, we obtain

$$a = 42.84 \frac{(1 - \epsilon_{mf})}{\phi} \quad (6.37a)$$

$$b = 0.5718 \epsilon_{mf}^3 \phi \frac{(1 - \alpha_{mf})^2}{K} \left(1 + \frac{\alpha_{mf} \rho_\ell}{\rho_s - \rho_\ell} \right) \quad (6.37b)$$

In order to avoid the bifurcation caused by Equation (6.31) which leads to numerical difficulties, we take $K = 1$. Equations (6.34) and (6.37), together with Song's α_{mf} [Eq. (6.26)], is called the Modified Song Model I.

When the gas velocity is zero, only liquid supports the particles and $\alpha_{mf} = 0$. According to Wen and Yu (1966),

$$\frac{1 - \epsilon_{mf}}{\epsilon_{mf}^3 \phi^2} = 11 \quad (6.38)$$

and

$$\frac{1}{\phi \epsilon_{mf}^3} = 14 \quad (6.39)$$

On substituting Equations (6.38) and (6.39) into Equation (6.34), with $U_g = 0$, Equation (6.34), in conjunction with either Equation (6.35) or Equation (6.37), degenerates to the well-known Wen and Yu (1966) equation:

$$\text{Re}_{\ell\text{mf}}'' = \sqrt{33.7^2 + 0.0408 \text{Ar}_{\ell}} - 33.7 \quad (6.40)$$

6.1.2.2 Modified Song model II

The gas holdup at minimum fluidization plays an important role in modelling minimum fluidization velocities (as discussed below). Instead of Equation (6.26), a recently developed correlation (Yang et al., 1993) for α , Equation (6.53) with $C_o = 0.16$, is used in Equation (6.37) (with $K = 1$ again). Together with Equations (6.34) and (6.37), these equations constitute the Modified Song Model II.

6.1.2.3 Pseudo-homogeneous fluid model

Here we develop two models for minimum fluidization in a cocurrent upward flow system. One is a pseudo-homogeneous fluid model while the other is a gas-perturbed liquid model. In the pseudo-homogeneous model, the gas-liquid mixture is treated as a single phase with physical properties expressed by:

$$\mu_{g\ell} \approx \left(1 + \frac{\varepsilon_g}{\varepsilon_g + \varepsilon_{\ell}}\right) \mu_{\ell} = (1 + \alpha) \mu_{\ell} \quad (6.41)$$

an approximation applicable up to $\alpha \approx 0.05$ (Wallis, 1969).

$$\rho_{g\ell} = \frac{\rho_g \varepsilon_g + \rho_{\ell} \varepsilon_{\ell}}{\varepsilon_g + \varepsilon_{\ell}} \approx (1 - \alpha') \rho_{\ell} \quad (6.42)$$

while

$$\text{Ar}_{g\ell} = \frac{d_p^3 \rho_{g\ell} (\rho_s - \rho_{g\ell}) g}{\mu_{g\ell}^2} \approx \frac{(1 - \alpha)}{(1 + \alpha)^2} \frac{[\rho_s - (1 - \alpha) \rho_{\ell}]}{\rho_s - \rho_{\ell}} \text{Ar}_{\ell} \quad (6.43)$$

$$\text{Re}_{g\ell\text{mf}} = \frac{d_p (U_{\ell\text{mf}} + U_g) \rho_{g\ell}}{\mu_{g\ell}} \approx \frac{d_p (U_{\ell\text{mf}} + U_g) \rho_{\ell} (1 - \alpha)}{\mu_{\ell} (1 + \alpha)} \quad (6.44)$$

At minimum fluidization, from Equation (6.40),

$$\text{Re}_{g\ell\text{mf}} = \sqrt{33.7^2 + 0.0408 \text{Ar}_{g\ell}} - 33.7 \quad (6.45)$$

so that

$$U_{\ell\text{mf}} = \frac{\mu_{\ell}}{d_p \rho_{\ell}} \frac{1+\alpha}{1-\alpha} (\sqrt{33.7^2 + 0.0408 \text{Ar}_{g\ell}} - 33.7) - U_g \quad (6.46)$$

Note that as U_g approaches zero, Equation (6.46) reduces to the Wen and Yu equation (6.40) for liquid-solid fluidization.

6.1.2.4 Gas-perturbed liquid model

In the gas-perturbed model, it is assumed that the only effect of the gas phase is to occupy space and hence to change the absolute liquid velocity. The pressure gradient of the pre-fluidization packed bed is assumed to result from the friction between liquid and solid. The hydraulic radius of the liquid channel is expressed by:

$$r_H = \frac{\phi d_p \varepsilon_{\ell}}{6(1-\varepsilon)} \quad (6.47)$$

which is equivalent to Equation (6.36), since the equivalent diameter is defined as four times the hydraulic radius. The Ergun equation is correspondingly modified (Zhang et al., 1995) to:

$$\left(-\frac{dp}{dz}\right)_{\ell-s} = 150 \frac{\mu_{\ell} \left(\frac{U_{\ell}}{1-\varepsilon_g}\right) \left(\frac{\varepsilon_s}{1-\varepsilon_g}\right)^2}{\phi^2 d_p^2 \left(\frac{\varepsilon_{\ell}}{1-\varepsilon_g}\right)^3} + 1.75 \frac{\rho_{\ell} \left(\frac{U_{\ell}}{1-\varepsilon_g}\right)^2 \left(\frac{\varepsilon_s}{1-\varepsilon_g}\right)}{\phi d_p \left(\frac{\varepsilon_{\ell}}{1-\varepsilon_g}\right)^3} \quad (6.48)$$

When minimum fluidization is reached,

$$\left(-\frac{dp}{dz} \right)_f^{\ell-s} = (1 - \varepsilon) (\rho_s - \rho_\ell) g \quad (6.49)$$

Combining Equations (6.48) and (6.49) at the minimum fluidization condition, one can obtain:

$$\text{Re}_{\ell\text{mf}} = \sqrt{\left(42.86 \frac{(1 - \varepsilon_{\text{mf}})}{\phi} \right)^2 + 0.5715 \phi \varepsilon_{\text{mf}}^3 (1 - \alpha_{\text{mf}})^3 \text{Ar}_\ell - 42.86 \frac{(1 - \varepsilon_{\text{mf}})}{\phi}} \quad (6.50)$$

which again reduces to the Wen and Yu (1966) equation as U_g goes to zero when Equations (6.38) and (6.39) are used.

6.1.2.5 Gas holdup at minimum fluidization

Two different kinds of models are derived above. When the gas and liquid are assumed to form a pseudo-fluid, the minimum fluidization velocity is obtained when the pressure drop caused by friction is equal to the buoyed weight of the solids per unit cross-section. The physical properties of the pseudo-fluid are expressed in terms of the physical properties of the gas and liquid, as well as the holdups of gas and liquid at minimum fluidization. The Costa et al. (1986) model and the above pseudo-homogeneous fluid model belong to this category.

Another way to approach the minimum fluidization velocity is to neglect the friction caused by the gas. The gas phase occupies some space in the packed bed; as the gas velocity is increased, gas holdup increases, reducing the liquid holdup. Hence the absolute velocity of the liquid is increased, causing an increase in frictional pressure drop between the liquid and solid. Beyond a certain gas velocity for a given liquid velocity (or vice versa), this drag causes the particles to be fluidized. The Song et al. (1989) model, as well as its modifications, and the above

gas-perturbed liquid model belong to this category. Both approaches require information on the gas holdup at minimum fluidization. Since gas holdup is a function of the superficial gas and liquid velocities, an iterative process is required to predict the minimum fluidization velocity.

Several correlations for α are available from the literature. The experimental conditions used to obtain these correlations are listed in Table 6.2.

Begovich and Watson (1978) correlated the gas holdup in a three-phase fluidized bed at minimum fluidization by:

$$\alpha_{mf} = 1.61 \frac{U_g^{0.720} d_p^{0.168} D^{-0.125}}{\epsilon_{mf}} \quad (6.51)$$

Costa et al. (1986) reported that in a three-phase fluidized bed, α can be expressed by Equation (6.17) generalized beyond minimum fluidization as shown in Table 6.3. However, this equation led to higher than average deviations close to minimum fluidization. Song et al. (1989) used Equation (6.26), generalized to $U_\ell \leq U_{\ell mf}$ to correlate α , based on the data of Chern et al. (1984) for packed beds. Based on a study of pressure drop for gas-liquid cocurrent flow in packed beds, Turpin and Huntington (1967) proposed

$$\alpha = 1.035 - 0.182 \left(\frac{U_\ell \rho_\ell}{U_g \rho_g} \right)^{0.24} \quad \text{for } 1.0 \leq \left(\frac{U_\ell \rho_\ell}{U_g \rho_g} \right)^{0.24} \leq 6.0 \quad (6.52)$$

for upward flow with tabular alumina of diameters 7.62 and 8.23 mm.

In a systematic study of liquid retention in fixed bed reactors, Yang et al (1993) found a major difference between non-foaming and foaming liquids. However, the effect of liquid

viscosity, surface tension and column diameter could be neglected. The low retention of liquid phase observed for foaming liquids may, as they claim, be explained by the stability of very small bubbles attached to the solid surface, causing a significant decrease in total liquid retention after introduction of gas.

Table 6.2. Experimental conditions used in correlations for α .

Author	Gas Phase	Liquid Phase	Solid Phase	Column
Begovich and Watson (1978)	Air: $U_g = 0 - 0.173 \text{ m/s}$	Water: $U_\ell = 0 - 0.120 \text{ m/s}$	Glass, plexiglas, alumina, and alumino-silicate: $d_p = 1.9 - 6.3 \text{ mm}$ $\rho_s = 1170 - 2240 \text{ kg/m}^3$	$D = 76.2$ and 152 mm
	Combines the gas holdup data from: Kim et al, 1975. Bhatia and Epstein, 1974. Michelsen and Ostergaard, 1970. Efremov and Vakhrushev, 1970. Ostergaard and Michelsen, 1968.			
Costa et al. (1986)	Air, carbon dioxide, helium, methane: $\rho_g = 0.15 - 1.6 \text{ kg/m}^3$ $\mu_g = 10^{-5} - 2 \times 10^{-5} \text{ kg/(ms)}$ $U_g = 0.020 - 0.16 \text{ m/s}$	Water and aqueous solutions of cellulose: $\rho_\ell = 994 - 998 \text{ kg/m}^3$ $\mu_\ell = 9.7 \times 10^{-4} - 8.12 \times 10^{-3} \text{ kg/(ms)}$ $U_\ell = 0.020 - 0.16 \text{ m/s}$	Glass, aluminum, and benzoic acid (paint film) $d_p = 3.0 - 5.9 \text{ mm}$ $\rho_s = 1200 - 2700 \text{ kg/m}^3$	$D = 46.0 - 151 \text{ mm}$ $H_o = 110 - 410 \text{ mm}$
Song et al. (1989) [from Chern et al. (1984)]	Air: $U_g = 0 - 0.257 \text{ m/s}$	Water: $U_\ell = 0.022 - 0.17 \text{ m/s}$	Glass and poly-vinyl chloride: $\phi_s d_p = 3.0 - 6.0 \text{ mm}$ $\rho_s = 1470 - 2520 \text{ kg/m}^3$	$D = 76.2 \text{ mm}$ $H_o = 600 - 690 \text{ mm}$
Turpin and Huntington (1967)	Air: $1.0 \leq \left(\frac{U_\ell \rho_\ell}{U_g \rho_g} \right)^{0.24} \leq 6.0$	Water:	Alumina tabular: $d = 7.62, 8.23 \text{ mm}$ $\rho_s \approx 4000 \text{ kg/m}^3$	$D = 50, 100,$ and 150 mm $H_o = 2133 \text{ mm}$
Yang et al. (1993)	Air and nitrogen: $U_g = 0 - 0.14 \text{ m/s}$	Water, aqueous solution of NaCl, heptane, cyclohexane, kerosene, propanol, L.C.O., and diesel fuel: $\rho_\ell = 684 - 1050 \text{ kg/m}^3$ $\mu_\ell = 1.7 \times 10^{-5} - 4.2 \times 10^{-3} \text{ Pa.s}$ $\gamma = 2.0 \times 10^{-2} - 7.4 \times 10^{-2} \text{ N/m}$ $U_\ell = 0 - 0.40 \text{ m/s}$	Alumina: $d_p = 2.2, 2.8 \text{ mm}$ $\rho_s = 2920, 3420 \text{ kg/m}^3$	$D = 50, 100,$ and 150 mm $H_o = 1150 - 2133 \text{ mm}$

In three-phase systems, the wettability of particles affects the hydrodynamics of the fluidized beds. Gas attaches to the non-wetting particles in the form of small bubbles, even when a non-foaming liquid is employed. This situation may be similar to the case of a foaming liquid with wettable particles as described by Yang et al. (1993), who proposed

$$\alpha = \frac{C_o}{\varepsilon} \frac{U_g}{U_g + U_\ell} \quad (6.53)$$

with $C_o = 0.16$ for non-foaming liquids and $C_o = 0.28$ for foaming liquids. This correlation was shown to be in good agreement with experimental data reported by others. The various correlations are summarized in Table 6.3.

In this study, each of these α correlations has been used to predict the minimum fluidization velocity with different theoretical models. Figure 6.1 shows typical predictions of α at minimum fluidization. The predictions are seen to be widely scattered.

Table 6.3. Empirical equations for α

Authors	Correlations (SI units)	System
Begovich and Watson (1978)	$\alpha = 1.61 \frac{U_g^{0.720} d_p^{0.168} D_T^{-0.125}}{\varepsilon}$	fluidized beds
Costa et al. (1986)	$\alpha = 3.464 \times 10^{-9} \frac{U_\ell^{-0.66} (\phi d_p)^{0.5} \rho_s^{2.3}}{1 + 1.74 \left(\frac{U_\ell}{U_\ell + U_g} \right)^{3.74} H_o^{0.43} (\rho_\ell - \rho_g)^{0.06} D_T^{0.23} \mu_\ell^{0.08}}$	fluidized beds
Song et al. (1989)	$\alpha = 0.531 U_\ell^{-0.350} U_g^{0.977} \quad d_p > 3 \text{ mm}$ $\alpha = 1.69 U_\ell^{-0.0902} U_g^{0.955} \quad d_p < 3 \text{ mm}$	fixed beds
Turpin and Huntington (1967)	$\alpha = 1.035 - 0.182 \left(\frac{U_\ell \rho_\ell}{U_g \rho_g} \right)^{0.24} ; \quad \text{for } 1.0 \leq \left(\frac{U_\ell \rho_\ell}{U_g \rho_g} \right)^{0.24} \leq 6.0$	fixed beds
Yang et al. (1993)	$\alpha = \frac{0.16}{\varepsilon} \frac{U_g}{U_g + U_\ell} ; \quad \text{for non-foaming liquid}$	fixed beds

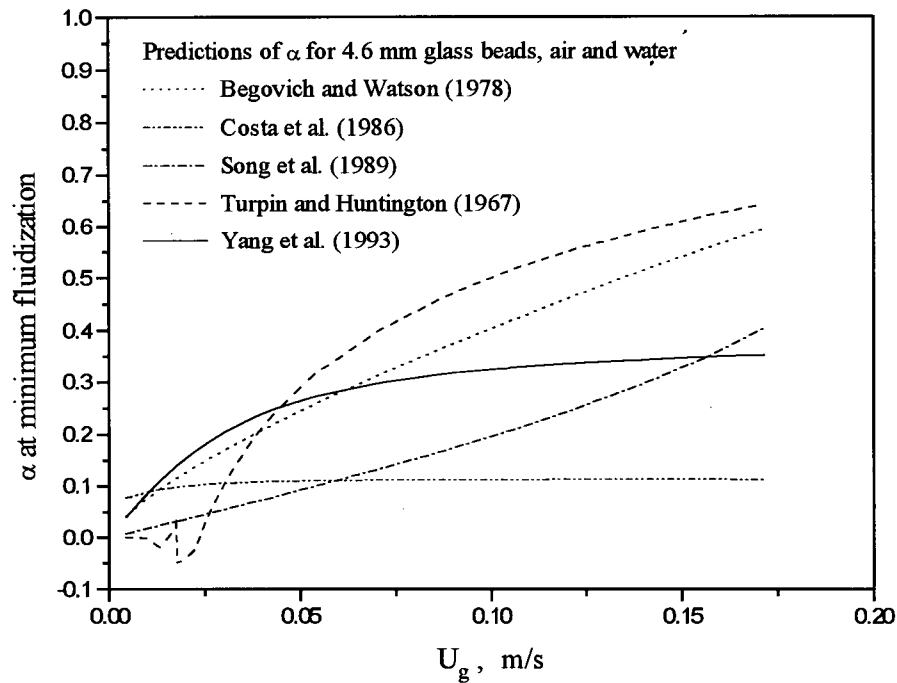


Figure 6.1. Prediction of gas holdup on solids-free basis at minimum fluidization, with properties corresponding to the experimental conditions of Begovich and Watson, 1978.

6.1.3 Experimental Study

The experimental apparatus employed in this work is described in Chapter 2. Six pressure transducers, located at 0.10 m intervals starting 0.15 m above the distributor, were used to obtain the pressure gradient along the test section. A personal computer (IBM 486 DX2-66 MHz) was used for data acquisition. Liquid temperature was measured at the outlet to determine the liquid viscosity and density, while gas and liquid flow rates were measured by inlet rotameters. Seven different types of particles were used, with key properties listed in Table 6.1.

6.1.3.1. Experimental procedure

Begovich and Watson (1978) and Lee and Al-Dabbagh (1978) obtained $U_{\ell mf}$ by plotting pressure drop vs. superficial liquid velocity, while Fan et al. (1985) plotted overall pressure gradient vs superficial liquid velocity. Figure 6.2 plots the pressure gradient and the pressure drop vs. superficial liquid velocity at constant gas flow rate for one of the present runs. It is seen that there is no significant difference between these two methods. In this study, all values of $U_{\ell mf}$ were determined from the intersection of the fixed bed and fluidized bed pressure gradient curves in plots of pressure gradient versus superficial liquid velocity at a constant gas flow rate, as shown in Figure 6.3. It can be seen from Figure 6.3 that there was negligible difference in $U_{\ell mf}$ obtained by increasing or decreasing the liquid velocity. The standard deviations, defined by Equation (2.4), of the pressure fluctuations are shown as the error bars in the same graph.

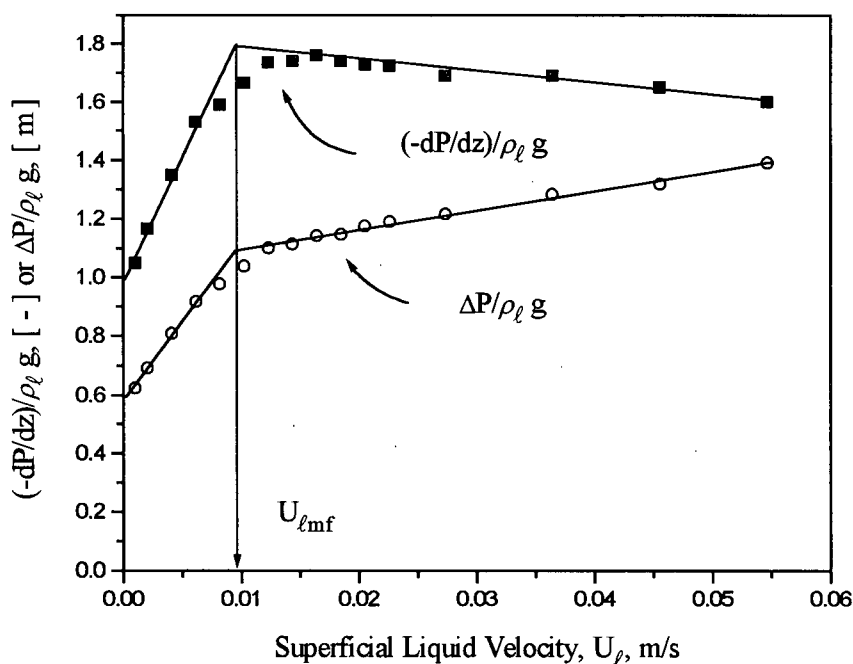


Figure 6.2. Determination of $U_{\ell mf}$ by pressure drop and pressure gradient methods for 2.5 mm glass beads with $U_g = 0.0509$ m/s.

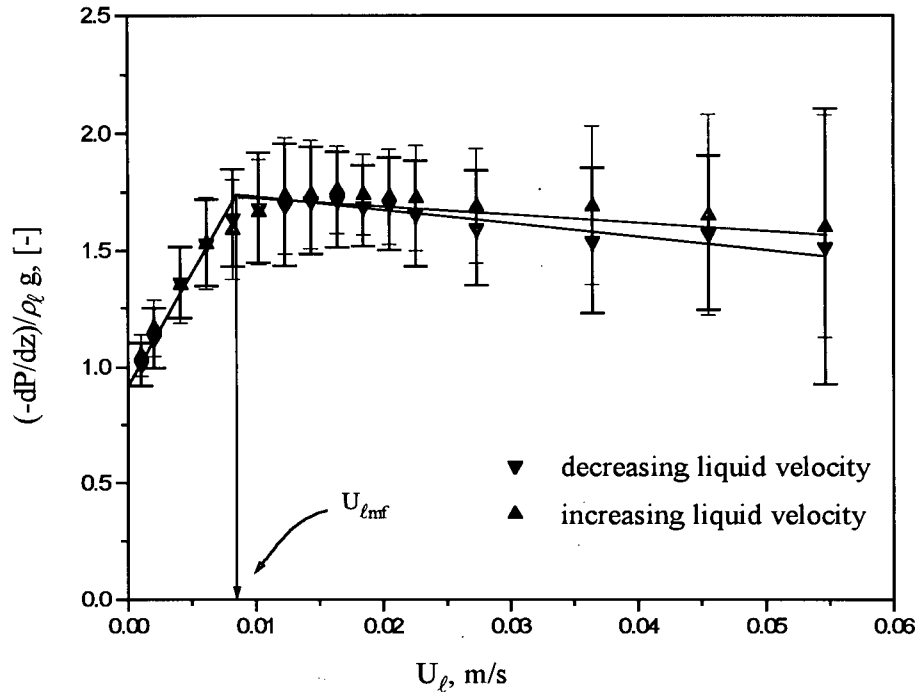


Figure 6.3. Effect of increasing or decreasing liquid velocity on determination of U_{lmf} for 2.5 mm glass beads with $U_g = 0.0509$ m/s.

6.1.3.2 Experimental results

The experimental minimum fluidization results are shown in Figures 6.4 and 6.5. As expected, U_{lmf} decreased with increasing gas velocity and increased with increasing particle diameter and particle density. Figure 6.5 shows the effect of particle wettability and sphericity on U_{lmf} . The minimum liquid fluidization velocity required for 2.5 mm glass beads coated with TFE was slightly less than for the same beads without coating. The decreased sphericity of the sand ($\phi \approx 0.8$) compared to the glass beads ($\phi = 1$) does not influence U_{lmf} very much in a three-phase fluidized bed, although there is obviously a significant difference in a liquid-solid fluidized bed (i.e. at $U_g = 0$), part of which may be due to the increased roughness of the sand.

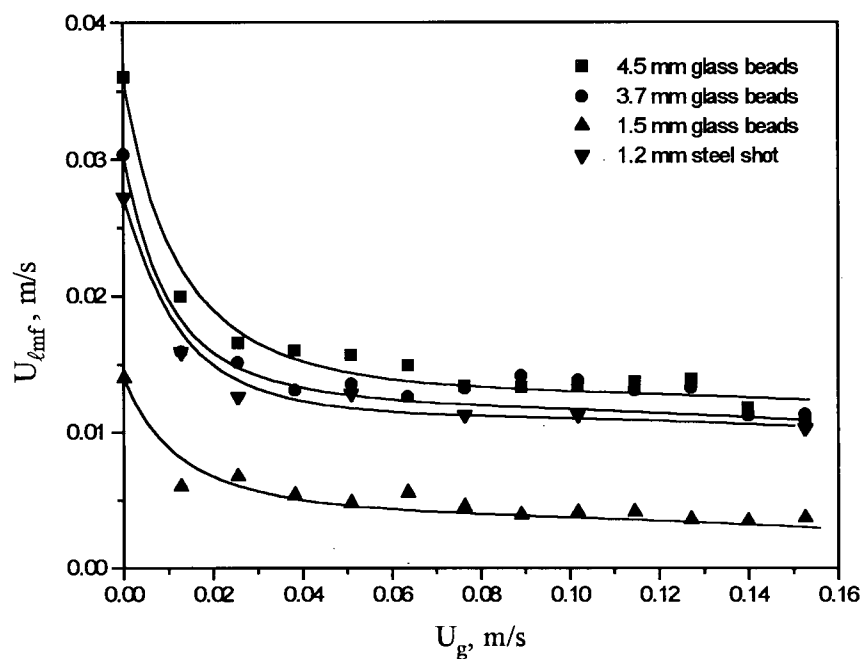


Figure 6.4. $U_{\ell mf}$ for different particle sizes and densities.

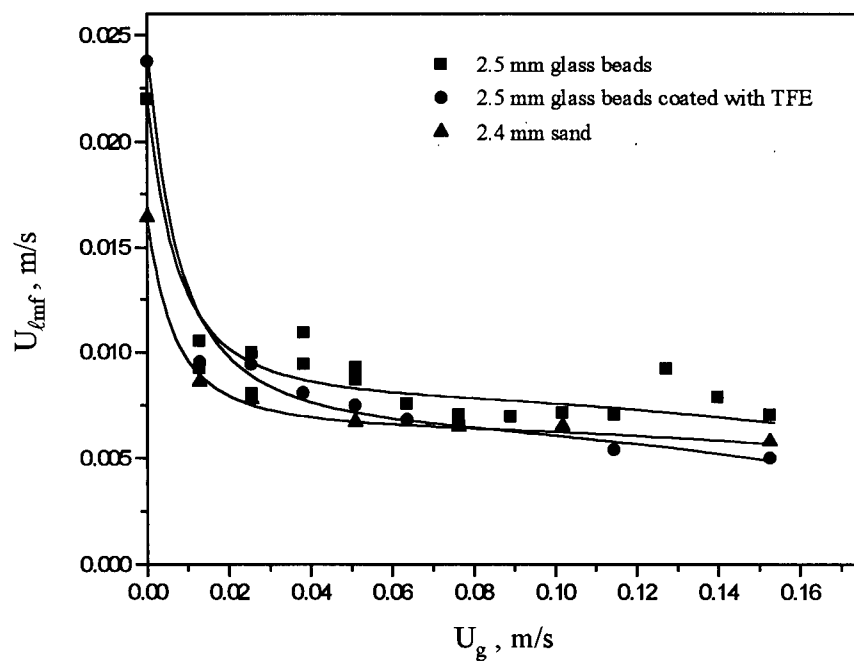


Figure 6.5. $U_{\ell mf}$ for particles of different wettability and sphericity.

6.1.4 Comparison and Discussion

6.1.4.1 Pressure gradient in fixed beds

The overall pressure gradient in a three-phase fixed bed in which the solids are enveloped by the continuous liquid phase can be expressed as the sum of hydrostatic and frictional terms:

$$\left(-\frac{dP}{dz} \right) = (1 - \epsilon_g) \rho_\ell g + \epsilon_g \rho_g g + \left(-\frac{dP}{dz} \right)_f^{\ell-s} \quad (6.54)$$

If Equation (6.48) is substituted into Equation (6.54), and the term containing gas density is neglected, the following equation can be obtained:

$$\frac{\left(-\frac{dP}{dz} \right)}{\rho_\ell g} = (1 - \epsilon_g) + 150 \frac{(1 - \epsilon_0)^2}{\phi^2 \epsilon_0^3 (1 - \alpha)^3} \frac{\mu_\ell}{d_p \rho_\ell U_\ell} \frac{U_\ell^2}{d_p g} + 1.75 \frac{(1 - \epsilon_0)}{\phi \epsilon_0^3 (1 - \alpha)^3} \frac{U_\ell^2}{d_p g} \quad (6.55)$$

If α is obtained from Yang's Equation (6.53) with $C_0 = 0.16$, the overall pressure gradient can be predicted by Equation (6.55). Figure 6.6 compares predictions and experimental results. At high gas velocities, predicted values are in good agreement with experimental values, especially at the minimum fluidizing condition; however, at low gas velocity, predictions are about 17% less than the corresponding experimental values, possibly due to some inaccuracy of Equation (6.53) at low values of U_g .

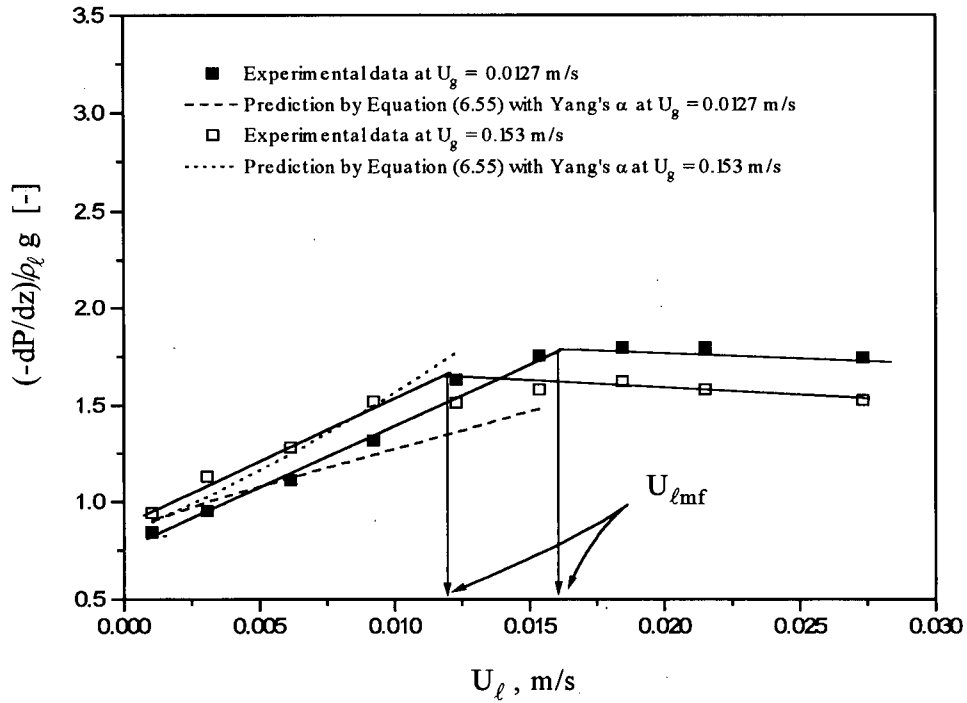


Figure 6.6. Three-phase fixed and fluidized bed pressure gradient measurements compared with fixed bed predictions for 3.7 mm glass beads.

6.1.4.2 Minimum fluidization velocity for liquid-solid fluidized beds

A number of investigators have studied minimum fluidization velocities in both gas-solid and liquid-solid fluidized beds. Figure 6.7 shows some predictions and corresponding experimental results for liquid-solid fluidized beds, generated by investigators of three-phase fluidization. The predictions by Wen and Yu (1966), Richardson (1971) as well as Grace (1982) are all in good agreement with the experimental data. The root mean square percentage deviations defined by

$$\bar{\delta}_s = \sqrt{\frac{1}{N} \sum_{i=1}^N \left(\frac{\text{predicted value} - \text{experimental value}}{\text{experimental value}} \right)^2} \quad (6.56)$$

were 10.3%, 11.7% and 13.4%, respectively, for these three correlations.

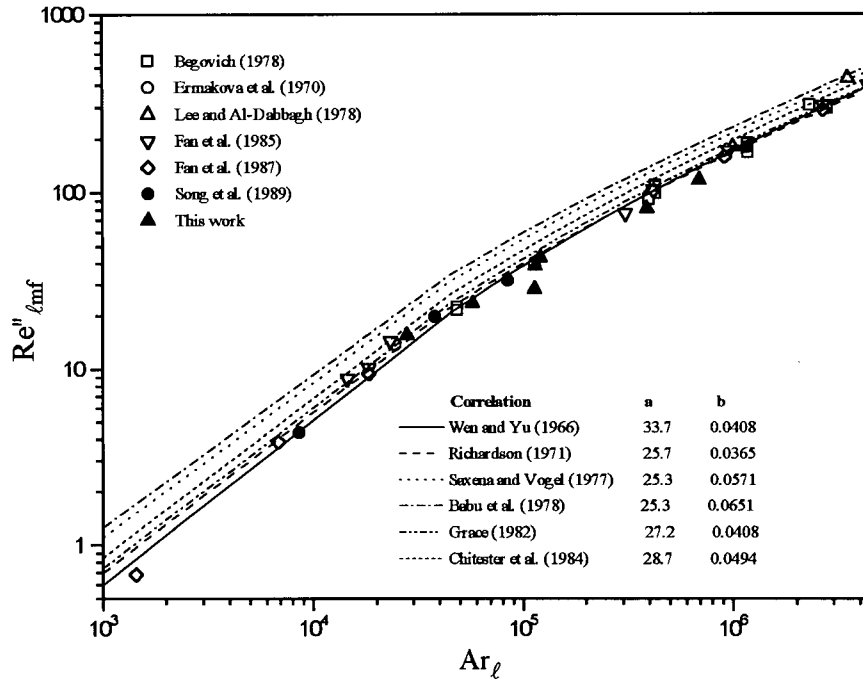


Figure 6.7. Comparison of minimum fluidization velocity predictions and experimental results for liquid-solid fluidized beds. Predictions are for an equation of the form

$$Re''_{l mf} = \sqrt{a^2 + b Ar_l} - a, \text{ with values of } a \text{ and } b \text{ as listed in the legend.}$$

6.1.4.3 Minimum fluidization velocity for three-phase fluidized beds

Five empirical correlations, Equations (6.1), (6.2), (6.18), (6.27) and (6.28), were used to predict $U_{l mf}$. The results for 2.5 mm glass beads are plotted in Figure 6.8. It can be seen that Equation (6.1) gives the best predictions. The average absolute percentage deviation, $\bar{\delta}_a$, defined by

$$\bar{\delta}_a = \frac{1}{N} \sum_{i=1}^N \left| \frac{\text{predicted value} - \text{experimental value}}{\text{experimental value}} \right| \quad (6.57)$$

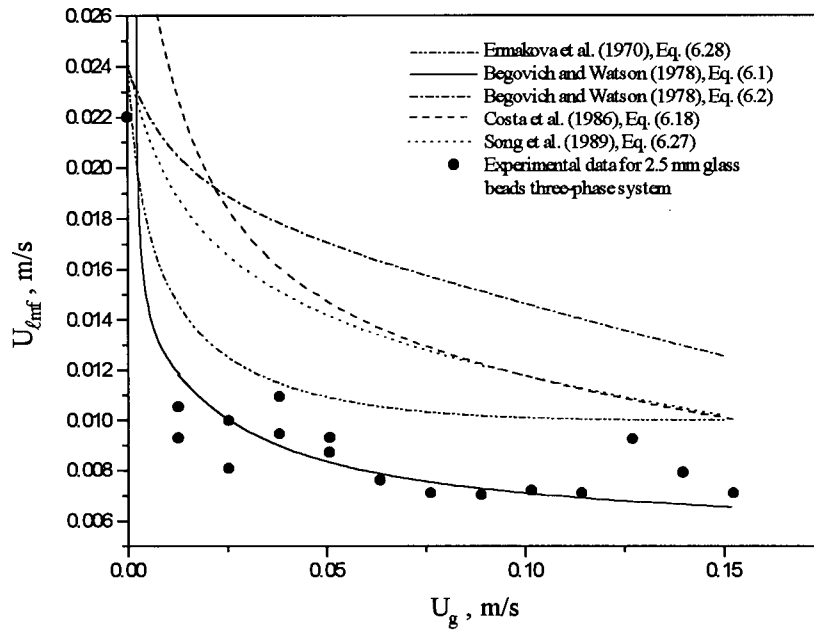


Figure 6.8. Experimental minimum fluidization velocities for 2.5 mm glass beads compared with predictions of various empirical equations.

and the root mean square percentage deviation, $\bar{\delta}_s$, defined by Equation (6.56), are listed in Table 6.4 for the various empirical correlations. The smallest deviations again correspond to Equation (6.1).

Figure 6.9 presents experimental data from this work (2.5 mm glass beads) compared with predictions of all the models. It is evident that both the pseudo-homogeneous fluid model and the Costa et al. model can be used only for very small gas velocities. For high gas velocities, they predict negative values of U_{lmf} . The other models all predict the correct trends, with the gas-perturbed liquid model giving the best results. It can also be seen that at low gas velocities, the gas perturbed model overestimates U_{lmf} somewhat. This probably results from underestimation of the overall pressure gradient at low U_g , as discussed previously.

Table 6.4 Average absolute percentage and root mean square percentage deviations between predictions from correlations for minimum fluidization velocity for three-phase fluidized beds and experimental data.

Mean percentage deviation	Data from this work		All data, excluding 6.3 mm plexiglas in shallow bed	
Authors	$\bar{\delta}_a$	$\bar{\delta}_s$	$\bar{\delta}_a$	$\bar{\delta}_s$
Ermakova et al., Eq. (6.28) *	37	42	28	38
Begovich and Watson, Eq. (6.1) *	12	15	18	28
Begovich and Watson, Eq. (6.2) *	90	98	54	73
Costa et al., Eq. (6.18) *	73	78	66	81
Song et al., Eq. (6.27) *	65	71	42	57
Costa et al. model	643	958	494	789
Song et al. model	57	73	43	57
Modified Song model 1	115	119	94	115
Modified Song model 2	80	85	68	93
Gas perturbed liquid model	19	24	26	34
Pseudo-homogeneous fluid model	803	1190	536	1030

* Empirical equations.

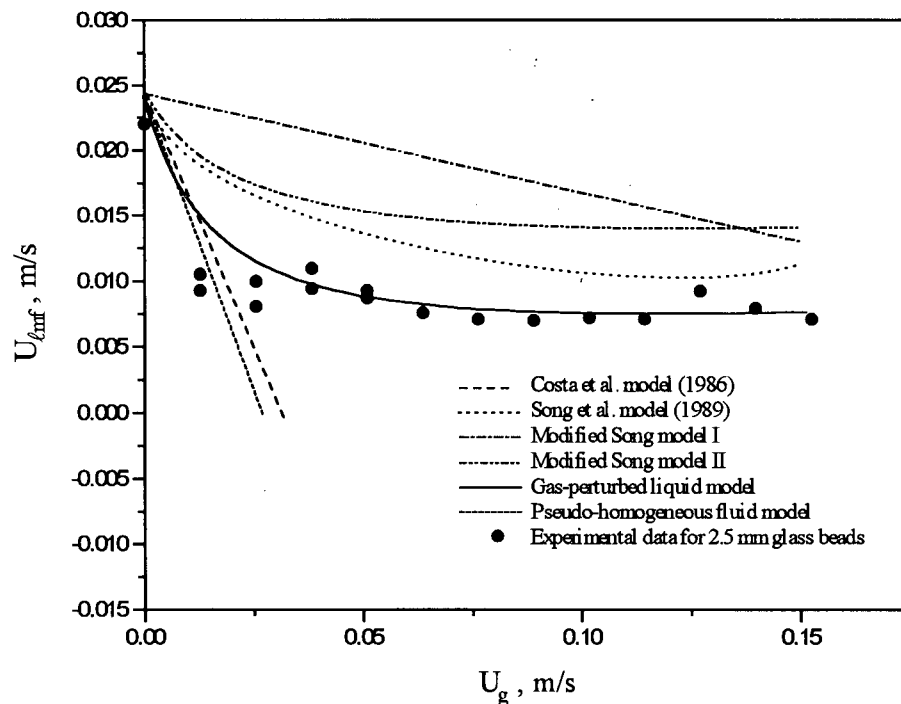


Figure 6.9. Experimental minimum fluidization velocities for 2.5 mm glass beads compared with predictions of various models.

Figure 6.10 presents the predictions of $Re_{\ell mf}$ by the gas-perturbed liquid model, Equation (6.50), versus all the available experimental data (275 data points). Most experimental data are in good agreement, including those for the non-wettable particles. For our own data the average absolute and the root mean square percentage deviations are 19.0% and 24.2%, respectively. The points represented by stars, taken from Begovich (1978), are for 6.3 mm plexiglas beads in a column of diameter 152 mm and static bed height 220 mm. The large deviations for these points could be due to the effect of relative bed shallowness (low H_0/D), since the author also had some data for 6.3 mm plexiglas beads in a column of diameter 76 mm and static bed height 273 and 408 mm which are in good agreement with the predictions.

Table 6.4 lists the average absolute and the root mean square percentage deviations for all the models tested. For the present experiments, ϵ_{mf} was taken as equal to the static bed voidage,

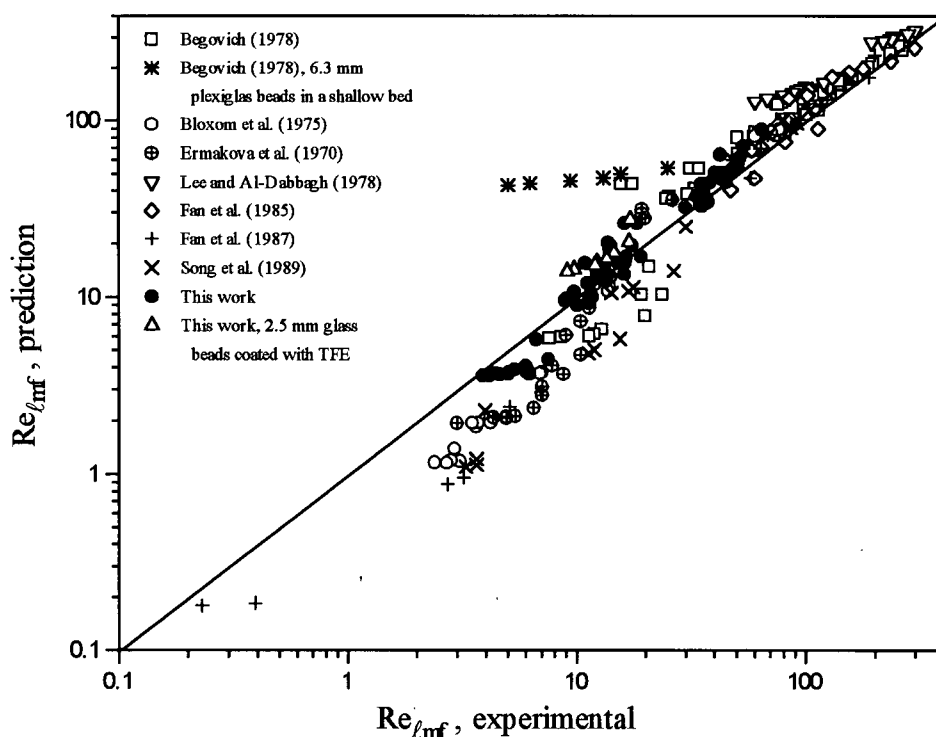


Figure 6.10. Comparison of all available experimental results for $U_{\ell mf}$ with predictions of gas-perturbed liquid model, Equation (6.50).

ϵ_o , while for other spherical particle studies, ϵ_{mf} was assigned a value of 0.39, after Lee and Al-Dabbagh (1978). For non-spherical particles, the Wen and Yu (1966) Equation (6.39) was employed to determine ϵ_{mf} or ϕ when one of these quantities was not available. The eleven shallow bed data points of Begovich (1978) are excluded from the comparisons in Table 6.4, as are data for $U_g = 0$. It is seen from this table that, amongst the models, the gas-perturbed liquid model decisively gives the best predictions. It is also seen that the relative performance of the various predictive methods with respect to the experimental data generated in the present work (72 data points) differs very little from that with respect to the combined data from this work and the literature (264 data points).

6.2 Minimum Gas Fluidization Velocity at Zero or Low Liquid Velocity

At low gas velocities, particles are suspended mainly by the liquid phase in a three-phase fluidized bed. At high gas velocities and zero or very low liquid velocities, however, particles are suspended mainly by the gas phase, which provides energy for generating intense turbulent flow in the liquid phase. The resulting liquid motion imparts energy to the solid particles by which they can remain in a suspended condition. Many studies have been devoted to this field. The gas velocity at which all particles are fully suspended at zero (or very low) liquid velocity is defined as the critical gas velocity (U_{gc}) for complete suspension of particles. The critical gas velocity is a function of particle loading, height of the stagnant liquid phase, physical properties of the particle and the liquid and column diameter.

6.2.1 Introduction

Knowledge of U_{gc} is crucial for the design of three-phase bubble columns. Investigations of this parameter have been carried out by Roy et al. (1964), Imafuku et al. (1968), Narayanan et al. (1969), Koide et al. (1983, 1984, 1986), Pandit and Joshi (1984, 1987), Smith et al. (1986),

Heck and Onken (1987) and Abraham et al. (1992). Experimental conditions and the range of variables covered in these studies are summarized in Table 6.5.

Roy et al. (1964) measured the critical gas velocity by means of a pressure transducer mounted below the gas distributor in a 50 mm i.d. column. A break point, observed in a plot of total pressure versus superficial gas velocity, was taken to correspond to the complete suspension of solid particles. Solids holdup at this condition was defined as the critical solids holdup. This critical solids holdup increased with U_{gc} . Two regions of critical solids holdup were observed. In the first, at lower gas velocity, the critical solids holdup depended on the nature of the sparger. In the second region, at higher gas velocity, the critical solids holdup was found to be independent of the nature of the sparger. The effects of sparger design, particle size, liquid surface tension, liquid viscosity and solid-liquid wettability on critical solids holdup were studied. An empirical correlation was proposed:

$$C_{SI} = \begin{cases} 6.84 \times 10^{-4} Re_g^{1.0} N_B^{-0.23} \left(\frac{U_t}{U_B} \right)^{-0.18} (\gamma_f)^{-3.0} C_\mu & \text{for } Re_g < 500 \\ 1.072 \times 10^{-1} Re_g^{0.2} N_B^{-0.23} \left(\frac{U_t}{U_B} \right)^{-0.18} (\gamma_f)^{-3.0} C_\mu & \text{for } Re_g \geq 500 \end{cases} \quad (6.58)$$

with

$$U_B = \frac{U_g}{\epsilon_g} \quad (6.60)$$

and

$$C_\mu = 0.1558 + 0.0264 \log(\mu_\ell) + 0.1026 \log^2(\mu_\ell) \quad (6.61)$$

Table 6.5 Summary of experimental and operating conditions for investigations of critical gas velocity.

Author	Gas and U_g , m/s	Liquid and U_l , m/s	Solid	d_p , mm	ρ_s , kg/m ³	U_t , m/s	Particle Loading	D, m	Measurement Technique
Roy et al. (1964)	air and N ₂	water, aq. alcohol soln. and oil.	quartz, coal, Ni-Al alloy and F-T catalyst	0.13 - 0.675	1440 - 3466	0.0135 - 0.11 in water	$C_{s1} = 7-15\%$	0.05	visual observation, pressure drop and sampling
Imafuku et al. (1968)	air	water	glass beads	0.111	2550	0.0103	$C_{s3} = 15.6 - 81.3 \text{ kg/m}^3$	0.05, 0.10 and 0.20	pressure drop
Narayanan et al. (1969)	air	zero-velocity	quartz	0.125 - 0.675	2630	0.0125 - 0.11	$C_{s2} = 2.5 - 18\%$	0.114 and 0.141	visual observation
Koide et al. (1983)	air	water, glycerol and aq. ethylene glycol soln.	glass beads and bronze spheres	0.0077 - 0.0846	2500 - 8770	0.0048 - 0.0749	$C_{s3} = 0 - 400 \text{ kg/m}^3$	0.10, 0.14 and 0.30	visual observation and pressure drop
Koide et al. (1984)	air	water, glycerol and aq. glycol soln.	glass beads and bronze spheres	0.079 - 0.498	2500 - 8770	0.0109 - 0.0779	$C_{s3} = 25 - 400 \text{ kg/m}^3$	0.10, 0.14, 0.218 and 0.30	visual observation and pressure drop
Pandit and Joshi (1984)	air	zero-velocity	glass beads and quartz	0.070 - 2.0	2260 - 2500	0.0085 - 0.164	$\varepsilon_s/(1 - \varepsilon_g) = 0 - 10\%$	0.10, 0.20 and 0.385	visual observation
Koide et al. (1986)	air	water	glass beads	0.079 - 0.20	2500 - 4680		$C_{s3} = 100 \text{ kg/m}^3$	0.14 Di = 0.066, 0.082, 0.094 and 0.104	visual observation and pressure drop
Smith et al. (1986)	air	water	glass beads and carborundum	0.0485 - 0.084	2420 - 3870	0.0020 - 0.021	$C_{s1} = 0-10\%$	0.0762	visual observation and sampling
Heck and Onken (1987)	air	water	glass beads	0.308	2440		$\varepsilon_s/(1 - \varepsilon_g) = 2 - 20\%$	0.20	pressure drop
Pandit and Joshi (1987)	air	aq. solns. of alcohols, electrolytes, glycerol, CMC, guar gum, polyethylene oxide and polyacrylamide	glass beads and quartz	0.110 - 2.0	2260 - 2500	0.0125 - 0.164	$\varepsilon_s/(1 - \varepsilon_g) = 0 - 10\%$	0.20	visual observation
Abraham et al. (1992)	air	water	glass beads and alumina particles	0.067 - 2.10	2500 - 4000	0.008 - 0.290	$C_{s4} = 5.8 - 80 \text{ mm}$	0.200 and 0.385	visual observation
Present work	air	water	glass beads and steel shot	1.2 - 4.5	2490 - 7510	0.195 - 0.395	$C_{s4} = 240 - 480 \text{ mm}$	0.0826	visual observation

Imafuku et al. (1968) studied the effect of solid concentration, sparger design and the shape of column bottom on U_{gc} in 50, 100 and 200 mm i.d. columns. A pressure transducer was mounted at the bottom of the column. The pressure difference between the total pressure at a non-zero gas velocity and at zero gas velocity was used to determine U_{gc} in a plot of the pressure difference versus the gas velocity. Contrary to the findings of Roy et al. (1964), U_{gc} was found to decrease with increasing solids concentration. U_{gc} increased with increasing column diameter. For the 50 mm column, the sparger design had no effect on U_{gc} . However, for larger columns, the shape of the column bottom and the position of the sparger strongly influenced U_{gc} .

Narayanan et al. (1969) studied solids suspension in 114 and 141 mm i.d. columns with $H_c/D = 1$. A theoretical model for U_{gc} , determined based on bubble movement, was proposed:

$$U_{gc} = \sqrt{2 g (\rho_s - \rho_\ell) \left(\frac{2 d_p}{3 \rho_\ell} + \frac{C_{S2} H_c}{\rho_s + C_{S2} \rho_\ell} \right)} - \frac{1}{3} \sqrt{2 g H_c \epsilon_g \left(\frac{\rho_\ell - \rho_g}{\rho_\ell} \right)} \quad (6.62)$$

with

$$\epsilon_g = \begin{cases} 0.062 U_g & \text{for } U_g \leq 0.067 \text{ m/s} \\ 0.133 U_g^{0.38} & \text{for } 0.067 \leq U_g \leq 0.213 \text{ m/s} \end{cases} \quad (6.63)$$

Experimental values of U_{gc} were as much as four times greater than the predicted values at low solids concentrations, but they were in good agreement for $C_{S2} > 0.10$. A correction factor was employed to obtain the final prediction:

$$U_{gc} = \begin{cases} 4.3 (19.69 D)^m U_g \exp(-10 C_{S2}) & \text{for } C_{S2} \leq 0.10 \\ 1.25 (19.69 D)^m U_g \exp(-3 C_{S2}) & \text{for } C_{S2} > 0.10 \end{cases} \quad (6.64)$$

$$\text{where } m = \begin{cases} 0.5 & \text{for } d_p \geq 0.2 \text{ mm} \\ 0.2 & \text{for } d_p \leq 0.1 \text{ mm} \end{cases}$$

Koide et al. (1983) worked with 100, 140 and 300 mm i.d. columns with conical bottom sections such that the ratio D_d/D could be varied, where D_d is the area of the distributor plate. It was found that U_{gc} increases with increasing particle size, solid loading and column diameter. However, no effect of liquid height on U_{gc} was found when H_c varied from 0.55 to 1.5 m (i.e., H_c/D ratio of 3.33 - 10). A reduction in U_{gc} can be achieved by using a conical bottom with a small value of D_d/D for the smallest diameter column. They proposed

$$\begin{aligned} \frac{U_{gc}}{U_t} = & 0.801 \left(\frac{\rho_s - \rho_\ell}{\rho_\ell} \right)^{0.600} \left(\frac{C_{S3}}{\rho_s} \right)^{0.146} \left(\frac{\sqrt{g D}}{U_t} \right)^{0.24} \left[1 + 807 \left(\frac{g \mu_\ell^4}{\rho_\ell \gamma^3} \right)^{0.578} \right] \\ & \times \left[1 - 1.20 \left(1 - \frac{D_d}{D} \right)^{0.0301} \left(\frac{D^2 g \rho_\ell}{\gamma} \right)^{0.559} \right] \end{aligned} \quad (6.65)$$

Pandit and Joshi (1984) carried out a systematic study of U_{gc} with an air-water-particle system for a wide range of particle sizes (110-2000 μm). The effects of ϵ_s , H_c/D ratio, superficial liquid velocity and column diameter on U_{gc} were investigated. U_{gc} was found to increase with particle terminal setting velocity (U_t) and solid holdup (ϵ_s), but was independent of H_c/D . However, U_{gc} decreased with increasing column diameter, contrary to the findings of Narayanan et al. (1969), Koide et al. (1983) and Imafuku et al. (1968). It was also found that, in the presence of liquid flow, U_{gc} was reduced significantly and the dependence of U_{gc} on C_{S4} (actual volume of solids per unit cross sectional area of the column) was considerably weakened. Pandit and Joshi suggested that complete suspension of the particles occurs when the axial component of liquid

fluctuating velocity, given by

$$U_z' = 0.3275 \left\{ g D \left[(U_g + U_\ell)(1 - \varepsilon_g) - \varepsilon_g U_{b\infty} - \varepsilon_s U_{SN} \left(\frac{\rho_s - \rho_c}{\rho_c - \rho_g} \right) - U_\ell \frac{\rho_\ell}{\rho_c - \rho_g} \right] \right\}^{1/3} \quad (6.66)$$

equals the settling velocity of the particles. Here

$$\rho_c = \rho_\ell \varepsilon_\ell + \rho_s \varepsilon_s \quad (6.67)$$

$$\text{and } U_{SN} = 1.44 U_t^{0.78} U_g^{0.23} \left(\frac{\varepsilon_\ell}{1 - \varepsilon_g} \right)^{3.5} \quad (6.68)$$

For air-water systems, they suggested:

$$\varepsilon_g = \frac{U_g}{2 U_g + U_{b\infty}} \quad (6.69)$$

with $U_{b\infty} = 0.3 \text{ m/s}$.

Koide et al. (1984) reported values of U_{gc} in bubble columns with draught tubes. They observed that draft tubes reduced the value of U_{gc} . U_{gc} increased with increasing terminal settling velocity, solids concentration, liquid surface tension, diameter of gas distributor and density difference between solid and liquid phases, but decreased with increasing column diameter (contrary to their early report) and liquid viscosity:

$$\begin{aligned} \frac{U_{gc}}{U_t} = & 4.60 \left(\frac{\rho_s - \rho_\ell}{\rho_\ell} \right)^{0.750} \left(\frac{C_{S3}}{\rho_s} \right)^{0.273} \left(\frac{U_t \mu_\ell}{\gamma} \right)^{-0.634} \left(\frac{D^2 g \rho_\ell}{\gamma} \right)^{-0.340} \left(\frac{S_c}{S_a} \right)^{0.546} \left(\frac{S_c}{S_d} \right)^{0.454} \\ & \times \left[1 + 897 \left(\frac{g \mu_\ell^4}{\rho_\ell \gamma^3} \right)^{0.290} \right] \times \left[\left(\frac{U_t}{\sqrt{g H_d}} \right) + 1.47 \times 10^{-4} \left(\frac{H_d}{D} \right) \right] \times \left[1 - 1.32 \left(1 - \frac{D_d}{D} \right)^{0.997} \left(\frac{D^2 g \rho_\ell}{\gamma} \right)^{0.172} \right] \end{aligned} \quad (6.70)$$

Koide et al. (1986) studied the effects of column size, properties of the solid particles and mixed particle sizes on U_{gc} in bubble columns with and without draft tubes. It was observed that the effect of column dimension on U_{gc} of mixed solid particles is similar to that on U_{gc} for

monosize particles. For a small weight fraction of particle having the largest value of U_t , the properties of the other particles had almost no effect on U_{gc} . When the weight fraction of particles having the largest value of U_t was greater than 0.33, the correlation of Koide et al. (1983) for monosize particles, Equation (6.70), was used to predict the U_{gc} of a mixed particle system by appropriately modifying C_{S3} and U_t in Equation (6.70).

Smith et al. (1986) proposed a sedimentation dispersion model for the axial concentration distribution of solids in slurry bubble columns. Using this model, U_{gc} was predicted when the solids concentration at the bottom of the column was less than the concentration of settled solids. However, this model gives very conservative estimates of U_{gc} :

$$C_{S3} = \frac{\rho_s \left[0.155 \ln(d_p) + 1.78 \right] \left[\exp(A) - 1 \right]}{(1 - \epsilon_g)(1 - A)A} \quad (6.71)$$

where

$$A = -\frac{\epsilon_\ell U_{SN} L_d}{(1 - \epsilon_g) E_s} \quad \text{and} \quad \epsilon_g = \left[2 + \left(0.35 / U_g \right) \left(\rho_\ell \gamma / 72 \right)^{1/3} \right]^{-1} \quad (\text{SI units}) \quad (6.72)$$

Here U_{SN} can be calculated from Equation (6.68).

Heck and Onken (1987) found a hysteresis effect when pressure drop was used to determine U_{gc} in bubble columns with and without draft tubes. U_{gc} , measured as the superficial gas velocity was increased, was higher than when the gas velocity was reduced.

Pandit and Joshi (1987) reported the effects of surface tension, liquid viscosity, pseudo-plasticity, drag reducing agents and the presence of electrolytes on U_{gc} in 200 mm i.d. column. Their model (Pandit and Joshi, 1984), Equation (6.66), was used to analyze the effect of these variables on U_{gc} (in terms of the effect of bubble size, bubble rise velocity, solids holdup and particle settling velocity) for zero superficial liquid velocity.

Abraham et al. (1992) studied the effect of sparger on U_{gc} . An empirical correlation for U_{gc} was proposed, in which particle terminal setting velocity, gas holdup, solids loading and column diameter served as the variables:

$$U_{gc} = 0.54 U_t^{0.46} \varepsilon_g^{0.66} C_{S4}^{0.39} D^{0.27} \quad (6.73)$$

where

$$\varepsilon_g = 1.44 \left[\frac{U_g^{0.71}}{\rho_\ell^{0.18} \gamma^{0.21} D^{0.04}} \left(1 + \frac{600}{d_o} \right) \right] \exp \left(- \frac{0.62 \varepsilon_s}{\varepsilon_\ell U_t^{0.47} U_g^{0.69}} \right) \quad (6.74)$$

Good agreement between the prediction and experimental results, including previously published data, was found for a wide range of operating conditions.

Careful analysis of the foregoing published literature reveals the following points: (1) Most investigators performed experiments in a semibatch manner. Predetermined batches of solid particles and liquid were added to a column while the gas flow was continuous. The effect of liquid velocity on U_{gc} is needed to complete the investigation of the transition from a three-phase fixed bed to a fluidized bed. (2) Experiments with large/heavy particles in three-phase systems are required to determine the effect of particle size and density on U_{gc} .

6.2.2 Zero Superficial Liquid Velocity

Experiments were carried out in an 82.6 mm i.d. Plexiglas column. The pressure drop between 50 mm and 650 mm above the distributor was measured to determine the critical gas velocity for the complete suspension of particles. Figure 6.11 shows a typical result for the 1.5 mm glass bead three-phase system at zero superficial liquid velocity.

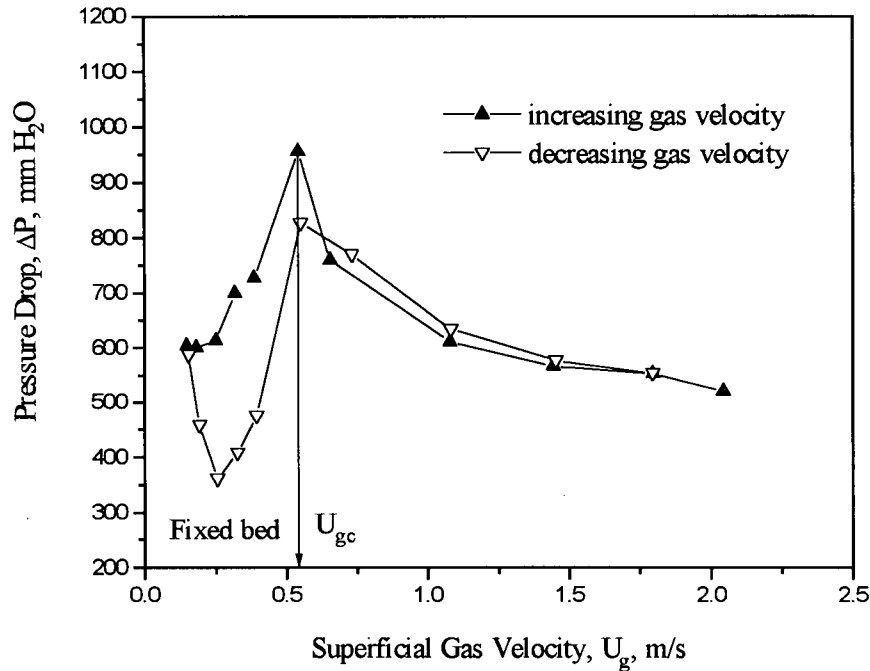


Figure 6.11. Determination of critical gas velocity for full suspension of particles: $d_p = 1.5$ mm, $\rho_s = 2530$ kg/m³, $H_0 = 770$ mm, $U_\ell = 0$, $\Delta P = P_{50} - P_{650}$

It is seen that as the gas velocity is increased, the total pressure drop increases before particles are suspended. This is due to the frictional pressure drop between the particles and the fluids. As the gas velocity is increased further, the pressure drop decreases after the particles are observed to be completely suspended, due to the relatively large gas holdup which now exists in the test section. A maximum pressure drop is observed corresponding to U_{gc} . As the gas velocity is subsequently decreased, the pressure drop also passes through a maximum at almost the same gas velocity, as shown in Figure 6.11. The pressure drop in the fixed bed regime, however, exhibits different values when the gas velocity decreases compared to when it increases. The transition velocity from fixed to fluidized bed is apparently unaffected by this hysteresis. This result was confirmed by Abraham et al. (1992) and Pandit and Joshi (1984).

The effect of measurement location on U_{gc} was examined before other experiments were carried out. Figure 6.12 compares the pressure drop across the lower part, the upper part and the combined interval. It can be seen that complete particle suspension condition is reached at the same gas velocity in each case. The particles in the upper part of the column were not suspended earlier than in the lower part. This implies that once the gas velocity is high enough, the entire solids phase is suspended, i.e. no gradual process of particle suspension is observed. In order to confirm this conclusion, different static bed heights were used to carry out the experiment.

Figure 6.13 shows how critical gas velocities were determined for different solid loadings. It is seen that U_{gc} for different static bed heights, $H_0 = 440$ and 770 mm, are the same at zero liquid velocity. This result, together with the results shown in Figure 6.12, suggests that the suspension of large particles could be caused by drag from the gas phase.

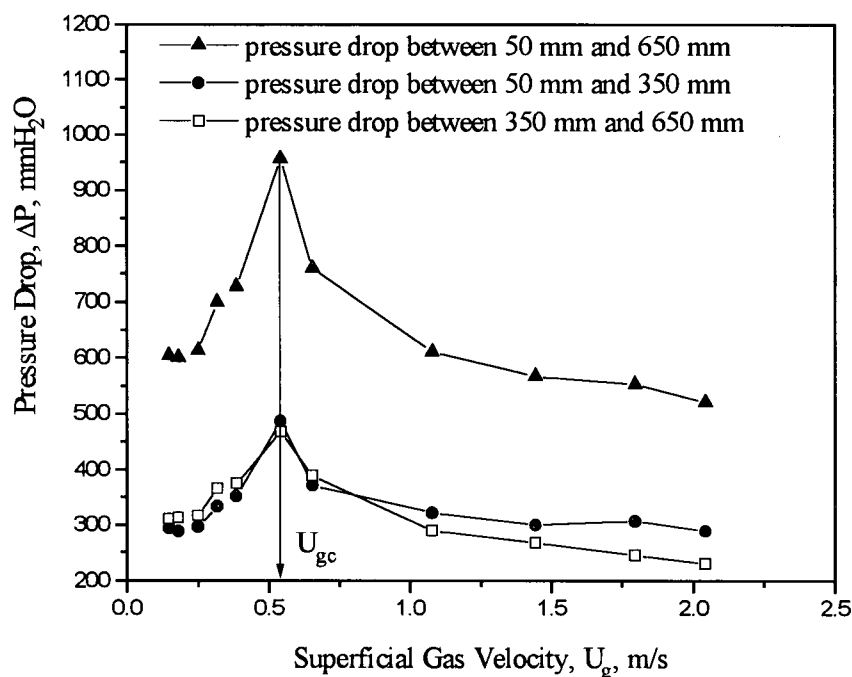


Figure 6.12. Determination of critical gas velocity at different bed heights: $d_p = 1.5$ mm, $\rho_s = 2530$ kg/m³, $H_0 = 770$ mm, $U_\ell = 0$, $\Delta P = P_{50} - P_{650}$, $P_{50} - P_{350}$ and $P_{350} - P_{650}$.

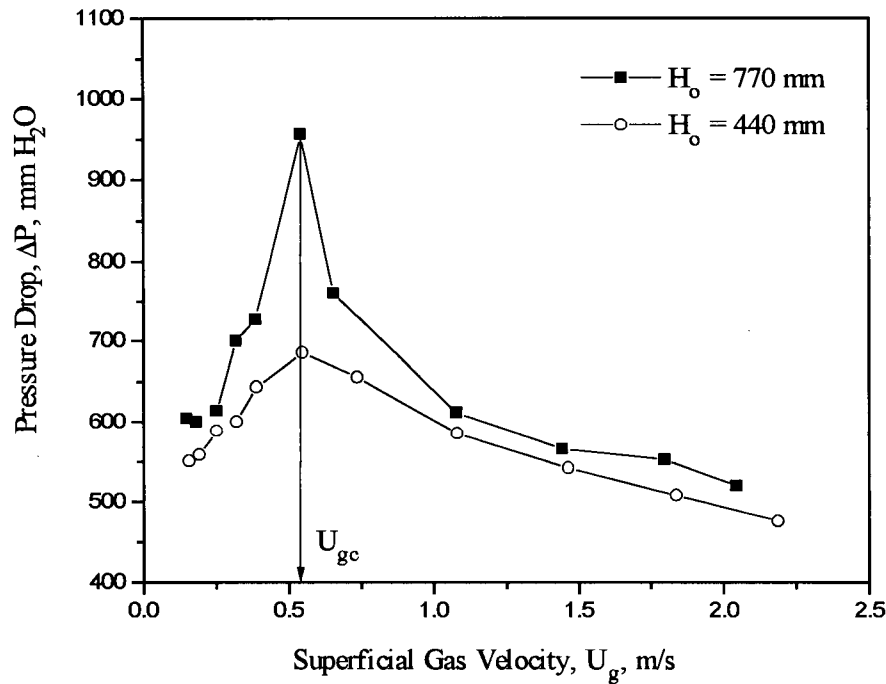


Figure 6.13. Effect of particle loading on critical gas velocity for complete solids suspension: $d_p = 1.5$ mm, $\rho_s = 2530$ kg/m³, $H_o = 440, 770$ mm, $U_\ell = 0$.

Three different types of particle with properties given in Table 2.1 were used to study U_{gc} . Figure 6.14 shows the variations of pressure drop with respect to superficial gas velocity for determining U_{gc} . The results are listed in Table 6.6. The predicted values of U_{gc} according to the Wen and Yu (1966) equation for gas-solid fluidization,

$$Re_{gmf}'' = \sqrt{33.7^2 + 0.0408 Ar_g} - 33.7 \quad (6.75)$$

are also listed in Table 6.6. The viscosity and density of air used here are 1.8×10^{-5} Pa.s and 1.25 kg/m³, respectively.

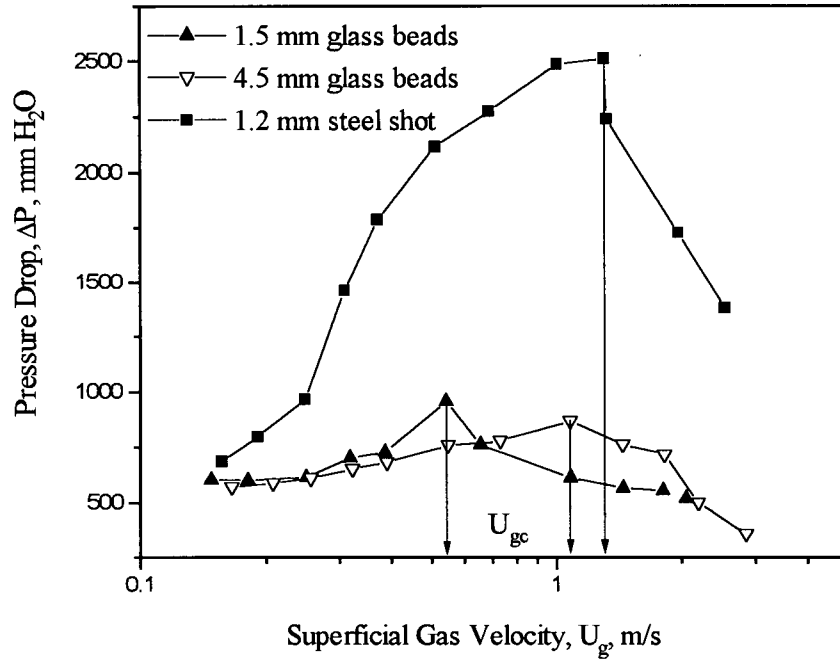


Figure 6.14. Determination of critical gas velocity at zero superficial liquid velocity.

Table 6.6. Experimental and predicted values of critical gas velocity (m/s) at zero superficial liquid velocity.

	1.5 mm glass beads	4.5 mm glass beads	1.2 mm steel shot
Experimental results	0.55	1.07	1.32
Prediction by Equation (6.75)	0.78	1.51	1.39
Prediction by Equations (6.66) and (6.69)	1.00	7.69	9.36
Prediction by Equations (6.66) and (6.51)	0.422	4.01	4.74
Prediction by Equations (6.66) and (6.53)	0.552	4.47	5.32

It is seen that the predicted values of U_{gc} for the 1.5 mm and 4.5 mm glass beads by Equation (6.75) are approximately 50% greater than the experimental data, while for the 1.2 mm

steel shot there is only a 5% difference between the predicted and the experimental results. This result implies that the suspension of large/heavy particles at $U_\ell = 0$ could be caused by two forces. One is the drag force resulting from the internal circulating motion of the liquid phase, generated by the gas phase. The other is the drag force directly resulting from contact between the particles and the gas phase. For particles of lower density, such as glass beads, both forces are significant in the suspension of the particles. For particles of higher density, such as steel shot, the latter force plays the main role in the suspension of the particles. In such a case, Equation (6.75) can be used to predict U_{gc} .

6.2.3 Non-Zero Superficial Liquid Velocity

As mentioned previously, most studies of critical gas velocity have focused on zero superficial liquid velocity. In this study, the superficial gas velocity required for complete suspension of particles at non-zero superficial liquid velocity, U_{gmf} , decreases with increasing superficial liquid velocity. This confirms the investigation by Pandit and Joshi (1984), in which 0.85 and 2.0 mm glass beads were used to study the effect of superficial liquid velocity on U_{gmf} . Figure 6.15 plots pressure drop versus gas velocity for determining U_{gmf} at three different low liquid velocities for the three-phase system using 1.5 mm glass beads. Determination of U_{gmf} for the 4.5 mm glass beads and the 1.2 mm steel shot systems are shown in Figures 6.16 and 6.17, respectively. All experimental results for U_{gmf} including those for (U_{gc}) with zero superficial liquid velocity, are summarized in Table 6.7.

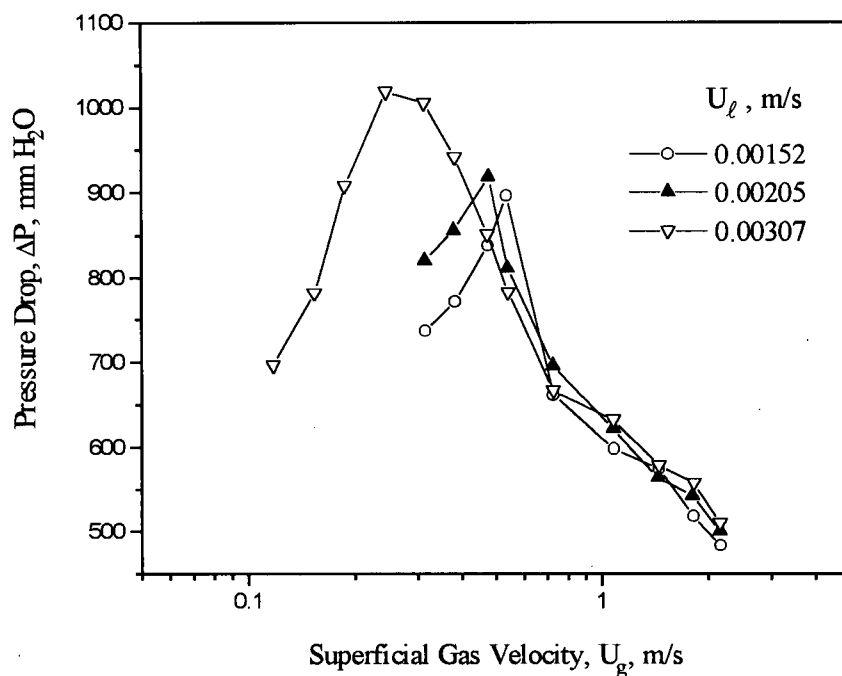


Figure 6.15. Determination of critical gas velocity for three-phase system with 1.5 mm glass beads at different liquid velocities.

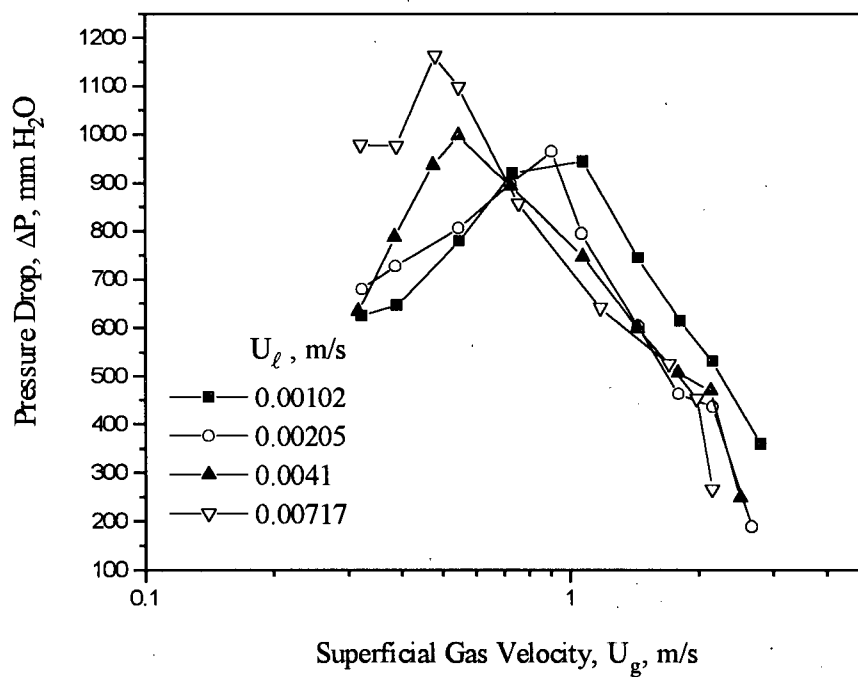


Figure 6.16. Determination of critical gas velocity for three-phase system with 4.5 mm glass beads at different liquid velocities.

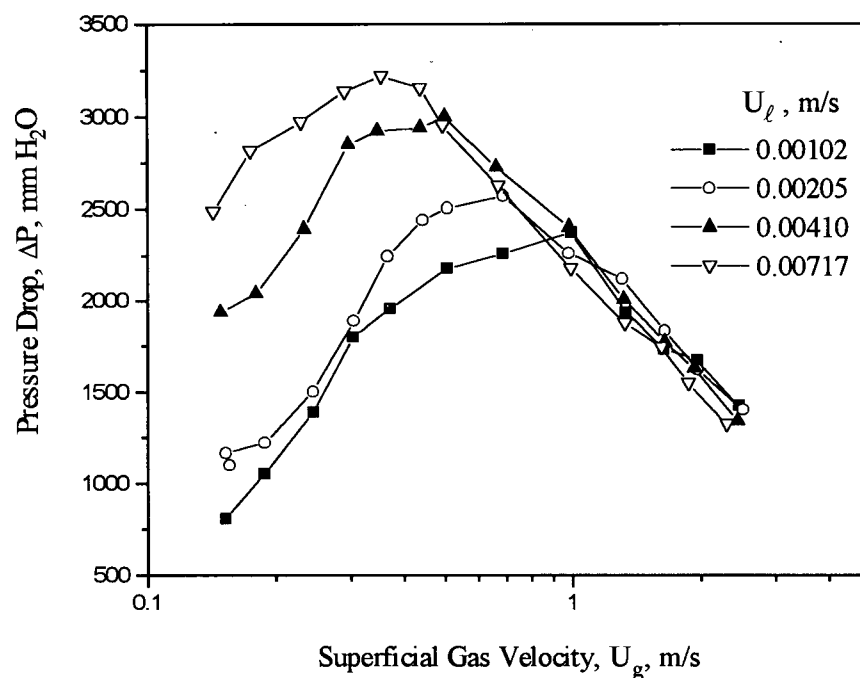


Figure 6.17. Determination of critical gas velocity for three-phase system with 1.2 mm steel shot at different liquid velocities.

Table 6.7. Minimum fluidization gas velocities at low liquid velocities.

U_l , m/s	U_{gmf} , m/s		
	1.5 mm Glass Beads	4.5 mm Glass Beads	1.2 mm Steel Shot
0	0.55	1.07	1.32
0.00102	-	1.00	0.99
0.00150	0.54	-	-
0.00205	0.48	0.91	0.69
0.00307	0.25	-	-
0.00410	-	0.54	0.50
0.00717	-	0.48	0.36

Figure 6.18 plots the minimum gas velocity versus superficial liquid velocity for 1.5 mm glass beads, 4.5 mm glass beads and 1.2 mm steel shot three-phase systems at zero and low liquid velocities. The predictions of Equation (6.66) with Equation (6.69) for these three systems are also plotted in the same figure. It is seen that these equations overestimate U_{gmf} significantly at zero liquid velocity. In addition, the predicted values for U_{gmf} do not change with increasing liquid velocity within the operating range. Other correlations for gas holdup, i.e. Equations (6.51) and (6.53) with $\varepsilon_g = \alpha \varepsilon$, have been used with Equation (6.66) to predict U_{gmf} . The predicted values of U_{gmf} level off again with increasing U_ℓ , no matter which correlation for gas holdup is used. However, the predicted U_{gc} (U_{gmf} at $U_\ell = 0$) with Equation (6.53) agrees well with the experimental data for the 1.5 mm glass beads (see Table 6.6).

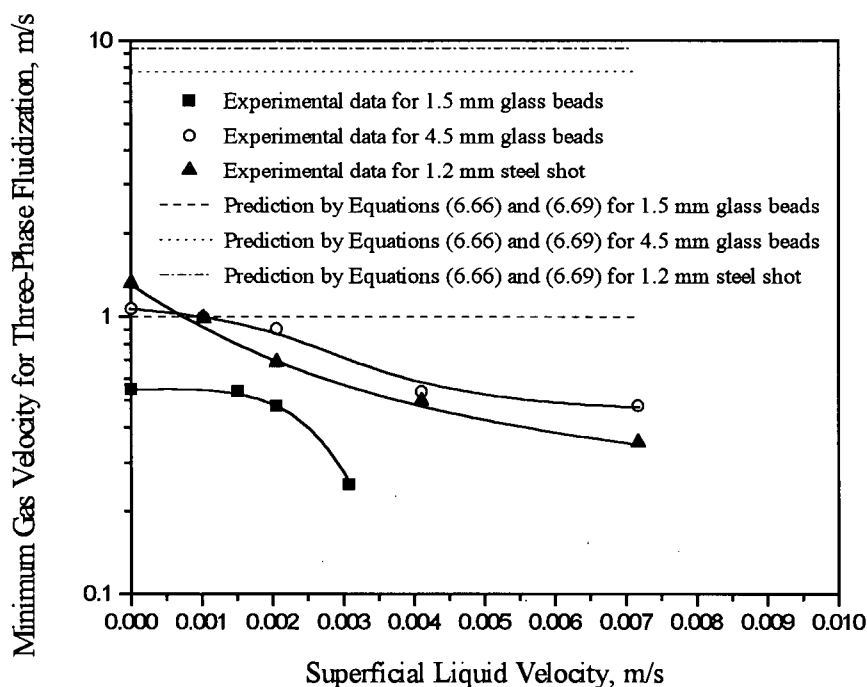


Figure 6.18. Experimental minimum fluidization gas velocities for three-phase system at zero and low liquid superficial velocities

6.3 Particle Transport Velocity in Gas-Liquid Mixture

6.3.1 Introduction

At high gas and/or liquid flow rates, solid particles can be entrained from the column. The particle transport velocity in a gas-liquid mixture demarcates the boundary between a fluidized bed and a transport three-phase system and sets the upper limit at which a three-phase fluidized bed can be operated. It is a function of gas and liquid superficial velocities, as well as the physical properties of the liquid and the solid particles. However, little information can be found regarding this aspect in the literature.

Jean and Fan (1987) determined the boundary between the expanded bed regime and the transport regime by extrapolating the overall voidage, $(\epsilon_g + \epsilon_\ell)$, to unity at a given gas velocity. They found that the transition liquid velocity decreased as the superficial gas velocity increased for glass beads of diameter greater than 0.46 mm. Fan et al. (1987) confirmed this finding. For 0.33 mm and 0.46 mm glass beads, Jean and Fan (1987) found that the transition velocity was nearly independent of U_g . A mechanistic model was developed to predict this transition velocity, based on a momentum balance on a single particle, taking into account the drag and buoyancy forces due to the liquid phase, bubble wake and particle interaction. This led to

$$\frac{3}{4} C_{DL} \frac{\rho_\ell}{d_p} \left[\frac{U_\ell - U_g k}{1 - (1+k) \epsilon_g} \right]^2 + \frac{3}{2} C_{DW} \frac{k \epsilon_g \rho_\ell}{d_p} \left[\frac{U_g}{\epsilon_g} \right]^2 - (\rho_p - \rho_\ell)g = 0 \quad (6.76)$$

where

$$C_{DL} = \frac{24}{Re_L} \left(1 + 0.173 Re_L^{0.657} \right) + \frac{0.413}{1 + 16300 Re_L^{-1.09}} \quad (6.77)$$

$$Re_L = \frac{V_L d_p \rho_\ell}{\mu_\ell} \quad (6.78)$$

$$V_L = \frac{U_\ell - U_g k}{1 - (1 + k)\epsilon_g} \quad (6.79)$$

$$k = 0.398 U_\ell^{0.246} U_g^{-0.646} \quad (6.80)$$

$$\epsilon_g = 0.00164 U_g^{0.988} (-0.221 \times 10^{-5} U_\ell^2 - 0.564 U_\ell + 28.821) \quad \text{for} \begin{cases} 0 < U_g \leq 0.0519 \text{ m/s} \\ 0.0327 \leq U_\ell \leq 0.3218 \text{ m/s} \end{cases} \quad (6.81)$$

$$\epsilon_g = \frac{0.2933 U_g^{0.34}}{\exp(-0.248 R) + \exp(0.243 R)}; \quad R = \frac{U_\ell}{U_g^{0.648}} - 2.03 \quad \text{for} \begin{cases} 0.0863 < U_g \leq 0.1208 \text{ m/s} \\ 0.0327 \leq U_L \leq 0.3218 \text{ m/s} \end{cases} \quad (6.82)$$

$$C_{DW} = \frac{1}{1 + 1.147 \text{Re}_t^{-2.876} \left(\frac{d_p}{D} \right)^{-4.0}} \quad (6.83)$$

$$\text{Re}_t = \frac{U_t d_p \rho_\ell}{\mu_\ell} \quad (6.84)$$

Note that C_{DW} was estimated by parameter regression in the study of Jean and Fan (1987).

Using the same experimental method, Song et al. (1989) proposed an empirical correlation for particle transport velocity in a gas-liquid medium:

$$\frac{U_t'}{U_t} = 1 - 0.518 \text{Fr}_g^{0.310} \left(\frac{\rho_s - \rho_\ell}{\rho_\ell} \right)^{-0.509} \quad (6.85)$$

where $\text{Fr}_g = \frac{U_g^2}{g d_p}$ and $d_p = \left(\frac{3}{2} d^2 \ell \right)^{1/3}$ for cylindrical particles.

Liang et al. (1995) studied the flow regimes in a three-phase circulating fluidized bed. An external loop for particle circulation allowed the apparatus to be operated with continuous particle feeding at the bottom and entrainment from the top of the column. Glass beads of 0.4 mm diameter were used as the solids phase, while air and water served as the gas and liquid phases.

The transition to a circulating bed was determined by the pressure drop between lower and upper sections of the particle riser. The solids circulation rate reached a constant value at $U_g = 2.0$ mm/s for $U_\ell > 61$ mm/s (slightly greater than the terminal velocity of a single particle in the liquid phase, 53 mm/s. With increasing gas velocity, the onset liquid velocity for the circulating bed decreased. A flow regime map at one gas velocity was plotted based on the solids circulation rate versus the superficial liquid velocity. Coalesced bubble flow, dispersed bubble flow, circulating bed and pneumatic transport flow regimes were observed.

6.3.2 Experimental Method

In this study, a high efficiency low pressure drop three-phase separator was used to prevent solid particles from being entrained from the column. At high gas and liquid flow rates, most particles were carried over to, and stored within, the separator, while some were allowed to return to the column. Due to entrainment and back-mixing of the particles, there was a solids concentration gradient in the column, with a dense region at the top and a dilute region at the bottom. The system typically took 30 s to reach a new steady state when either the gas or the liquid flow rate was changed. The transition from a fluidized bed to a transport flow regime was considered to occur when the bottom section (one diameter of the column above the distributor) of the column was emptied of particles as the liquid flow rate was increased at a given gas velocity (or vice versa).

6.3.3 Experimental Results and Discussion

Three different types of particles (1.5 mm glass beads, 4.5 mm glass beads and 1.2 mm steel shot) were used to investigate the effects of particle size and density on the transition from a fluidized bed and a transport flow regime. The experimental results are summarized in Table 6.8.

Table 6.8. Experimental results for the boundary between fluidized bed and transport flow regimes.

1.5 mm Glass Beads		4.5 mm Glass Beads		1.2 mm Steel Shot	
U_g , m/s	U_ℓ , m/s	U_g , m/s	U_ℓ , m/s	U_g , m/s	U_ℓ , m/s
0.0	0.227	0.0	0.472	0.0	0.500
0.0021	0.223	0.0030	0.467	0.021	0.498
0.0058	0.187	0.0054	0.467	0.037	0.482
0.015	0.178	0.010	0.467	0.053	0.482
0.022	0.169	0.016	0.451	0.074	0.482
0.039	0.160	0.021	0.404	0.11	0.482
0.055	0.160	0.037	0.388	0.14	0.482
0.077	0.160	0.053	0.357	0.17	0.482
0.11	0.154	0.075	0.326	0.22	0.482
0.89	0.100	0.11	0.311	0.32	0.482
1.6	0.0729	0.14	0.295	0.34	0.482
3.0	0.0364	0.17	0.280	0.49	0.404
3.7	0.0184	0.23	0.233	1.6	0.311
4.1	0.0103	0.21	0.218	3.4	0.200
4.9	0.00512	0.64	0.155	4.6	0.155
		0.89	0.128	5.9	0.100
		1.3	0.100		
		1.9	0.0729		
		2.1	0.0638		
		2.3	0.0546		
		2.7	0.0455		
		2.8	0.0364		

It is evident that the superficial liquid velocity required for transport flow decreases with increasing gas velocity. The presence of gas bubbles in the column may affect the particles in two ways: (a) they increase the interstitial liquid velocity by occupying some of the volume in the column; and (b) bubble wakes entrain particles due to the fact that the average bubble velocity always exceeds the interstitial liquid velocity.

Assuming that the only effect of the gas bubbles is to increase the interstitial liquid velocity, the particle transport velocity in a gas-liquid mixture can be obtained from a force balance on a single spherical particle:

$$\frac{1}{6} \pi d_p^3 (\rho_s - \rho_\ell) g = C_{DL} \frac{\rho_\ell \left(\frac{U_{\ell t}}{\varepsilon_\ell} \right)^2}{2} \frac{\pi d_p^2}{4} \quad (6.86)$$

Hence

$$U_{\ell t} = \varepsilon_\ell \sqrt{\frac{4 d_p (\rho_s - \rho_\ell) g}{3 C_{DL} \rho_\ell}} \quad (6.87)$$

where the drag coefficient can be estimated from

$$C_{DL} = \begin{cases} 24/Re_t & \text{for } Re_t \leq 0.1 \\ 24(1 + 0.14 Re_t^{0.7})/Re_t & \text{for } 1 < Re_t \leq 1000 \\ 0.445 & \text{for } 1000 < Re_t \leq 3.5 \times 10^5 \end{cases} \quad \begin{matrix} (6.88a) \\ (6.88b) \\ (6.88c) \end{matrix}$$

where $Re_t = \frac{d_p \frac{U_{\ell t}}{\varepsilon_\ell} \rho_\ell}{\mu_\ell}$.

For a cylindrical particle, according to Clift et al. (1978), the terminal velocity of a single cylinder with its axis normal to the flow can be expressed as:

$$U_{\ell t} = \varepsilon_\ell \sqrt{\frac{\pi d (\rho_s - \rho_\ell) g}{2 C_{DL} \rho_\ell}} \quad (6.89)$$

where for long cylinders,

$$\frac{C_{DL}}{9.689 Re_t^{-0.78}} = \begin{cases} (1 + 0.147 Re_t^{0.82}) & \text{for } 0.1 \leq Re_t \leq 5 \\ (1 + 0.227 Re_t^{0.55}) & \text{for } 5 < Re_t \leq 40 \\ (1 + 0.083847 Re_t^{0.82}) & \text{for } 40 < Re_t \leq 400 \end{cases} \quad \begin{matrix} (6.90a) \\ (6.90b) \\ (6.90c) \end{matrix}$$

The liquid holdup, ε_ℓ , in above equations must be determined before the particle transport velocity can be calculated. Many correlations exist for liquid holdup in bubble columns and three-phase fluidized beds (Hughmark, 1967; Kato and Nishiwaki, 1972; Kim et al., 1972; Akita and

Yoshida, 1973; Hikita and Kikukawa, 1974; Darton and Harrison, 1975; Gestrich and Rahse, 1975; Kim et al., 1975; Kumar et al., 1976; Kito et al., 1976; Begovich and Watson, 1978; Bach and Pilhofer, 1978; Mersmann, 1978; Hikita et al., 1980; Friedel et al., 1980; Iordache and Nuntean, 1981; Jean and Fan, 1987). Most of these, however, are based on experiments in the batch operation mode, i.e., $U_\ell = 0$, or are only applicable over small ranges of gas and liquid flow rates.

Based on the Wallis (1969) drift flux theory, Darton and Harrison (1975) found that the correlation

$$U_g (1 - \varepsilon_g) - U_\ell \varepsilon_g (1 - \varepsilon_g) / \varepsilon_\ell = 0.18 \varepsilon_g \quad (6.91)$$

fitted the experimental data of Michelson and Ostergaard (1970) for the dispersed bubble flow regime of three-phase fluidized beds. At the transition from fluidized bed to transport flow, the solids holdup approaches 0. With $\varepsilon_g + \varepsilon_\ell = 1$ and $U_\ell = U_{\ell t}$ at this point, ε_ℓ can then be derived as:

$$\varepsilon_\ell = \frac{0.18 + U_{\ell t}}{0.18 + U_{\ell t} + U_g} \quad (6.92)$$

Jean and Fan (1987) conducted experiments in an air-water bubble column of 72.6 mm diameter. Based on 72 experimental results, two complementary empirical correlations, Equations (6.81) and (6.82), were obtained for gas holdup in bubble columns. The accuracy of these correlations was within $\pm 22\%$ of their experimental results. These correlations cover wide ranges of U_g and U_ℓ , with a gap for $0.0519 < U_g \leq 0.0863$ m/s. In the present work, the gas holdup within the gap was calculated by linear interpolation between the two correlations:

$$\varepsilon_g = \left(\frac{\varepsilon_g|_{U_g=0.0863} - \varepsilon_g|_{U_g=0.0519}}{0.0863 - 0.0519} \right) (U_g - 0.0519) + \varepsilon_g|_{U_g=0.0519} \quad (6.93)$$

In this study, gas holdup correlations proposed by Darton and Harrison (1975) and Jean and Fan (1989) were used with Equations (6.87) and (6.88) to predict the transition between fluidized bed and transport flow regimes. Equations (6.87) and (6.88) together with Equation (6.92) are referred to as Transport Velocity Model I. Equations (6.87) and (6.88), together with Equations (6.81), (6.82), (6.93) and $\varepsilon_\ell = 1 - \varepsilon_g$, will be referred to as the Transport Velocity Model II. For cylindrical particles, Equations (6.87) and (6.88) are replaced by Equations (6.89) and (6.90) in both models. Figure 6.19 compares the predictions of the Jean and Fan (1987) model, the Song et al. (1989) empirical correlation, and Models I and II with the experimental data for the air-water-1.5 mm glass beads three-phase system. The experimental results also appear in the figure.

It is seen that all four models work well for U_g less than approximately 0.2 m/s. For higher superficial gas velocities, only the Transport Velocity Model II follows the trend of the experimental results. The theoretical model proposed by Jean and Fan (1987) fits the experimental results only for $U_g < 1$ m/s for the air-water-1.5 mm glass bead system.

Figure 6.20 compares predicted values with the experimental results for the air-water-4.5 mm glass bead system. Again, Model II agrees with the experimental results very well for $U_g < 3.0$ m/s. A strange peak is seen for the Jean and Fan model at low gas velocity for the 4.5 mm glass bead system. A similar result can be observed for their experiments with 6.1 mm glass beads, as shown in Figure 6.21, although the authors did not comment on this. In addition, this model fails in Figure 6.20 for $U_g > 0.2$ m/s, as does the empirical correlation of Song et al., Equation (6.85). It is seen that the Jean and Fan model gives accurate predictions only for small particles and low U_g . Model I gives better predictions for the 4.5 mm glass bead than for the 1.5 mm glass beads. This is because Equation (6.92) was developed for the dispersed bubble flow regime, and the bubble characteristics in the 4.5 mm glass bead system are much closer to that regime than in the 1.5 mm glass bead system.

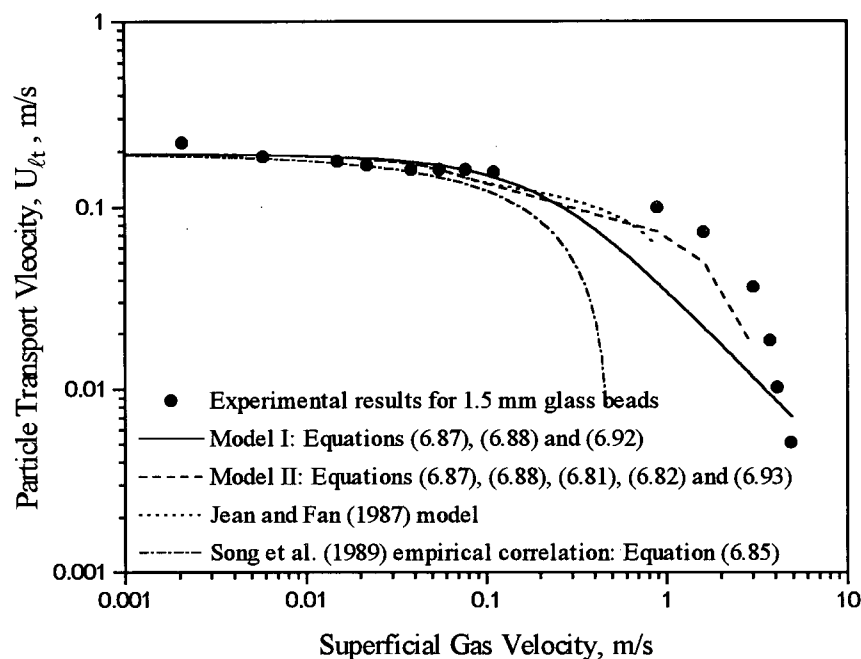


Figure 6.19. Predictions and experimental results for transition from fluidized bed to transport flow regime: air-water-1.5 mm glass beads.

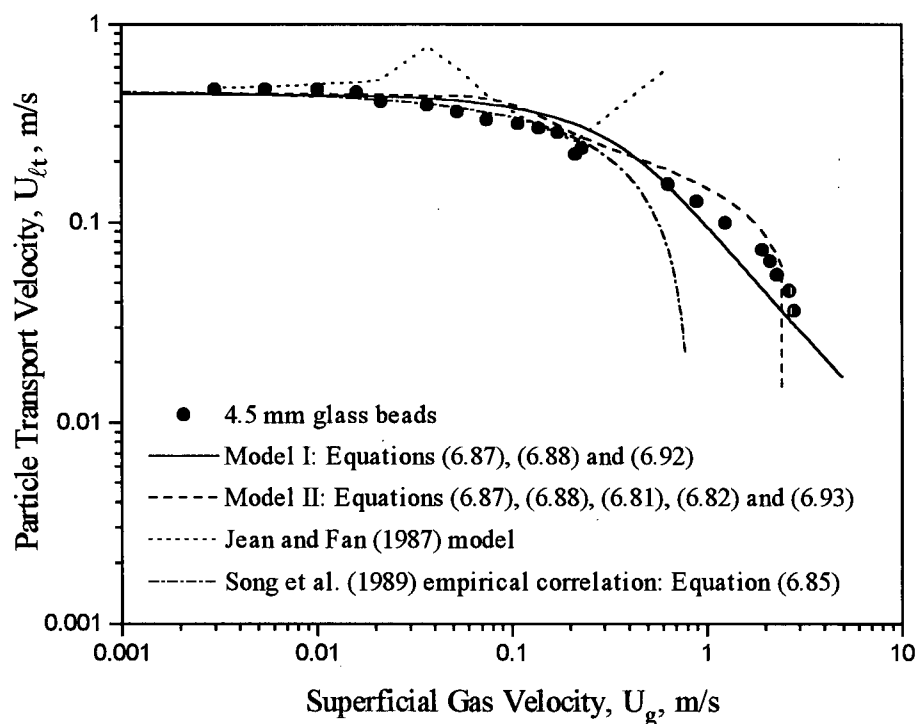


Figure 6.20. Predicted and experimental particle transport velocities for 4.5 mm glass beads in air-water mixture

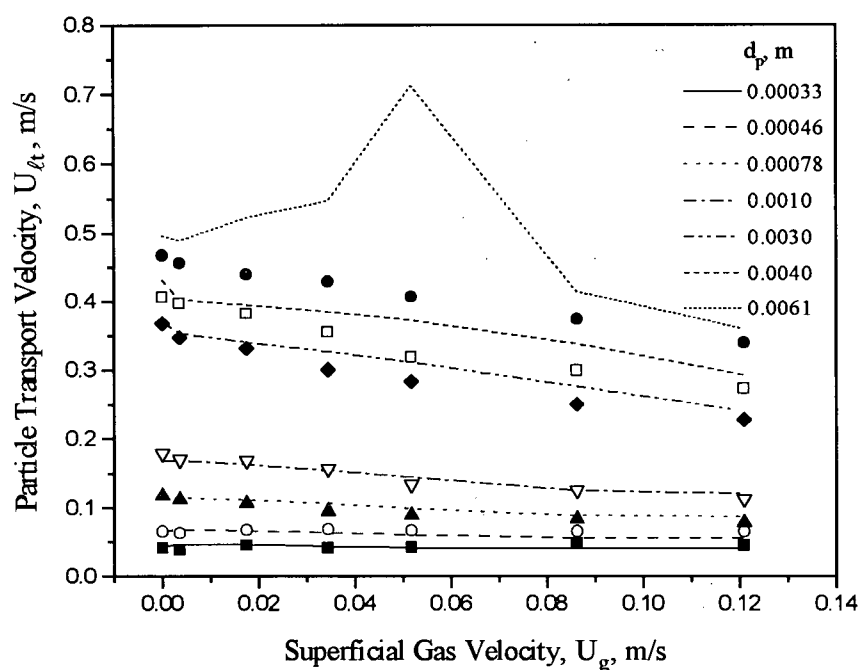


Figure 6.21. Particle transport velocity predictions compared with experimental results of Jean and Fan (1987).

A comparison of the various model predictions with all available experimental data, including those of Song et al. (1989), Jean and Fan (1987) and this study, is shown in Table 6.9 as average absolute percentage deviation between predicted value and experimental results, given by Equation (6.57). The empirical correlation of Song et al. (1989) is seem to work well for three-phase systems with glass bead particles of diameter greater than 0.5 mm or cylindrical particles when $U_g < 0.23$ m/s. Model II, given by Equations (6.87), (6.88), (6.81), (6.82) and (6.93), is the best theoretical model which covers all operating conditions and fluid flow rates for the low particle density systems. Although Equations (6.81), (6.82) and (6.93) are based on experimental data which are limited to small gas and liquid velocity ranges, they can evidently be extended to 3.0 m/s and 0.5 m/s for the gas and the liquid velocities, respectively, to predict the particle transport velocity with Equations (6.87) and (6.88) or Equations (6.89) and (6.90).

Table 6.9. Average absolute percentage deviation between experimental results and model predictions for particle transport velocity in gas-liquid mixture.

Average absolute percentage deviation, $\bar{\delta}_a$, %	No. data points	Song et. al (1989) empirical correlation, Eq. (6.85)	Jean and Fan (1987) model, Eqs. (6.76) to (6.84)	Model I, Eqs. (6.87) and (6.88) [or (6.89) and (6.90)] with (6.92)	Model II, Eqs. (6.87) and (6.88) [or (6.89) and (6.90)] with (6.81), (6.82) and (6.93)	Empirical correlation, Eq. (6.94)
Data from Jean and Fan (1987) for small size glass beads, $d_p = 0.33$ and 0.46 mm	14	30.5	8.2	15.0	15.5	14.9
Data from Jean and Fan (1987) for middle size glass beads, $d_p = 0.78 - 4.0$ mm	28	8.2	6.2	8.14	8.6	5.6
Data from Jean and Fan (1987) for large size glass beads, $d_p = 6.11$ mm	7	2.2	21.6	4.3	7.6	8.1
Data from Song et al (1989) for cylindrical catalysts, $d = 0.89$ and 0.94 mm; $\ell = 2.9 - 5.18$ mm; $\rho_s = 1890 - 2000$ kg/m ³	30	10.9	24.7	22.4	19.5	17.9
Data from this work for glass beads, $d_p = 1.5$ and 4.5 mm; $U_g \leq 0.23$ m/s	23	7.8	16.4	12.0	11.3	11.6
Data from this work for glass beads, $d_p = 1.5$ and 4.5 mm; $U_g \leq 3.0$ m/s	33	175.5	244.6	17.9	14.2	16.7
Data from this work for the 1.2 mm steel shot, $U_g \leq 5.5$ m/s	15	115.0	—	—	—	14.0
Experimental data excluding the steel shot when $U_g \leq 0.23$ m/s	102	11.5	15.3	14.0	13.3	12.0
Experimental data excluding the steel shot when $U_g \leq 3.0$ m/s	112	60.6	82.7	15.6	14.2	14.4
All experimental data when $U_g \leq 0.23$ m/s	111	11.7	—	—	—	11.7
All experimental data when $U_g \leq 3.0$ m/s	125	57.1	—	—	—	13.8

The two best prediction methods are compared with available low density experimental data in Figure 6.22. It can be seen that most data points lie on both sides of the diagonal line on the plot of the predicted $U_{\ell t}$ versus experimental $U_{\ell t}$. Exceptions are those points underestimated by the Song et al. empirical correlation, Equation (6.85), for high gas velocities.

The experimental measured transport velocities in water for the three types of particles studied here are 0.227, 0.472 and 0.50 m/s for the 1.5 mm glass beads, 4.5 mm glass beads and 1.2 mm steel shot, respectively. The theoretical predicted terminal velocity for these particles in water are 0.195, 0.444 and 0.395 m/s, respectively. The measured particle transport velocity for the 1.2 mm steel shot is significantly greater than its single particle terminal velocity. This is probably due to the occurrence of particle clusters.

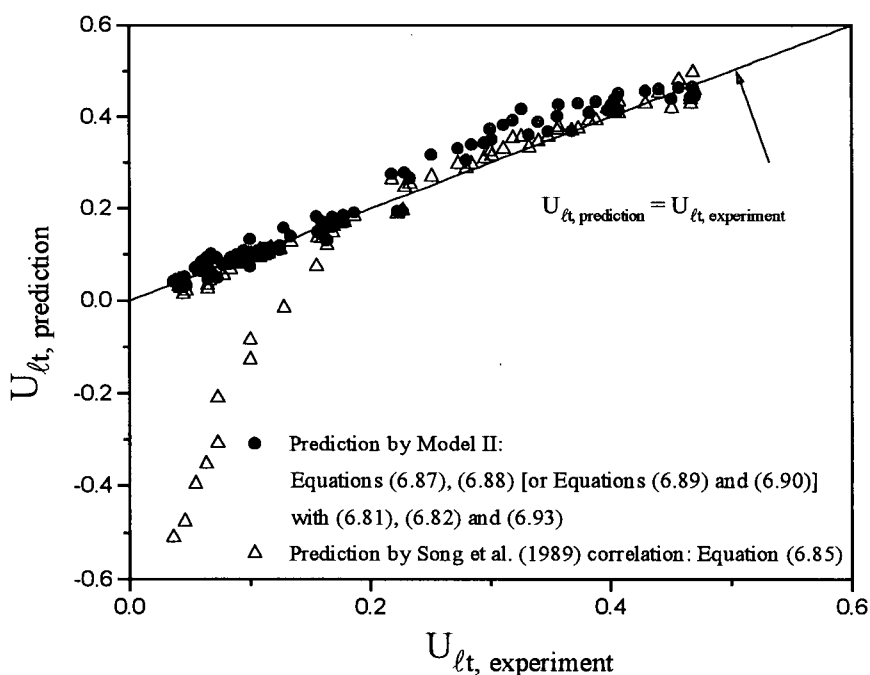


Figure 6.22. Experimental data for low density ($\rho_s \leq 2876 \text{ kg/m}^3$) particle transport velocity compared with predictions of Song et al. (1989) empirical correlation and Model II.

In gas-solid fluidization, fine solids can combine loosely into assemblies, defined as clusters (Yerushalmi et al., 1976; Grace and Tuot, 1979; Li and Kwauk, 1980; Horio and Clift, 1992; Brereton, and Grace, 1993). The mean effective size and density of the clusters are usually such that their terminal velocities exceed the gas velocity, causing the transport velocity of the particles to be an order of magnitude greater than the terminal velocity of individual particles (Yerushalmi, 1986). For the 1.2 mm steel shot, clusters were observed at high U_ℓ both in the water and the air-water mixtures, leading to higher transport velocities compare to single particle terminal velocity.

Equations (6.87) and (6.88), or Equations (6.89) and (6.90), can be applied to predict single particle terminal velocities, which are close to the transport velocity when particle clusters are not formed. For the particles which form clusters, the transport velocity in liquid can be obtained through experiments. The transport velocity of the liquid in gas-liquid mixtures can be estimated by the empirical correlation:

$$\frac{U_{\ell t}}{U_t} = 1 - 0.2172 Fr_g^{0.2072} Ar_\ell^{0.1013} \left(\frac{\rho_s - \rho_\ell}{\rho_\ell} \right)^{-0.5} \quad (6.94)$$

based on 125 sets of experimental data, 79 from the literature and 46 from this study, including three-phase systems with glass beads, cylindrical particles and steel shot. As indicated in Table 6.9, the mean deviation is 11.7% for $U_g \leq 0.23$ m/s and 13.8% for $U_g \leq 3.0$ m/s. For steel shot, the mean deviation between the experimental data and Equation (6.94) is 14.0%, while the mean deviation for the Song et al. (1989) correlation, i.e. Equation (6.85), is 115.0%. Figure 6.23 compares the transport velocity predictions for the 1.2 mm steel shot with the experimental results. It can be seen that Equation (6.94) works well over a wide range of U_g . A comparison of Equation (6.94) with other experimental results is also given in Table 6.9.

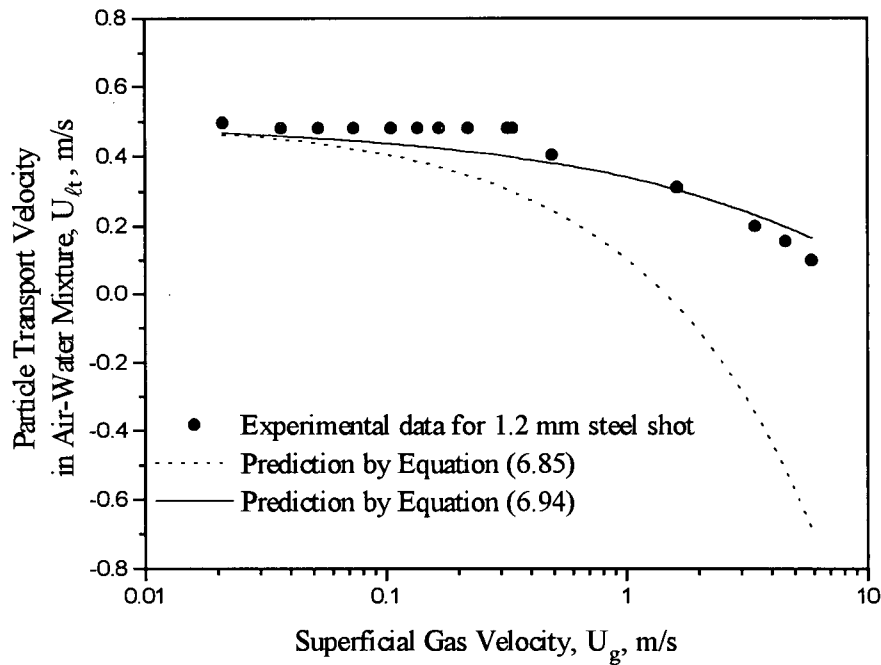


Figure 6.23. Comparison between particle transport velocity empirical correlations and experimental results for 1.2 mm steel shot.

6.4 Regime Maps of Three-Phase Systems

Three-phase systems can be generally classified into three operating regimes: fixed beds, fluidized beds and transport flow. Minimum fluidization velocities demarcate the boundary between a fixed bed and a fluidized bed, while particle transport velocities delineate the boundary between a fluidized bed and the transport regime. Regime maps which illustrate these three regimes for the 1.5 mm glass beads, 4.5 mm glass beads and 1.2 mm steel shot with air and water are presented in Figure 6.24, 6.25 and 6.26, respectively.

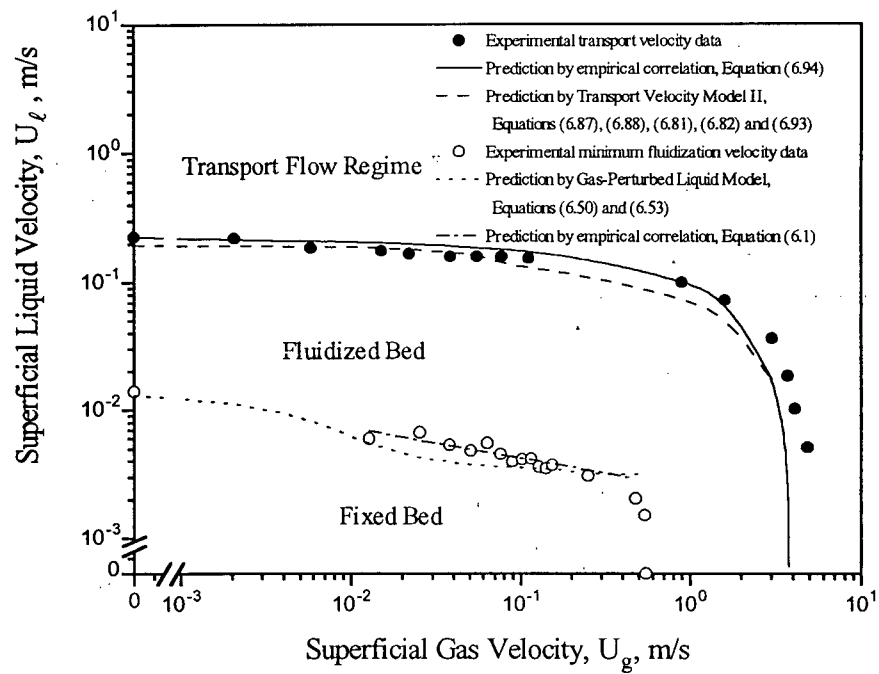


Figure 6.24. Regime map for air-water-1.5 mm glass bead three-phase system.

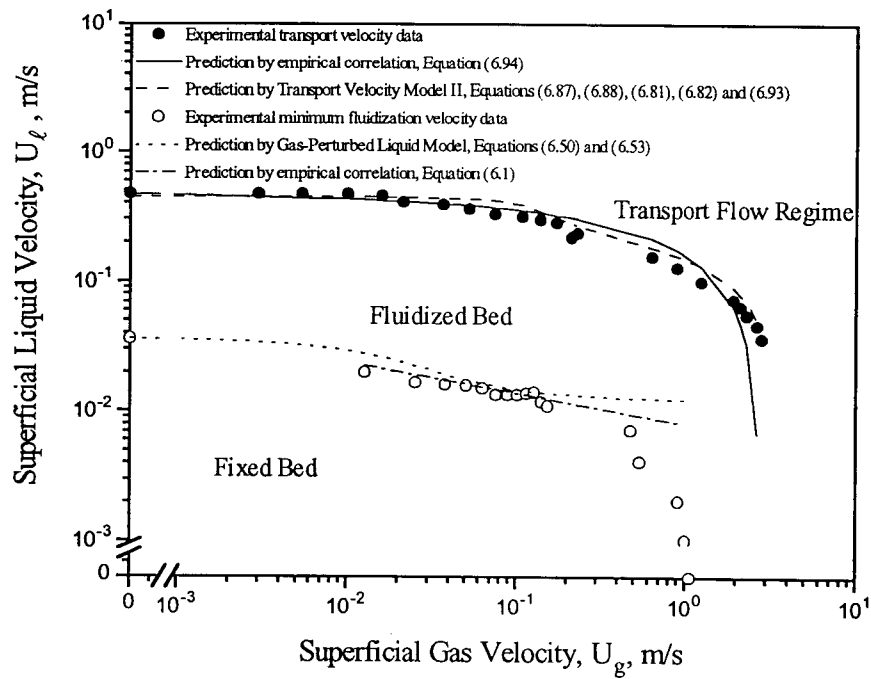


Figure 6.25. Regime map for air-water-4.5 mm glass bead three-phase system.

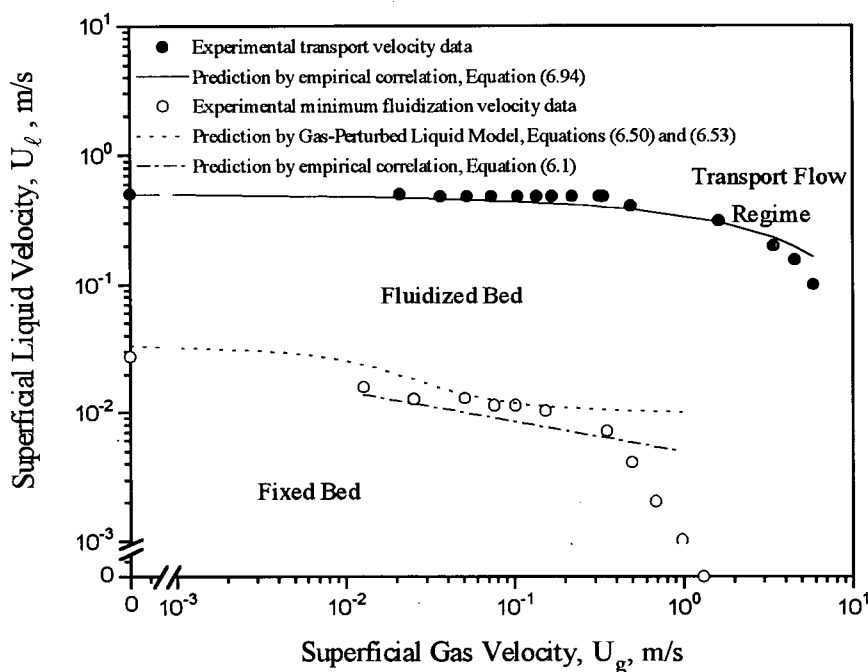


Figure 6.26. Regime map for air-water-1.2 mm steel shot three-phase system.

It is clear that both the particle size and particle density affect the transitions. The greater the particle density and size, the higher the minimum gas and/or liquid fluidization velocities. For the onset of transport flow, the particle transport velocities increase with particle density over the entire operating range. For the glass beads, the particle transport velocities increase with particle size at low gas velocities but appear to be independent of particle size at high gas velocities.

6.5. Summary

Several correlations are available to predict the minimum fluidization velocity in three-phase fluidized beds. Pseudo-homogeneous fluid models do not predict the minimum fluidization velocity well. The best agreement with experimental data was obtained from the first empirical equation of Begovich and Watson (1978), Equation (6.1). Nearly as good agreement was obtained from a "gas-perturbed liquid model", in which the gas is assumed to decrease the area available for liquid flow. This model has the advantage of having no new fitted constants and goes

to the proper limit, the Wen and Yu (1966) equation for a liquid-solid fluidized bed, as the superficial gas velocity approaches zero. The resulting generalized minimum fluidization model, Equation (6.50), can thus be used to predict incipient fluidization velocity in both two-phase and three-phase fluidization. However, the model is expected to break down when the momentum transfer to the particles is provided mainly by the gas. The ratio, α , of gas holdup to bed voidage plays a very important role in the model. Among several correlations for α , the correlation proposed by Yang et al. (1993), Equation (6.53), is recommended.

At zero or very low liquid velocities and high gas velocities, particles are mainly supported by the gas phase. The gas provides energy for generating turbulence in the liquid phase, which imparts energy to the solid phase so that particles can remain suspended. This mechanism has been established by many investigators for small or light particles. For large or heavy particles, the particles could be supported by the drag force caused by gas flow, similar to the incipient fluidization mechanism in a gas-solid system. In such a case, e.g. for the 1.2 mm steel shot, Equation (6.75) can be used to predict the critical gas velocity for complete suspension of the particles at zero superficial liquid velocity. The minimum gas fluidization velocity is reduced significantly by increasing the liquid velocity. Further study is needed to understand the effect of U_l on the minimum fluidization velocity at high gas velocities.

The particle transport velocity delineates the transition between a fluidized bed and the transport flow regime. For particles which do not form clusters, i.e., 1.5 and 4.5 mm glass beads, the particle transport velocity of the liquid is similar to the single particle terminal velocity in the liquid phase, which can be calculated using Equations (6.87) and (6.88) for spherical particles. In gas-liquid mixtures, the particle transport velocity of the liquid decreases with increasing gas velocity, since the gas phase occupies some of the column cross-section, leading to an increase of the interstitial liquid velocity, which plays the main role in supporting the particles. The effect of the bubble wakes on the particle transport velocity can be ignored for large particles at low

superficial gas velocities. The Transport Velocity Model II, Equations (6.87) and (6.88) for spherical particles or Equations (6.89) and (6.90) for cylindrical particles, together with Equations (6.81), (6.82) and (6.93), is based on the above mechanism. It agrees with 112 sets of experimental data, including 79 data sets from the literature, but excluding the 1.2 mm steel shot results obtained in the present work, with an average absolute deviation of 14.2% for gas velocities up to 3.0 m/s. For the 1.2 mm steel shot, particles aggregate to form particle clusters, causing the particle transport velocity of the liquid to be significantly greater than the single particle terminal velocity in the liquid phase. Knowing the particle transport velocity in the liquid phase, an empirical correlation proposed in the present work, Equation (6.94), can be used to predict the transport velocity in air-water mixtures. This correlation also gives good agreement with 125 sets of experimental data, including 79 data sets from the literature, with an average absolute deviation of 13.8% for gas velocities up to 3.0 m/s, a much higher value than explored previously, previous upper limits being of order 0.1 m/s.

Chapter 7

Flow Regimes in Three-Phase Fluidized Beds

7.1 Introduction

Many flow pattern characteristics are shared by three-phase fluidized beds and gas-liquid two-phase flow. For example, at low gas and liquid velocities, three-phase fluidized beds can operate in the coalesced bubble flow regime. As liquid velocity is increased, the dispersed bubble flow regime is commonly encountered. Correspondingly, two similar regimes, often labelled heterogeneous flow and homogeneous flow, respectively, exist in (gas-liquid) bubble columns. As the gas velocity is increased, three-phase fluidized beds can operate in the slug flow, churn flow, bridging flow or annular flow regime. These hydrodynamic regimes are analogous to similar regimes in gas-liquid two-phase flow systems. The definitions of the flow patterns in Chapter 1 are also applicable to three-phase fluidized beds.

7.1.1 Visual Observations

A number of studies have been devoted to the investigation of flow patterns and flow regime transitions in three-phase fluidized beds. Most of these studies have relied solely on visual observation.

Mukherjee et al. (1974) reported that three distinct flow patterns could be observed in a three-phase fluidized bed. At very low gas flow rates, bubble flow was encountered. As the gas flow rate was increased, slug flow occurred. At an even higher gas flow rate, gas continuous flow was observed. The range of gas flow rates for the bubble flow and slug flow regimes was wider at higher liquid flow rates.

Muroyama et al. (1978) found that, with low to intermediate gas and liquid flow rates, coalesced bubble flow, dispersed bubble flow and slug flow could be observed in an air-water-large particle system. They also reported a transition regime between the dispersed bubble flow regime and the slug flow regime. The boundary between the dispersed bubble flow regime and this transition regime was a positively inclined line on a plot of U_ℓ vs. U_g . Similar flow regime maps have been presented by Fan et al. (1984), Matsuura and Fan (1984) and Fan et al. (1985).

For a given fluidized bed, Fan et al. (1985) found that there was a strong correlation between the free-settling particle terminal velocity in the liquid phase, U_t , and the superficial liquid velocity, $(U_\ell)_{dc}$, separating the coalesced bubble flow regime from the dispersed bubble flow regime. As U_t increased, $(U_\ell)_{dc}$ increased and reached a maximum at $U_t = 0.343$ m/s (corresponding to the terminal velocity of 2.55 mm glass beads with a density of 2520 kg/m³ in water). The variation of $(U_\ell)_{dc}$ with U_t could be expressed by:

$$(U_\ell)_{dc} = \begin{cases} 0.696 U_t^{1.50} & \text{for } U_t \leq 0.343 \text{ m/s} \\ 0.0228 U_t^{-1.70} & \text{for } U_t \geq 0.343 \text{ m/s} \end{cases} \quad (7.1)$$

These four different flow regimes (coalesced bubble flow, dispersed bubble flow, transition flow and slug flow) were also observed in three-phase fluidized beds of binary mixtures of particles with different sizes and/or densities. The gas velocity exhibited negligible influence on $(U_\ell)_{dc}$ for both monocomponent and binary solids systems. On the other hand, the boundary between coalesced bubble flow and slug flow was strongly affected by gas velocity and only slightly by liquid velocity. Slug flow occurred at a relatively high gas velocity for a binary mixture.

Fan et al. (1986) analyzed the statistical properties of wall pressure fluctuations in a 0.102 m ID column. Pressure transducers were used to determine absolute pressure fluctuations, while the flow regime boundaries were determined by visual observation. It was found that the

transition velocity between the coalesced bubble and the dispersed bubble regimes increased with particle terminal velocity for small particles and decreased for large particles. This trend is the same as that given by Equation (7.1) above. The transition velocity, $(U_\ell)_{dc}$, shifted upward in the large column for systems with low particle terminal velocities. However, the transition velocity, $(U_\ell)_{dc}$, remained the same in both columns for systems with higher particle terminal velocities. The boundaries between coalesced bubble flow and slug flow, as well as between dispersed bubble flow and slug flow, were independent of particle terminal velocity.

Ermakova et al. (1970) reported three regimes: (a) fixed bed at low gas and liquid velocities; (b) heterogeneous fluidization; (c) homogeneous fluidization at high liquid velocities. The boundary on a U_ℓ vs. U_g plot between the fixed bed regime and heterogeneous fluidization began at $U_g = 0$, $U_\ell = U_{\ell mf}$; as the gas velocity was increased, $U_{\ell mf}$ decreased. The boundary between homogeneous and heterogeneous fluidization at high liquid velocity also began at $U_g = 0$, $U_\ell = U_{\ell mf}$, but as the gas velocity was increased, $(U_\ell)_{dc}$ also increased. An empirical equation

$$(U_\ell)_{dc} = U_{\ell mf} \left[1 + 13.4 \left(\frac{U_g}{d_p^2} \right)^{0.5} \right] \quad (7.2)$$

was proposed to predict the transition between homogeneous and heterogeneous fluidization.

Song et al. (1989) studied the effect of surface tension on bubble hydrodynamics in three-phase fluidized beds. The flow regimes in surfactant systems were found to differ from those in air-water systems. Dispersed large bubbles ($d_b = 5$ to 7 mm) appeared at low liquid velocities and low to intermediate gas velocities ($U_g = 0$ to 0.15 m/s). Dispersed small bubbles ($d_b = 1$ mm) were found at high liquid velocities. Between these two regimes there was a transition regime in which bubble size exhibited a bimodal distribution. At high gas velocities a foaming regime was observed instead of slug flow.

The effect of liquid properties on flow patterns was also investigated by Nacef et al. (1992, 1995). The dispersed bubble regime was more extended when water + 1% ethanol was employed as liquid phase compared with water alone. A solid piston flow (or square-nose slug) regime was observed, characterized by the appearance of several moving packed beds separated by a liquid-gas mixture. Solids rained down through this liquid-gas mixture. The average diameter of the gas bubbles in the liquid-gas slabs was of order 1 mm.

7.1.2 Instrumental Measurements

Soria and de Lasa (1992) measured the liquid volume fraction using electrical conductivity sensors in bubble columns and three-phase fluidized beds. These sensors were composed of several pairs of square electrodes which measured the conductivity of a multiphase mixture. In a three-phase fluidized bed, it was found that the transition between dispersed bubble flow and coalesced bubble flow was governed by the superficial liquid velocity. In a plot of ε_ℓ vs. U_ℓ , a common crossover point was found for three sets of experiments, each at a different but constant value of U_g . This crossover point was hypothesized to be the transition between the coalesced bubble flow and dispersed bubble flow regimes.

Han and Kim (1990) proposed a flow regime map using coordinates of the ratio of gas holdup to bed porosity, $\alpha (= \varepsilon_g / (\varepsilon_g + \varepsilon_\ell))$, and gas-liquid slip velocity, $U_s (= U_g / \varepsilon_g - U_\ell / \varepsilon_\ell)$, noting that previous flow regime maps did not take particle size and liquid properties into account. The dispersed bubble flow regime was characterized by relatively low gas-liquid slip velocities (0.4 - 0.5 m/s), with α in the range 0 to 0.4. The coalesced bubble flow regime required higher slip velocities (0.4 to 0.8 m/s), with α varying from 0 to 0.2. The slug flow regime was found to be associated with high slip velocities with α from 0.2 to 0.4.

Lee et al. (1990) determined flow regimes based on mean bubble sizes throughout a fluidized bed fitted with a single pipe gas distributor. A progressive increase in mean bubble length as bubbles rose indicated coalesced bubble flow. A decrease in mean bubble length with height implied dispersed bubble flow. Based on four experimental runs and some literature data, a flow regime map was proposed using particle diameter and superficial liquid velocity as coordinates. The fixed bed, coalesced bubble flow, dispersed bubble flow, and transport regimes appeared on this map.

Kitano and Ikeda (1988) used pressure transducers to study the transition between the dispersed bubble flow and coalesced bubble flow regimes. The integral of the power spectra density function of the pressure fluctuations between 0 and 10 Hz was used to detect the transition. For the dispersed bubble flow regime, this integral increased linearly with decreasing liquid velocity at a given gas flow rate. The transition from dispersed flow to coalesced flow was assumed to take place when the values began to deviate from this linear relationship. It was also found that there was a transition regime between dispersed bubble flow and the coalesced bubble flow regime.

Absolute and differential pressure fluctuations have also been used to determine the flow regimes for other three-phase systems (Zheng et al., 1988; Chen et al., 1995; Vunjak-Novakovic et al., 1992). Table 7.1 summarizes previous investigations of flow regime transitions in three-phase fluidized beds.

Table 7.1. Summary of previous investigations on flow regime transitions in three-phase fluidized beds.

Author and year	Particles & their density, kg/m ³	Particle diameter, m	Coordinates	Gas and its velocity, m/s	Liquid and its velocity, m/s	Measurement technique	Column diameter, m	Flow regimes identified	Map or correlation
Ernakova et al. 1970	Glass beads	0.0006 0.0012 0.0020	U_g vs. U_l	Air: 0 - 0.20	Water; Aqueous solution of glycerin; Aqueous solution of n-heptane. $\mu_c = 0.42 - 6.05 \times 10^{-3}$ Pa.s 0-0.10	Visualization	0.10 0.20	Fixed bed Homogeneous Heterogeneous	Map and correlation
Mukherjee et al. 1974	Glass beads 2780 2920 2860 2960	0.00412 0.0028 0.0014 0.000287	U_l U_g vs. U_l	Air: 0 - 0.13 0 - 0.10 0 - 0.08 0 - 0.06	Water: 0.0927 - 0.2136 0.0921 - 0.1386 0.0131 - 0.1203 0.0098 - 0.0675	Visualization	0.052	Bubble Slug Gas continuous	Map
Muroyama et al. 1978	Glass beads 2475	0.0026 0.0048 0.0069	U_g vs. U_l	Air: 0 - 0.30	Water: 0.0845 - 0.168	Visualization	0.060 0.10	Coalesced bubble Dispersed bubble Slug Transition (D-S)	Map
Fan et al. 1984	Glass beads 2520	0.003 0.004 0.006	U_g vs. U_l	Air: 0 - 0.124	Water: 0 - 0.169	Visualization	0.076	Coalesced bubble Dispersed bubble Slug Transition (D-S)	Map
Matsuura and Fan 1984	Glass beads 2590 2520	0.003 0.006	U_g vs. U_l	Air: 0.050 - 0.198	Water: 0.0516 - 0.129	Visualization	0.076	Coalesced bubble Dispersed bubble Slug Transition (D-S)	Map

Table 7.1. Continued.

Author and year	Particles & their density, kg/m ³	Particle diameter, m	Coordinates	Gas and its velocity, m/s	Liquid and its velocity, m/s	Measurement technique	Column diameter, m	Flow regimes identified	Map or correlation
Fan et al. 1985	Nylon beads 1150	0.00250	U_L vs. U_L	Air: 0 - 0.22	Water: 0 - 0.16	Visualization	0.0762	Coalesced bubble Dispersed bubble	Map and correlation
	Activated carbon 1280	0.00174							
	Glass beads 2870	0.00100							
	2520	0.00304							
	2530	0.00399							
	2200 Alumina beads 3690	0.00611 0.00227 0.00550							
Hu et al. 1985	Glass beads 2407	0.001	U_g vs. U_L	Air: 0.022 - 0.068	Water: 0.018 - 0.040	Visualization	0.284	Coalesced bubble Transition (C-D) Dispersed bubble	Map
Fan et al. 1986	Glass beads	0.0010 0.00304 0.00611	U_L vs. U_L or U_g	Air: 0 - 0.22	Water: 0 - 0.16	Visualization (& Pressure fluctuations)	0.102	Coalesced bubble Dispersed bubble Slug	Map
	Nylon beads	0.0025							
	Alumina	0.00227							
	Activated carbon	0.00070							
	Cylindrical Hydrotreating Catalysts (alumina support) $\phi=0.68 - 0.75$ $P_g=1890 - 2000$	$d = 0.00089$ $- 0.00094$ $l = 0.0029 - 0.00518$							
Song et al. 1989			U_g vs. U_L	Air: 0 - 0.08	Water: $\gamma = 72.8 \times 10^{-3}$ N/m 0.5% aqueous t-pentanol solution $\gamma = 58 \times 10^{-3}$ N/m 0.0035 - 0.15	Visualization (Pressure drop)	0.076 0.152	Dispersed small bubble Dispersed large bubble Transition regime Transport regime	Map and correlation
Kitano and Ikeda 1988	Glass beads 2490	0.00129	U_g vs. U_L	Air: 0.0128 - 0.0396 0.0128 - 0.0698 0.0146 - 0.0426 0.0146 - 0.05	Water: 0.0176 - 0.0917 0.0262 - 0.144 0.0172 - 0.106 0.0319 - 0.116	Pressure fluctuations	0.090 and 0.200	Dispersed Transition (D-C) Coalesced	Map
	2480	0.00308							

Table 7.1. Continued.

Author and year	Particles & their density, kg/m ³	Particle diameter, m	Coordinates	Gas and its velocity, m/s	Liquid and its velocity, m/s	Measurement technique	Column diameter, m	Flow regimes identified	Map or correlation
Han and Kim 1990	Glass beads 2500	0.0010 - 0.0080	a vs. U_s $U_s = U_b - \frac{U_t}{\epsilon_t}$	Air: 0.0 - 0.12	Water, Glycerol aqueous solution $\mu_t = 1 - 60 \times 10^{-3}$ Pa.s 0.01 - 0.14	Visualization (Bubble velocity)	0.152	Bubble coalescing Bubble disintegrating Slug	Map
Lee et al. 1990	Glass beads	0.00025	d_p vs. U_t	Air: 0.06	Water 0.0039 - 0.0156	Visualization (Bubble size)	0.200	Fixed bed Transport bed Dispersed bubble regime Coalesced bubble regime	Map
Nacef et al. 1992, 1995	Glass beads 2525 Polypropylene particles $\phi = 0.82, 0.87$ $\rho_s = 1350, 1700$	0.0012 0.0020 0.0030 0.0040 0.0021 0.0031	U_g vs. U_t	Nitrogen 0 - 0.12	Water Water + ethanol Water + sodium chloride Water + n-pentanol Water + t-pentanol $\gamma = 51-72 \times 10^{-3}$ N/m $\mu_t = 0.91 - 1 \times 10^{-3}$ Pa.s 0 - 0.12	Visualization	0.152	Dispersed bubble flow Coalesced bubble flow Solid piston flow	Map
Soria and de Lasa 1992	Glass beads (2500)	0.000250		Air: 0 - 0.05	Water 0 - 0.025	Liquid volume fraction	0.200	Coalesced bubble Dispersed bubble	

7.2 Experimental Results

All experiments were carried out in an 82.6 mm I.D. Plexiglas column as described in Chapter 2 with air and water as the gas and liquid phases. Three types of solid particles were used to study flow regime transitions: 1.5 mm glass beads, 4.5 mm glass beads and 1.2 mm steel shot, with static bed heights of 0.72 m, 0.82 m and 0.74 m, respectively. Superficial gas velocities ranged from 0.0026 to 5.9 m/s, while superficial liquid velocities varied from 0 to 0.6 m/s. Since the liquid temperature was 7 to 8 °C, the liquid density and viscosity were 1000 kg/m³ and 0.0014 Pa.s, respectively. At high gas and/or liquid flow rates, large quantities of particles can be entrained by the gas/liquid flow. Some of the particles are returned to the test section by internal circulation of the liquid within the separator designed in this study, while the rest are stored within the separator. The conductivity probe was mounted at the center of the column, 0.65 m above the distributor. Details of the experimental apparatus, the probe configuration and data processing are provided in Chapter 2.

In a three-phase fluidized bed, bubble characteristics differ from those in a gas-liquid system at the same gas and liquid flow rates due to the particles. The changes are reflected by the raw signals of the conductivity probe. Figure 7.1 compares the raw signals of the two-phase and three-phase systems. It is clear that the bubble frequency in the two-phase system is greater than in the three-phase system, while the bubble chord length is smaller for the same gas and liquid flow rates. The variations of these two parameters with U_g in the two-phase and the three-phase systems at $U_l = 0.0184$ m/s are presented in Figures 7.2 and 7.3. The bubble frequency in the three-phase system is significantly lower than in the two-phase system until after the maximum value representing the transition between slug flow and churn flow is reached. The average bubble chord length in the three-phase system is significantly greater than in the two-phase system for superficial gas velocities less than approximately 1 m/s.

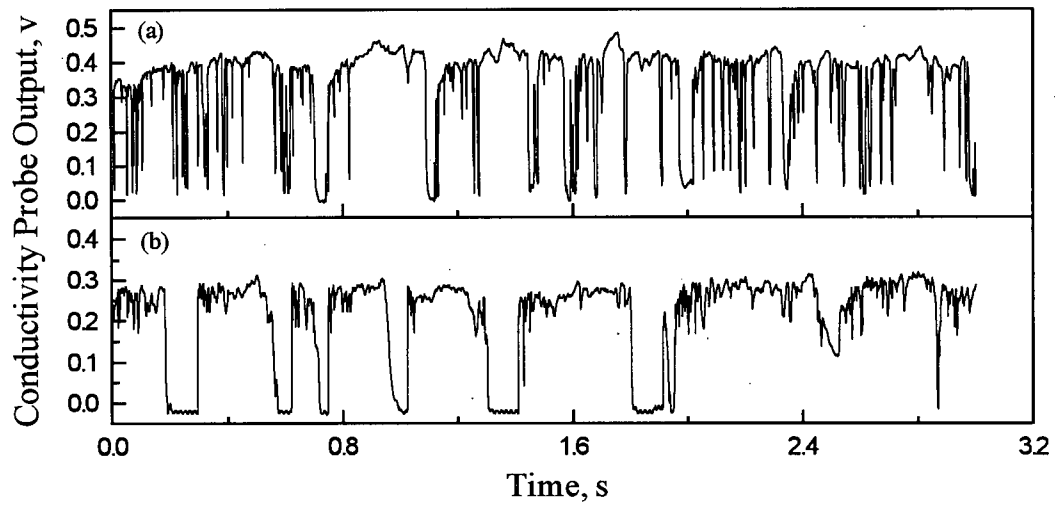


Figure 7.1. Comparison of conductivity probe signals in two-phase and three-phase systems at $Z = 0.65$ m and $U_\ell = 0.0184$ m/s: (a) air-water two-phase, $U_g = 0.040$ m/s; (b) air-water-1.5 mm glass beads three-phase, $U_g = 0.039$ m/s.

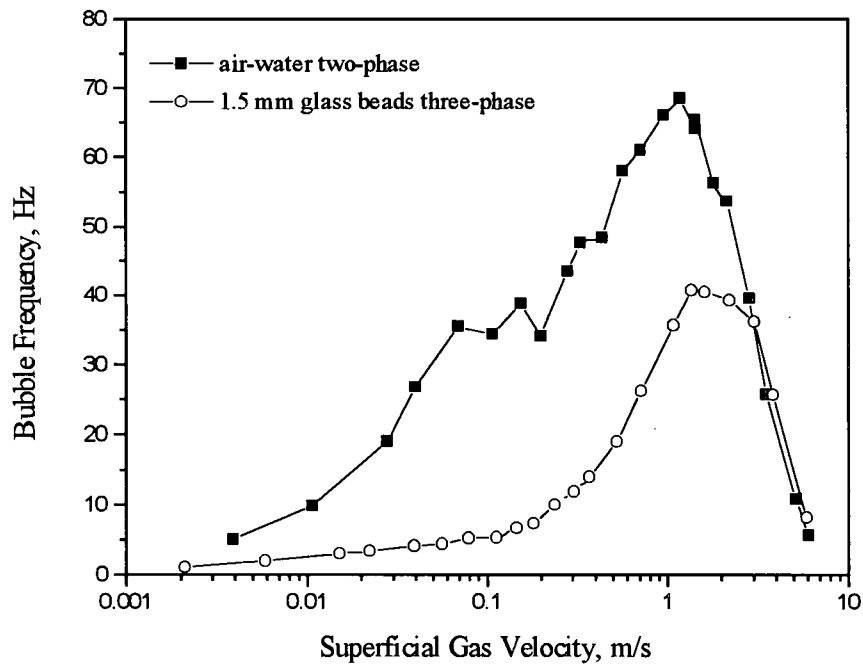


Figure 7.2. Bubble frequency in two-phase and three-phase systems for the same liquid flow rate at $Z = 0.65$ m and $U_\ell = 0.0184$ m/s.

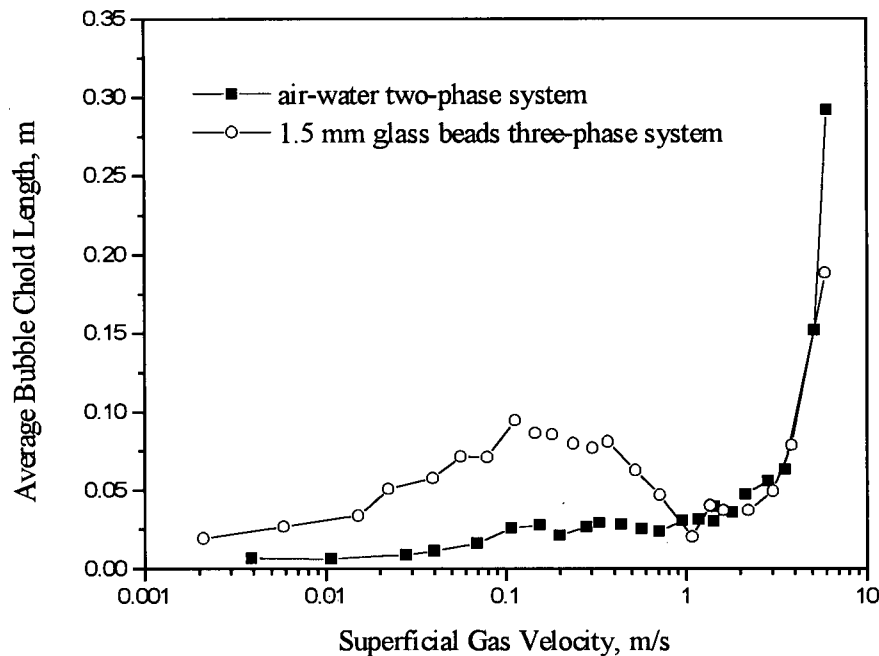


Figure 7.3. Average bubble chord length in two-phase and three-phase systems for the same liquid flow rate at $Z = 0.65$ m and $U_\ell = 0.0184$ m/s.

At $U_\ell = 0.0184$ m/s, three-phase systems with 4.5 mm glass beads and 1.2 mm steel shot operated in the fixed bed regime. Hence Figures 7.2 and 7.3 do not contain data for these systems. Comparisons at a higher liquid velocity for all four systems investigated appear in Figures 7.4 and 7.5 for the bubble frequency and average bubble chord length, respectively. At $U_\ell = 0.0455$ m/s, the bubble frequency in a 1.5 mm glass bead three-phase fluidized bed is always smaller than for the other systems at low to intermediate gas velocities, as shown in Figure 7.4. The average bubble chord length in the 1.5 mm glass bead fluidized bed is greater than for the other systems, as shown in Figure 7.5. This is because small particles lead to coalescence of gas bubbles. The average bubble chord length in the 4.5 mm glass beads and the 1.2 mm steel shot three-phase fluidized beds are almost the same as in the air-water two-phase system at low gas velocities.

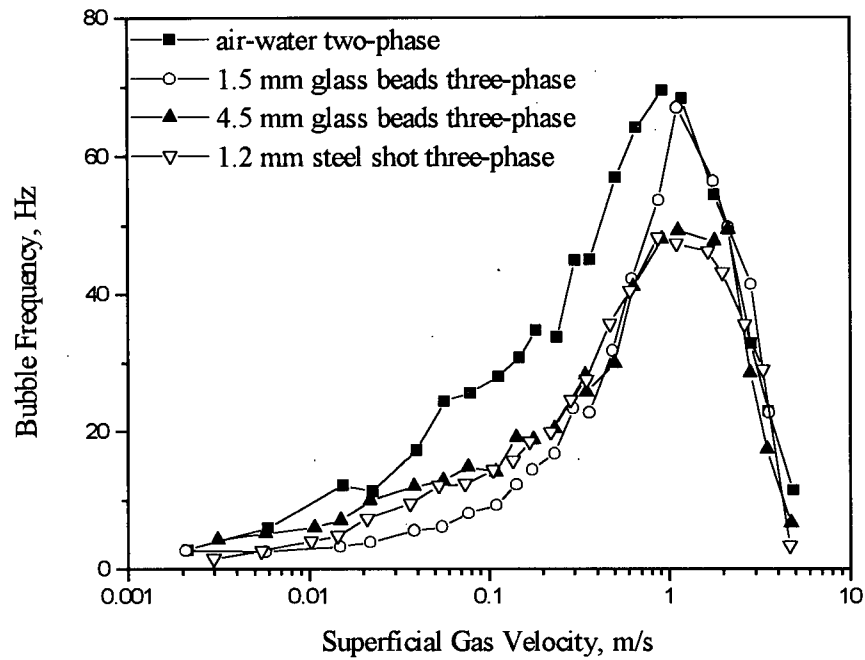


Figure 7.4. Comparison of bubble frequency in different systems at $Z = 0.65$ m and $U_g = 0.0455$ m/s.

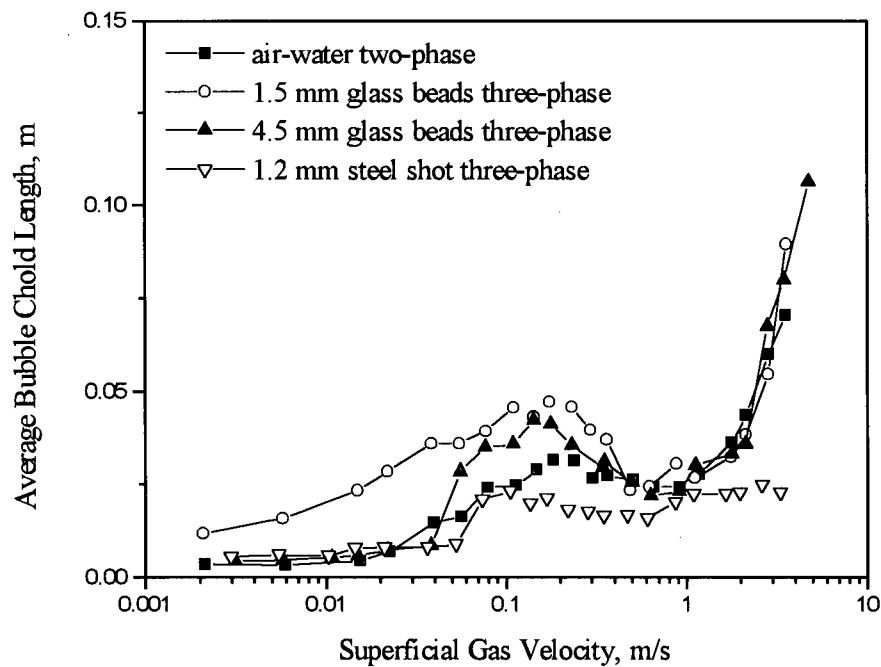


Figure 7.5. Comparison of average bubble chord length in different systems at $Z = 0.65$ m and $U_g = 0.0455$ m/s.

7.3 Flow Regime Transitions

In this study, the experimental criteria for flow regime transitions in three-phase fluidized beds are assumed to be qualitatively the same as those described in Chapter 4 for air-water two-phase flow. A brief summary is given in Figure 7.6.

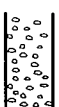

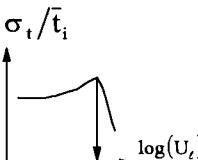
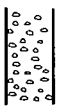

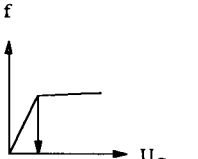
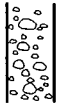

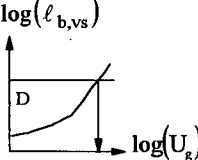
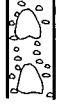

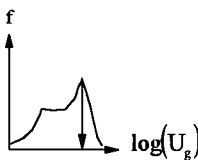


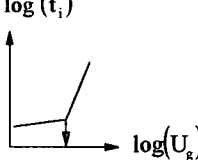


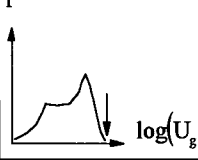
Flow Regime Transition	Criterion	Schematic Diagram
 Discrete Bubble Flow  Dispersed Bubble Flow	Dimensionless standard deviation of bubble time reaches its maximum with respect to liquid velocity.	
 Discrete Bubble Flow  Coalesced Bubble Flow	Bubble frequency deviates from a straight line in a plot of bubble frequency versus gas velocity.	
 Coalesced Bubble Flow  Slug Flow	Sauter mean bubble chord length equals column diameter.	
 Slug Flow  Churn Flow	Bubble frequency reaches its maximum.	
 Churn Flow  Bridging Flow	Average bubble time increases sharply with respect to gas velocity.	
 Bridging Flow  Annular Flow	Bubble frequency approaches zero.	

Figure 7.6. Summary of flow regime transition criteria.

7.3.1 Transition between Discrete (or Dispersed) and Coalesced Bubble Flow

The transition between discrete and coalesced bubble flow regimes was determined from plots of bubble frequency versus superficial gas velocity as shown in Figures 7.7 to 7.10. According to the criterion established in Chapter 4, the transition occurs when the bubble frequency deviates from a straight line through the origin. Figure 7.7 presents experimental results for 1.5 mm glass bead three-phase fluidized beds at different superficial liquid velocities. At superficial liquid velocities of 0.064 to 0.16 m/s, the bubble frequency increases first linearly with gas velocity, with a slope of 545 m^{-1} . When the gas velocity was increased further, coalesced bubble flow or slug flow was encountered and the bubble frequency deviated from the linear line. The transition velocities were determined by the points at which the bubble frequency deviated significantly from the linear line.

At low liquid velocities ($U_\ell = 0.0154$ to 0.0455 m/s), instead of discrete bubble flow, coalesced bubble flow was encountered at very low gas velocities in the 1.5 mm glass bead three-phase fluidized bed due to coalescence. This is in good agreement with visual observations both in this study and in previous investigations (Ermakova et al., 1970; Fan et al., 1986, 1987; Kitano and Ikeda, 1988; Song et al., 1989; Han and Kim, 1990). Therefore, the bubble frequency deviates immediately from $f = 545U_g$ for low liquid velocities, as shown in Figure 7.7.

Figure 7.8 plots bubble frequency against superficial gas velocity for a three-phase fluidized bed containing 4.5 mm glass beads at different superficial liquid velocities. At low gas velocities, discrete bubble flow was encountered and the bubble frequency varies linearly with gas velocity. As the gas velocity was increased, coalesced bubble flow and slug flow were encountered. The flow regime transition velocities were again determined by the points at which the bubble frequency deviates significantly from the initial linear relationship.

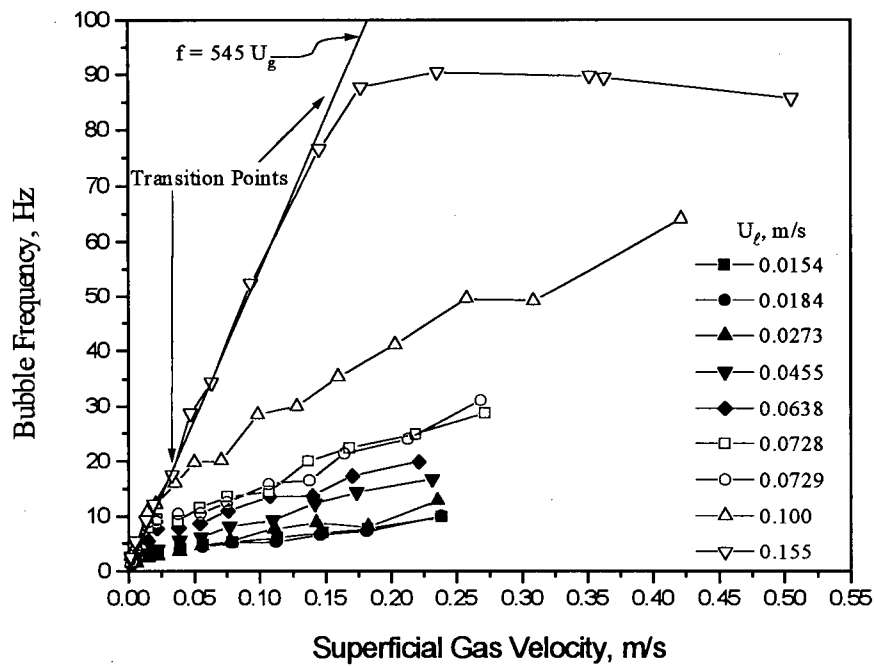


Figure 7.7. Transition between discrete and coalesced bubble flow regime in a three-phase fluidized bed containing 1.5 mm glass beads at different superficial liquid velocities.

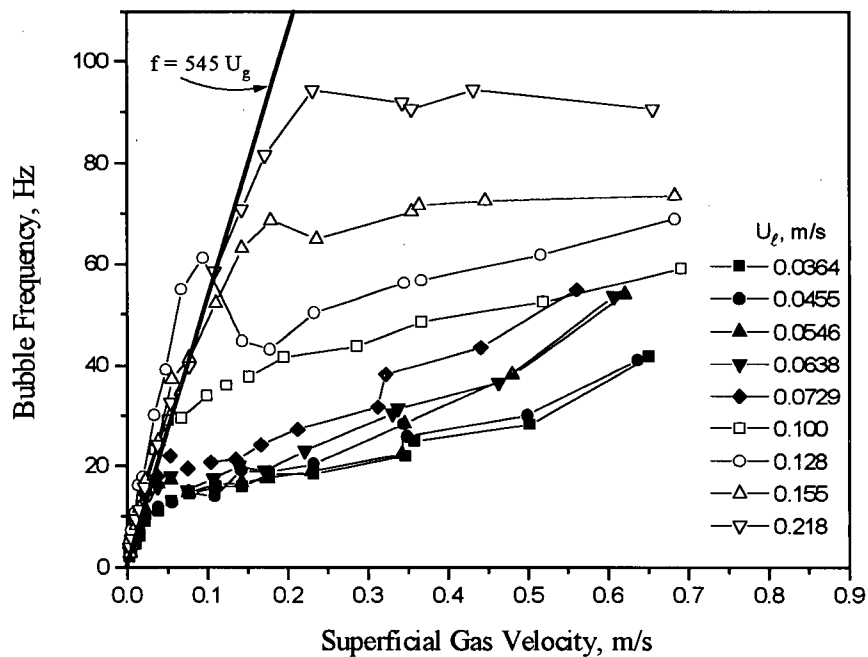


Figure 7.8. Transition between discrete and coalesced bubble flow regime in a three-phase fluidized bed containing 4.5 mm glass bead at different superficial liquid velocities.

The behaviour for the three-phase fluidized bed containing 1.2 mm steel shot was similar, with discrete bubble flow encountered at low U_g . Increasing U_g led to coalesced bubble flow and slug flow. Figures 7.9 and 7.10 show the variation of bubble frequency with U_g for the 1.2 mm steel shot three-phase fluidized bed at different U_ℓ . The relationship between f and U_g is linear at low U_g with a proportionality constant of 545 and 860 m^{-1} , respectively, for low U_ℓ in Figure 7.9 and higher U_ℓ in Figure 7.10. For the steel shot, f in the case of the discrete-coalesced transition spanned a much larger range than for the other systems because of the larger liquid velocities required to expand the bed. The flow regime transition data are given in Tables 7.2, 7.3 and 7.4.

Table 7.2. Flow regime transition velocities for air-water-1.5 mm glass bead fluidized beds.

	Dispersed / Coalesced	Coalesced / Slug	Slug / Churn	Churn / Bridging	Bridging / Annular	Coalesced / Dispersed	
U_ℓ , m/s	U_g , m/s					U_ℓ , m/s	U_g , m/s
0.0051			1.9	3.2	7.6	0.046	0.0025
0.0082			1.6	3.6	7.6	0.046	0.0031
0.0154			1.6	3.0	7.6	0.064	0.005
0.0184		0.016	1.5	3.0	7.4	0.064	0.008
0.0273		0.017	1.4	2.6	6.7	0.064	0.012
0.0455		0.018	1.1	2.1	6.2	0.100	0.02
0.0638	0.010	0.016	0.97	1.7	6.0	0.100	0.03
0.0728	0.016	0.019	1.1	1.75	5.7	0.100	0.05
0.0729	0.016	0.019	1.1	1.75	5.7		
0.100	0.036	0.027	1.0	1.73	5.3		
0.155	0.16	0.14	1.0	1.73	5.1		

Table 7.3. Flow regime transition velocities for air-water-4.5 mm glass bead fluidized bed.

	Discrete / Coalesced	Coalesced / Slug	Slug / Churn	Churn / Bridging	Bridging / annular	Discrete / Dispersed	
U_ℓ , m/s	U_g , m/s					U_ℓ , m/s	U_g , m/s
0.0364	0.020	0.028	1.2	2.1	6.3	0.0729	0.0035
0.0455	0.020	0.031	1.2	2.1	6.1	0.0729	0.0050
0.0546	0.028	0.031	1.1	1.5	6.0	0.0729	0.0080
0.0638	0.028	0.031	1.2	1.6	6.0	0.0729	0.012
0.0729	0.035	0.051	1.0	1.6	6.2	0.100	0.020
0.100	0.050	0.056	1.0	1.5	5.7	0.100	0.030
0.128	0.069	0.078	1.0	1.4	5.5	0.100	0.040
0.155	0.11	0.10	1.0	1.4	6.0		
0.218	0.16	0.23	0.98	1.4	5.0		

Table 7.4. Flow regime transition velocities for air-water-1.2 mm steel shot fluidized bed.

	Discrete / Coalesced	Coalesced / Slug	Slug / Churn	Churn / Bridging	Bridging / annular	Discrete / Dispersed	
U_{ℓ} , m/s	U_g , m/s					U_{ℓ} , m/s	U_g , m/s
0.0364	0.021	0.043	1.4	2.8	5.0	0.0820	0.0035
0.0455	0.027	0.050	1.4	2.8	4.8	0.0860	0.0050
0.0546	0.027	0.059	1.6	2.5	4.8	0.100	0.0080
0.0638	0.027	0.061	1.6	2.2	4.7	0.100	0.012
0.0729	0.025	0.059	1.7	1.8	4.8	0.155	0.020
0.100	0.027	0.052	1.6	1.6	4.6	0.155	0.030
0.155	0.22	0.10	0.77	1.3	4.7	0.155	0.040
0.200	0.51	0.19	0.92	1.2	4.8		
0.311	0.13	0.44	0.62	1.8	4.9		
0.404	0.18	0.32	0.32	1.8	3.9		

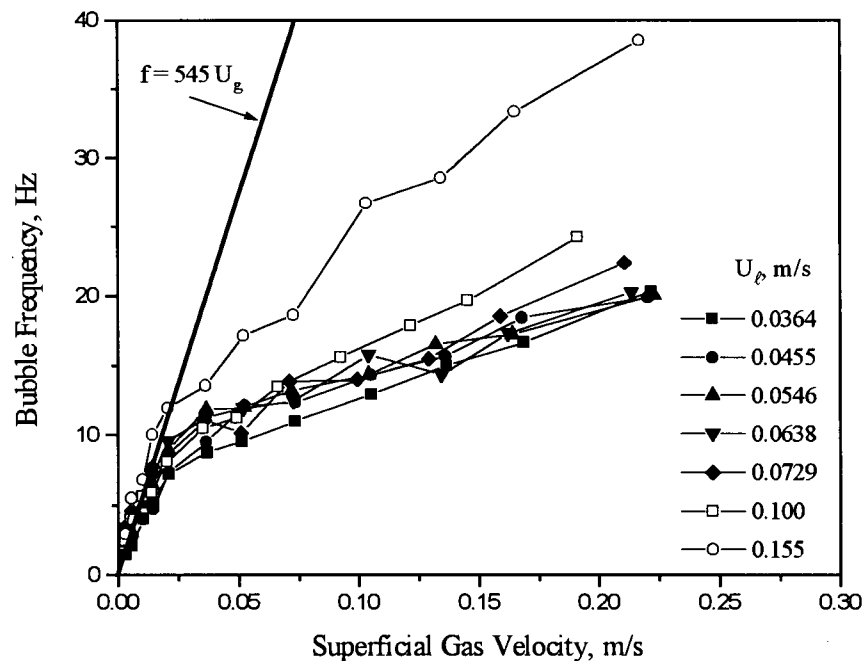


Figure 7.9. Transition between discrete and coalesced bubble flow regimes in a three-phase fluidized bed containing 1.2 mm steel shot at low superficial liquid velocities.

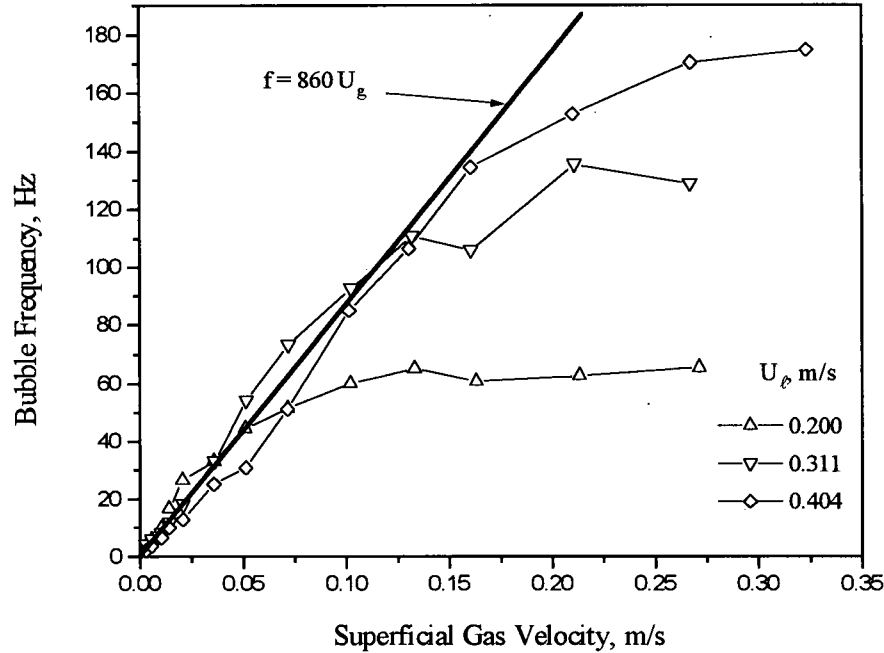


Figure 7.10. Transition between discrete and coalesced bubble flow regimes in a three-phase fluidized bed containing 1.2 mm steel shot at high superficial liquid velocities.

7.3.2 Transition between Coalesced Bubble Flow and Slug Flow

Transitions between the coalesced bubble flow and slug flow regimes were determined from plots of the logarithm of the Sauter mean bubble chord length versus $\log(U_g)$ as shown in Figure 7.6. As described in Chapter 4, the transition occurs when the Sauter mean bubble chord length equals the column diameter, 0.0826 m in this study. Figures 7.11, 7.12 and 7.13 plot the Sauter mean bubble chord length against superficial gas velocity on log-log coordinates at different liquid velocities for three-phase fluidized beds of 1.5 mm glass beads, 4.5 mm glass beads and 1.2 mm steel shot, respectively. The experimental data are summarized in Tables 7.2, 7.3 and 7.4.

The gas velocity for the transition from coalesced bubble flow to slug flow does not vary significantly with respect to the liquid flow rate at low superficial liquid velocities. At higher liquid velocities, however, the transition velocities increase with U_l .

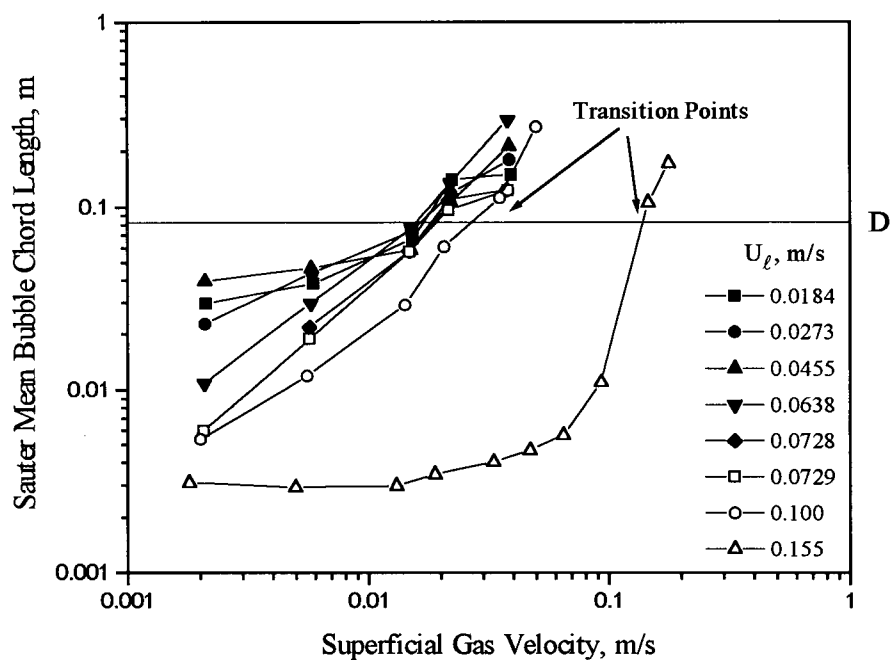


Figure 7.11. Transition between coalesced bubble flow and slug flow in a three-phase fluidized bed containing 1.5 mm glass beads at various superficial liquid velocities.

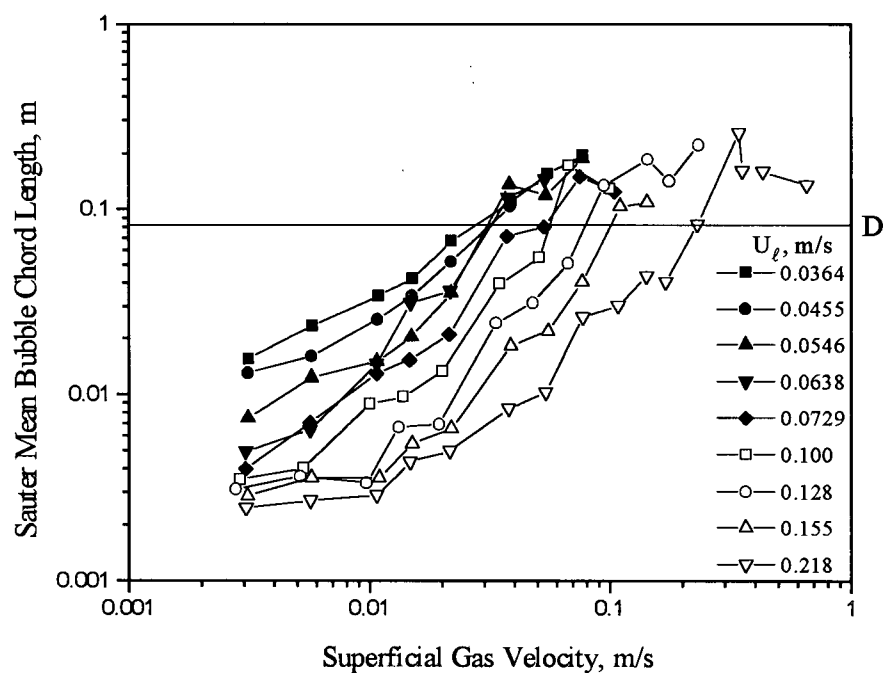


Figure 7.12. Transition between coalesced bubble flow and slug flow in a three-phase fluidized bed containing 4.5 mm glass beads at various superficial liquid velocities.

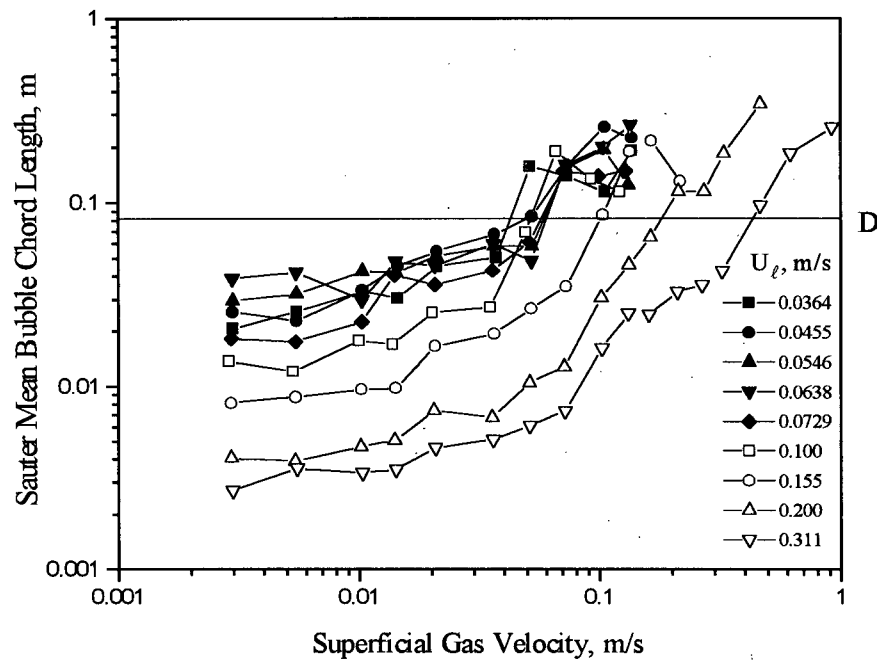


Figure 7.13. Transition between coalesced bubble flow and slug flow in a three-phase fluidized bed containing 1.2 mm steel shot at various superficial liquid velocities.

7.3.3 Transition between Slug Flow and Churn Flow

Transitions between slug flow and churn flow were taken to occur at the points at which the bubble frequency reaches a maximum with increasing U_g , as shown in Figures 7.14 to 7.16 for three-phase fluidized beds of 1.5 mm glass beads, 4.5 mm glass beads and 1.2 mm steel shot, respectively. It should be noted that under certain circumstances, two maximum bubble frequency values appear in the same curve, e.g. for $U_\ell = 0.155$ m/s in Figure 7.14 and for $U_\ell = 0.128$ m/s in Figure 7.15. The first maximum in both curves corresponds to the transition between dispersed and coalesced bubble flow or slug flow, while the second maximum was used to delineate the transition between the slug and churn flow regimes.

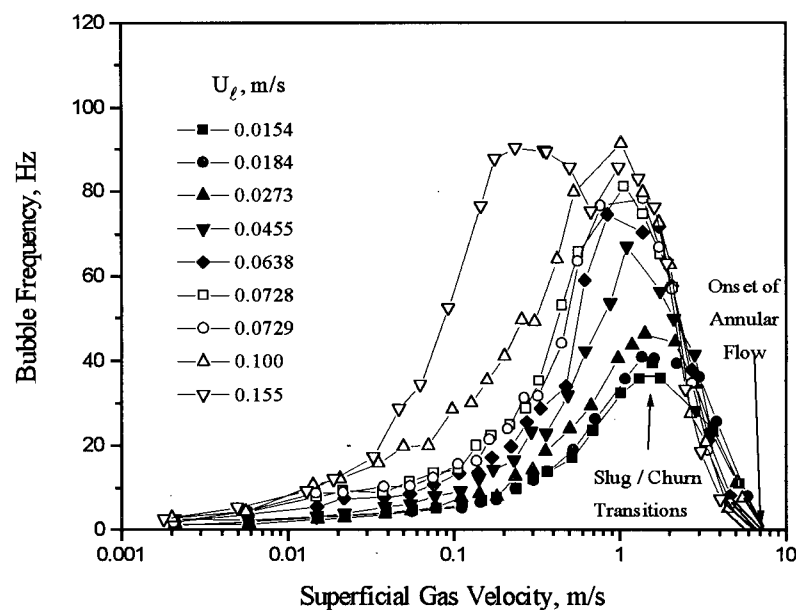


Figure 7.14. Local bubble frequency at axis of column versus superficial gas velocity showing transition between slug flow and churn flow and the onset of annular flow for three-phase fluidized bed containing 1.5 mm glass beads at different superficial liquid velocities.

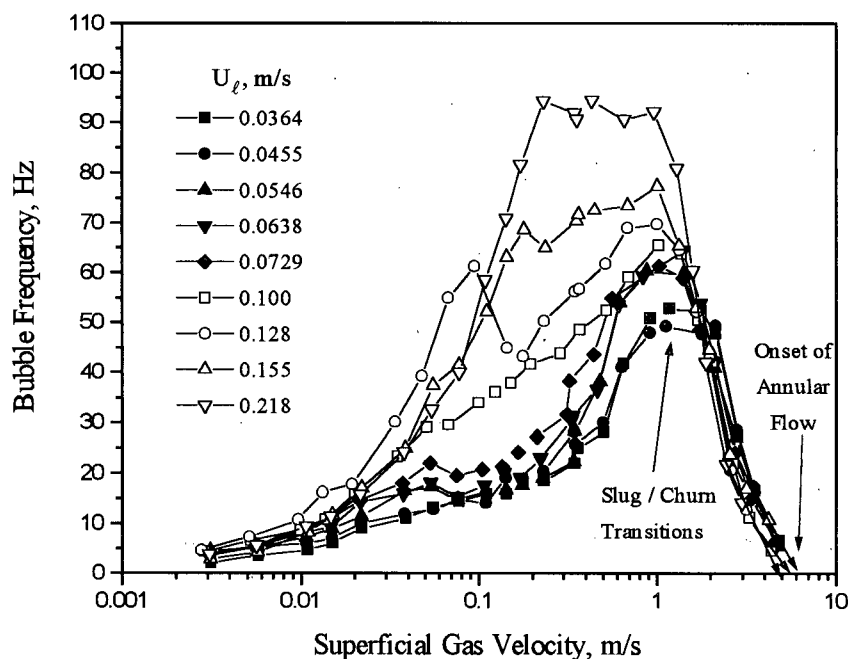


Figure 7.15. Local bubble frequency at axis of column versus superficial gas velocity showing transition between slug flow and churn flow and onset of annular flow for three-phase fluidized bed containing 4.5 mm glass beads at different superficial liquid velocities.

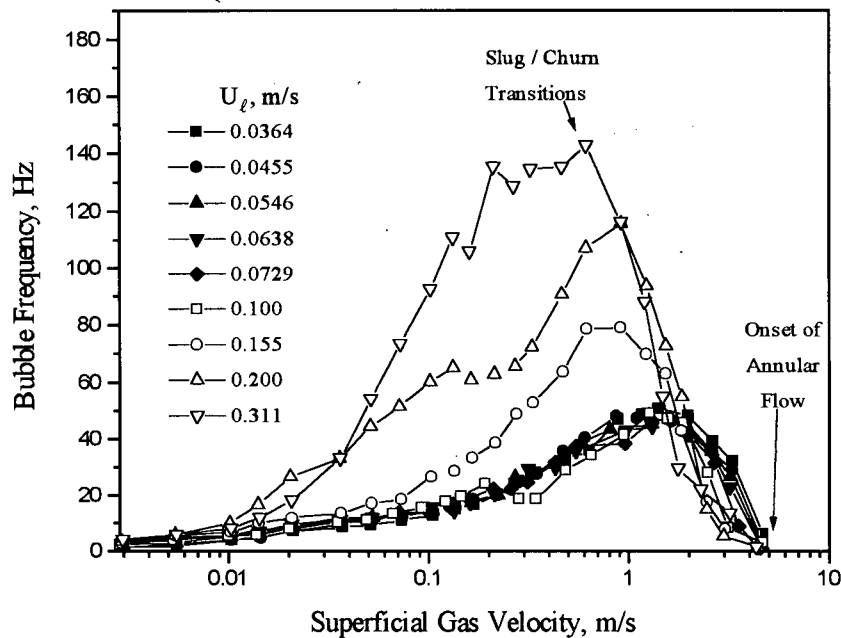


Figure 7.16. Plot of local bubble frequency at axis of column versus superficial gas velocity showing transition between slug flow and churn flow and the onset of annular flow for three-phase fluidized bed containing the 1.2 mm steel shot at different superficial liquid velocities.

7.3.4 Transition between Churn Flow and Bridging Flow

Transitions between churn flow and bridging flow were determined from the points where the average bubble time increases sharply with gas velocity on log-log plots, as shown in Figures 7.17 to 7.19. Figure 7.17 presents the average bubble time vs. superficial gas velocity for a three-phase fluidized bed of 1.5 mm glass beads, while Figures 7.18 and 7.19 are for 4.5 mm glass beads and 1.2 mm steel shot, respectively.

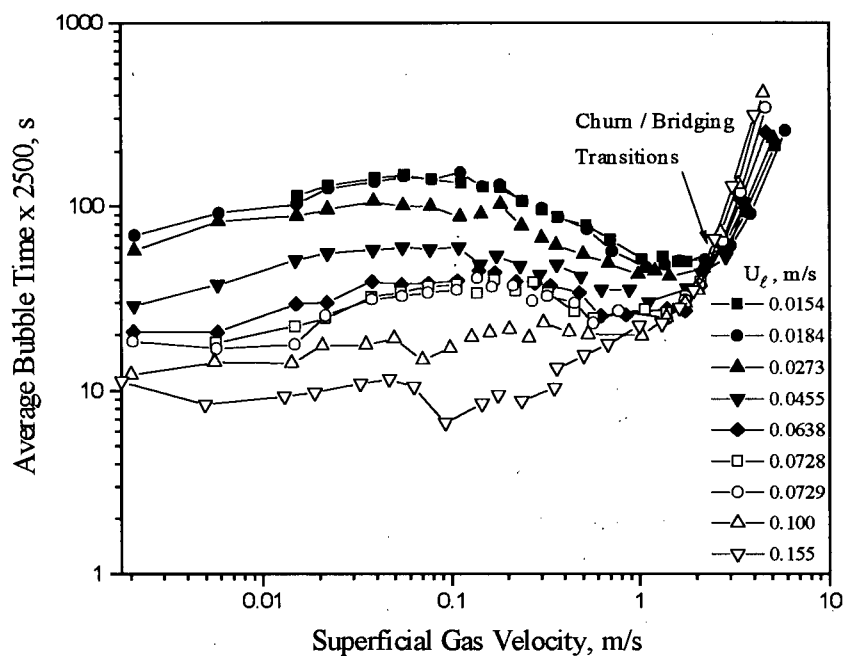


Figure 7.17. Average bubble time versus superficial gas velocity showing transition between churn flow and bridging flow for a three-phase fluidized bed containing 1.5 mm glass beads at different superficial liquid velocities.

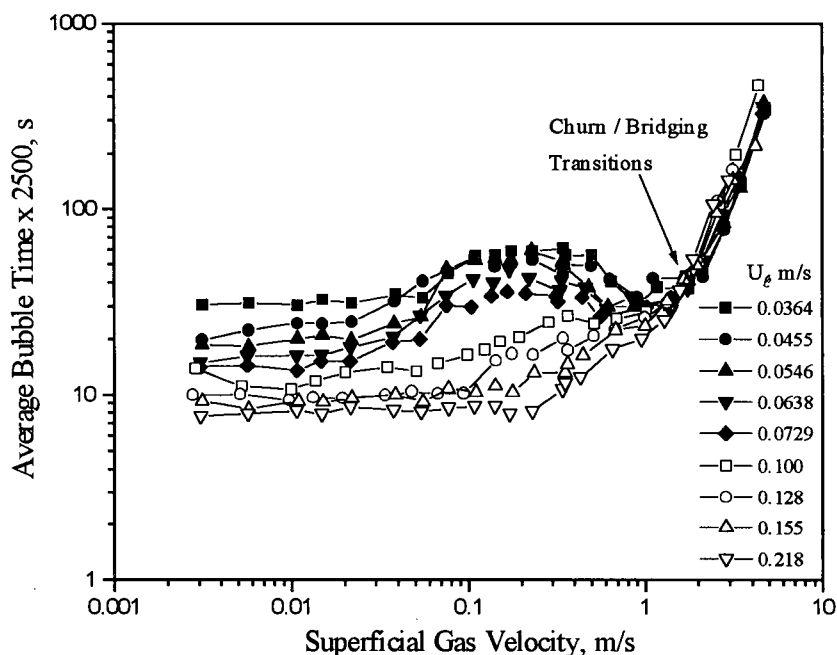


Figure 7.18. Average bubble time versus superficial gas velocity showing transition between churn flow and bridging flow for a three-phase fluidized bed containing 4.5 mm glass beads at different superficial liquid velocities.

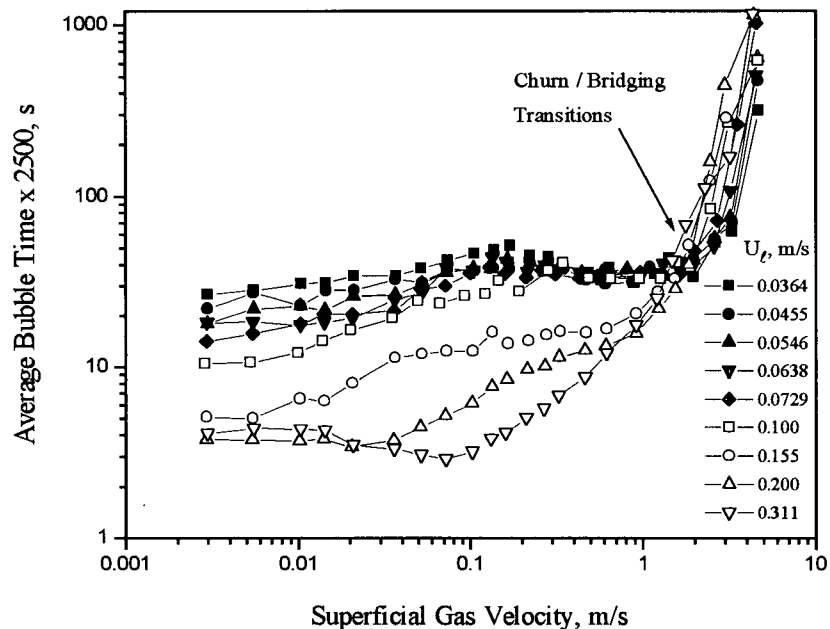


Figure 7.19. Average bubble time versus superficial gas velocity showing transition between churn flow and bridging flow for a three-phase fluidized bed containing 1.2 mm steel shot at different superficial liquid velocities.

7.3.5 Transition between Bridging Flow and Annular Flow

The onset of annular flow was determined from the point when the bubble frequency approaches zero in a plot of bubble frequency vs. superficial gas velocity, as described in Chapter 4. Figures 7.14, 7.15 and 7.16 present the experimental results for three-phase fluidized beds of 1.5 mm glass beads, 4.5 mm glass beads and 1.2 mm steel shot, respectively. The transition velocities are also summarized in Tables 7.2, 7.3 and 7.4.

7.3.6 Transition between Discrete (or Coalesced) and Dispersed Bubble Flow

At low gas and liquid velocities, coalesced bubble flow was encountered for the 1.5 mm glass bead three-phase fluidized beds, while there was discrete bubble flow for both the 4.5 mm

glass bead and 1.2 mm steel shot three-phase fluidized beds. With increasing liquid velocity, dispersed bubble flow was encountered for all these systems. The transition between the discrete (or coalesced) and dispersed bubble flow regimes was obtained by plotting the dimensionless standard deviation of bubble time vs. superficial liquid velocity at constant gas velocities. The transition occurs when the dimensionless standard deviation of bubble time, σ_t/\bar{t} , reaches a maximum with increasing liquid velocity.

Figure 7.20 shows the transition between coalesced and dispersed bubble flow for 1.5 mm glass bead three-phase fluidized beds. An obvious maximum value of σ_t/\bar{t} appears for each gas velocity, indicating the flow regime transitions. Figure 7.21 presents the same type of plot for the 4.5 mm glass beads. It is seen that at low gas and liquid velocities, σ_t/\bar{t} does not vary significantly with U_L . On further increasing the liquid velocity, σ_t/\bar{t} decreases without showing a peak as observed in the air-water two-phase and 1.5 mm glass bead three-phase systems. The reason could be the breakup effect of large particles on the gas bubbles as reported by previous studies (Ostergaard, 1971; Lee et al., 1974; Fan, 1989). Hence, the bubble characteristics in the discrete bubble flow do not significantly differ from those in the dispersed bubble flow, making it difficult to distinguish between these flow regimes for the 4.5 mm glass bead three-phase fluidized bed. For these curves, the transition velocities were determined by the points at which σ_t/\bar{t} starts to decrease in the plot of σ_t/\bar{t} vs. liquid velocity.

The transition between the discrete and dispersed bubble flow for the 1.2 mm steel shot three-phase fluidized bed is presented in Figure 7.22. A maximum value of σ_t/\bar{t} can be found for each curve. The flow regime transition velocities for 1.5 mm glass beads, 4.5 mm glass beads and 1.2 mm steel shot three-phase fluidized beds are summarized in Tables 7.2, 7.3 and 7.4, respectively.

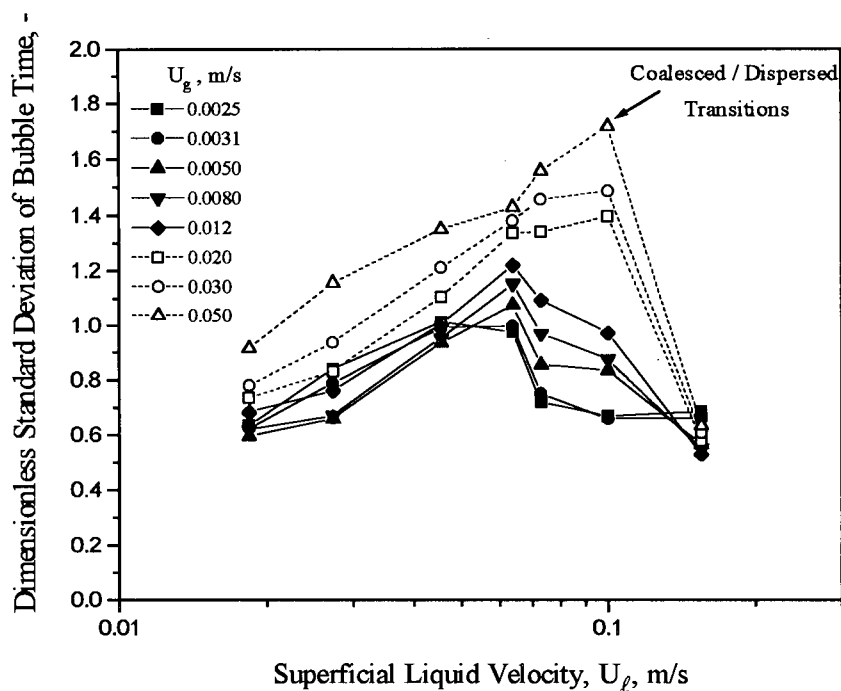


Figure 7.20. Dimensionless standard deviation of bubble time plotted against superficial liquid velocity showing transition between coalesced bubble flow and dispersed bubble flow for the 1.5 mm glass bead three-phase fluidized bed at different superficial gas velocities.

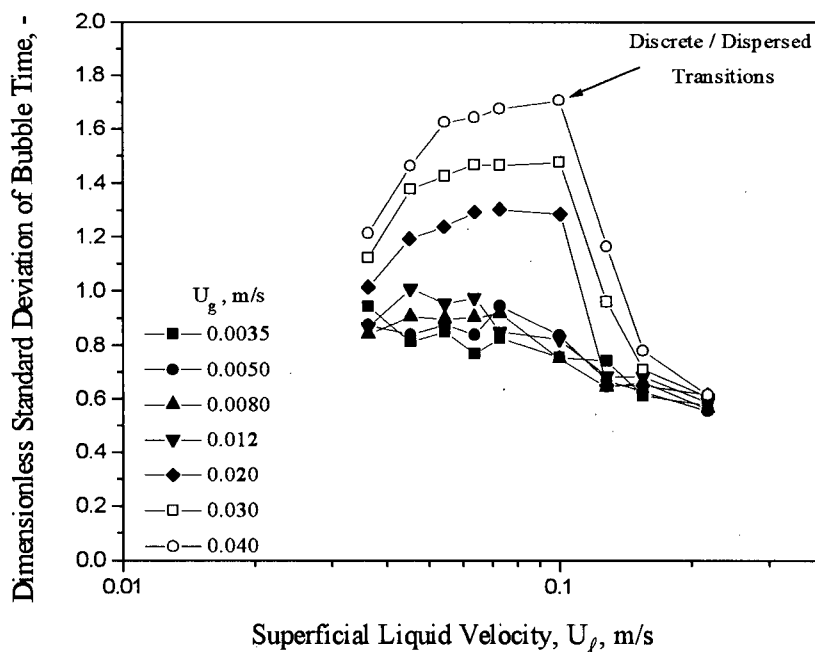


Figure 7.21. Dimensionless standard deviation of bubble time plotted against superficial liquid velocity showing transition between discrete bubble flow and dispersed bubble flow for the 4.5 mm glass bead three-phase fluidized bed at different superficial gas velocities.

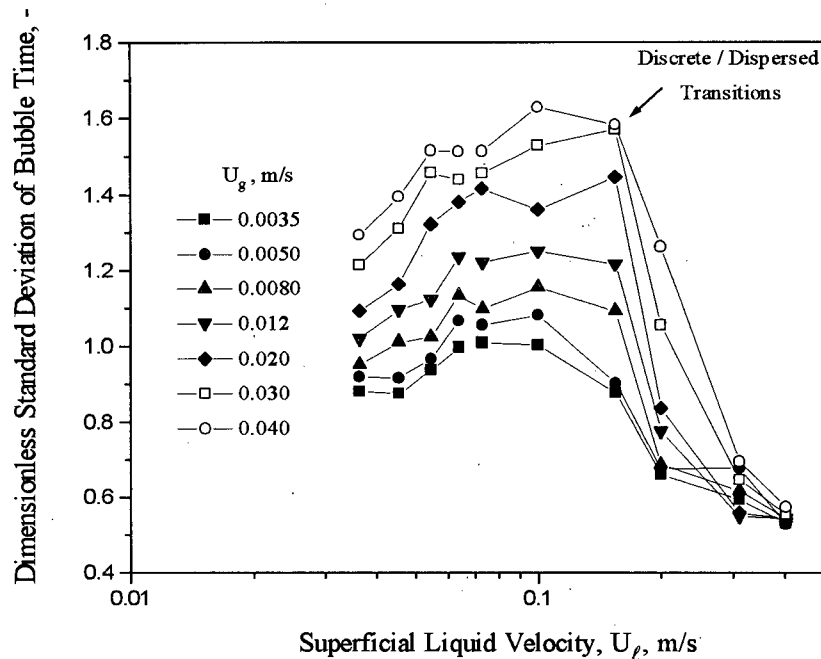


Figure 7.22. Dimensionless standard deviation of bubble time plotted against superficial liquid velocity showing transition between discrete bubble flow and dispersed bubble flow for the 1.2 mm steel shot three-phase fluidized bed at different superficial gas velocities.

7.4 Flow Regime Maps

7.4.1 Flow Regime Map for 1.5 mm Glass Bead Fluidized Bed

A flow regime map for 1.5 mm glass bead three-phase fluidized bed is presented in Figure 7.23. Note that the discrete bubble flow regime does not exist due to the effect of the relatively small particles on bubbles. It has been found (Darton, 1985; Henriksen and Ostergaard, 1974) that bubble coalescence is more intensive in air-water systems containing glass beads of diameter less than 2.5 mm, compared to a corresponding gas-liquid system, since small particles increase both the apparent continuous phase viscosity and density. Figure 7.23 indicates that a dispersed bubble flow regime exists at high liquid velocities. This is because the solids holdup of the three-phase fluidized bed decreases towards zero as the liquid velocity is increased, and the system approaches the corresponding gas-liquid two-phase limit.

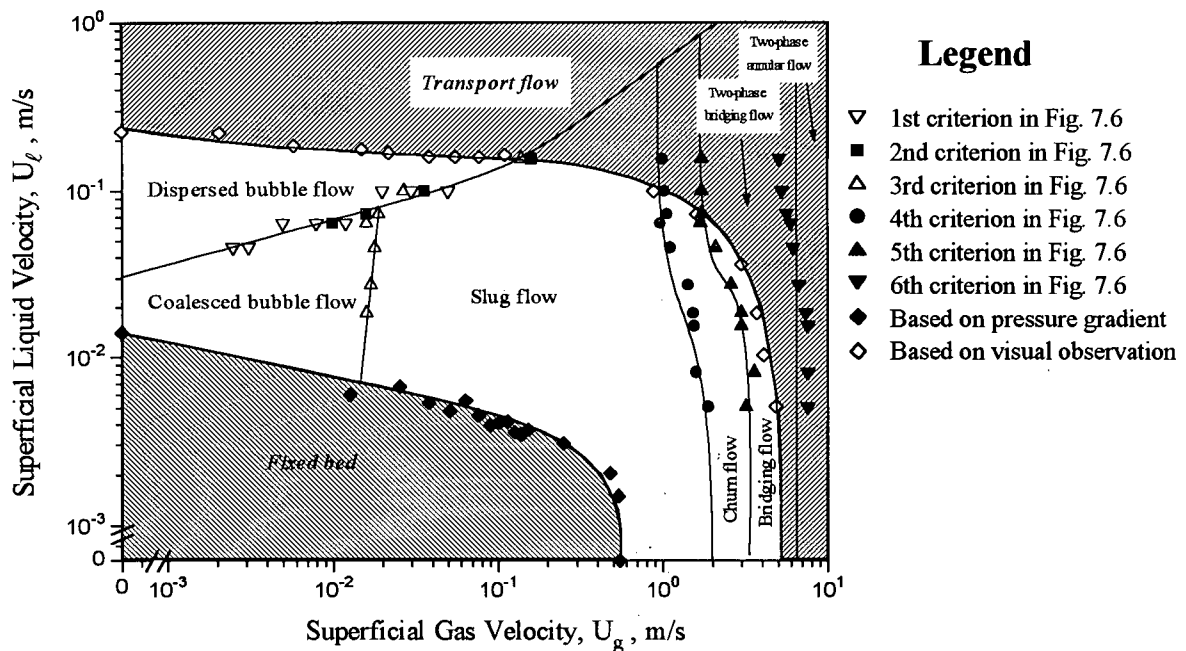


Figure 7.23. Flow regime map for air-water-1.5 mm glass bead three-phase fluidized bed with $D = 0.0826$ m and $Z = 0.65$ m. Distributor: perforated plate containing 62 2-mm circular holes.

7.4.2 Flow Regime Map for 4.5 mm Glass Bead Fluidized Bed

Figure 7.24 presents a flow regime map for the 4.5 mm glass bead three-phase fluidized bed. A discrete bubble flow regime is observed, and the domain of the coalesced bubble flow regime is decreased. This feature is due to the large particles that break up bubbles. It has been found (Ostergaard, 1971; Lee et al., 1974) that dispersed bubbles of uniform small size occur for glass beads of diameters greater than 2.5 mm in air-water systems. Findings of the present study are in good agreement with previous investigations. The coalesced bubble flow regime exists at $U_g = 0.02$ to 0.04 m/s and $U_l = 0.02$ to 0.05 m/s. In this regime, the gas passes through the liquid-solid mixture as bubbles of irregular shape and large size at low liquid velocities. This differs from what is observed in the 1.5 mm glass bead system, where bubble shapes are either spherical or spherical-cap in the coalesced bubble flow regime.

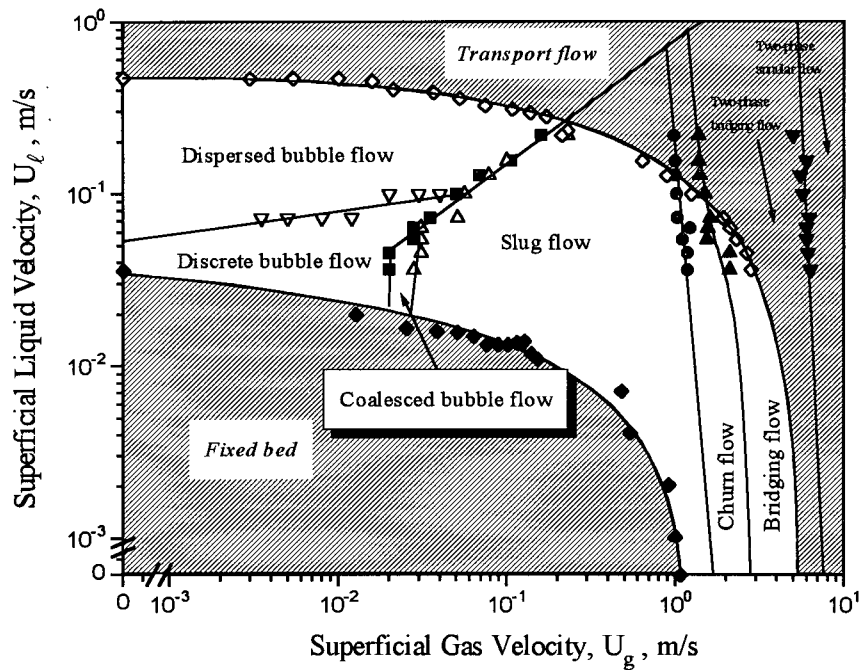


Figure 7.24. Flow regime map for air-water-4.5 mm glass bead three-phase fluidized bed with $D = 0.0826$ m and $Z = 0.65$ m. Distributor: perforated plate containing 62 2-mm circular holes.

7.4.3 Flow Regime Map for 1.2 mm Steel Shot Fluidized Bed

Figure 7.25 shows the flow regime map for the 1.2 mm steel shot three-phase fluidized bed system. Both the discrete bubble flow and coalesced bubble flow regimes are present. Since the density of the steel shot, 7800 kg/m^3 , is much greater than that of glass beads, the particles are able to penetrate and break bubbles at lower gas and liquid superficial velocities, causing the fluidized bed to operate in the discrete bubble flow regime. As the gas velocity is further increased at low liquid velocities, coalesced bubble flow is encountered. At high liquid velocities, coalesced bubble flow is also found between dispersed bubble flow and slug flow, which appears at relatively high gas velocities. This may be related to the solids holdup. Since the particle density is larger than that of the glass beads, the solids holdup in the dispersed bubble flow regime is expected to be higher for the same operating conditions. The higher apparent continuous phase

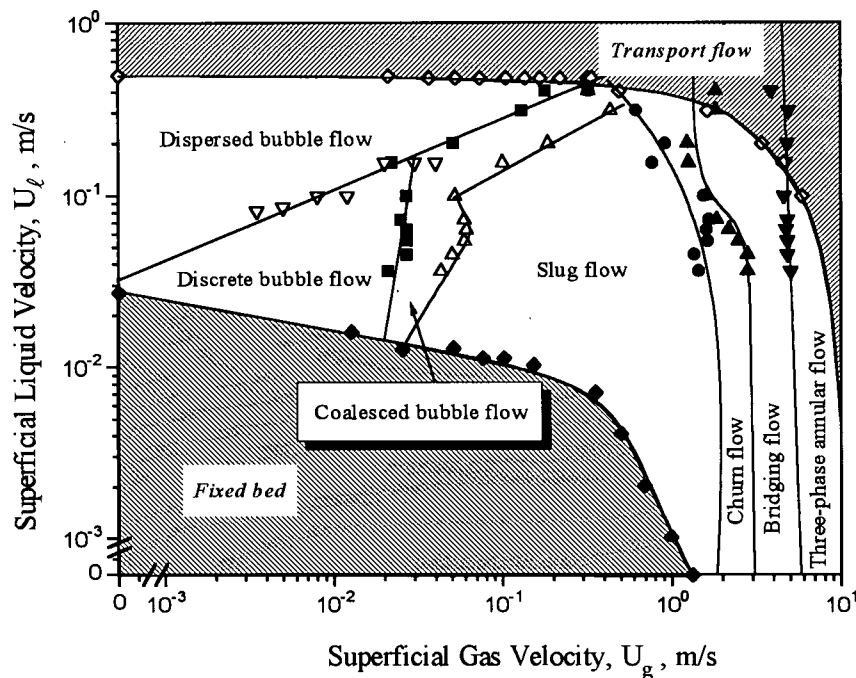


Figure 7.25. Flow regime map for air-water-1.2 mm steel shot three-phase fluidized bed with $D = 0.0826$ m and $Z = 0.65$ m. Distributor: perforated plate containing 62 2-mm circular holes.

density and viscosity cause gas bubbles to coalesce and form Taylor bubbles at relatively high gas velocities.

Churn flow, bridging flow and annular flow are also observed in three-phase fluidized beds at high gas velocities. Since the glass beads are already entrained from the column before the transition from bridging to annular flow occurs, the boundaries between the bridging and the annular flow regimes in Figures 7.23 and 7.24 are similar to those for the corresponding gas-liquid two-phase system. On the other hand, for the 1.2 mm steel shot three-phase system, three-phase annular flow is observed. In this regime, particles are observed in the annular region, which contains liquid film and some small gas bubbles ($d_b = 2$ to 4 mm).

7.4.4 Comparison and Discussion

Figure 7.26 presents the onset velocities for dispersed bubble flow for the two-phase and three-phase systems. For the 4.5 mm glass beads and the 1.2 mm steel shot at low gas velocities, the transition liquid velocities from discrete to dispersed bubble flow are greater than for the corresponding two-phase system. A similar situation exists at higher gas velocities for the transition from slug flow (or coalesced bubble flow) to dispersed bubble flow. For the 1.5 mm glass beads, coalesced bubble flow is encountered at low gas velocities instead of the discrete bubble flow observed for other systems. For these particles, the transition liquid velocity increases with gas velocity and approaches the value for two-phase systems at high gas flow rate due to the low concentration of solids. By comparing the 1.5 mm glass bead system with the 4.5 mm glass bead system, it can be seen that the onset liquid velocity for dispersed bubble flow increases with particle size at low gas velocities. No clear influence of particle size is observed at the higher gas velocities. However, there is a clear effect of particle density when one compares the 1.5 mm

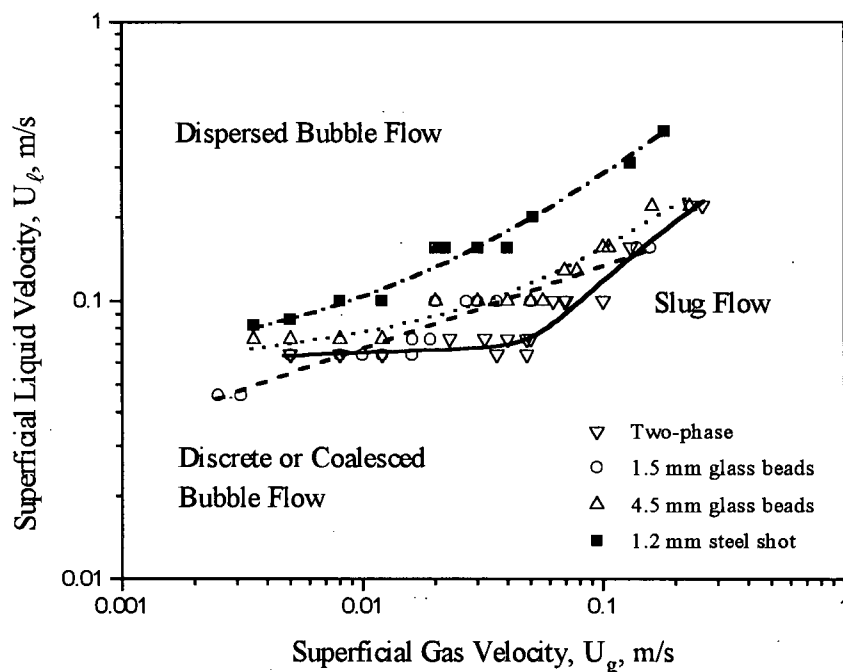


Figure 7.26. Boundaries between various bubble flow regimes.

glass beads with the 1.2 mm steel shot in Figure 7.26.

An empirical correlation, Equation (7.3), is proposed to predict the transition liquid velocity for the onset of the dispersed bubble flow regime:

$$\frac{U_g}{U_\ell} = 0.721 \times Fr_g^{0.339} Ar_\ell^{0.0746} \left(\frac{\rho_s}{\rho_\ell} \right)^{-0.667} \quad (7.3)$$

Values of U_ℓ from Equation (7.3) are plotted against the experimental data in Figure 7.27. The average absolute percentage deviation, calculated by Equation (6.57), is 8.0% for 44 sets of experimental results.

Many investigators have studied the transition between the coalesced bubble flow and dispersed bubble flow regimes. Different particle sizes and densities were used in their investigation, making directly comparison between each other difficult. Hence, Equation (7.3) is used to predict the transition liquid velocity for the onset of the dispersed bubble flow regime.

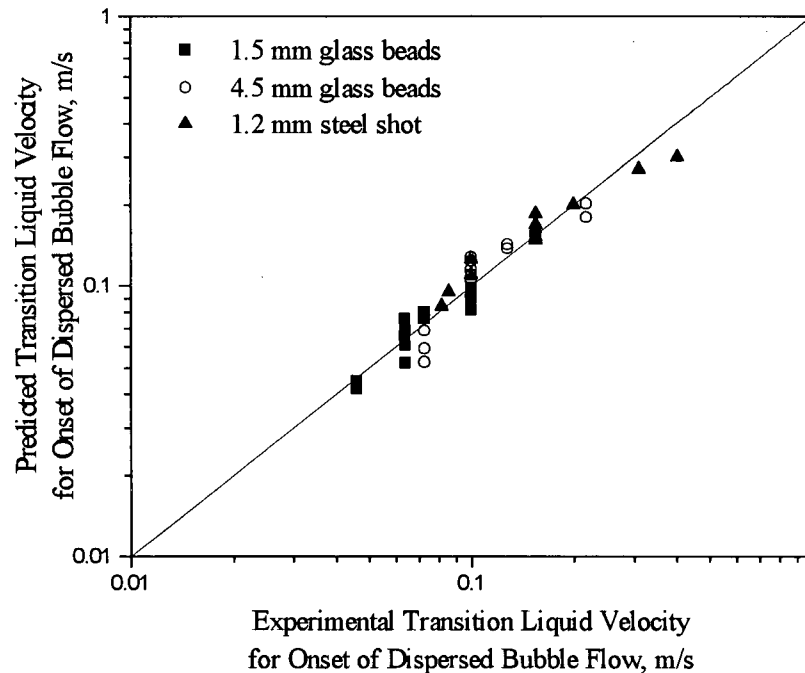


Figure 7.27. Comparison between predictions of Equation (7.3) and experimental results.

Figure 7.28 plots the predicted results versus their experimental data. The prediction goes through the middle for 102 sets of data from literature, but there is considerable scatter, with an average absolute percentage deviation of 70.3% between the predicted and experimental values. The worst prediction (open square and circles) come from the data of Fan et al. (1985, 1986), in which the authors argued that the transition liquid velocity for the onset of dispersed bubble flow is only a function of particle settling velocity and independent of the superficial gas velocity.

Figure 7.29 shows the onset of the slug flow regime for all four systems. At low liquid velocities, the onset gas velocity increases with both particle size and density in the three-phase systems. At high liquid velocities, the onset of the slug flow regime does not differ significantly for the systems tested. For low superficial liquid velocity, when

$$U_{\ell} \leq 8.82 \left(\frac{\rho_{\ell} d_p}{\mu_{\ell}} \right)^{-0.376} (g D)^{0.312} Ar_{\ell}^{0.419} \left(\frac{D}{d_p} \right)^{0.744} \quad (\text{SI units}) \quad (7.4)$$

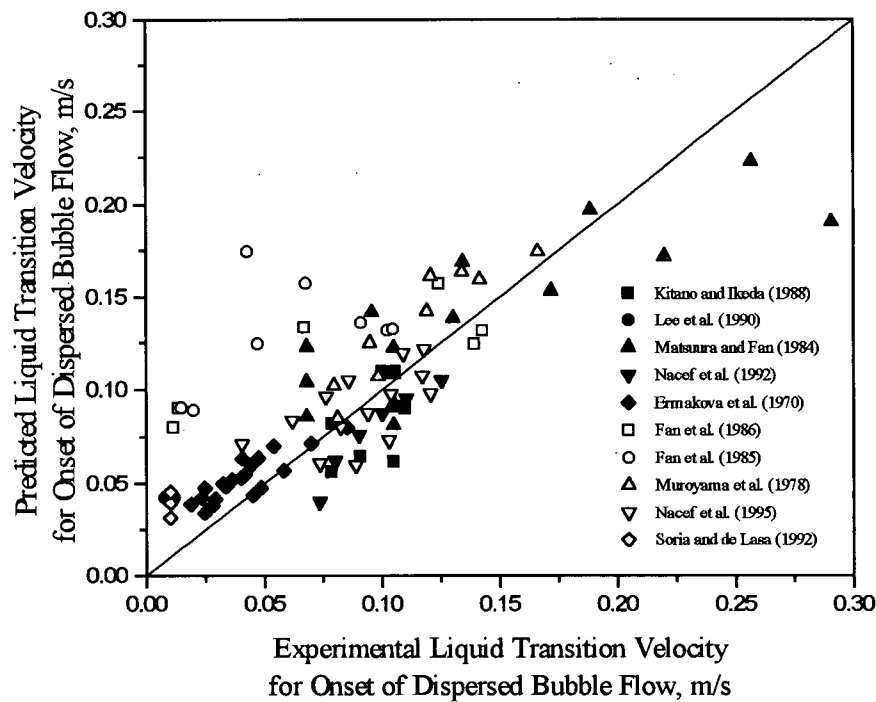


Figure 7.28. Comparison between predictions of Equation (7.3) and experimental data from literature.

the transition gas velocity for the onset of slug flow can be predicted by:

$$\frac{U_g}{U_\ell} = 6.97 \times 10^{-5} \text{Re}_\ell^{-0.918} \text{Ar}_\ell^{0.805} \left(\frac{D}{d_p} \right)^{1.01} \quad (7.5)$$

For high superficial liquid velocity, when U_ℓ is greater than the right-hand term of Equation (7.4), the transition gas velocity for the onset of slug flow can be predicted by:

$$\frac{U_g}{U_\ell} = 20.3 \times \text{Fr}_{gD}^{0.302} \text{Ar}_\ell^{-0.0861} \left(\frac{D}{d_p} \right)^{-0.318} \quad (7.6)$$

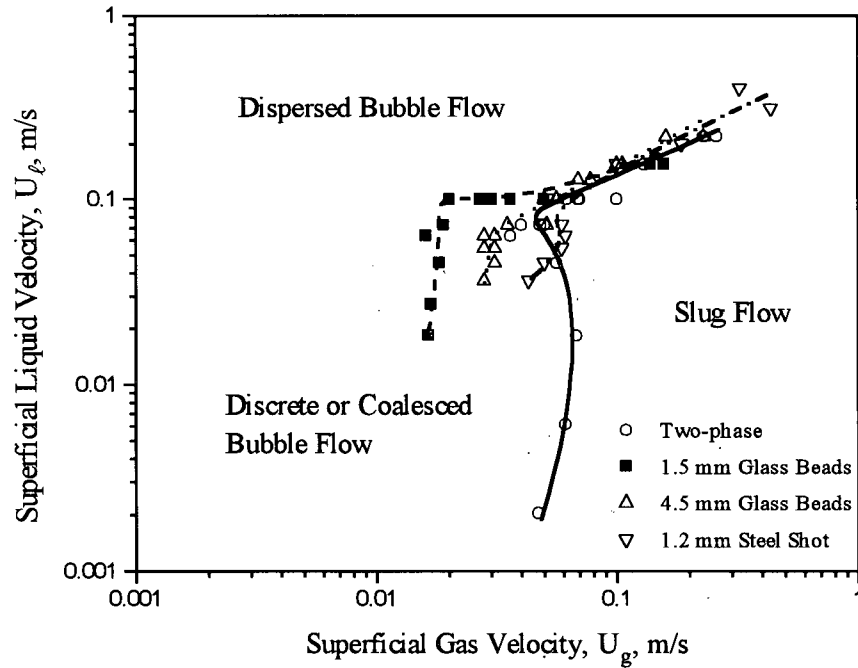


Figure 7.29. Boundaries for onset of slug flow regime.

Comparisons between the experimental data and the predictions of Equations (7.5) and (7.6) are presented in Figures 7.30 and 7.31, respectively. The average absolute percentage deviation between Equation (7.5) and the experimental data of the present study is 6.7%, based on 20 sets of data. For the 8 sets of available literature data obtained by visualization, the predicted transition gas velocity is overestimated with a mean deviation of 52.3%. The deviation between Equation (7.6) and the experimental data of the present study is 12.4%, based on 19 sets of data. For 14 sets of data from the literature, the mean deviation is 22.3%.

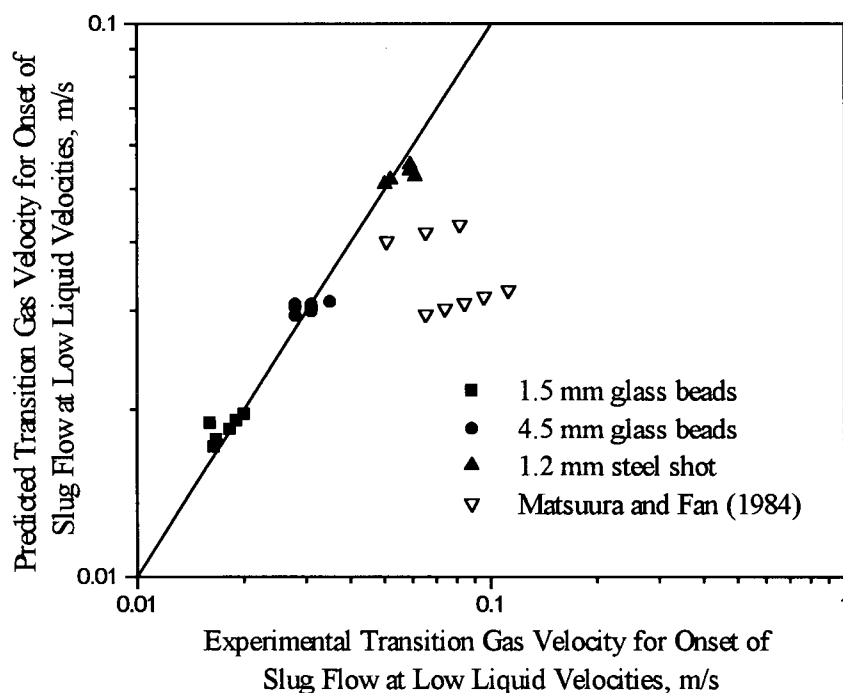


Figure 7.30. Comparison between predictions of Equation (7.5) and experimental data.

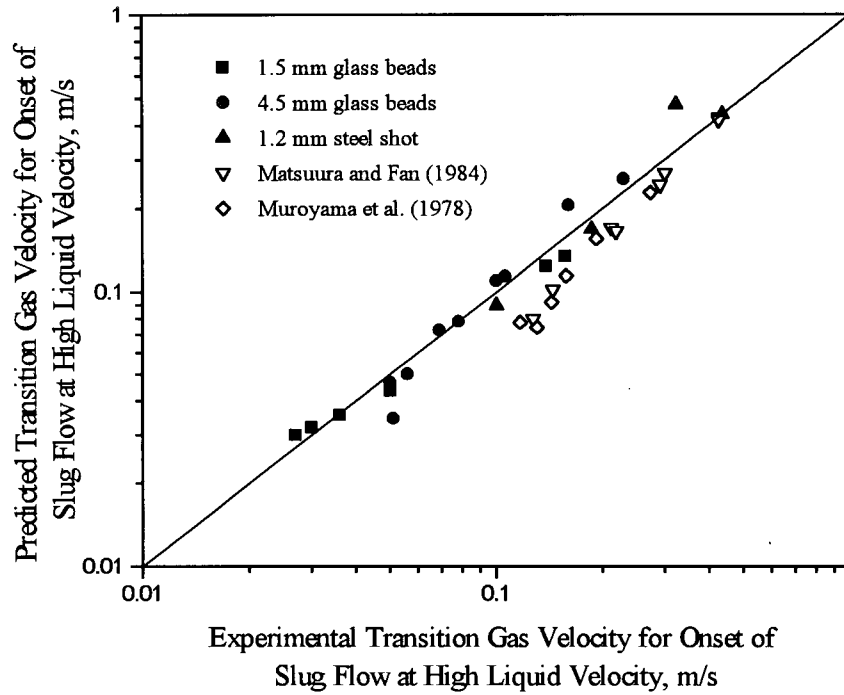


Figure 7.31. Comparison between predictions of Equation (7.6) and experimental data.

Figure 7.32 presents the boundaries between the slug flow and churn flow regimes for all four systems. It is seen that the particles affect this transition only slightly. The presence of the smaller glass beads results in an increase of the transition gas velocity at low liquid velocities, but does not significantly affect this transition at higher liquid velocities where there is a low solids concentration. The dense particles in most cases lead to higher transition gas velocities at given liquid velocities. Equation (7.7) below can be used to predict the boundary between the slug and churn flow regimes. This correlation is based on 30 sets of data for three-phase systems of the present study with an average absolute percentage deviation of 14.3%. No reports are available for the slug/churn flow transition in three-phase systems, so that only the data of the present study are plotted in Figure 7.33.

$$\frac{U_g}{U_\ell} = 53.4 \times \text{Re}_\ell^{-1.30} \text{Ar}_\ell^{0.468} \left(\frac{\rho_s}{\rho_\ell} \right)^{-0.454} \quad (7.7)$$

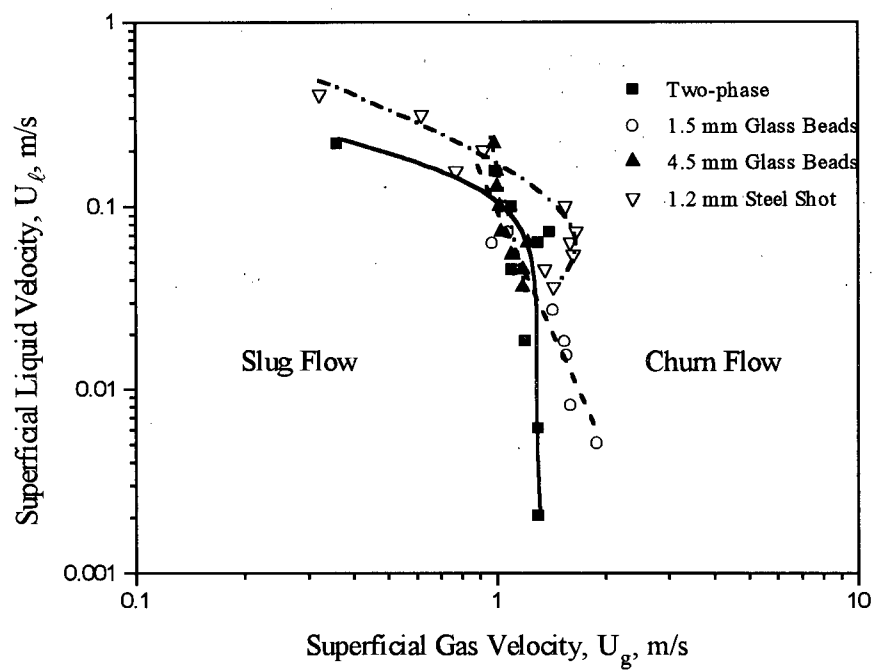


Figure 7.32. Boundaries between slug and churn flow regimes.

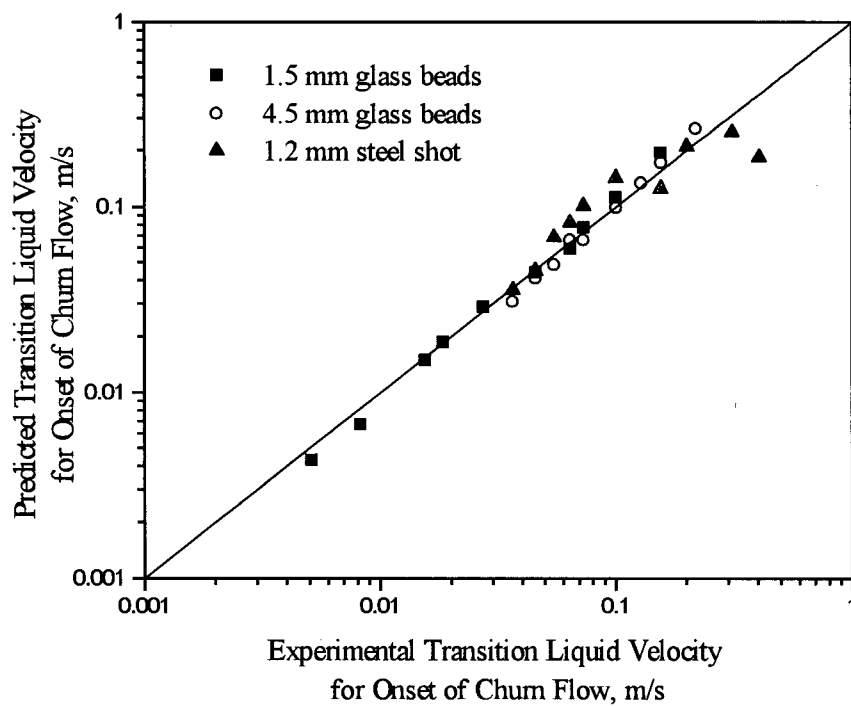


Figure 7.33. Comparison between predictions of Equation (7.7) and experimental data.

Figure 7.34 shows boundaries between churn flow and bridging flow. For the gas-liquid system, this transition is independent of superficial liquid velocity. For the three-phase systems, the transition gas velocities increase with decreasing U_ℓ . By comparing the transitions for the three types of particles, it is seen that particle size does not affect this transition, but the increase of particle density leads to increases in transition liquid velocities, at least at higher U_g . Equation (7.8) below is proposed to present the boundary between the churn/bridging flow regimes. Figure 7.35 compares the predicted and experimental values. The average absolute percentage deviation for the 30 sets of data of the present study is 11.1%. No other data have been found in the literature.

$$\frac{U_g}{U_\ell} = 219 \times \text{Re}_\ell^{-1.24} \text{Ar}_\ell^{0.367} \left(\frac{\rho_s}{\rho_\ell} \right)^{-0.444} \quad (7.8)$$

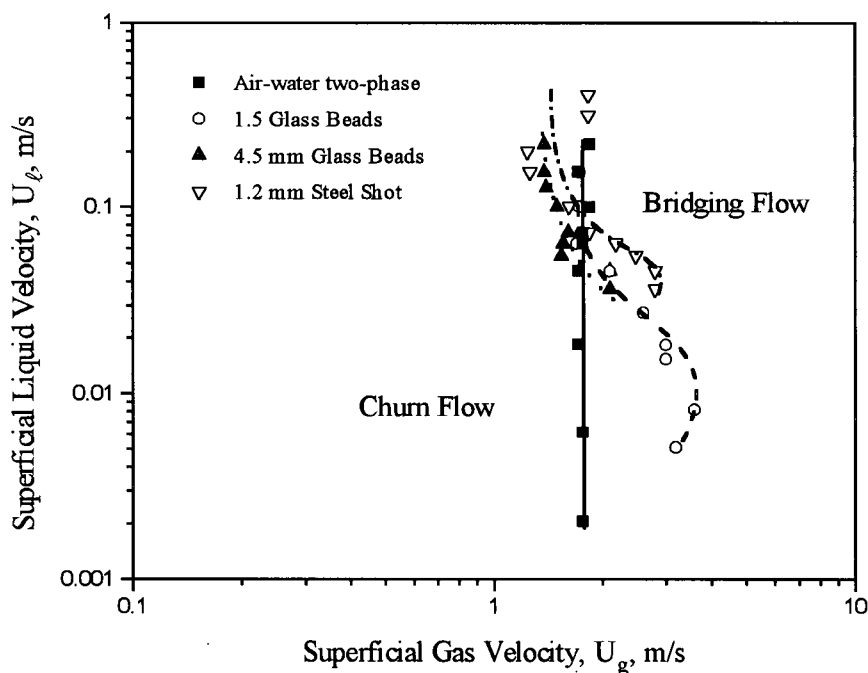


Figure 7.34. Boundaries between churn and bridging flow regimes.

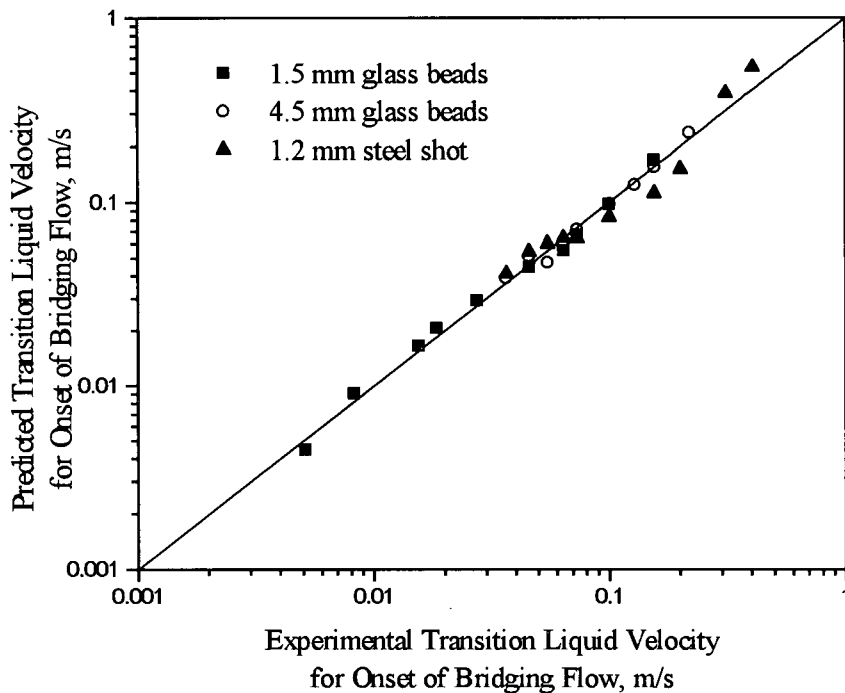


Figure 7.35. Comparison between predictions of Equation (7.8) and experimental data.

Figure 7.36 presents the transition between bridging flow and annular flow. For the two-phase system, the transition gas velocities decrease with increasing liquid velocities at high liquid flow rates, but remain almost constant at lower U_ℓ . For the glass beads, before this transition occurs, the particles have all been entrained from the column, so the transitions from bridging flow to annular flow are virtually identical to those for the gas-liquid system. For the 1.2 mm steel shot, however, the presence of solid particles causes a decrease of transition gas velocities. Most experimental data for this transition obtained in the present study correspond to absence of particles. There are insufficient data to construct an empirical correlation for three-phase systems.

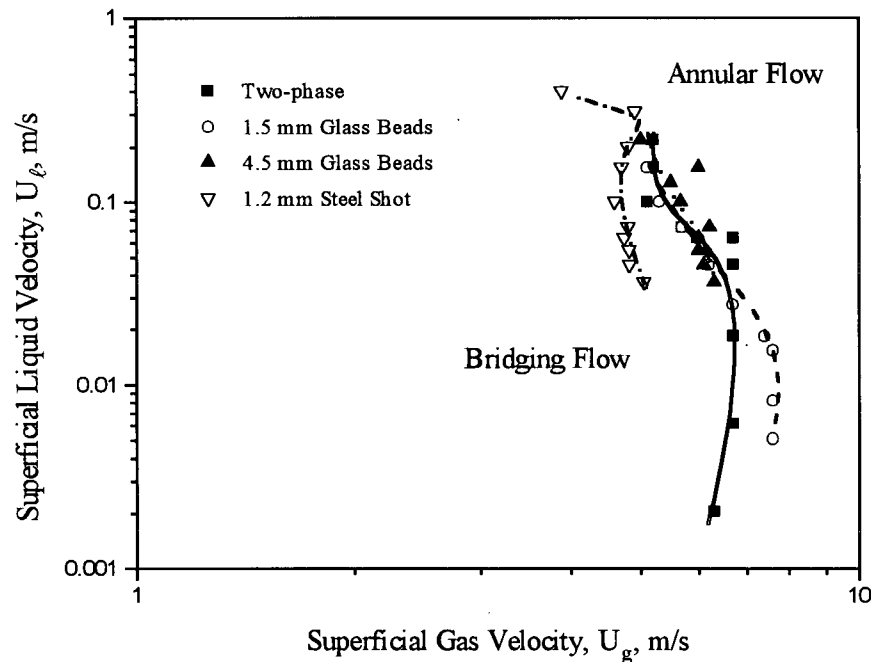


Figure 7.36. Boundaries between bridging and annular flow regimes.

7.5. Summary

Experimental criteria for determining flow regime transitions in an air-water two-phase system have been successfully extended to gas-liquid-solid three-phase fluidized beds. Flow regime maps have been presented based on experimental data for three different three-phase systems. Relatively small/light particles, i.e. 1.5 mm glass beads, cause gas bubbles to coalesce. Hence coalesced bubble flow can be observed at low gas and liquid velocities in three-phase fluidized beds of such particles. However, dispersed bubble flow still can be observed at high liquid velocity for three-phase fluidized beds of 1.5 mm glass beads, since the increase of liquid velocity leads to a decrease in solids concentration. Large or dense particles (4.5 mm glass beads or 1.2 mm steel shot) lead to bubble coalescence only at relatively high gas velocities. At low gas velocities, discrete and dispersed bubble flow can be observed at low and high liquid velocities, respectively. As in two-phase systems, slug flow, churn flow, bridging flow and annular flow can

be observed at high gas velocities in three-phase fluidized beds. Particle properties clearly influence flow regime transition for the onset of slug flow, bridging flow and annular flow.

Five empirical correlations are proposed for the flow regime boundaries. The average absolute percentage deviation between the experimental data and the predictions is 8.0% for the onset of dispersed bubble flow, 6.7% and 12.4% for the onset of slug flow at low and high liquid velocity respectively, 14.3% for the boundary between the slug and churn flow regimes and 11.1% for the churn/bridging flow transition.. These correlations give favourable agreement with experimental data from the literature, especially considering the variation in measurement techniques employed in the literature.

Chapter 8

Bubble Characteristics in Three-Phase Fluidized Beds

8.1 Introduction

In Chapter 7, it was shown that discrete bubble flow, dispersed bubble flow, coalesced bubble flow, slug flow, churn flow, bridging flow and annular flow exist in three-phase systems. The presence of particles changes the characteristics of bubbles significantly, compared to solids-free gas-liquid systems. Many studies have been devoted to bubble behavior in three-phase fluidized beds under different operating conditions (Rigby et al., 1970; Page and Harrison, 1972; Henriksen and Ostergaard, 1974; Darton and Harrison, 1975, 1985; Kim et al., 1977; de Lasa et al., 1983; Sisak and Ormos, 1985a, b; Lee and de Lasa, 1986; Peterson et al., 1987; Kim et al., 1988; Lee and de Lasa, 1988; Meernik and Yuen, 1988a, b; Muroyama et al., 1988; Sun and Furusaki, 1988; Yu and Kim, 1988; Lee and de Lasa, 1989; Bly and Worden, 1992; Deshpande et al., 1992; Han and Kim, 1993; Chen et al., 1995). This chapter demonstrates some bubble characteristics for the different flow regimes in three-phase fluidized beds. Three types of particles were used in the fluidized beds with air and water as gas and liquid phases, respectively. The variations of bubble frequency, bubble chord length and its distribution as well as average bubble velocity are presented in this chapter.

8.2 Bubble Frequency

The variation of the bubble frequency with respect to the gas velocity in various flow regimes for the three-phase fluidized bed containing 1.5 mm glass beads is presented in Figures 7.7 and 7.14 of Chapter 7. A linear relationship with a proportionality constant of 545 m^{-1} between the bubble frequency and the superficial gas velocity can be seen for the dispersed bubble

flow regime in Figure 7.7. As with the air-water two-phase system, this constant does not change with superficial liquid velocity in the dispersed bubble flow regime. The bubble frequency in the coalesced bubble flow and slug flow regimes increases with the superficial gas and liquid velocities, but decreases as U_g is increased in the churn and bridging flow regimes, as shown in Figure 7.14.

For the 4.5 mm glass beads, depending on the liquid velocity, dispersed and discrete bubble flow were observed at low gas velocities. In these two flow regimes the bubble frequency is proportional to the superficial gas velocity as shown in Figure 7.8. On further increasing the gas velocity, the bubble frequency increases at a slowly increasing rate in the slug flow regime and reaches a maximum value at the transition between the slug and churn flow regimes. The bubble frequency continues to decrease in the bridging flow regime and approaches zero in the annular flow regime, as shown in Figure 7.15.

For the three-phase fluidized bed of 1.2 mm steel shot, the bubble frequency in the discrete and the dispersed bubble flow regimes is proportional to the superficial gas velocity and also a function of the liquid velocity as shown in Figures 7.9 and 7.10. For low liquid velocities, the proportionality constant relating the bubble frequency to the superficial gas velocity is approximately 545 m^{-1} , while for high U_ℓ , the constant is 860 m^{-1} . The bubble frequency continues to increase slowly with the gas velocity in the coalesced bubble flow and slug flow regimes, but decreases in the churn and bridging flow regimes as shown in Figure 7.16. It is also seen that the bubble frequency increases with the liquid velocity at higher liquid velocities, but does not change significantly with U_ℓ in the coalesced and slug flow regimes at low liquid velocities.

8.3 Bubble Chord Length and its Distribution

Bubble characteristics strongly depend on particle size and density in three-phase fluidized beds. Relatively small/light particles (e.g. 1.5 mm glass beads) generally cause bubbles to coalesce to form larger bubbles, while large/heavy particles (such as 4.5 mm glass beads and 1.2 mm steel shot) promote bubble breakup and formation of smaller bubbles. In a three-phase fluidized bed, the solids holdup decreases with increasing superficial liquid velocity, so that the system approaches a gas-liquid two-phase system.

For the three-phase fluidized bed with 1.5 mm glass beads, the coalesced bubble flow regime was observed at low superficial gas and liquid velocities. Figure 8.1 shows the average bubble chord length in the dispersed and coalesced bubble flow regimes. The average bubble chord length increases with increasing superficial gas velocity, but decreases as the superficial liquid velocity increases. The average bubble chord length in the coalesced bubble flow regime is significantly greater than in the dispersed bubble flow regime. The transition between the coalesced and dispersed bubble flow regimes, however, is a gradual process from the average bubble chord length point of view. The average and the Sauter mean bubble chord lengths are plotted against U_g at two different values of U_ℓ in Figure 8.2. It is seen that the average value of bubble chord length is always less than the corresponding Sauter mean value. In the slug flow regime, at $U_\ell = 0.0184$ m/s, both the average and Sauter mean bubble chord length increase with U_g at low gas velocities. On further increasing U_g , the average bubble chord length decreases due to the increased number of small bubbles. The variation of the average bubble chord length in the air-water-1.5 mm glass bead fluidized bed differs from that in the air-water two-phase system (Chapter 5) in which the average and Sauter mean bubble chord lengths increased slightly or levelled off in the slug flow regime.

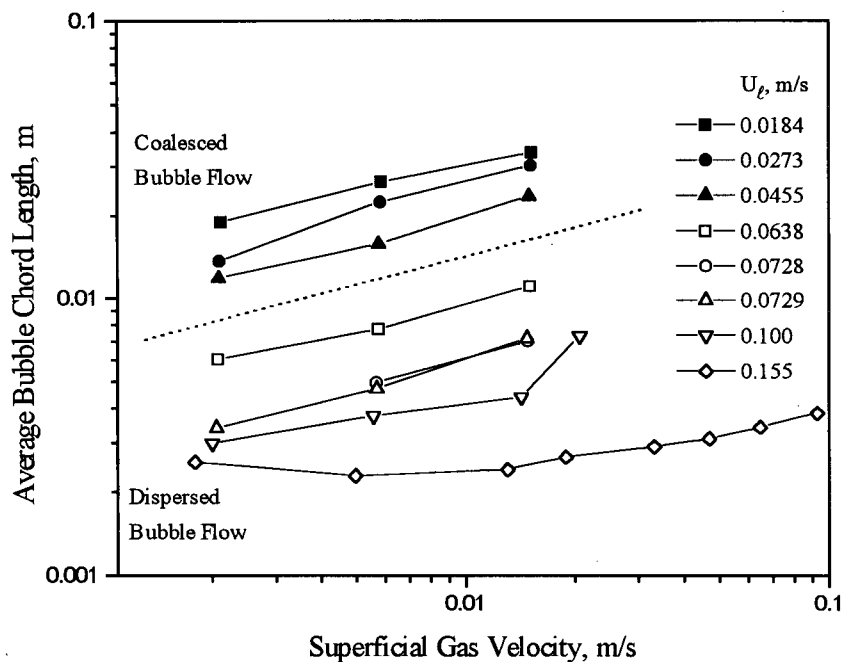


Figure 8.1 Average bubble chord length in coalesced and dispersed bubble flow regime for air-water-1.5 mm glass bead system.

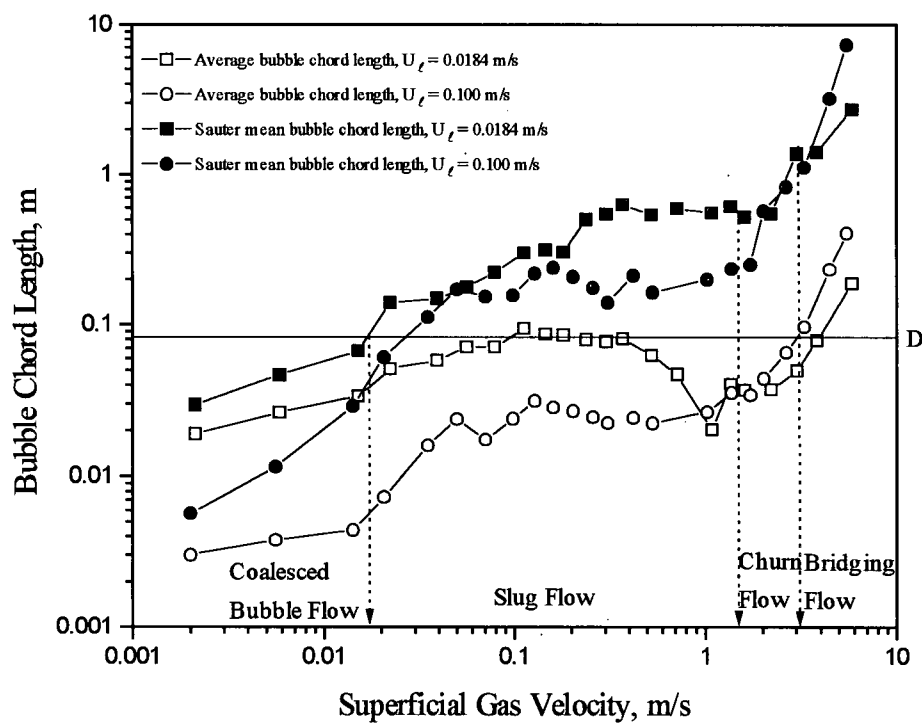


Figure 8.2 Average and Sauter mean bubble chord length in slug and churn flow regime for air-water-1.5 mm glass bead system.

Figure 8.3 shows some typical probability density distributions of the bubble chord length in the different flow regimes. Narrow distributions with peaks which occur between 2.1 and 2.6 mm are observed in the dispersed bubble flow regime. As the superficial liquid velocity is decreased to the coalesced bubble flow regime, the bubble chord length distributions become wider and the average bubble chord length increases by almost an order of magnitude. As U_g is increased, the average bubble chord length and the standard deviation increase significantly in the slug flow regime. However, the peaks of the PDF curves occur at small bubble chord lengths, due to the large number of small bubbles in the slug flow regime. Even in the churn flow and bridging flow regimes, there are still many small bubbles present due to the turbulence of the gas and liquid flows. In bridging flow, the standard deviation of the bubble chord length increases sharply, although the average bubble chord length does not change as much as in the churn flow regime. This indicates that large bubbles exist in the system since the bridging flow regime is transitional between the churn flow and the annular flow regimes.

A number of investigators have reported that large particles cause bubbles to break up in air-water fluidized beds. In the present study, small bubbles with a narrow size distribution were found in the discrete and dispersed bubble flow regimes. Figure 8.4 shows the measured average bubble chord length in these two flow regimes for the air-water-4.5 mm glass bead fluidized bed. It is seen that the average bubble chord length increases with increasing gas velocity but decreases with increasing liquid velocity. The average bubble chord length in the discrete bubble flow regime is always greater than in the dispersed bubble flow regime at the same gas velocity. The transition between the discrete and dispersed bubble flow regimes occurs gradually from the point of view of bubble size.

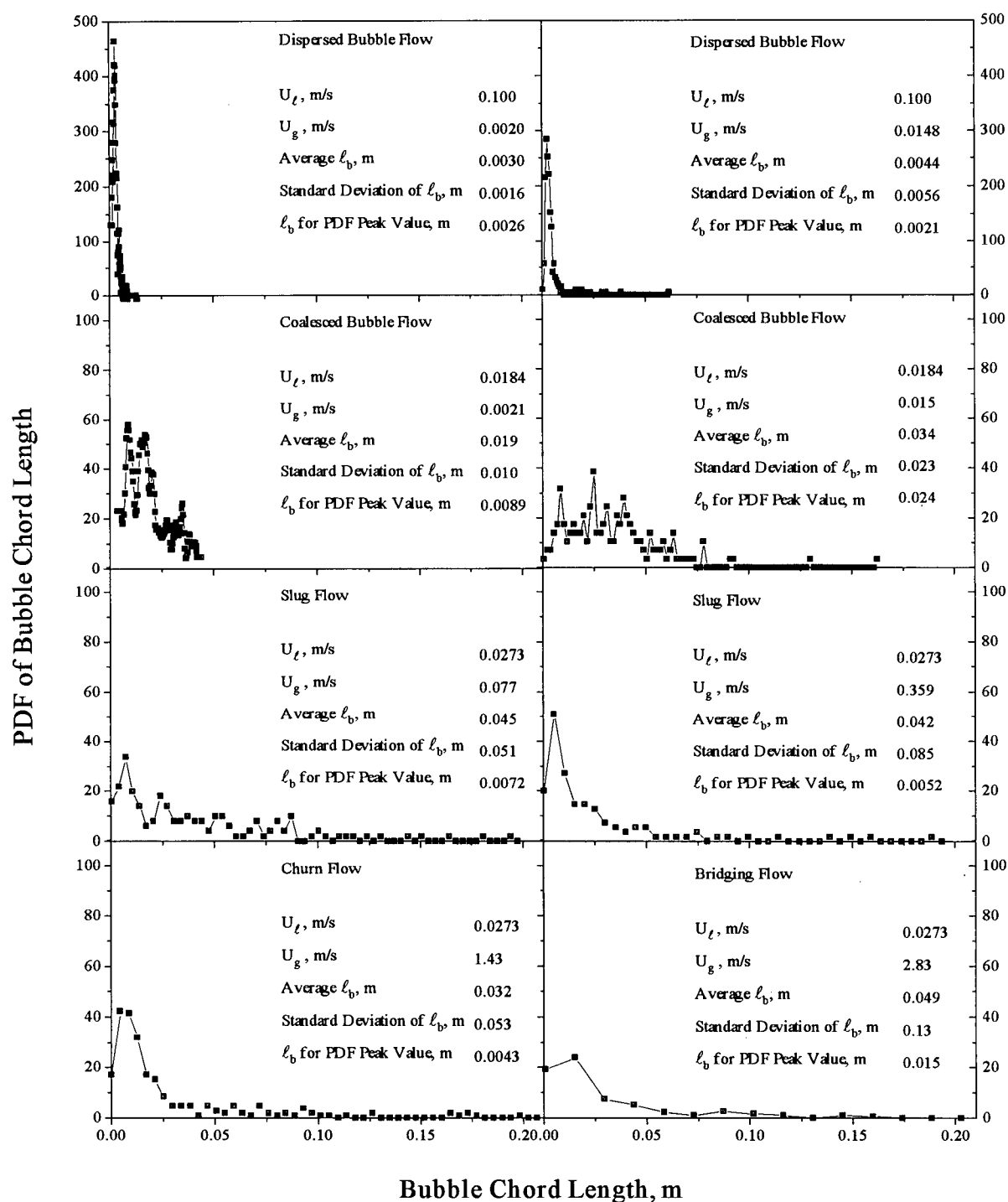


Figure 8.3 Bubble chord length distributions in different flow regimes for air-water-1.5 mm glass bead fluidized beds.

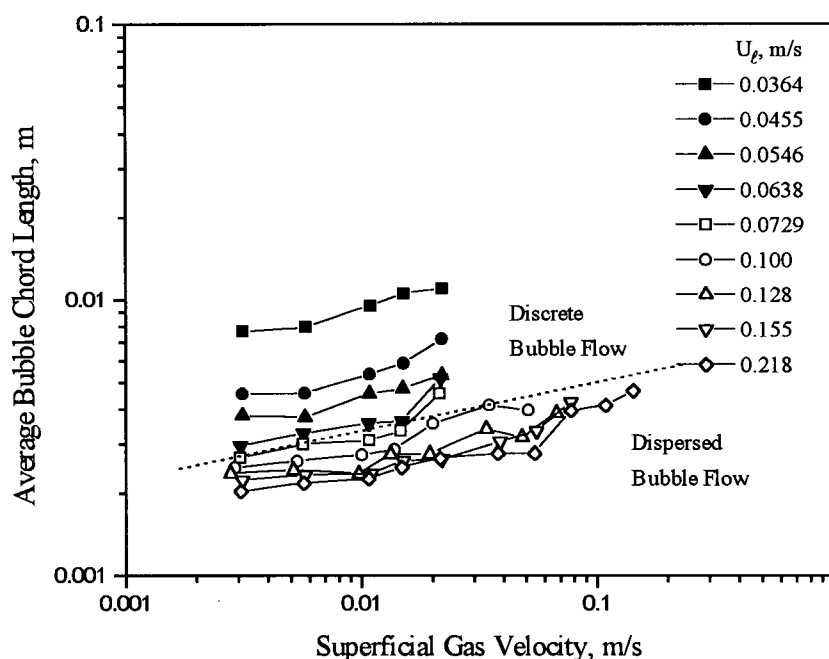


Figure 8.4 Average bubble chord length in discrete and dispersed bubble flow regimes for air-water-4.5 mm glass bead fluidized bed.

The variation of the bubble chord length with gas velocity in other flow regimes is presented in Figure 8.5 for two typical sets of results at $U_l = 0.0455$ and 0.155 m/s. The flow regimes labeled in the figure are for the lower liquid velocity (i.e. 0.0455 m/s). Both the average and the Sauter mean bubble chord length increase with increasing superficial gas velocity in the discrete and coalesced bubble flow regimes. The Sauter mean bubble chord length continues to increase at a lower rate in the slug and the churn flow regimes, then increases sharply in the bridging flow regime. However, the average bubble chord length first increases sharply at low gas velocities and then decreases slightly at intermediate gas velocities in the slug flow regime for $U_l = 0.0455$ m/s. At high liquid velocity, viz. $U_l = 0.155$ m/s, the average bubble chord length always increases with the superficial gas velocity.

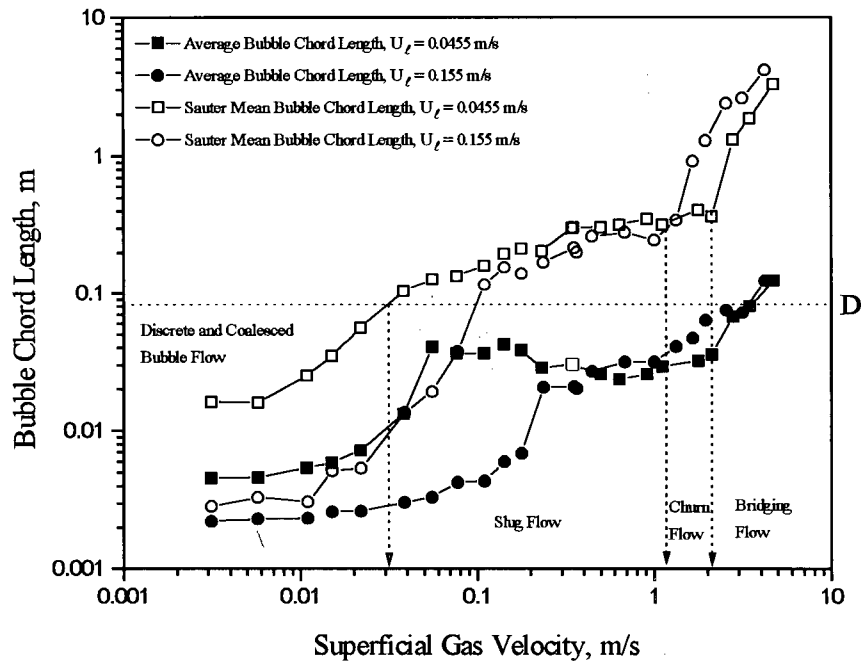


Figure 8.5 Average and Sauter mean bubble chord length in different flow regimes for air-water-4.5 mm glass bead fluidized bed.

The bubble chord length distribution in different flow regimes for this system is shown in Figure 8.6. For the dispersed bubble flow regime, the distributions of bubble chord length are generally narrow with average bubble chord length ranging from 2.2 to 2.4 mm and the standard deviation from 0.8 to 1.1 mm for gas velocities from 0.00311 to 0.011 m/s. The peaks of the PDF of bubble chord length occur at a bubble chord length of 1.7 mm. In the discrete bubble flow regime, the average bubble chord length, the standard deviation of bubble chord length and the bubble chord length at which the peak of the PDF occurs are greater than for the dispersed bubble flow regime, but bubble chord length distributions remain narrow, as shown in Figure 8.6.

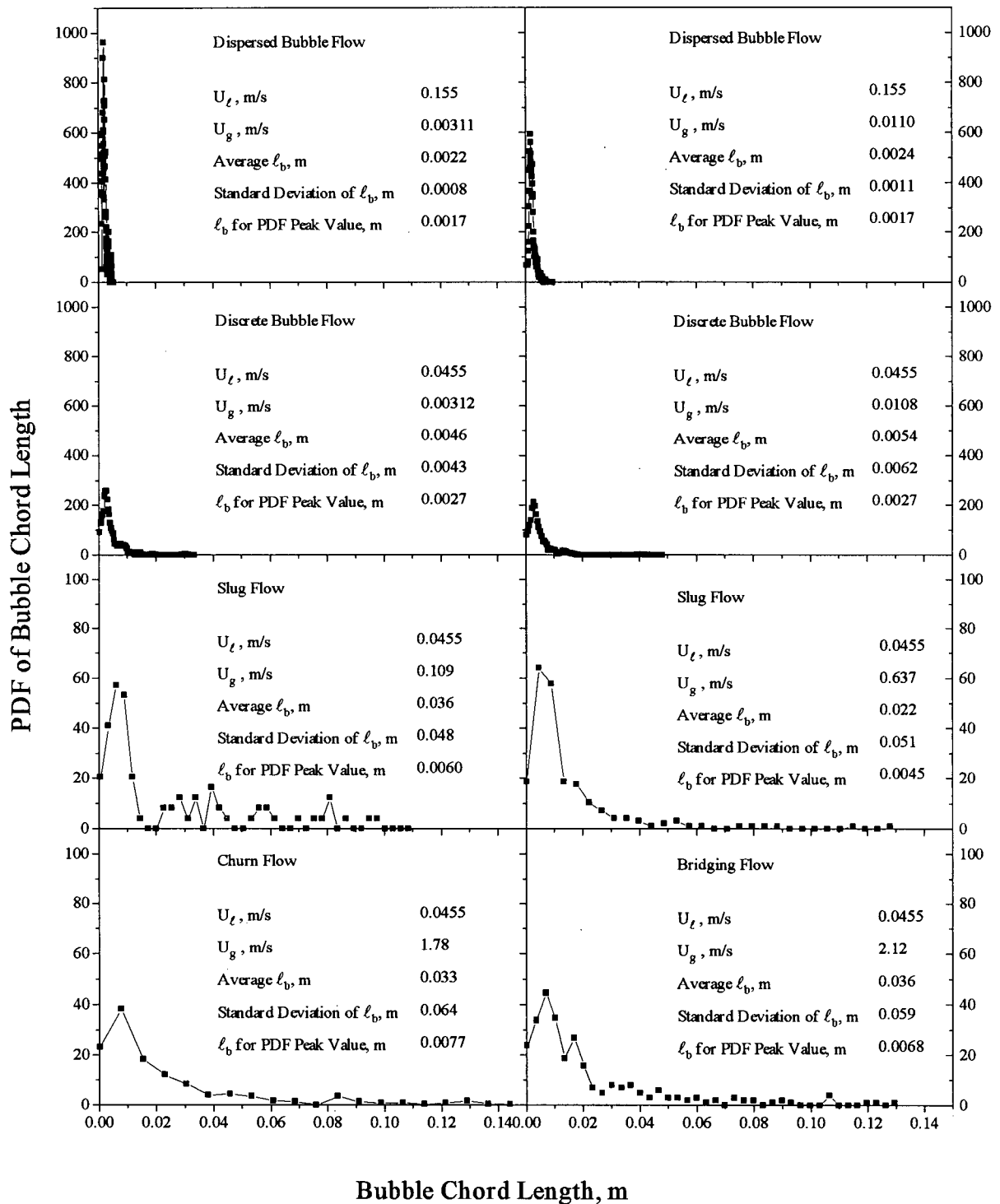


Figure 8.6 Bubble chord length distributions in different flow regimes for air-water-4.5 mm glass bead fluidized bed.

The bubble chord length distributions in the slug flow regime are wider than in the dispersed and discrete bubble flow regimes, with average values and standard deviations of bubble chord length approximately one order of magnitude greater than in the discrete bubble flow regime. Despite the increase in ℓ_b and its standard deviation in the slug flow, churn flow and bridging flow regimes, the peaks of the distributions remain at a small bubble chord length, indicating that many small bubbles are present in these flow regimes.

For the 1.2 mm steel shot fluidized bed, discrete, dispersed and coalesced bubble flow regimes were observed at low superficial gas velocities. Figure 8.7 shows the average bubble chord length in the discrete and dispersed bubble flow regimes. It is seen that the average bubble chord length increases with increasing superficial gas velocity and decreases with increasing superficial liquid velocity. The average bubble chord length in the discrete bubble flow regime is greater than in the dispersed bubble flow regime.

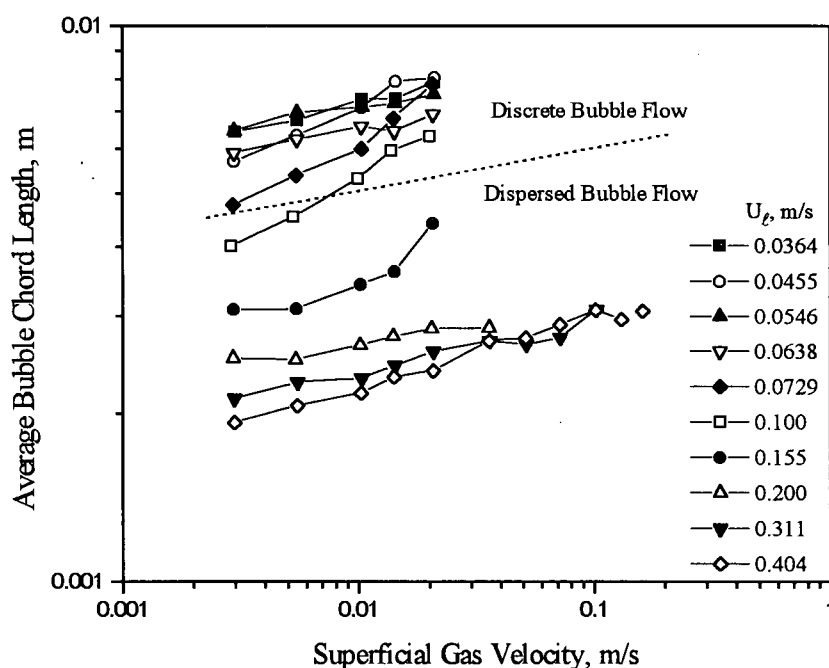


Figure 8.7 Average bubble chord length in discrete and dispersed bubble flow regimes for air-water-1.2 mm steel shot fluidized bed.

The experimental average and Sauter mean bubble chord lengths at two different superficial liquid velocities are presented in Figure 8.8. The demarcations for the flow regimes shown are for $U_\ell = 0.0455$ m/s. The Sauter mean bubble chord length mainly increases with the superficial gas velocity.

Figures 8.9 and 8.10 show typical bubble chord length distributions for different flow regimes. Small bubbles with narrow size distribution were seen in the dispersed bubble flow regime at high liquid velocity. On decreasing the superficial liquid velocity, discrete bubble flow is encountered, leading to higher values of both the average and the standard deviation of bubble chord length.

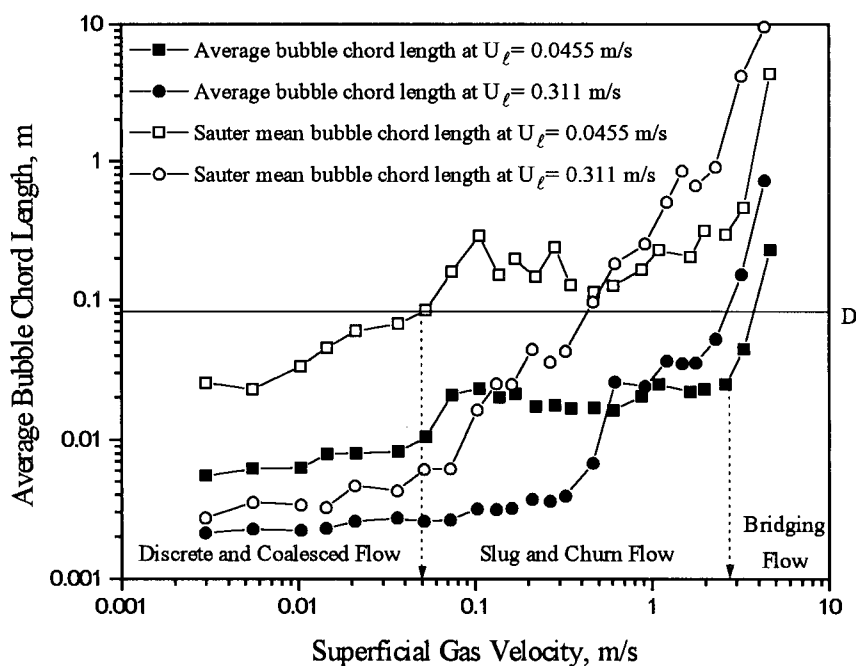


Figure 8.8 Average and Sauter mean bubble chord length in different flow regimes for air-water-1.2 mm steel shot at $U_\ell = 0.0455$ and 0.311 m/s.

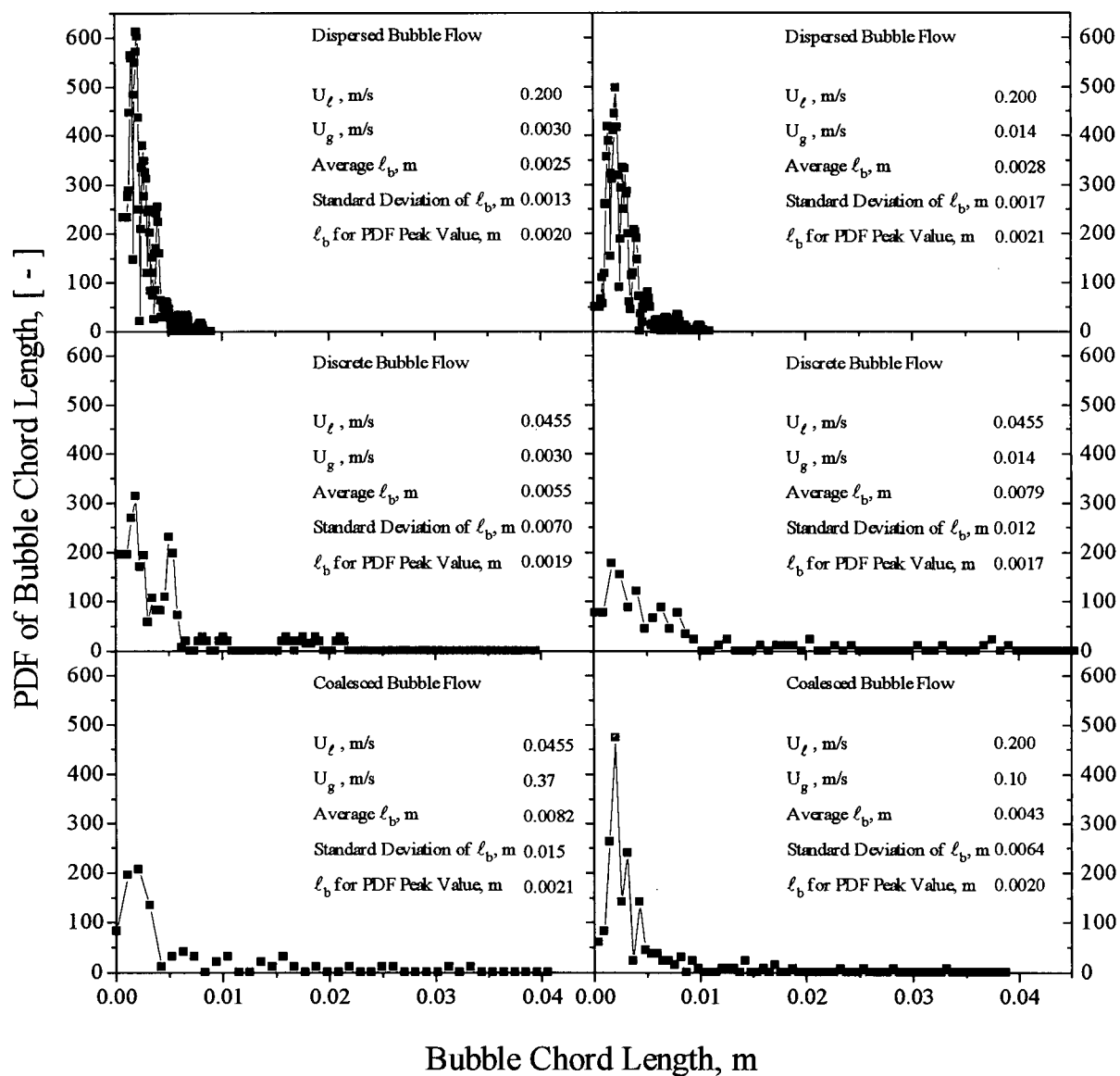


Figure 8.9 Bubble chord length distribution in different flow regimes at low gas velocity for air-water-1.2 mm steel shot fluidized bed.

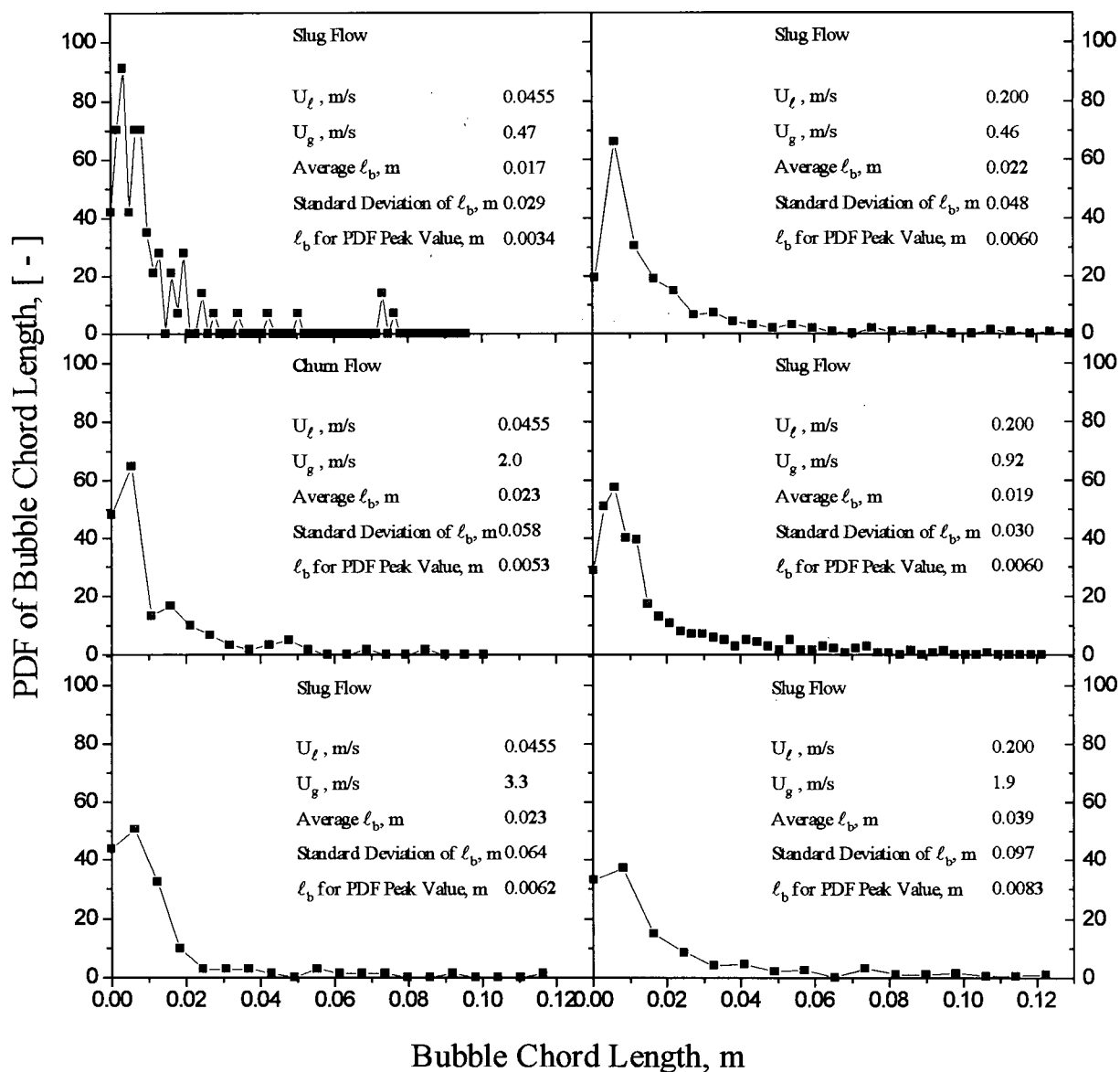


Figure 8.10 Bubble chord length distribution in different flow regimes at high gas velocity for air-water-1.2 mm steel shot fluidized bed.

As the superficial gas velocity is increased, the average value and the standard deviation of bubble chord length increase. The peaks of the PDF curves occur at low values of the bubble chord length, indicating that there are still many small bubbles in the slug, churn and bridging flow regimes.

8.4 Average Bubble Velocity

The average bubble velocity is plotted against the average bubble chord length in the dispersed and coalesced bubble flow regimes for the air-water-1.5 mm glass bead fluidized bed in Figure 8.11. It is seen that the average bubble velocity increases with the average bubble chord length and the superficial liquid velocity. The rate of increase of the average bubble velocity with respect to the average bubble chord length in the dispersed bubble flow regime is greater than in the coalesced bubble flow regime.

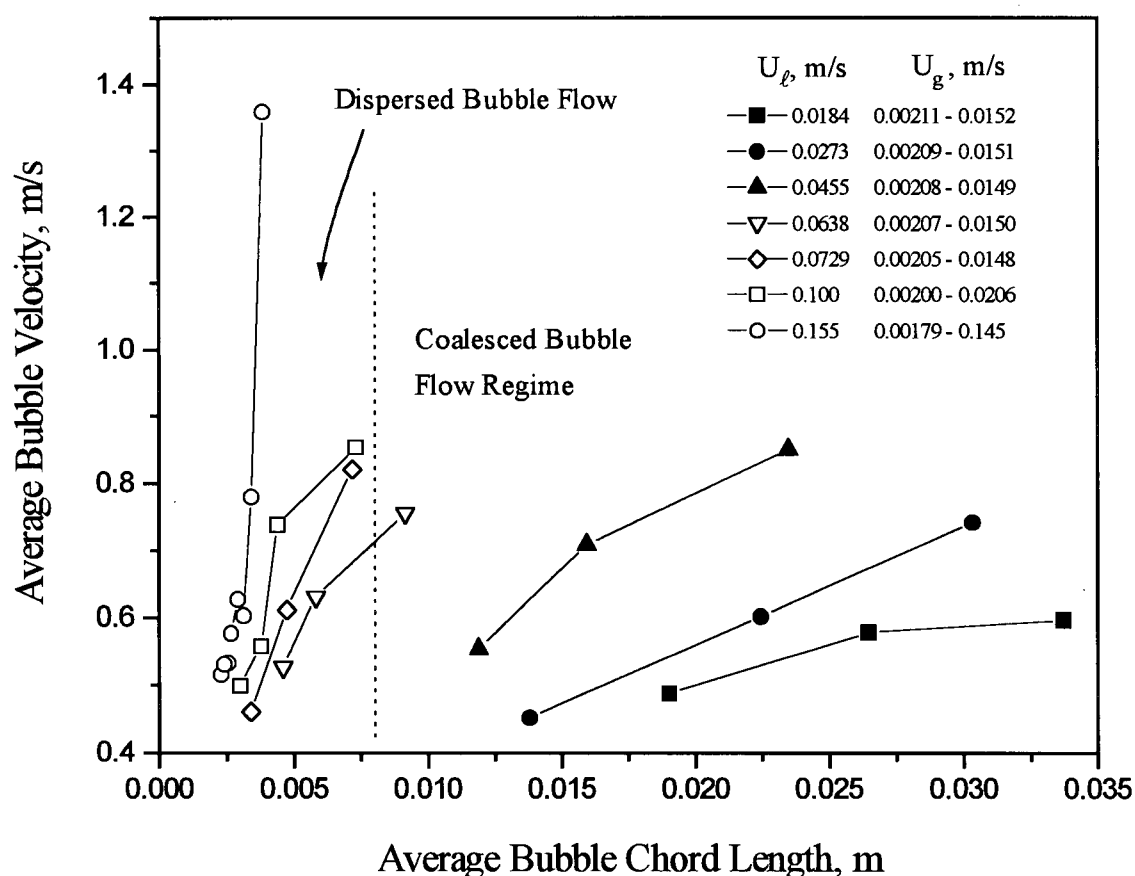


Figure 8.11 Average bubble velocity plotted against average bubble chord length in dispersed and coalesced bubble flow regimes for air-water-1.5 mm glass bead fluidized beds, $U_g = 0.0018 - 0.145$ m/s.

The average bubble velocity is plotted against the average bubble chord length at three different superficial liquid velocities in the slug and churn flow regimes in Figure 8.12. It is seen that the average bubble velocity increases consistently with the superficial gas velocity, while the average bubble chord length at first increases as the gas velocity increases and then describes an S-shape with respect to the average bubble velocity.

The relationship between average bubble velocity and average bubble chord length can be correlated by Equation (5.3) for the dispersed and discrete bubble flow regimes in the air-water two-phase system as described in Chapter 5. Figure 8.13 shows the bubble travel length versus the average bubble chord length in the dispersed and coalesced bubble flow regimes for the air-water-1.5 mm glass bead fluidized beds. It is seen that Equation (5.3) also agrees well with the experimental data in the dispersed bubble flow regime well. A linear relationship between the

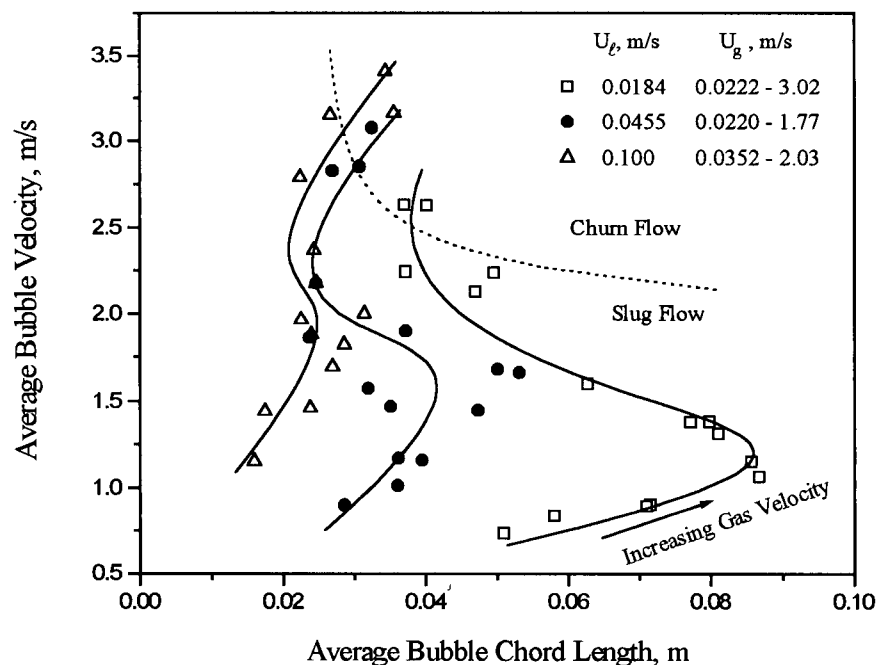


Figure 8.12 Variation of average bubble velocity plotted against average bubble chord length in slug and churn flow regimes for air-water-1.5 mm glass bead fluidized beds.

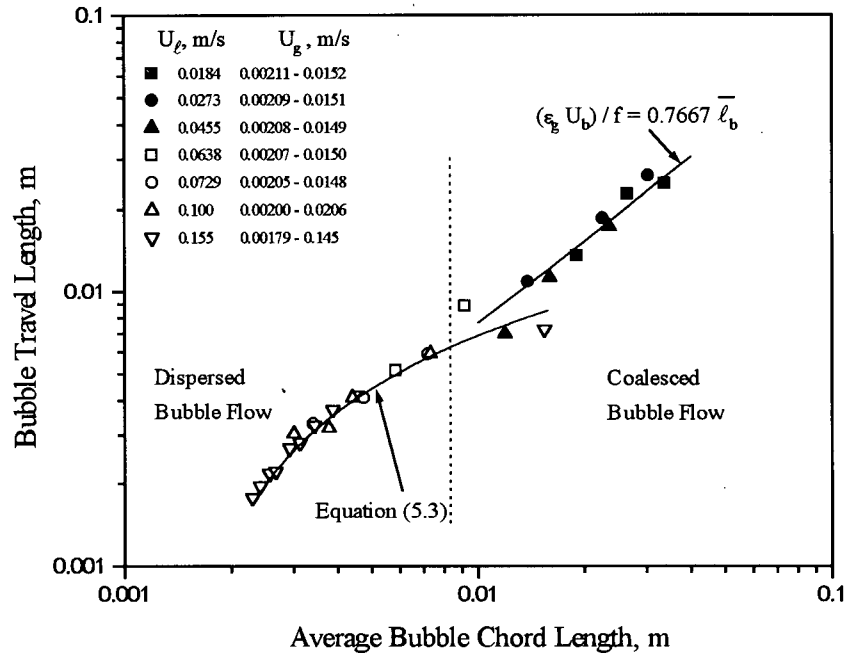


Figure 8.13 Bubble travel length plotted against average bubble chord length in coalesced and dispersed bubble flow regimes for air-water-1.5 mm glass bead fluidized beds.

bubble travel length and the average bubble chord length is obtained for the coalesced bubble flow regime in the air-water-1.5 mm glass bead fluidized bed, expressed by:

$$\epsilon_g \frac{U_b}{f} = 0.7667 \bar{\ell}_b \quad (8.1)$$

The variation of the bubble travel length with the average bubble chord length in other flow regimes at low liquid velocities is shown in Figure 8.14. It can be seen that the linear relationship between the bubble travel length and the average bubble chord length for the coalesced bubble flow regime can be extended to the slug flow regime at low gas velocities. At high gas velocities in the slug flow regime, the average bubble chord length decreases with the gas velocity (see Figure 8.2), but the bubble travel length is independent of both U_g and U_l .

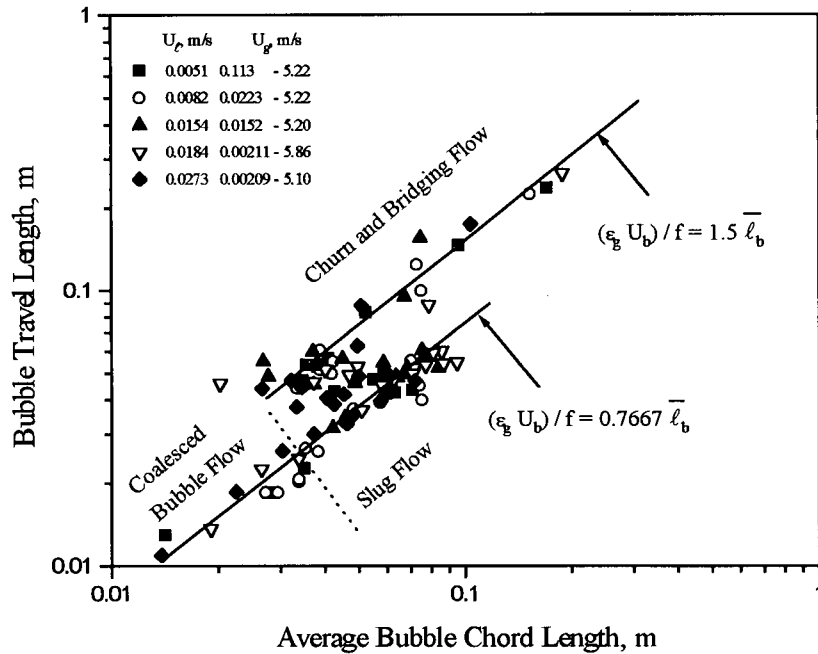


Figure 8.14 Bubble travel length plotted against average bubble chord length in different flow regimes at low liquid velocities for air-water-1.5 mm glass bead fluidized bed.

At high liquid velocities, the solids holdup decreases significantly for the air-water-1.5 mm glass bead fluidized bed; the relationship between the bubble travel length and the average bubble chord length then approaches that in the corresponding air-water two-phase system. It can be seen in Figure 8.15 that the experimental results for the dispersed bubble flow and the slug/churn flow regimes agree well with Equations (5.3) and (5.4), respectively, both developed for the air-water two-phase system.

The average bubble velocity is plotted against the average bubble chord length in the discrete and dispersed bubble flow regimes for the air-water-4.5 mm glass bead fluidized bed in Figure 8.16. The average bubble velocity is seen to increase with both the average bubble chord length and the liquid velocity in both these flow regimes.

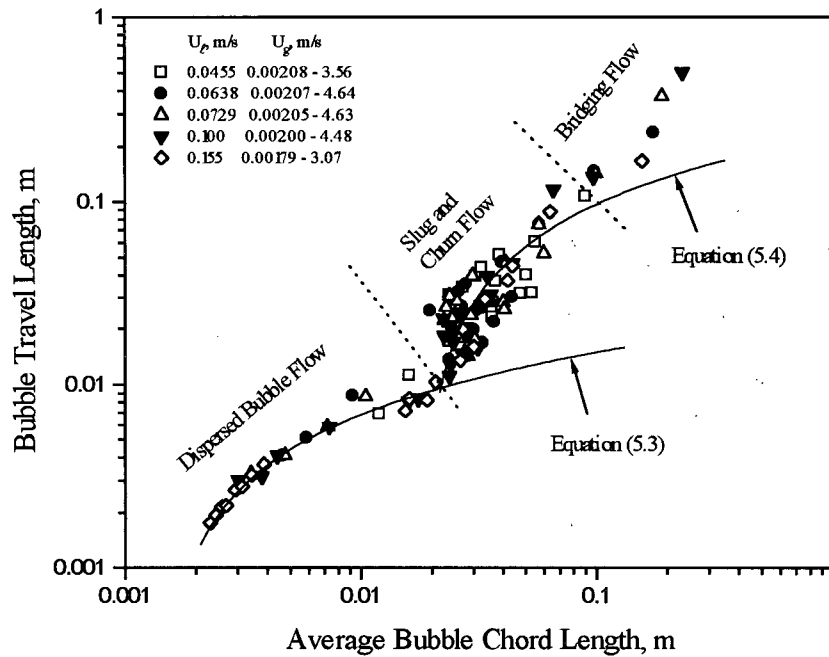


Figure 8.15 Bubble travel length plotted against average bubble chord length in different flow regimes at high liquid velocities for air-water-1.5 mm glass bead fluidized bed.

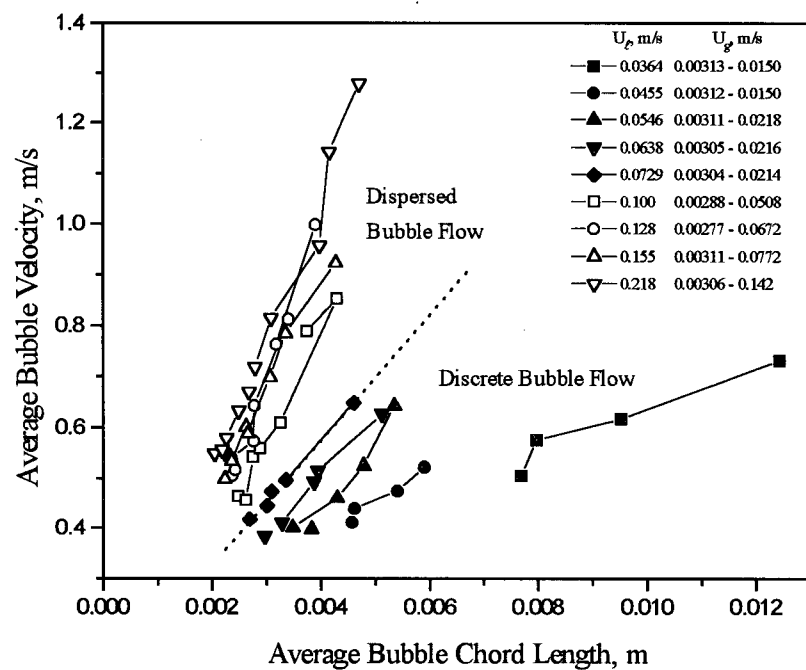


Figure 8.16 Average bubble velocity in discrete and dispersed bubble flow regimes for air-water-4.5 mm glass bead fluidized bed.

The average bubble velocity in the coalesced, slug and churn flow regimes at three typical liquid velocities is shown in Figure 8.17. S-shape curves can be seen for the relationship between the average bubble velocity and the average bubble chord length at low liquid velocities. This indicates that the average bubble velocity is not only a function of the average bubble chord length but also of the superficial gas velocity. At high superficial liquid velocity, viz. $U_\ell = 0.155$ m/s, the solids holdup decreases so that the three-phase fluidized bed approaches an air-water two-phase column, and the average bubble velocity increases with the average bubble chord length.

The relationship between the bubble travel length and the average bubble chord length for the three-phase fluidized bed is shown in Figure 8.18. The variation of the bubble travel length with the average bubble chord length is different in different flow regimes. In the discrete and dispersed bubble flow regimes, Equation (5.3) adequately describes the relationship between the

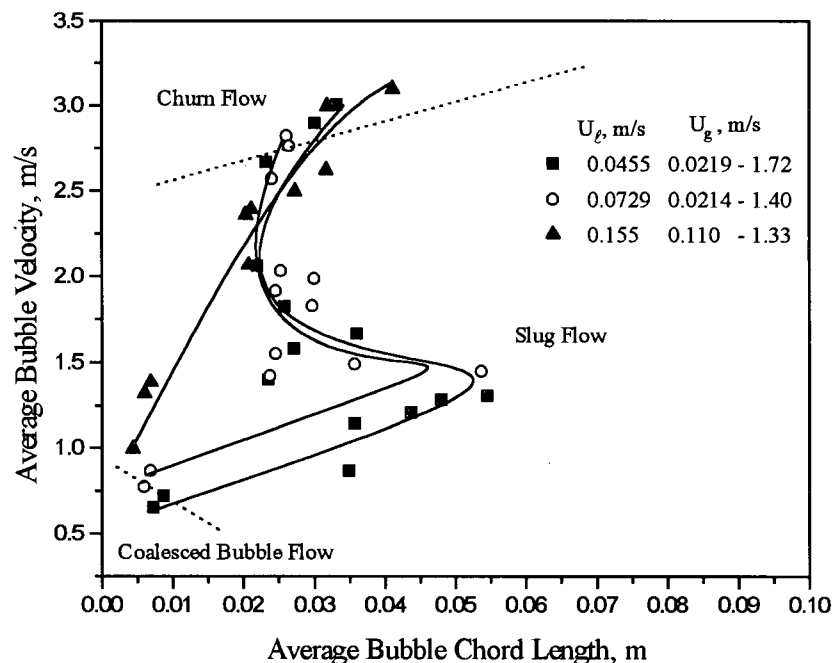


Figure 8.17 Average bubble velocity in different flow regimes for air-water-4.5 mm glass bead fluidized bed.

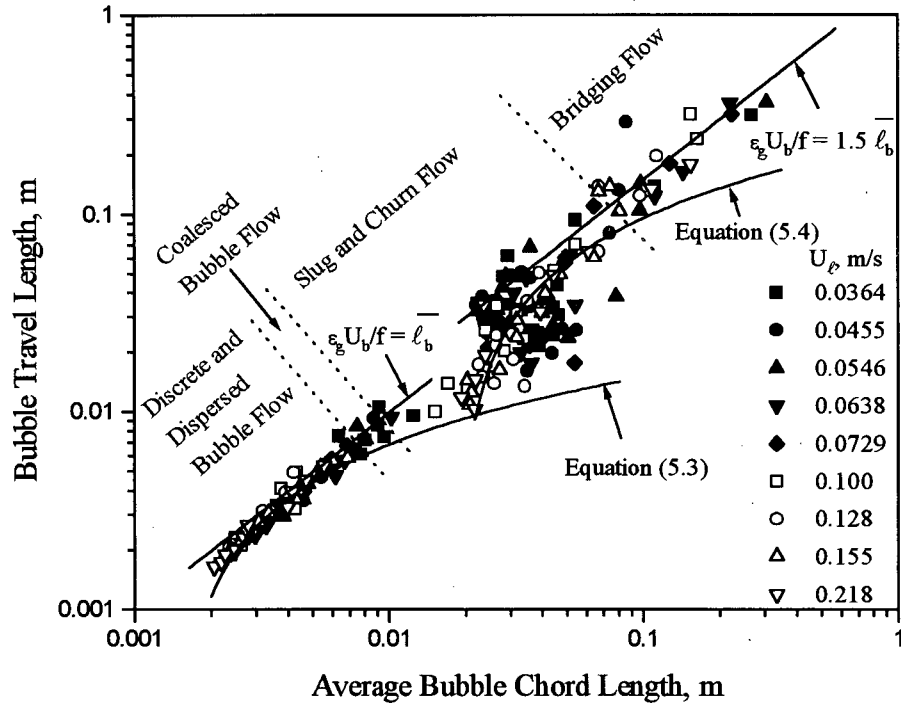


Figure 8.18 Bubble travel length plotted against average bubble chord length in different flow regimes for air-water-4.5 mm glass bead fluidized bed. $U_g = 0.003 - 4.5$ m/s

bubble travel length and the average bubble chord length. In the slug and the churn flow regimes, at high liquid velocities, Equation (5.4) represents the experimental data well. In the bridging flow regime, the relationship between the bubble travel length and the average bubble chord length can be described by:

$$\epsilon_g \frac{U_b}{f} = 1.5 \bar{\ell}_b \quad (8.2)$$

as shown in the figure.

The variation of the average bubble velocity with the average bubble chord length for the air-water-1.2 mm steel shot fluidized bed is presented in Figure 8.19. It can be seen that the average bubble velocity increases with the average bubble chord length in the dispersed bubble flow regime. For other flow regimes, the relationships between the average bubble velocity and

the average bubble chord length are not very clear. Nevertheless, it still can be seen that for discrete bubble flow, the average bubble chord length ranges from 5 to 10 mm, while the average bubble velocity ranges from 0.5 to 1 m/s. For slug and churn flow, the average bubble chord length ranges from 10 to 40 mm, while the average bubble velocity varies from 1 to 5 m/s.

The relationship between the bubble travel length and the average bubble chord length for the air-water-1.2 mm steel shot fluidized bed is shown in Figure 8.20. It is seen that the two parameters can be correlated by Equation (5.3) for the discrete and dispersed bubble flow regimes and, at higher superficial liquid velocities, by Equation (5.4) for the slug and churn flow regimes.

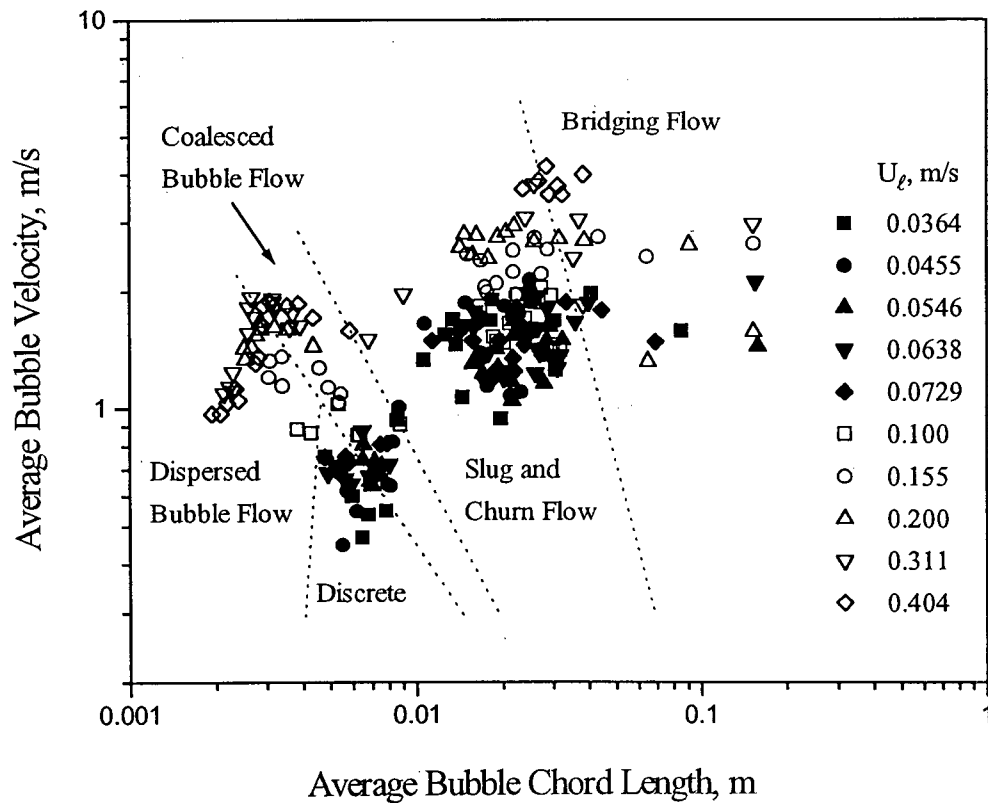


Figure 8.19 Average bubble velocity plotted against average bubble chord length in different flow regimes for air-water-1.2 mm steel shot fluidized bed. $U_g = 0.003 - 4.5$ m/s

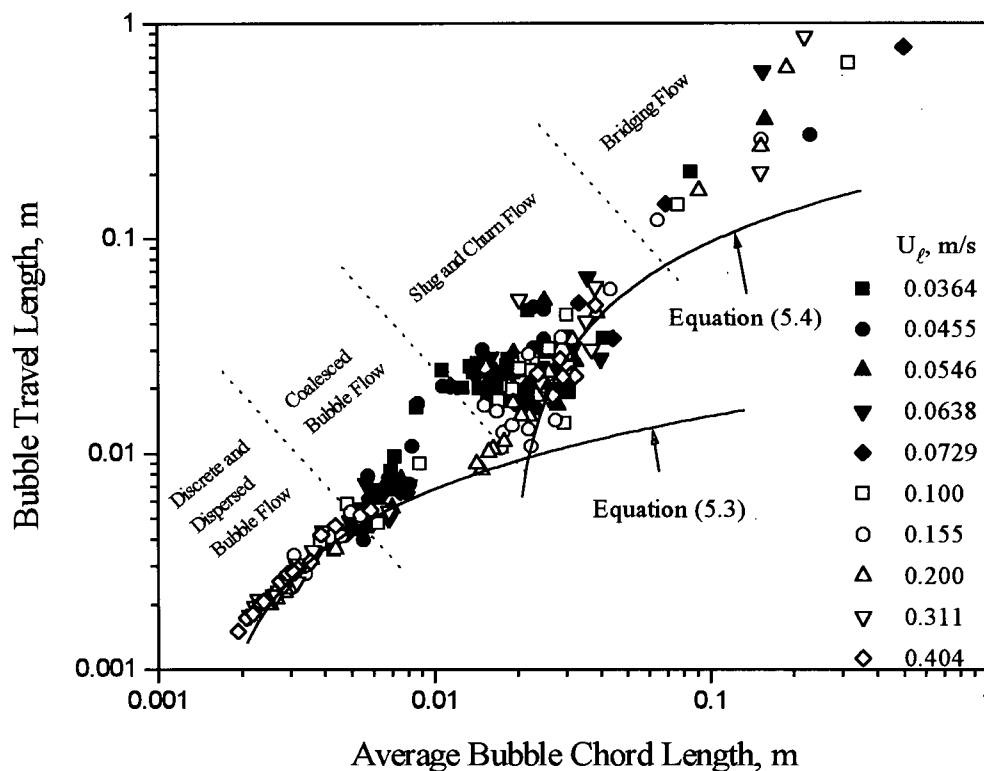


Figure 8.20 Bubble travel length plotted against average bubble chord length for air-water-1.2 mm steel shot fluidized bed. $U_g = 0.003 - 4.5$ m/s

8.5 Summary

Although particle properties affect bubble characteristics and consequently govern the flow regimes, the variation of bubble characteristics in turn depends on flow regime. In the discrete and dispersed bubble flow regimes, bubble frequency changes proportionally with the superficial gas velocity for the different particles tested in this study. It increases at a slower rate with the superficial gas velocity in the coalesced bubble flow and slug flow regimes, but decreases in the churn and bridging flow regimes for the different systems studied in this work. Average bubble chord length increases with the superficial gas velocity but decreases with the superficial

liquid velocity in the discrete, dispersed and coalesced bubble flow regimes. The average bubble chord length in the coalesced bubble flow regime is greater than in the discrete bubble flow regime, and the latter is greater than in the dispersed bubble flow regime. In the bridging flow regime, the average bubble chord length increases sharply with the superficial gas velocity. The distributions of bubble chord length reveal that, despite the increase of average bubble chord length, there still exist many small bubbles in the slug, churn and bridging flow regimes in the three-phase fluidized beds. The standard deviation of the bubble chord length increases with increasing superficial gas velocity but decreases with the superficial liquid velocity. For the 1.5 mm and 4.5 mm glass beads, the average bubble velocity increases with both the average bubble chord length and the superficial liquid velocity in the discrete, dispersed and coalesced bubble flow regimes. For other fluidized beds flow regimes with the 1.5 mm and 4.5 mm glass beads as well as the fluidized bed with 1.2 mm steel shot, the relationship between the average bubble velocity and the average bubble chord length is complex due to the interaction of the effects of the gas and liquid velocities.

The bubble travel length, defined as $(\epsilon_g U_b)/f$ in Chapter 5, can also be used to correlate the bubble characteristics in three-phase fluidized beds. Equation (5.3), developed in Chapter 5, describes the relationship between the bubble travel length and the average bubble chord length in the discrete and dispersed bubble flow regimes for the three-phase fluidized beds. Equation (5.4) is applicable to the slug and churn flow regimes at high liquid velocity in the three-phase fluidized beds. The relationship between bubble travel length and average bubble chord length appears to provide an alternative method to determine flow regimes in multi-phase systems. Further study is needed to extend this finding.

Chapter 9

Conclusions and Recommendations

9.1 General Conclusions

1. A new set of flow regime transition criteria based on conductivity probe measurements of bubble characteristics, summarized in Figure 7.6, was developed to determine flow regime transitions in an air-water bubble column and then successfully applied to air-water-solid three-phase fluidized beds. Other measurement techniques, such as absolute and differential pressure fluctuation methods and the conductivity probe based on the original signal, were carefully studied and shown to be unsuitable for flow regime determination.
2. The best agreement with new and previously published experimental data was obtained from the first empirical equation of Begovich and Watson (1978), Equation (6.1). However, this correlation breaks down when superficial gas velocity approaches zero. Agreement was nearly as good with the Gas-Perturbed Liquid Model, which has the advantage of having no new fitted constants and goes to the appropriate limit as the superficial gas velocity approaches zero. The resulting generalized minimum fluidization model, Equation (6.50), can thus be used to predict the incipient fluidization liquid velocity in both two-phase and three-phase fluidization.
3. The Transport Velocity Model II, Equations (6.87) and (6.88) for spheres, or Equations (6.89) and (6.90) for cylindrical particles, together with Equations (6.81), (6.82) and (6.93), was proposed to predict the boundary between fluidized beds and particle transport flow. It gives good agreement (average deviation of 14.2%) with 112 sets of experimental data for superficial gas velocity up to 3.0 m/s, including 79 data sets from the literature, but excluding the results from the 1.2 mm steel shot in the present work. An empirical correlation, Equation

(6.94), was also proposed to predict the transport velocity in air-water mixtures for all systems. It gives good agreement with 125 sets of experimental data with an average absolute deviation of 13.8%, again for gas velocities as high as 3.0 m/s, a much higher value than explored previously.

4. New complete flow regime maps were presented based on experimental data for cocurrent upward three-phase systems. According to particle movement, three different operating regimes can be observed: fixed bed, fluidized bed and particle transport flow. Based on bubble characteristics, the flow patterns in a three-phase fluidized bed can be classified into dispersed bubble flow, discrete bubble flow, coalesced bubble flow, slug flow, churn flow, bridging flow and annular flow. The same flow patterns were observed for air-water systems, also in a column of inside diameter 82.6 mm.
5. Several empirical correlations were developed to predict the flow regime boundaries in the three-phase fluidized beds investigated. Equation (7.3) can be used to predict the onset of dispersed bubble flow, Equations (7.5) and (7.6) for the onset of slug flow, Equation (7.7) for the onset of churn flow and Equation (7.8) for the onset of bridging flow, respectively.

In addition, the following new findings were also observed in this work:

1. At high superficial liquid velocity, two types of particle movement were observed. For 1.2 mm steel shot, i.e. small heavy particles, clustering occurs. In such a case, the particle transport velocity of the liquid (with superficial gas velocity equal to zero) is significantly greater than the settling velocity of single particles in the liquid phase. For 1.5 and 4.5 mm glass beads, on the other hand, no clusters were observed. In the latter case, the particle transport velocity of

the liquid (for superficial gas velocity equal to zero) is similar to the single particle terminal velocity in the liquid phase.

2. Bubble characteristics in three-phase systems exhibit different trends with respect to variation of gas and liquid flowrates in the different flow regimes. As in bubble columns, many small bubbles exist in slug, churn and bridging flow. This differs from what is observed in slug and turbulent flow for gas-solid fluidized beds at high gas velocities.
3. The relationship between bubble travel length and average bubble chord length in the discrete and dispersed bubble flow regimes of a three-phase fluidized bed is the same as that in the corresponding flow regimes of a bubble column. This relationship is given by Equation (5.3), regardless of the different combinations of superficial gas and liquid velocities and of differences in particle properties.

9.2 Recommendations for Future Work

Bubble characteristics exhibit different dependencies on gas and liquid superficial velocities in different flow regimes. It is important to keep the flow regime in mind when undertaking further study of hydrodynamics and scale-up of multiphase systems.

Flow patterns and their transitions are governed by bubble characteristics, which depend not only on the gas and liquid superficial velocities, but also on the physical properties of the liquid phase. More work is needed to investigate the influence of the liquid properties, such as viscosity and surface tension, on flow regime transitions.

At different levels in a column, the flow patterns can be different for the same operating conditions. For example, at low gas velocities, bubbles grow as they ascend in coalesced bubble flow and this can lead to flow regime transition within the column. More work is needed to investigate flow regime transitions at different levels of the column, especially for the coalesced/slug transition in small columns. In addition, further study is needed to investigate the effect of column diameter on the flow regime transitions.

The relationship between bubble travel length and average bubble chord length provides a potential alternative method to determine flow patterns in multi-phase systems. This new method needs further exploration and development.

Nomenclature

A	parameter defined by Equation (6.72)
a	parameter defined by Equations (6.35a) and (6.37a)
A_c	cross-sectional area of column, m
A_g	area that corresponds to Taylor bubbles in a plot of probability density distribution function for differential pressure fluctuations
A_ℓ	area that corresponds to liquid phase in a plot of probability density distribution function for differential pressure fluctuations
A_p	projected surface of the particles per unit volume of the particles in the direction of the flow, 1/m
Ar_g	gas Archimedes number, $d_p^3 \rho_g (\rho_s - \rho_g) g / \mu_g^2$
Ar_ℓ	liquid Archimedes number, $d_p^3 \rho_\ell (\rho_s - \rho_\ell) g / \mu_\ell^2$
$Ar_{g\ell}$	gas-liquid Archimedes number defined by Equation (6.43)
b	parameter defined by Equations (6.35b) and (6.37b)
C_0	parameter defined by Equation (6.53)
C_D	drag coefficient, defined by Equation (6.6)
C_{DL}	drag coefficient due to liquid flow
C_{DW}	bubble-wake and particle interaction coefficient
$C_{D\infty}$	drag coefficient for individual particle.
C_{S1}	critical solids concentration, solid weight/slurry weight
C_{S2}	solids concentration, solid weight/liquid weight
C_{S3}	average solids concentration in gas-free solid-liquid system, kg-solids/m ³ -slurry
C_{S4}	actual volume of solids per unit cross sectional area of the column, m ³ /m ²
C_μ	viscosity correction factor defined by Equation (6.62)
D	column diameter, m
D_d	distributor plate diameter, m

D_e	hydraulic diameter of liquid channel defined by Equation (6.19), m
D_e'	hydraulic diameter of liquid channel defined by Equation (6.36), m
d	cylindrical particle diameter, m
d_b	bubble diameter, m
d_N	diameter of distributor orifice, m
d_o	diameter of distributor orifice, m
d_p	equivolume sphere diameter, m
d_{vs}	Sauter mean diameter or volume-surface diameter of bubble, m
E_s	longitudinal dispersion coefficient for solids, m^2/s
Fr_g	gas Froude number, $U_g^2/(gd_p)$
Fr_ℓ	liquid phase Froude number, $U_\ell^2/(gD)$
Fr_m	gas-liquid Froude number, $(U_g + U_\ell)^2/(gD)$
Fr_{gD}	gas Froude number based on column diameter, $U_g^2/(gD)$
f	local bubble or liquid bridging frequency, s^{-1}
f_c	modified friction factor in gas-liquid-solid fixed bed
$f_{\ell-s}$	modified friction factor in liquid-solid fixed bed
f_s	signal frequency, Hz
g	gravitational acceleration, m/s^2
H_o	static bed height, m
H_c	static height of slurry above the bottom plate, m
H_d	height of draft tube, m
K	parameter defined by Equation (6.31)
k	ratio of the wake volume fraction to the gas holdup
L	distance between two elements of conductivity probe, m
L_d	dispersion height of slurry, m
ℓ	length of cylindrical particle, m
ℓ_b	local individual bubble chord length, m

$\ell_{b, vs}$	Sauter mean bubble chord length, m
$\bar{\ell}_b$	local number average bubble chord length, m.
M	number of bubbles observed during observation period
M_3	skewness of a distribution
M_4	kurtosis of a distribution
m	exponent in Equation (6.64)
N	number of signal increments
N_B	modified bubble flow number, $\gamma/(U_b \mu_\ell)$
n	bed expansion index in Equation (6.8)
n_i	number of signals having value of $V_i \pm (\Delta V/2)$
P	pressure, mm H ₂ O
$P(V_i, \Delta V)$	probability distribution function of V_i with signal increment of ΔV
P_0	$= P(V_0, \Delta V)$
P_1	$= P(V_1, \Delta V)$
$p(d_b, \ell_b)$	probability density distribution function of measured chord length, ℓ_b , when bubble diameter is d_b
$p(V_i)$	probability density distribution function of V_i
Q_g	gas phase volumetric flow rate, m ³ /s
Q_ℓ	liquid phase volumetric flow rate, m ³ /s
R	parameter defined by Equation (6.82)
$R(d_b)$	bubble size distribution function
Re_g	superficial gas Reynolds number, $U_g \rho_g D / \mu_g$
Re''_{gmf}	Reynolds number at minimum liquid-solid fluidization, $U_{gmf}'' d_p \rho_g / \mu_g$
Re_L	Reynolds number defined by Equation (6.78)
Re'_ℓ	modified Reynolds number with equivalent diameter, $De \rho_\ell U_\ell / (\mu_\ell \epsilon_\ell)$
$Re_{\ell mf}$	Reynolds number at minimum gas-liquid-solid fluidization, $U_{\ell mf} d_p \rho_\ell / \mu_\ell$
$Re''_{\ell mf}$	Reynolds number at minimum liquid-solid fluidization, $U_{\ell mf}'' d_c \rho_\ell / \mu_\ell$

$Re_{mfg\ell}$	gas-liquid Reynolds number defined by Equation (6.44)
Re_N	Reynolds number for gas at distributor orifice, $U_N d_N \rho_g / \mu_g$.
Re_t	Reynolds number for particle terminal velocity in liquid phase, $U_t d_p \rho_\ell / \mu_\ell$.
$Re_{\ell t}$	Reynolds number for linear liquid velocity, $(U_\ell / \epsilon_\ell) d_p \rho_\ell / \mu_\ell$.
Re_∞	Reynolds number for particle terminal velocity in homogeneous fluid, $U_\infty d_p \rho_H / \mu_H$
r_H	hydraulic radius of liquid channel, m
S_a	cross-sectional area of annulus when a draft tube is installed, m^2
S_c	cross-sectional area of column, m^2
S_d	cross-sectional area of draft tube, m^2
t	observation period, s
t_{1-4}	time sequence
t_i	duration of conductivity probe in gas bubble or bubble time, s
\bar{t}_i	average bubble time, s
t_{i1}	bubble time measured from the upper element of probe, s
t_{i2}	bubble time measured from the lower element of probe, s
t_{tot}	total test time, s
U_b	local number average bubble velocity, m/s
U_g	superficial gas velocity, $\frac{\text{gas volumetric flow rate}}{\text{cross-sectional area of column}}$, m/s
U_{gc}	critical gas velocity for complete suspension of particles at zero liquid velocity, m/s
U_{gmf}	minimum gas velocity for three-phase incipient fluidization, m/s
U_{gmf}''	minimum gas velocity for gas-solid incipient fluidization, m/s
U_H	homogeneous fluid velocity, defined by Equation (6.3), m/s
U_ℓ	superficial liquid velocity, $\frac{\text{liquid volumetric flow rate}}{\text{cross-sectional area of column}}$, m/s
$(U_\ell)_{dc}$	transition liquid velocity between dispersed and coalesced bubble flow, m/s.
$U_{\ell mf}$	minimum liquid velocity for three-phase fluidization, m/s

$U_{\ell mf}''$	minimum liquid velocity for liquid-solid fluidization, m/s
$U_{\ell t}$	particle transport liquid velocity in gas-liquid medium, m/s.
U_N	superficial gas velocity based on orifice area, m/s.
U_s	gas-liquid slip velocity, $= U_g/\varepsilon_g - U_\ell/\varepsilon_\ell$, m/s
U_{SN}	settling velocity of solid particles in aerated column, m/s
U_t	particle terminal velocity in liquid phase, m/s
U_z'	axial component of liquid turbulence intensity, m/s
U_∞	terminal velocity of individual particle in homogeneous fluid, m/s
V	signal voltage, V
V_i	discrete signal value, V
V_L	relative linear velocity between liquid and particles defined by Equation (6.78), m/s
V_{max}	maximum of the signal voltage, V
V_s	particle pickup velocity, m/s
$V(t)$	voltage-time trace signal, V
\bar{V}	mean value of $V(t)$
V_0	signal voltage of gas phase for conductivity probe, V
V_1	signal voltage of liquid phase for conductivity probe, V
Var	variance of a distribution
Z	height above distributor, m
$Z(\ell_b)$	measured bubble length distribution function

Greek letters:

α	fraction of gas phase holdup over total fluid volume fraction, $= \varepsilon_g/(\varepsilon_g + \varepsilon_\ell)$
α_{mf}	fraction of gas phase holdup over total fluid volume fraction at minimum fluidization.
β	$= U_g / (U_g + U_\ell)$

ΔP	pressure drop, mm H ₂ O
Δt	time increment, s
$\Delta \tau$	time shift between two signals from same probe, s
ΔV	signal increment, V
$\bar{\delta}_a$	average absolute deviation defined by Equation (6.56)
$\bar{\delta}_s$	root mean square deviation defined by Equation (6.57)
ε	total fluid volume fraction = $\varepsilon_g + \varepsilon_\ell$, m ³ /m ³
ε_o	static bed voidage, m ³ /m ³
ε_g	gas holdup, m ³ /m ³
ε_ℓ	liquid holdup, m ³ /m ³
ε_{mf}	total fluid volume fraction under incipient fluidization condition, m ³ /m ³
ε_s	solids holdup, m ³ /m ³
ϕ	particle sphericity
γ	liquid surface tension, N/m
γ_f	solids relative wettability; for all systems tested in this study, $\gamma_f = 1$
μ_g	gas viscosity, Ns/m ²
$\mu_{g\ell}$	viscosity of gas-liquid mixture defined by Equation (6.41), Ns/m ²
μ_H	pseudo-homogeneous fluid viscosity defined by Equation (6.5), Ns/m ²
μ_ℓ	liquid viscosity, Ns/m ²
ρ_c	apparent continuous phase density defined by Equation (6.67), kg/m ³
ρ_g	gas phase density, kg/m ³
$\rho_{g\ell}$	density of gas-liquid mixture defined by Equation (6.42), kg/m ³
ρ_H	pseudo-homogeneous fluid density defined by Equation (6.4), kg/m ³
ρ_ℓ	liquid phase density, kg/m ³
ρ_s	particle density, kg/m ³
σ_ℓ	standard deviation of bubble chord length, m
σ_t	standard deviation of bubble time, s

σ_v standard deviation of $V(t)$, V
 τ_1, τ_2 time shift between two elements of conductivity probe defined in Figure 2.8, s

References

- Abraham, M., A. S. Khare, S. B. Sawant and J. B. Joshi, "Critical Gas Velocity for Suspension of Solid Particles in Three-Phase Bubble Columns", *Ind. Eng. Chem. Res.*, **31**, 1136-1147 (1992).
- Akita, K. and F. Yoshida, "Gas Holdup and Volumetric Mass Transfer Coefficient in Bubble Columns," *Ind. Eng. Chem. Proc. Des. Dev.*, **12**, 76-80 (1973).
- Annunziato, M. and G. Girardi, "Statistical Methods to Identify Two-Phase Regimes: Experimental Results for Vertical Large Diameter Tubes", *2nd International Conference on Multi-Phase Flow*, London, 361-380, (1985).
- Babu, S. P., B. Shah and A. Talwalkar, "Fluidization Correlations for Coal Gasification Materials — Minimum Fluidization Velocity and Fluidized Bed Expansion Ratio," *AIChE Symp. Ser.*, **74**(176): 176-186 (1978).
- Bach, H. F. and T. Pilhofer, "Variation of Gas Holdup in Bubble Columns with Physical Properties of Liquids and Operating Parameters of Columns," *Germ. Chem. Eng.*, **1**, 270-275 (1978).
- Barnea, D., O. Shohan and Y. Taitel, "Flow Pattern Characterization in Two Phase Flow by Electrical Conductance Probe," *Int. Multiphase Flow*, **6**, 387-397 (1980).
- Beaver, L. E. and L.-S. Fan, "Experimental Observations in a Cocurrent Gas-Liquid-Solid Semifluidized Bed with Gas as the Continuous Phase," *J. Chinese Inst. Chem. Engrs.*, **15**, 159-168 (1984).
- Begovich, J. M. and J. S. Watson, "Hydrodynamic Characteristics of Three-Phase Fluidized Beds," in *Fluidization*, Eds., J. F. Davidson and D. L. Keairns, Cambridge Univ. Press, Cambridge, 190-195 (1978).
- Begovich, J. M., *Hydrodynamics of Three-Phase Fluidized Beds*, Oak Ridge National Laboratory, ORNL/TM-6448, Virginia (1978).
- Brereton, C. M. H. and J. R. Grace, "Microstructural Aspects of the Behaviour of Circulating Fluidized Beds," *Chem. Eng. Sci.*, **48**, 2565-2572 (1993).
- Bhatia, V. K. and N. Epstein, "Three-Phase Fluidization: A Generalised Wake Model," in *Fluidization and Its Applications*, Ed., H. Angelino, Cépadues-Editions, Toulouse, 380-392 (1974).

- Bloxom, S. R., J. M. Costa, J. Herranz, G. L. Maxwell and S. R. Roth, *Determination and Correlation of Hydrodynamic Variables in a Three-Phase Fluidized Bed*, Part IV, ORNL-MIT-219, M. I. T. School of Chem. Eng. Practice, Oak Ridge, Tennessee (1975).
- Bly, M. J. and R. M. Worden, "The Effects of Solids Density and Void Fraction on the Bubble Rise Velocity in a Liquid-Solid Fluidized Bed," *Chem. Eng. Sci.* 47, 3281-3288, (1992).
- Brauner, N. And D. Barnea, "Slug/Churn Transition in Upward Gas-Liquid Flow," *Chem. Eng. Sci.*, 41, 159-163 (1986).
- Burgess, J. M. and P. H. Calderbank, "The Measurement of Bubble Parameters in Two-Phase Dispersions-I," *Chem. Eng. Sci.* 30, 743-750 (1975).
- Burgess, J. M. and P. H. Calderbank, "The Measurement of Bubble Properties in Two-Phase Dispersions-III," *Chem. Eng. Sci.*, 30, 1511-1518 (1975).
- Burgess, J. M., A. G. Fane and C. J. D. Fell, "Application of an Electroresistivity Probe Technique to a Two-Dimensional Fluidized Bed," *Trans. IChemE*, 59, 249-252 (1981).
- Chen, Z., C. Zheng, Y. Feng and H. Hofmann, "Modeling of Three-Phase Fluidized Beds based on Local Bubble Characteristics Measurements," *Chem. Eng. Sci.*, 50, 231-236 (1995).
- Chern, S.-H., K. Muroyama and L.-S. Fan, "Hydrodynamics of Constrained Inverse Fluidization and Semifluidization in a Gas-Liquid-Solid System," *Chem. Eng. Sci.*, 38, 1167-1174 (1983).
- Chern, S.-H., L.-S. Fan and K. Muroyama, "Hydrodynamics of Cocurrent Gas-Liquid-Solid Semifluidization with Liquid as the Continuous Phase," *AIChE J.*, 30, 288-294, (1984).
- Chitester, D. C., R. M. Kornosky, L.-S. Fan and J. P. Danko, "Characteristics of Fluidization at High Pressure," *Chem. Eng. Sci.*, 39, 253-261 (1984).
- Choi, J. M., J. E. Soh and S. D. Kim, "Bubble Size and Frequency in Gas Fluidized Beds," *J. Chem. Eng. Japan*, 21, 171-178 (1988).
- Clark, N. N. and R. Turton, "Chord Length Distributions Related to Bubble Size Distributions in Multiphase Flows," *Int. J. Multiphase Flow*, 14, 413-424(1988).
- Clift, R., J. R. Grace and M. E. Weber, *Bubbles, Drops and Particles*, Academic Press, New York (1978).
- Costa, E., A. de L., and P. Garcia, "Fluid Dynamics of Gas-Liquid-Solid Fluidized Beds," *Ind. Eng. Chem. Process Des. Dev.*, 25, 849-854 (1986).

- Darton, R. C., "The Physical Behaviour of Three-Phase Fluidized Beds," Chapter 15 in *Fluidization*, Second Edition, Eds., J. F. Davidson, R. Clift and D. Harrison, 495-528 (1985).
- Darton, R. C. and D. Harrison, "Gas and Liquid Hold-up in Three-Phase Fluidization," *Chem. Eng. Sci.*, 30, 581-586 (1975).
- Darton, R. C., and D. Harrison, "Some Properties of Gas Bubbles in Three-Phase Fluidized Beds," *Multi-Phase Flow Systems Symposium* (2nd International Conference on Multi-phase Flow), p.B1-28, London, England (1985).
- Das, R. K. and S. Pattanayak, "Electrical Impedance Method For Flow Regime Identification in Vertical Upward Gas- Liquid Two-Phase Flow," *Meas. Sci. Technol.*, 4, 1457-1463 (1993).
- Das, R. K. and S. Pattanayak, "Bubble to Slug Flow Transition in Vertical Upward Two-Phase Flow Through Narrow Tubes," *Chem. Eng. Sci.*, 49, 2163-2172 (1994).
- Dayan, A. and S. Zalmanovich, "Axial Dispersion and Entrainment of Particles in Wakes of Bubble," *Chem. Eng. Sci.*, 37, 1253-1257 (1982).
- de Lasa, H., S.L.P.Lee, and M.A.Bergougnou, "Bubble Measurement in Three-Phase Fluidized Beds Using a U-Shaped Optical Fiber," *Can. J. Chem. Eng.*, 62, 166-169 (1984).
- Deshpande, D. A., M. D. Deo and F. V. Hanson, "Correlations for Effective Bubble Rise Velocity in Three-Phase Ebbulleted Beds," *Fuel Processing Technology*, 32, 3-23 (1992).
- Efremov, G. I. and I. A. Vakhrushev, "A Study of the Hydrodynamics of Three-Phase Fluidized Beds," *Intern. Chem. Engng.*, 10, 37-48 (1970).
- El-Temtamy, S.A. and N. Epstein, "Simultaneous Solids Entrainment and De-Entrainment above a Three-Phase Fluidized Bed," in *Fluidization*, Eds., J. R. Grace and J. M. Matsen, 519-528 (1980).
- Epstein, N., "Three-Phase Fluidization: Some Knowledge Gaps," *Can. J. Chem. Eng.*, 59, 649-657 (1981).
- Ergun, S., "Fluid Flow through Packed Columns," *Chem. Eng. Prog.*, 48, 89-94 (1952).
- Ermakova, A., G. K. Ziganskin and M. G. Slin'ko, "Hydrodynamics of a Gas-Liquid Reactor with a Fluidized Bed of Solid Matter," *Theor. Found. Chem. Eng.*, 4, 84-89, (1970).
- Fan, L.-S., S. H. Chern and K. Muroyama, "Solids Mixing in a Gas-Liquid-Solid Fluidized Bed Containing a Binary Mixture of Particles," *AIChE J.*, 30, 858-860, (1984).

- Fan, L.-S., A. Matsuura and S.-H. Chern, "Hydrodynamic Characteristics of a Gas-Liquid-Solid Fluidized Bed Containing a Binary Mixture of Particles," *AIChE J.*, 31, 1801-1810 (1985).
- Fan, L.-S., S. Satija and K. Wisecarver, "Pressure Fluctuation Measurements and Flow Regime Transitions in Gas-Liquid-Solid Fluidized Beds," *AIChE J.*, 32, 338-340 (1986).
- Fan, L.-S., R.-H. Jean and K. Kitato, "On the Operating Regimes of Cocurrent Upward Gas-Liquid-Solid Systems with Liquid as the Continuous Phase," *Chem. Eng. Sci.*, 47, 1853-1856 (1987).
- Fan, L.-S., *Gas-Liquid-Solid Fluidization Engineering*, Butterworth Publishers, Boston, Massachusetts (1989).
- Fernandes, R. C., R. Semiat and A. E. Dukler, "Hydrodynamic Model for Gas-Liquid Slug Flow in Vertical Tubes," *AIChE J.*, 29, 981-989 (1983).
- Franca, F., M. Acikgoz, R. T. Lahey and A. Clausse, "The Use of Fractal Techniques for Flow Regime Identification," *Int. J. Multiphase Flow*, 17, 545-552 (1991).
- Friedel, L., P. Herbrechtsmeier and R. Steiner, "Mean Gas Holdup in Down-Flow Bubble Columns," *Ger. Chem. Eng.*, 3, 342-346 (1980).
- Geldart, D. and J. R. Kelsey, "The Use of Capacitance Probes in Gas Fluidized Beds," *Powder Technol.*, 6, 45-50 (1972).
- Glicksman, L. R., W. K. Lord and M. Sakagam, "Bubble Properties in Large-Particle Fluidized Beds," *Chem. Eng. Sci.*, 42, 479-491 (1987).
- Grace, J. R. and J. Tuot, "A Theory for Cluster Formation in Vertically Conveyed Suspension of Intermediate Density," *Trans. IChemE.*, 57, 49-54 (1979).
- Grace, J. R., "Fluidization", Chapter 8 in *Handbook of Multiphase Systems*, Ed., G. Hetsroni, Hemisphere, Washington, D. C., 1-240 (1982).
- Griffith, P. and G. B. Wallis, "Two-Phase Slug Flow," *J. Heat Transfer*, 83, 307-320 (1961).
- Govier, G. W. and L. Short, "The Upwards Vertical Flow of Air-Water Mixtures II. Effect of Tubing Diameter on Flow Pattern, Holdup and Pressure Drop," *Can. J. Chem. Eng.*, 35, 58-70 (1957).
- Govier, G. W., B. A. Radford and J. S. C. Dunn, "The Upwards Vertical Flow of Air-Water Mixtures I. Effect of Air and Water-Rates on Flow Pattern, Holdup and Pressure Drop," *Can. J. Chem. Eng.*, 36, 195-202 (1958).

- Gunn D. J. and H. M. Al-Doori, "The Measurement of Bubble Flows in Fluidized Beds by Electrical Probe," *Int. J. Multiphase Flow*, 11, 535-551 (1985).
- Han, J. H. and S. D. Kim, "Radial Dispersion and Bubble Characteristics in Three-Phase Fluidized Beds," *Chem. Eng. Comm.*, 94, 9-26 (1990).
- Han, J. H. and S. D. Kim, "Bubble Chord Length Distribution in Three-Phase Fluidized Beds," *Chem. Eng. Sci.*, 48, 1033-1039 (1993).
- Hasan, A. R., and C. S. Kabir, "Two-Phase Flow in Vertical and Inclined Annuli," *Int. J. Multiphase Flow*, 18, 279-293 (1992).
- Hatano, H., I. A. H. Khattab, K. Nakamura and M. Ishida, "Spatio-Temporal Measurement of Bubble Properties in Free-Bubble Fluidized Beds," *J. Chem. Eng. Japan*, 19, 425-430 (1986).
- Heck, J. and U. Onken, "Hysteresis Effects in Suspended Solid Particles in Bubble Columns with and without Draft Tube," *Chem. Eng. Sci.*, 42, 1211-1212 (1987).
- Henriksen, H. K. and K. Ostergaard, "On the Mechanism of Break-Up of Large Bubble in Liquids and Three-Phase Fluidised Beds," *Chem. Eng. Sci.*, 29, 626-629 (1974).
- Hewitt, G. F., *Measurement of Two-Phase Flow Parameters*, Academic Press, London (1978).
- Hikita, H., S. Asai, K. Tanigawa, K. Segawa and M. Kitao, "Gas Holdup in Bubble Column," *Chem. Eng. J.*, 20, 59-67 (1980).
- Horio, M. and R. Clift, "A Note on Terminology: 'Clusters' and 'Agglomerates'," *Powder Technol.*, 70, 196-196 (1992).
- Hu, T., Y. Zhang, H. Chao, B. Yu and Y. Wang, "A Study of Hold-up and Liquid Mixing in a Three-Phase Fluidized Bed," in *Fluidization'85 Science and Technology* (Proceedings of Second Chinese-Japan Symposium, Kunming), Eds., M. Kwauk and D. Kunii, Science Press, Beijing, 262-273 (1985).
- Hughmark, G. A., "Holdup and Mass Transfer in Bubble Columns," *Ind. Eng. Chem. Proc. Des. Dev.*, 6, 218-220 (1967).
- Imafuku, K., T-Y Wang, K. Koide and H. Kubota, "The Behavior of Suspended Solid Particles in the Bubble Column," *J. Chem. Eng. Japan*, 1, 153-158 (1968).
- Iordache, M. and O. I. Muntean, "Stochastic Approach to the Hydrodynamics of Gas-Liquid Dispersions," *Ind. Eng. Chem. Fund.*, 20, 204-207 (1981).

- Jayanti, S. and G.F. Hewitt, "Prediction of the Slug-to-Churn Flow Transition in Vertical Two-Phase Flow," *Int. J. Multiphase Flow*, **18**, 847-860 (1992).
- Jean, R.-H. and L.-S. Fan, "On the Particle Terminal Velocity in a Gas-Liquid Medium with Liquid as the Continuous Phase," *Can. J. Chem. Eng.*, **65**, 881-886 (1987).
- Jones, O. C. and N. Zuber, "The Interrelation between Void Fraction Fluctuations and Flow Patterns in Two-Phase Flow," *Int. J. Multiphase Flow*, **2**, 273-306 (1975).
- Kato, Y., A. Nishiwaki, T. Kago, T. Fukuda and S. Tanaka, "Gas Holdup and Overall Volumetric Absorption Coefficient in Bubble Columns with Suspended Solid Particles: Absorption Rate of Oxygen by an Aqueous Solution of Sodium Sulfite," *Int. Chem. Eng.*, **13**, 562-567 (1973).
- Kelessidis, V. C. and A. E. Dukler, "Modeling Flow Pattern Transitions for Upward Gas-Liquid Flow in Vertical Concentric and Eccentric Annuli," *Int. J. Multiphase Flow*, **15**, 173-191 (1989).
- Kim, S.D., C.G. Baker and M.A. Bergougnou, "Holdup and Axial Mixing Characteristics of Two Phase and Three Phase Fluidized Beds," *Can. J. Chem. Eng.*, **50**, 695-701 (1972).
- Kim, S.D., C.G. Baker and M.A. Bergougnou, "Phase Holdup Characteristics of Three Phase Fluidized Beds," *Can. J. Chem. Eng.*, **53**, 134-139 (1975).
- Kim, S.D., C.G.J. Baker and M.A. Bergougnou, "Bubble Characteristics in Three-Phase Fluidized Beds," *Chem. Eng. Sci.*, **32**, 1299-1306 (1977).
- Kim, Y. H., Y. Tsuchiyama, A. Tsutsumi and K. Yoshida, "Bubble Characteristics of Three-Phase Reactors," *Proceedings of the Asian Conference on Fluidized-Bed and Three-Phase Reactors*, Eds., K. Yoshida and S. Morooka, Sanjio-Kaikan, Tokyo, 369-375 (1988).
- Kitano, K., and K. Ikeda, "Flow Regimes of Three-Phase Fluidized Beds," *Proceedings of the Asian Conference on Fluidized-Bed and Three-Phase Reactors*, Eds., K. Yoshida and S. Morooka, Sanjio-Kaikan, Tokyo, 361-367 (1988).
- Kito, M., M. Shimida, T. Sakai, S. Sugiyama and C.Y. Wen, "Performance of Turbulent Bed Contactor: Gas Holdup and Interfacial Area under Liquid Stagnant Flow," in *Fluidization Technology*, Ed., D. L. Keairns, Hemisphere, Washington, Vol. I, 411-430 (1976).
- Koide, K., T. Yasuda, S. Iwamoto and E. Fukuda, "Critical Gas Velocity Required for Complete Suspension of Solid Particles in Solid-Suspended Bubble Column," *J. Chem. Eng. Japan*, **16**, 7-12 (1983).

- Koide, K., K. Horibe, H. Kawabata and S. Ito, "Critical Gas Velocity Required for Complete Suspension of Solid Particles in Solid-Suspended Bubble Column with Draught Tube," *J. Chem. Eng. Japan*, 17, 368-374 (1984).
- Koide, K., M. Terasawa and H. Takekawa, "Critical Gas Velocity Required for Complete Suspension of Multicomponent Solid Particle Mixture in Solid-Suspended Bubble Columns with and without Draught Tube," *J. Chem. Eng. Japan*, 19, 341-344 (1986).
- Kölbel, H. and M. Ralek, "The Fischer-Tropsch Synthesis in the Liquid Phase," *Catal. Rev.-Sci. Eng.*, 21, 225-274 (1980).
- Kumar, A., T. T. Dagaleesan, G. S. Laddha, and H. E. Hoelscher, "Bubble Swarm Characteristics in Bubble Columns," *Can. J. Chem. Eng.*, 54, 503-508 (1976).
- Kwon, H. W., Y. Kang, S. D. Kim, M. Yashima and L. T. Fan, "Bubble Length and Pressure Fluctuations in Three-Phase Fluidized Beds," *Ind. Eng. Chem. Res.*, 33 1852-1857 (1994).
- Lee, J. C., A. J. Sherrard and P.S. Buckley, "Optimum Particle Size in Three-Phase Fluidized Bed Reactors," in *Fluidization and Its Applications*, Ed., H. Angelino, Cepadues-Editions, Toulouse, 407-416 (1974).
- Lee, J. C. and N. Al-Dabbagh, "Three-Phase Fluidized Beds Onset of Fluidization at High Gas Rates," in *Fluidization*, Eds., J. F. Davidson and D. L. Keairns, Cambridge Univ. Press, Cambridge, 184-189 (1978).
- Lee, S. L. P. and H. I. de Lasa, "Characterization of Bubbles in Three Phase Fluidized Beds Using U-Shaped Optical Fiber Probes," in *Fluidization V*, Eds., K. Ostergaard and A. Sorensen, Engineering Foundation, New York, 361-368 (1986).
- Lee, S. L. P. and H. I. de Lasa, "Phase Holdups in Three-Phase Fluidized Beds," *AIChE J.*, 33, 1359-1370 (1987).
- Lee, S. L. P. and H. I. de Lasa, "Radial Dispersion Model for Bubble Phenomena in Three-Phase Fluidized Beds," *Chem. Eng. Sci.*, 43, 2445-2449 (1988).
- Lee, S. L. P. and H. I. de Lasa, "Application of a Dispersion Model for Bubble Dynamics in Three-Phase Fluidized Beds," in *Fluidization VI*, Eds., J. R. Grace, L. W. Shemilt and M. A. Bergougnou, Engineering Foundation, New York, 531-538 (1989).
- Lee, S. L. P., A. Soria and H. I. de Lasa, "Evolution of Bubble Length Distributions in Three-Phase Fluidized Beds," *AIChE J.*, 36, 1763-1767 (1990).
- Li, Y. and M. Kwauk, "The Dynamics of Fast Fluidization," in *Fluidization*, Eds., J. R. Grace and J. M. Matsen, Plenum Press, New York, 537-544 (1980).

- Liang, W. G., Q. W. Wu, Z. Q. Yu, Y. Jin and H. T. Bi, "Flow Regimes of the Three-Phase Circulating Fluidized Bed," *AIChE J.*, 41, 267-270 (1995).
- Lim, K. S. and P. K. Agarwal, "Bubble Velocity in Fluidized Beds: the Effect of Non-Vertical Bubble Rise on its Measurement using Submersible Probes and its Relationship with Bubble Size," *Powder Technol.*, 69, 239-248 (1992).
- Lin, P. Y. and T. J. Hanratty, "Detection of Slug Flow from Pressure Measurements," *Int. J. Multiphase Flow*, 13, 13-21 (1987).
- Mao, Z.-S. and A. E. Dukler, "An Experimental Study of Gas-Liquid Slug Flow Experiments in Fluids," *Experiments in Fluids*, 8, 169-182 (1989).
- Matsui, G., "Identification of Flow Regimes in Vertical Gas-Liquid Two-Phase Flow using Differential Pressure Fluctuations," *Int. J. Multiphase Flow*, 10, 711-720 (1984).
- Matsui, G., "Automatic Identification of Flow Regimes in Vertical Two-Phase Flow using Differential Pressure Fluctuations," *Nucl. Eng. Des.*, 95, 221-231 (1986).
- Matsuura, A. and L.-S. Fan, "Distribution of Bubble Properties in a Gas-Liquid-Solid Fluidized Bed," *AIChE J.*, 30, 894-903, (1984).
- Matuszkiewicz, A., J. C. Flamand and J. A. Boure, "The Bubble-Slug Flow Pattern Transition and Instabilities of Void Fraction Waves," *Int. J. Multiphase Flow*, 13, 199-217 (1987).
- Meernik, P.R. and M.C.Yuen, "An Optical Method for Determining Bubble Size Distributions--Part I: Theory," *J. Fluids Eng.*, 110, 325-331 (1988a).
- Meernik, P.R. and M.C.Yuen, "An Optical Method for Determining Bubble Size Distributions--Part II: Application to Bubble Size Measurement in a Three-Phase Fluidized Bed," *J. Fluids Eng.*, 110, 332-338 (1988b).
- Mersmann, A., "Design and Scale-Up of Bubble and Spray Columns," *Ger. Chem. Eng.*, 1, 1-11 (1978).
- Michelsen, M. K. and K. Ostergaard, "Hold-Up and Fluid Mixing in Gas-Liquid Fluidised Beds," *Chem. Eng. J.*, 1, 37-45 (1970).
- Monji, H., "Transition Mechanism from Bubble Flow to Slug Flow in a Riser," *Fluid Dynamics Research*, 11, 61-74 (1993).
- Mukherjee, R. N., P. Bhattacharya, and D. K. Taraphdar, "Studies on the Dynamics of Three-Phase Fluidization," in *Fluidization and Its Applications*, Ed., H. Angelino, Cepadues-Editions, Toulouse, 372-379 (1974).

- Muroyama, K. et al., (in Japanese) "Axial Liquid Mixing in Three-Phase Fluidized Beds," *Kagaku Kogaku Ronbunshu*, **4**, 622-628 (1978).
- Muroyama, K. and L. S. Fan, "Fundamentals of Gas-Liquid-Solid Fluidization," *AIChE J.*, **31**, 1-34 (1985).
- Muroyama, K., T. Kashiwagi and A. Yasunishi, "Bubble Swarm Characteristics in a Gas-Liquid-Solid Fluidized Bed with Gas-Liquid Cocurrent Upflow," *Proceedings of the Asian Conference on Fluidized-Bed and Three-Phase Reactors*, Eds., K. Yoshida and S. Morooka, Sanjio-Kaikan, Tokyo, 376-384 (1988).
- Nacef, S., G. Wild and A. Laurent, "Scale effects in gas-liquid-solid fluidization," *Int. Chem. Eng.*, **32**, 51-61 (1992).
- Nacef, S., S. Poncin and G. Wild, "Onset of Fluidisation and Flow Regimes in Gas-Liquid-Solid Fluidisation — Influence of the Coalescence Behaviour of the Liquid," in preprints for *Fluidization VIII*, 359-366 (1995).
- Nakazatomi, M., H. Shimizu, G. Miyake and K. Sekoguchi, "Rising Characteristics of a Single Measure of Gas Slug in Stagnant Liquid (Effect of Pressure)," *JSME International J., Series II*, **35**, 388-394 (1992).
- Narayanan, S., V. K. Bhatia and D. K. Guha, "Suspension of Solids by Bubble Agitation," *Can. J. Chem. Eng.*, **47**, 360-364 (1969).
- Nishiyama, M., T. Kawano, N. Ootake and N. Yutani, "Fluctuations in Static Pressure and the Mode of Flow in a Three-Phase Fluidized Bed," *Intern. Chem. Eng.*, **29**, 287-294 (1989).
- Ostergaard, K., "Gas-Liquid-Particle Operations in Chemical Reaction Engineering," *Adv. Chem. Eng.*, **7**, 71-137 (1968).
- Ostergaard, K. and M. L. Michelson, "Hold-Up and Axial Dispersion in Gas-Liquid Fluidized Beds. The Effect of Fluid Velocities and Particle Size," *Symp. Fund. Appl. Fluidization*, Tampa, Florida, Preprint 31D (1968).
- Ostergaard, K., "Three-Phase Fluidization," Chapter 18 in *Fluidization*, Eds., J. F. Davidson and D. Harrison, Academic Press, New York, 751-782 (1971).
- Page, R.E. and D. Harrison, "The Size Distribution of Gas Bubbles Leaving a Three-Phase Fluidized Bed," *Powder Technology*, **6**, 245-249 (1972).
- Page, R.E. and D. Harrison, "Particle Entrainment from a Three-Phase Fluidized Bed," in *Fluidization and Its Applications*, Ed., H. Angelino, Cepadues-Editions, Toulouse, 393-406 (1974).

- Pandit, A. B., and J. B. Joshi, "Three Phase Sparged Reactors -- Some Design Aspects," *Rev. Chem. Eng.*, 2, 1-84, (1984).
- Pandit, A. B., and J. B. Joshi, "Effect of Physical Properties on the Suspension of Solid Particles in Three-Phase Sparged Reactors," *Int. J. Multiphase Flow*, 13, 415-427 (1987).
- Park, W. H., W. K. Kang, C. E. Capes and G. L. Osberg, "The Properties of Bubbles in Fluidized Beds of Conducting Particles as Measured by an Electroresistivity Probe," *Chem. Eng. Sci.*, 24, 851-865 (1969).
- Peterson, D.A., R.S. Tankin and S.G. Bankoff, "Bubble Behavior in a Three-Phase Fluidized Bed," *Int. J. Multiphase Flow*, 13, 477-491 (1987).
- Ramachandran, P.A. and R. V. Chaudhari, *Three-Phase Catalytic Reactors*, Gordon and Breach Science Publishers, New York (1983).
- Richardson, J. F., "Incipient Fluidization and Particulate Systems" Chapter 2 in *Fluidization*, Eds., J. F. Davidson and H. Harrison, Academic Press, New York, 25-64 (1971).
- Rigby, G. R., G. P. Van Blockland, W. H. Park and C. E. Capes, "Properties of Bubbles in Three Phase Fluidized Beds as Measured by an Electroresistivity Probe," *Chem. Eng. Sci.*, 25, 1729-1741 (1970).
- Roy, N. K., D. K. Guha and M. N. Rao, "Suspension of Solids in a Bubbling Liquid -- Critical Gas Flow Rates for Complete Suspension," *Chem. Eng. Sci.*, 19, 215-225 (1964).
- Saxena, S. C. and G. J. Vogel, "The Measurement of Incipient Fluidisation Velocities in a Bed of Coarse Dolomite at Temperature and Pressure", *Trans. Inst. Chem. Eng.*, 55, 184-189 (1977).
- Shah, Y. T., *Gas-Liquid-Solid Reactor Design*, McGraw-Hill, New York (1979).
- Shah, Y. T., B. G. Kelkar, S. P. Godbole and W.-D. Deckwer, "Design Parameters Estimations for Bubble Column Reactors", *AIChE J.*, 28, 353-379 (1982).
- Sisak, Cs. and Z. Ormos, "Investigation of Three-Phase Fluidised Systems. II.----The Effect of Distributor Type and Flow Conditions on the Parameters of Bubble Size Distribution," *Hungarian Journal of Industrial Chemistry*, 13, 503-519 (1985a).
- Sisak, Cs. and Z. Ormos, "Investigation of Three-Phase Fluidised Systems. III.----Characterization of Size Distributions of Bubbles Produced by a Venturi-Type Gas Distributor," *Hungarian Journal of Industrial Chemistry*, 13, 521-531 (1985b).

- Smith, D. N., J. A. Ruether, Y. T. Shah and M. N. Badgujar, "Modified Sedimentation-Dispersion Model for Solids in a Three-Phase Slurry Column," *AIChE J.*, 32, 426-436 (1986).
- Snedecor, G. W. and W. G. Cochran, *Statistical Methods*, 8th ed., Iowa State Univ. Press, Ames (1989).
- Song, G.-H., F. Bavarian and L.-S. Fan, "Hydrodynamics of Three-Phase Fluidized Bed Containing Cylindrical Hydrotreating Catalysts," *Can. J. Chem. Eng.*, 67, 265-275 (1989).
- Soria, A. and H. de Lasa, "Kinematic Waves and Flow Patterns In Bubble Columns and Three-Phase Fluidized Beds," *Chem. Eng. Sci.*, 47, 3403-3410 (1992).
- Spedding, P. L. and V. T. Nguyen, "Regime Maps for Air Water Two Phase Flow," *Chem. Eng. Sci.*, 35, 779-793 (1980).
- Spedding, P. L. and D. R. Spence, "Flow Regimes in Two-Phase Gas-Liquid Flow," *Int. J. Multiphase Flow*, 19, 245-280 (1993).
- Sun, Y. and S. Furusaki, "Characteristics of Immobilized Acetobacter Aceti in a Three-Phase Fluidized Bed Bioreactor," in *Fluidization VI*, Eds., J. R. Grace, L. W. Shemilt and M. A. Bergougnou, Engineering Foundation, New York, 475-484 (1989).
- Taitel, Y., D. Bornea, and A. E. Dukler, "Modelling Flow Pattern Transitions for Steady Upward Gas-Liquid Flow in Vertical Tubes," *AIChE J.*, 26, 345-354 (1980).
- Turpin, J. L. and R. L. Huntington, "Prediction of Pressure Drop for Two-Phase, Two-Component Concurrent Flow in Packed Beds," *AIChE J.*, 13, 1196-1202 (1967).
- Tutsui, T. and T. Miyauchi, "Fluidity of a Fluidized Catalyst Bed and its Effect on the Behavior of the Bubbles," *Int. Chem. Eng.*, 20, 386-393 (1980).
- Tutu, N. K., "Pressure Fluctuations and Flow Pattern Recognition in Vertical Two Phase Gas-Liquid Flows," *Int. J. Multiphase Flow*, 8, 443-447 (1982).
- Tutu, N. K., "Pressure Drop Fluctuations and Bubble-Slug Transition in Vertical Two Phase Gas-Liquid Flow," *Int. J. Multiphase Flow*, 10, 211-216 (1984).
- Ueyama, K., S. Morooka, K. Koide, H. Kaji, and T. Miyauchi, "Behavior of Gas Bubbles in Bubble Columns," *Ind. Eng. Chem. Proc. Des. Dev.*, 19, 592-599 (1980).
- Vince, M. A. and R. T. Lahey, Jr., "On the Development of an Objective Flow Regime Indicator," *Int. J. Multiphase Flow*, 8, 93-124 (1982).

- Vunjak-Novakovic, G., G. Jovanovic, Lj. Kundakovic and B. Obradovic, "Flow Regimes and Liquid Mixing in a Draft Tube Gas-Liquid-Solid Fluidized Bed," *Chem. Eng. Sci.*, **47**, 3451-3458 (1992).
- Wallis, G. B., *One-Dimensional Two-Phase Flow*, McGraw-Hill, New York (1969).
- Weimer, A. W., D. C. Gyure and D. E. Clough, "Application of a Gamma-Radiation Density Gauge for Determining Hydrodynamic Properties of Fluidized Beds," *Powder Technol.*, **44**, 179-194 (1985).
- Weisman, J. and S. Y. Kang, "Flow Pattern Transitions in Vertical and Upwardly Inclined Lines," *Int. J. Multiphase Flow*, **7**, 271-291 (1981).
- Wen, C. Y. and Y. H. Yu, "Mechanics of Fluidization," *Chem. Eng. Prog. Symp. Ser.*, **62**(62), 100-111 (1966).
- Werther, J., "Bubbles in Gas Fluidized Bed - Part I," *Trans. IChemE*, **52**, 149-159 (1974).
- Wittmann, K., H. Helmrich and K. Schugerl, "Measurements of Bubble Properties in Continuously Operated Fluidized Bed Reactors at Elevated Temperatures," *Chem. Eng. Sci.*, **36**, 1673-1677 (1981).
- Wild, G., M. Saberian, J.-L. Schwartz, and J.-C. Charpentier, "Gas-Liquid-Solid Fluidized-Bed Reactors: State of the Art and Industrial Possibilities," *Intern. Chem. Engng.*, **24**, 639-678 (1984).
- Yang, X. L., G. Wild and J. P. Euzen, "Study of Liquid Retention in Fixed-Bed Reactors with Upward Flow of Gas and Liquid," *Intern. Chem. Engng.*, **33**, 72-84 (1993).
- Yerushalmi, J., D. H. Turner and A. M. Squires, "The Fast Fluidized Bed," *Ind. Eng. Chem. Process Des. Dev.*, **15**, 47-53 (1976).
- Yerushalmi, J., "High Velocity Fluidized Beds," Chapter 7 in *Gas Fluidization Technology*, Ed., D. Geldart, John Wiley & Sons, Chichester, 155-196 (1986).
- Yu, Y. H. and S. D. Kim, "Bubble Characteristics in the Radial Direction of Three-Phase Fluidized Beds," *AIChE J.*, **34**, 2069-2072 (1988).
- Zhang, J.-P., N. Epstein, J. R. Grace and J. Zhu, "Minimum Liquid Fluidization Velocity of Gas-Liquid Fluidized Beds," *Trans. IChemE*, **73**, 347-353 (1995).
- Zheng, C., B. Yao and Y. Feng, "Flow Regime Identification and Gas Hold-up of Three-Phase Fluidized System," *Chem. Eng. Sci.*, **43**, 2195-2200 (1988).

Appendix A Computer Programs for Data Acquisition and Processing

A.1 Program for Data Acquisition and Calculation of PDF

```
*****
' COND1.BAS                                DAS-1600/1400/1200
'
' - To run from the QuickBASIC Enviroment (up to Ver 4.5) you must load
'   the appropriate quick library using the command line switch /L,
'   as follows
'
'       QB /L D1600Q40 QBEXAMP1      (using version 4.0)
'       QB /L D1600Q45 QBEXAMP1      (using version 4.5)
'
' - To run from the QuickBASIC Enviroment (Ver 7.0 and up) you must load
'   the supplied quick library: D1600QBX.QLB using the command line
'   switch /L, as follows
'
'       QBX /L D1600QBX QBEXAMP1
'
' [IMPORTANT] When using QBX, make sure to replace the $INCLUDE file
'       Q4IFACE.BI below with Q7IFACE.BI (both supplied to you
'       with this software)
'
*****

' This file includes all function DECLARation supported by the driver.
'   $INCLUDE: 'Q4IFACE.BI'
' Dimension integer array to recieve A/D data. Note that, for reliable
' operation, this array should dimensioned twice a big as needed.
'
' Statement of subroutine

COMMON SHARED max1, max2, min1, min2 AS SINGLE
COMMON SHARED p1(), p2()
COMMON SHARED X1(), Y1(), X2(), Y2()
COMMON SHARED contr1, K1, K2, MA, MI AS INTEGER 'bubble number, control the loop
DECLARE SUB SignalMM (FIN$, TP AS INTEGER)
DECLARE SUB Compress (FIN$, TP AS INTEGER)
DECLARE SUB Probability (FIN$, TP AS INTEGER)

REM $DYNAMIC
DIM BUFFA(30000) AS INTEGER
REM $STATIC

' Variable used by driver functions.
DIM NumOfBoards AS INTEGER
DIM DERR AS INTEGER      ' Error flag
DIM STARTINDEX AS INTEGER ' Actual Index where data starts
DIM DEVHANDLE AS LONG    ' Device Handle
DIM ADHANDLE AS LONG     ' A/D Frame Handle
```

```

DIM STATUS AS INTEGER      ' Holds Status durin DMA
DIM count AS LONG          ' Holds DMA transfer count
DIM ADDR AS LONG           ' Holds address needed by KSetDMABuf
DIM TFP AS LONG            ' TOTAL SAMPLE POINT

DIM FF AS STRING           ' SAVED DATA FILE NAME
DIM CR AS LONG             ' CLOCK RATE=10MHz/F
DIM D1 AS SINGLE           ' REAL DATA CHANNEL 1
DIM D2 AS SINGLE           ' REAL DATA CHANNEL 2

DIM FIN AS STRING          'EXPERIMENT RUN NUMBER
DIM KEY1 AS STRING         'TEMPERATELY FILE NAME
DIM FF1 AS STRING          'FOR CHECKING THE PROGRAM
DIM DELAY AS STRING        'TOTAL POINT IN TEMPERATELY FILE
DIM TP AS INTEGER

DIM p1(110), p2(110), XP1(110), XP2(110) 'PROBABILITY FUNCTION
DIM X1(3000), Y1(3000), X2(3000), Y2(3000) 'COMPRESSED DATA
DIM I AS INTEGER
DIM X, Y AS SINGLE         'USED FOR SCREEN DISPLAY
DIM FB1, FB2, EPG1, EPG2 AS SINGLE      'BUBBLE FREQUENCY AND HOLDUP

DIM PTR1, PTR2 AS SINGLE   'USED FOR SEARCH PDF PEAK
DIM TRA1, TRA2, TRB1, TRB2 AS INTEGER   'USED FOR PDF PEAKS POSITION

```

```

-----
CLS
COLOR 10, 8
LOCATE 1, 3:
PRINT "COND1.BAS          DAS-1600/1400/1200"
PRINT
PRINT "  This program can be used to"
PRINT "    (1) acquise data, "
PRINT "    (2) calculate the probability density function (PDF) of the data"
PRINT "    (3) calculate the probability function of Ti"
PRINT
PRINT "  Make sure follow things before start this program"
PRINT
PRINT "    1. Two channels, 0# and 1# will be scanned"
PRINT "    2. Sampling frequency is 2500 Hz"
PRINT "    3. Sampling time is 3 sec. for every loop."
PRINT "      Note, the total sampling time will equal to (3 sec.X contr1)"
PRINT "      The max. contr1 is 40. "
PRINT "    4. If the number of the bubble is greater than 300, this program"
PRINT "      will stop even at (contr1 < 10)."
PRINT "    5. Several results are available."
PRINT "      (a) PDF (in the form of 4 column, 1st and third are X-axes)"
PRINT "          will be saved in E:\JP\XXXX-p.dat"
PRINT "      (b) Compressed data (in the form 4 column,X1(),Y1()....)"
PRINT "          will be saved in E:\JP\XXXX-c.dat"
PRINT "      (c) The probability function of bubble time (4 columns)"
PRINT "          will be saved in E:\JP\XXXX-s.dat"

PRINT

```



```

COLOR 7, 8
DELAY$ = INPUT$(1)
-----
'Name the results file.

  INPUT "Input 4 characters to name the results file (automatic with '.DAT'):"; FF1$
5 IF LEN(FF1$) <> 4 THEN
  BEEP: INPUT "File name should has 4 charaters. Type it again. ", FF1$
  PRINT
  GOTO 5
END IF
ON ERROR GOTO ErrorHandler
  OPEN "E:\JP\" + FF1$ + ".DAT" FOR INPUT AS #2
  OPEN "E:\JP\" + FF1$ + "-p.DAT" FOR INPUT AS #2
  CLOSE #2
  COLOR 13, 8
  BEEP: PRINT FF1$; : COLOR 14, 8: PRINT " has been used. Enter another file name. "
  COLOR 12, 8: INPUT "If you want to overwrite it TYPE y, if not TYPE file name again"; a$
  PRINT
  COLOR 7, 8
  IF a$ = "Y" OR a$ = "y" THEN
  GOTO ok
  ELSE
  FF1$ = a$
  END IF
  GOTO 5
ok:
  CLOSE #2

  PRINT "Sampling time (T) times Sampling frequency (f) should <=7500"
1010 INPUT "What is the sampling time"; T
  INPUT "What is the sampling frequency"; F
  COLOR 11, 12
  PRINT "Time="; T; " sec.", "Frequency="; F; "Hz."
  COLOR 7, 8
  INPUT "Are you sure for T and F ? Y/N"; KEY1$
  IF KEY1$ = "Y" OR KEY1$ = "y" THEN GOTO 1020 ELSE GOTO 1010
  T = 3
  F = 2500
1020 CLS
-----
' STEP 1: This step is mandatory; it initializes the internal data tables
' according to the information contained in the configuration file
' DAS1600.CFG. Specify another filename if you are using a different
' configuration file. (ie. DAS1400.CFG, DAS1200.CFG)
,
a$ = "U3-P1200.CFG" + CHR$(0)
DERR = DAS1600DEVOPEN%(SSEGADD(a$), NumOfBoards)
IF DERR <> 0 THEN BEEP: PRINT "ERROR "; HEX$(DERR); " OCCURRED DURING '..DEVOPEN'":
STOP
-----
' STEP 2: This step is mandatory; it establishes communication with the driver
' through the Device Handle.
DERR = DAS1600GETDEVHANDLE%(0, DEVHANDLE)

```

```

IF (DERR <> 0) THEN BEEP: PRINT "ERROR "; HEX$(DERR); " OCCURRED DURING
'..GETDEVHANDLE'": STOP
-----
' STEP 3: To perform any A/D operations, you must first get a Handle to an
' A/D Frame (Data tables inside the driver pertaining to A/D operations).
DERR = KGetADFrame%(DEVHANDLE, ADHANDLE)
IF (DERR <> 0) THEN BEEP: PRINT "ERROR "; HEX$(DERR); " OCCURRED DURING
'KGETADFRAME'": STOP
-----
' STEP 4: Before specifying the destination buffer for the acquired data, you
' must first call KMAKEDMABuf% to determine a suitable buffer address for the
' DMA controller to use.
TFP = INT(T * F * 2)
LOCATE 15, 1
' IF TFP > 15000 OR TFP = 0 THEN COLOR 11, 12: BEEP: PRINT "WARNING!!! Buffa is too large OR =0.
Reduce T or F. T*F<=7500 BUT <> 0": COLOR 7, 8: GOTO 1010
DERR = KMAKEDMABuf%(TFP, BUFFA(), ADDR, STARTINDEX)
IF DERR <> 0 THEN PRINT "Make Dma Buffer Error": STOP
-----
' STEP 5: Assign the data buffer address to the A/D Frame and specify the
' number of A/D samples.
DAS1600ERR = KSetDMABuf%(ADHANDLE, ADDR, TFP)
IF DAS1600ERR <> 0 THEN BEEP: PRINT "ERROR "; HEX$(DAS1600ERR); " OCCURRED DURING
'KSetDMABuf'": STOP
-----
' STEP 6: Choose the Start and Stop channels and overall gain code to use
' during acquisition.
DERR = KSetStartStopChn%(ADHANDLE, 0, 1)
IF DERR <> 0 THEN BEEP: PRINT "ERROR "; HEX$(DERR); " OCCURRED DURING 'KSetStrtStpChn'":
STOP
-----
' STEP 7: This example program uses the internal (by default) conversion clock
' source; the following call specifies the divisor to the Clock Source
' (1MHz or 10MHz)
CR = 10000000 / INT(F)
DERR = KSetClkRate%(ADHANDLE, CR)
IF DERR <> 0 THEN BEEP: PRINT "ERROR "; HEX$(DERR); " OCCURRED DURING 'KSetClkRate'":
STOP
-----
' STEP 8 : Specify Free Run mode.
DERR = KSetADFreeRun%(ADHANDLE)
IF DERR <> 0 THEN BEEP: PRINT "ERROR "; HEX$(DERR); " OCCURRED DURING 'KSetADFreeRun'":
STOP
COLOR 17, 11
LOCATE 15, 1: PRINT "Press a key to START A/D Acquisition..."
COLOR 7, 8
DO
LOOP WHILE INKEY$ = ""
-----
' STEP 9: Start data acquisition according to the setup performed above.
CLS
LOCATE 10, 3
COLOR 16, 11
PRINT "THE COMPUTER IS ACUQISITING THE DATA "

```

```

PRINT ""
PRINT "DONT TOUCH THE KEYBOARD"
PRINT ""
PRINT "Time="; T; " sec.", "Frequency="; F; "Hz."
COLOR 7, 8
FOR contr1 = 1 TO 10
  DERR = KDMAStart%(ADHANDLE)
  IF DERR <> 0 THEN BEEP: PRINT "ERROR "; HEX$(DERR); " OCCURRED DURING 'KDMA'": STOP
  COLOR 16, 11
  LOCATE 15, 1: PRINT "Press a key to STOP Acquisition...  "
  COLOR 7, 8
  -----
  ' STEP 10: Monitor the status and sample transfer count untill done
  100 DERR = KDMAStatus%(ADHANDLE, STATUS, count)
  IF DERR <> 0 THEN BEEP: PRINT "ERROR "; HEX$(DERR); " OCCURRED DURING 'KDMAStatus'":
  GOTO 300
  LOCATE 13, 1: PRINT "COUNT : "; count
  IF INKEY$ <> "" GOTO 300
  IF (STATUS = 1) THEN GOTO 100
  LOCATE 15, 1: PRINT "Data acquisition completed. . .  "
  -----
  ' STEP 11: Stop DMA operation in case user interrupted or an error occurred.
  ' This step is not required upon normal termination of DMA; but it can't hurt!
  300 DERR = KDMAStop%(ADHANDLE, STATUS, count)
  IF DERR <> 0 THEN BEEP: PRINT "ERROR "; HEX$(DERR); " OCCURRED DURING 'KDMAStop'": STOP
  -----
  ' STEP 12: Save the data just acquisited. . .Use StartIndex as
  ' obtained earlier through call to KMAKEDMABuf as shown.
  COLOR 3, 9
  LOCATE 15, 1
  FF$ = "e:\jp\" + FF1$ + ".DAT"
  FF$ = "e:\jp\pzte.DAT"
  OPEN FF$ FOR OUTPUT AS #1
  FOR I% = 0 TO TFP / 2 - 1
    D1 = BUFFA(2 * I% + 1 + STARTINDEX) / 16
    D1 = SGN(D1) * (ABS(D1) - 2048) / 4096 * 10
    D2 = BUFFA(2 * I% + 2 + STARTINDEX) / 16
    D2 = SGN(D2) * (ABS(D2) - 2048) / 4096 * 10
    PRINT #1, D1, D2
  PRINT ; D1, D2
  NEXT I%
  CLOSE #1
  -----
  ' STEP 13: Free a frame and return it to the pool of available frames
  DERR = KFreeFrame%(ADHANDLE)
  IF DERR <> 0 THEN BEEP: PRINT "ERROR "; HEX$(DERR); " OCCURRED DURING 'KDMAFreeRun'":
  STOP
  -----
  ' STEP 14: Display the data on the screen in the form of graph
  TP% = TFP
  COLOR 11, 12
  LOCATE 20, 5
  INPUT "Do you want to display the ORIGINAL DATA? Y/N "; KEY1$
  IF (KEY1$ = "n" OR KEY1$ = "N") THEN GOTO 1030 ELSE 1025

```

```

' COLOR 7, 8
'1025     SignalMM FF$, TP%, max1, min1, max2, min2
'         DisplaySignal FF$, TP%, max1, min1, max2, min2
'-----
' Step 15 calculate the probability of the signal
'1030 COLOR 11, 13
'     LOCATE 20, 5
'     INPUT "Do you want to calculate the PROBABILITY DISTRIBUTION? Y/N "; KEY1$
'     IF (KEY1$ = "n" OR KEY1$ = "N") THEN GOTO 1040 ELSE 1035
'     COLOR 7, 8
1035     SignalMM FF$, TP%
         Probability FF$, TP%
         FOR I% = 1 TO 101
             XP1(I%) = XP1(I%) * (FIX(contr1) - 1) / FIX(contr1) + p1(I%) / FIX(contr1)
             XP2(I%) = XP2(I%) * (FIX(contr1) - 1) / FIX(contr1) + p2(I%) / FIX(contr1)
         NEXT I%
'-----
' Step 16: display PDF
SCREEN 1
COLOR 11, 0
LOCATE , , 0
CLS
LINE (30, 15)-(300, 90), 1, BF
LINE (30, 110)-(300, 185), 1, BF
LOCATE 1, 1
PRINT "Distribution of the DATA"
LOCATE 3, 5
PRINT "UPPER---2"
LOCATE 15, 5
PRINT "LOWER---1"
FOR I% = 1 TO 101
    X = INT(FIX(I% - 1) * 2 + 30.5)
    Y = INT(90 - XP2(I%) * 600 + .5)
    LINE (X, 90)-(X, Y), 2
    Y = INT(185 - XP1(I%) * 600 + .5)
    LINE (X, 185)-(X, Y), 2
NEXT I%
'-----
' Step 17: compress the data
         Compress FF$, TP%
'     KILL "e:\jp\TEMP.DAT"
         IF (K1 >= 500 AND K2 >= 500 AND contr1 >= 6) THEN GOTO 1050
NEXT contr1
contr1 = contr1 - 1
1050
LOCATE 13, 1: PRINT "Data acquisition completed. . . "
         BEEP: BEEP: BEEP
         DELAY$ = INPUT$(1)
LOCATE , , 1
SCREEN 0
WIDTH 80
'-----
' Step 18: save PDF
LOCATE 15, 5

```

```

PRINT "Save the PROBABILITY data."
PRINT "PDF's data will be saved in"
PRINT "   e:\jp\"; FF1$; "-p.dat"
OPEN "E:\JP\" + FF1$ + "-P.DAT" FOR OUTPUT AS #2
FOR I% = 1 TO 101
PRINT #2, FIX(I% - 1) * .01, XP1(I%), FIX(I% - 1) * .01, XP2(I%)
NEXT I%
CLOSE #2

```

'Step 19: save compressed data

```

PRINT "Compressed data will be saved in"
PRINT "   e:\jp\"; FF1$; "-c.dat"
EPG1 = 0
FOR I% = 1 TO K1
EPG1 = EPG1 + Y1(I%)
NEXT I%
EPG1 = EPG1 / F / FIX(contr1) / T
EPG2 = 0
FOR I% = 1 TO K2
EPG2 = EPG2 + Y2(I%)
NEXT I%
EPG2 = EPG2 / F / FIX(contr1) / T
FB1 = FIX(K1) / FIX(contr1) / T
FB2 = FIX(K2) / FIX(contr1) / T
OPEN "E:\JP\" + FF1$ + "-c.DAT" FOR OUTPUT AS #2
OPEN "E:\JP\TEM1.DAT" FOR OUTPUT AS #3
PRINT #2, "Sampling Time=", FIX(contr1) * T, "Sampling frequency=", F
PRINT #2, "Measuring loop", contr1
PRINT #2, "          Channel 0      Channel 1"
PRINT #2, "No. of bubbles", K1, K2
PRINT #2, "Bubble freq. ", FB1, FB2
PRINT #2, "Gas holdup   ", EPG1, EPG2
IF K1 >= K2 THEN MA% = K1 ELSE MA% = K2
FOR I% = 1 TO MA%
PRINT #2, X1(I%), Y1(I%), X2(I%), Y2(I%)
PRINT #3, Y1(I%), Y2(I%)
NEXT I%
CLOSE #3
CLOSE #2

```

'Step 20: calculate the distribution of bubble length

```

IF K1 <= K2 THEN MI% = K1 ELSE MI% = K2
TP% = 2 * MI%
FIN$ = "E:\JP\TEM1.DAT"
SignalMM FIN$, TP%
Probability FIN$, TP%

```

'Step 21: save the distribution of bubble size

```

PRINT "PDF data of the (Ti) will be saved in"
PRINT "   e:\jp\"; FF1$; "-s.dat"
OPEN "E:\JP\" + FF1$ + "-s.DAT" FOR OUTPUT AS #2
FOR I% = 1 TO 101
PRINT #2, FIX(I% - 1) * .01 * (max1 - min1) + min1, p1(I%), FIX(I% - 1) * .01 * (max2 - min2) + min2,
p2(I%)

```

```

NEXT I%
CLOSE #2
BEEP
DELAY$ = INPUT$(1)

```

'Step 22: display the distribution of the bubble size

```

SCREEN 1
COLOR 5, 3
LOCATE , , 0
CLS
LINE (30, 15)-(300, 90), 1, BF
LINE (30, 110)-(300, 185), 1, BF
LOCATE 1, 1
PRINT "Distribution of (Ti)"; "CONTR1="; contr1
LOCATE 3, 5
PRINT "UPPER---2", "K2="; K2
LOCATE 15, 5
PRINT "LOWER---1", "K1="; K1
FOR I% = 1 TO 101
X = INT(FIX(I% - 1) * 2 + 30.5)
Y = INT(90 - p2(I%) * 300 + .5)
LINE (X, 90)-(X, Y), 2
Y = INT(185 - p1(I%) * 300 + .5)
LINE (X, 185)-(X, Y), 2
NEXT I%
DELAY$ = INPUT$(1)
LOCATE , , 1
SCREEN 0
WIDTH 80
1100 END

```

ErrorHandler:
RESUME ok

SUB Compress (FIN\$, TP%)

```

PTR1 = p1(1): TRA1 = 1
PTR2 = p2(1): TRA2 = 1
FOR I = 2 TO 101
IF PTR1 < p1(I) THEN PTR1 = p1(I): TRA1 = I
IF PTR2 < p2(I) THEN PTR2 = p2(I): TRA2 = I
NEXT I
IF TRA1 >= 20 AND TRA1 <= 70 THEN
PRINT "#1---The peak is within 20%-70%"
thres1 = min1 + .5 * (max1 - min1)
ELSEIF TRA1 < 19 THEN
PTR1 = p1(101): TRB1 = 101
FOR I = 71 TO 100
IF PTR1 < p1(I) THEN PTR1 = p1(I): TRB1 = I
NEXT I
thres1 = min1 + ((FIX(TRA1) + FIX(TRB1)) / 2 - 1) * (max1 - min1) * .01
ELSE
TRB1 = TRA1
PTR1 = p1(1): TRA1 = 1

```

```

FOR I = 2 TO 19
  IF PTR1 < p1(I) THEN PTR1 = p1(I): TRA1 = I
NEXT I
thres1 = min1 + ((FIX(TRA1) + FIX(TRB1)) / 2 - 1) * (max1 - min1) * .01
END IF
IF TRA2 >= 20 AND TRA2 <= 70 THEN
  PRINT "#2---The peak is within 20%-70%"
  thres2 = min2 + .5 * (max2 - min2)
ELSEIF TRA2 < 19 THEN
  PTR2 = p2(101): TRB2 = 101
  FOR I = 71 TO 100
    IF PTR2 < p2(I) THEN PTR2 = p2(I): TRB2 = I
  NEXT I
  thres2 = min2 + ((FIX(TRA2) + FIX(TRB2)) / 2 - 1) * (max2 - min2) * .01
ELSE
  TRB2 = TRA2
  PTR2 = p2(1): TRA2 = 1
  FOR I = 2 TO 19
    IF PTR2 < p2(I) THEN PTR2 = p2(I): TRA2 = I
  NEXT I
  thres2 = min2 + ((FIX(TRA2) + FIX(TRB2)) / 2 - 1) * (max2 - min2) * .01
END IF
ST1 = max1
ST2 = max2
OPEN FIN$ FOR INPUT AS #1
FOR I = 1 TO TP% / 2
  INPUT #1, s1, s2
  IF (ST1 > thres1 AND s1 <= thres1) THEN X1(K1) = I + (contr1 - 1) * TP% / 2
  IF (ST1 <= thres1 AND s1 > thres1) THEN Y1(K1) = I + (contr1 - 1) * TP% / 2 - X1(K1): K1 = K1 + 1
  ST1 = s1
  IF (ST2 > thres2 AND s2 <= thres2) THEN X2(K2) = I + (contr1 - 1) * TP% / 2
  IF (ST2 <= thres2 AND s2 > thres2) THEN Y2(K2) = I + (contr1 - 1) * TP% / 2 - X2(K2): K2 = K2 + 1
  ST2 = s2
NEXT I
CLOSE #1
END SUB

SUB Probability (FIN$, TP%)
' This programm is used for calculation of the probability density
' distribution function of the signal or bubble chold length, etc..
' DIM P1(500), P2(500)
'3125 LET ii1 = INT((max1 - min1) * 100 + .5) + 2
'3127 LET ii2 = INT((max2 - min2) * 100 + .5) + 2
' IF ii1 > ii2 THEN ii = ii1 ELSE ii = ii2
  II = 101
  FOR I = 1 TO II
    p1(I) = 0
    p2(I) = 0
  NEXT I
  OPEN FIN$ FOR INPUT AS #1
  FOR I = 1 TO TP% / 2
    INPUT #1, s1, s2
    I1 = INT(100 * (s1 - min1) / (max1 - min1) + 1.5)
    p1(I1) = p1(I1) + 2 / TP%
  
```



```

WRITE(*,*) 'Last LETTER of the data file e.g. p or s, etc.'
READ(*, '(A)') LLD
WRITE(*,*) 'Data file name series, e.g. 123,132, etc.'
READ(*,*) L1,L2
DO 3000 L=L1,L2
Y(1)=(MOD(L,10))
Y(2)=(MOD(L/10,10))
Y(3)=(MOD(L/100,10))
X(1)=CHAR(Y(1)+48)
X(2)=CHAR(Y(2)+48)
X(3)=CHAR(Y(3)+48)
FNAME=FLD // X(3) // X(2) // X(1) // '-' // LLD
WRITE(*,*) FNAME
FN='e:\jp\' // FNAME // '.dat'
OPEN(UNIT=1,FILE=FN,STATUS='OLD')
ND=0
DO WHILE (EOF(1) .NEQV. .TRUE.)
ND=ND+1
READ(1,*) S1(ND),P1(ND),S2(ND),P2(ND)
ENDDO
CLOSE(1)

```

c-----
c Step 2: calculate mean, SD and skewness

```

MEAN1=0.
MEAN2=0.
DO I=1, ND
MEAN1=MEAN1+S1(I)*P1(I)
MEAN2=MEAN2+S2(I)*P2(I)
ENDDO
SD1=0.
SD2=0.
DO I=1, ND
SD1=SD1+P1(I)*(S1(I)-MEAN1)**2
SD2=SD2+P2(I)*(S2(I)-MEAN2)**2
ENDDO
SD1=SQRT(SD1)
SD2=SQRT(SD2)
SK1=0.
SK2=0.
DO I=1, ND
SK1=SK1+P1(I)*((S1(I)-MEAN1)/SD1)**3
SK2=SK2+P2(I)*((S2(I)-MEAN2)/SD2)**3
ENDDO
write(*,*) mean1,sd1,sk1
write(*,*) mean2,sd2,sk2

```

C-----
C Step 3: calculate Chi-squared, F-test and T-test

```

DO I=1,ND
P1(I)=P1(I)*ND
P2(I)=P2(I)*ND
ENDDO
CALL CHSTWO(P1,P2,ND,1,DFCH,CHSQ,PROBCH)

```

```

WRITE (*,*) DFCH,CHSQ,PROBCH

C-----
C Step 3.1: F-test
  IF (SD1 .GT. SD2) THEN
    F=(SD1/SD2)**2
  ELSE
    F=(SD2/SD1)**2
  ENDIF
  ND=2*ND
  DFF=ND-1
  PROBF=2.*BETAI(0.5*DFF,0.5*DFF,1/(1+F))
  IF (PROBF .GT. 1.)PROBF=2.-PROBF
  write(*,*) dff,F,PROBF

C-----
C Step 3.2: T-test
c   DFT=2*ND-2
c   VAR=(ND-1)/DFT*(SD1**2+SD2**2)
c   T=(MEAN1-MEAN2)/SQRT(VAR*(2./ND))
c   PROBT=BETAI(0.5*DFT,0.5,DFT/(DFT+T**2))
c   write(*,*) dft, t, probt

C-----
c Step 4: save the result
  FN1='E:\JP\\\FNAME\\"R.DAT'
  OPEN(UNIT=2,FILE=FN1,STATUS='UNKNOWN')
  write(2,('1x,a/')) 'Moments of the original signal distribution'
  write(2,('1x,t29,a,t42,a/')) 'Channel1','Channel2'
  write(2,('1x,a,t25,2f12.4')) 'Mean :',MEAN1,MEAN2
  write(2,('1x,a,t25,2f12.4')) 'Standard Deviation :',sd1,sd2
  write(2,('1x,a,t25,2f12.4')) 'Skewness :',sk1,sk2
  write(2,('1x,a,t25,2e12.4')) 'Chi-squared :',chsqr,probch
  write(2,('1x,a,t25,2e12.4')) 'F-test :',f,probf
  CLOSE(2)
3000 CONTINUE
  STOP
  END

```

A.3 Calculation of Bubble Velocity and Bubble Chord Length

```

DECLARE SUB Compress (FLN$, TP%)
'BVC.BAS
' This is used to calculate bubble velocity and bubble chord length.
' Source file shall be in E:\JP\ File name would be xxxx-c.dat.
' When file name is been asked by the computer, only xxxx is needed to key in.
' The probability density function of bubble velocity and cord length will
'   be saved in E:\JP\ under the name of xxxx-cr.dat.
' Total number of the bubble (K1 and K2), number of the bubbles which
' meet the criteria, as well as the distribution of the bubble velocity and
' bubble cord length will be record in this file.

```

'Statement of subroutine

```
COMMON SHARED maxv, maxl, minv, minl AS SINGLE
COMMON SHARED pv(), pl() AS SINGLE
COMMON SHARED Vb(), Lb() AS SINGLE
COMMON SHARED CONTR1, K1, K2, MA, MI AS INTEGER 'bubble number 'contrall the loop
DECLARE SUB SignalMM (TP AS INTEGER)
DECLARE SUB Probability (TP AS INTEGER)
REM $STATIC
```

' Variable used by this program.

```
DIM FF AS STRING          ' SAVED DATA FILE NAME
DIM D1 AS SINGLE          ' REAL DATA CHANNEL 1
DIM D2 AS SINGLE          ' REAL DATA CHANNEL 2
DIM FLN AS STRING         'EXPERIMENT RUN NUMBER
DIM KEY1 AS STRING
DIM S, T, FFF AS STRING   'TEMPERATELY FILE NAME
DIM DELAY AS STRING       'FOR CHECKING THE PROGRAM
DIM TP AS INTEGER         'TOTAL POINT IN TEMPERATELY FILE
DIM pv(110), pl(110) AS SINGLE 'PROBABILITY FUNCTION
DIM X1(4000), Y1(4000), X2(4000), Y2(4000) 'COMPRESSED DATA
DIM Vb(4000), Lb(4000) AS SINGLE 'BUBBLE VELOCITY AND CORD LENGTH
DIM I, J, N, Ifn, I1, I2 AS INTEGER
DIM X, Y AS SINGLE        'USED FOR SCREEN DISPLAY
DIM FB1, FB2, EPG1, EPG2 AS SINGLE 'BUBBLE FREQUENCY AND HOLDUP
DIM F AS SINGLE           'SAMPLING FREQUENCY
DIM AVEV, AVEL, SDV, SDL, SKV, SKL AS SINGLE 'AVERAGE, SD, AND SKEWNESS
DIM SUMAV, SUMAL AS SINGLE 'FOR MOMENTS CALN
```

```
-----
COLOR 10, 8
LOCATE 1, 3:
PRINT " Bubble Velocity and Bubble Cord Length.....BVC.BAS "
PRINT ""
PRINT " This program calculates bubble velocity and bubble cord length."
PRINT " Source file shall be in E:\JP\ File name would be xxxx-c.dat."
PRINT " When file name is been asked, only xxxx is needed to key in."
PRINT ""
PRINT " The results will be saved be saved in E:\JP\ under the name"
PRINT " of xxxx-cr.dat."
PRINT ""
PRINT " Total number of the bubble (K1 and K2), number of the bubbles"
PRINT " which meet the critera, as well as the distribution of the"
PRINT " bubble velocity and bubble; cord length will be recorded"
PRINT " in this file."
COLOR 3, 9
```

'Step 1: input the file name

```
INPUT "Type the FRIST letter of the experamental run No. e.g. R or C"; FFF$
INPUT "What is the serial number? (Begin with and end with. e.g. from I1 to I2)", I1, I2
FOR Ifn = I1 TO I2
  S$ = FFF$ + LTRIM$(STR$(Ifn))
  T$ = STRING$(4 - LEN(S$), "0")
  S$ = FFF$ + T$ + LTRIM$(STR$(Ifn))
  FF$ = "E:\JP\" + S$ + "-C.DAT"
INPUT "Source file? 4 characters (automatic with '-c.DAT'):"; FF1$
```

```

COLOR 7, 8
FF$ = "e:\jp\" + FF1$ + "-c.DAT"
OPEN FF$ FOR INPUT AS #1
INPUT #1, XX, XX, T, XX, XX, F
INPUT #1, XX, XX, CONTR1
INPUT #1, A$
INPUT #1, XX, XX, XX, K1, K2
INPUT #1, A$, B$
IF K1 >= K2 THEN
    MA = K1
ELSE MA = K2
END IF
FOR I% = 1 TO MA
    INPUT #1, X1(I%), Y1(I%), X2(I%), Y2(I%)
NEXT I%
CLOSE #1

```

```

' Calculate bubble velocity and cord length
J% = 0
N = 0
FOR I = 1 TO K1 - 1
100 IF I - N >= K2 - 2 THEN GOTO 300
    IF (X1(I) < X2(I - N) AND X2(I - N) < X1(I) + Y1(I) AND X1(I) + Y1(I) < X2(I - N) + Y2(I - N)) THEN
        J% = J% + 1
        Vb(J%) = .001 * F * 2 / (2 * X2(I - N) + Y2(I - N) - 2 * X1(I) - Y1(I))
        Lb(J%) = Vb(J%) * Y1(I) / F
        GOTO 200
    ELSEIF X1(I) > X2(I - N) THEN
        N = N - 1
        GOTO 100
    ELSE
        N = N + 1
    END IF
200 NEXT I
300 PRINT "OOOK"

```

```

' Calculate mean, SD, and skewness
SUMAV = 0
SUMAL = 0
FOR I = 1 TO J%
    SUMAV = SUMAV + Vb(I)
    SUMAL = SUMAL + Lb(I)
NEXT I
AVEV = SUMAV / FIX(J%)
AVEL = SUMAL / FIX(J%)
SUMAV = 0
SUMAL = 0
FOR I = 1 TO J%
    SUMAV = SUMAV + (AVEV - Vb(I)) ^ 2
    SUMAL = SUMAL + (AVEL - Lb(I)) ^ 2
NEXT I
SDV = SQR(SUMAV / FIX(J% - 1))
SDL = SQR(SUMAL / FIX(J% - 1))
SUMAV = 0

```

```

SUMAL = 0
FOR I = 1 TO J%
SUMAV = SUMAV + ((AVEV - Vb(I)) / SDV) ^ 3
SUMAL = SUMAL + ((AVEL - Lb(I)) / SDL) ^ 3
NEXT I
SKV = SUMAV / FIX(J%)
SKL = SUMAL / FIX(J%)

```

```

' Calculate the probability of the signal
      SignalMM J%
      Probability J%

```

```

'Display PDF
SCREEN 1
COLOR 11, 0
LOCATE , , 0
CLS
LINE (30, 15)-(300, 90), 1, BF
LINE (30, 110)-(300, 185), 1, BF
LOCATE 1, 1
PRINT "K1="; K1; "K2="; K2; "J%="; J%
LOCATE 2, 13
PRINT "Distribution of Velocity"
LOCATE 4, 18
PRINT "AVE-V="; AVEV
LOCATE 5, 19
PRINT "SD-V="; SDV
LOCATE 6, 19
PRINT "SK-V="; SKV
LOCATE 14, 10
PRINT "Distribution of Cord Length"
LOCATE 16, 18
PRINT "AVE-L="; AVEL
LOCATE 17, 19
PRINT "SD-L="; SDL
LOCATE 18, 19
PRINT "SK-L="; SKL
FOR I% = 1 TO 101
X = INT(FIX(I% - 1) * 2 + 30.5)
Y = INT(90 - pv(I%) * 500 + .5)
LINE (X, 90)-(X, Y), 2
Y = INT(185 - pl(I%) * 500 + .5)
LINE (X, 185)-(X, Y), 2
NEXT I%
      DELAY$ = INPUT$(1)
      LOCATE , , 1
      SCREEN 0
      WIDTH 80

```

```

'Save the distribution of bubble velocity and cord length
PRINT "PDF data of Vb and Lb will be saved in"
PRINT "      e:\jp\"; S$; "-vr.dat"
OPEN "E:\JP\" + S$ + "-vr.DAT" FOR OUTPUT AS #2
' PRINT #2, "K1=", K1, "K2=", K2, "J%=", J%

```

```

' PRINT #2, "Average", AVEV, AVEL
' PRINT #2, "SD", SDV, SDL
' PRINT #2, "Skewness", SKV, SKL
' PRINT #2, "Vb", "PDFVb", "lb", "PDFlb"
FOR I% = 1 TO 101
  PRINT #2, FIX(I% - 1) * .01 * (maxv - minv) + minv, pv(I%), FIX(I% - 1) * .01 * (maxl - minl) + minl,
  pl(I%)
NEXT I%
CLOSE #2
NEXT Ifn
END

```

SUB Probability (TP%)

' This program is used for calculation of the probability density
' distribution function of the signal or bubble chord length, etc..

```

  II = 101
  FOR I = 1 TO II
    pv(I) = 0
    pl(I) = 0
  NEXT I
  FOR I = 1 TO TP%
    I1 = INT(100 * (Vb(I) - minv) / (maxv - minv) + 1.5)
    pv(I1) = pv(I1) + 1 / FIX(TP%)
    I2 = INT(100 * (Lb(I) - minl) / (maxl - minl) + 1.5)
    pl(I2) = pl(I2) + 1 / FIX(TP%)
  NEXT I
END SUB

```

SUB SignalMM (TP%)

```

  LET maxv = -5: LET minv = 100
  LET maxl = -5: LET minl = 100
  FOR I = 1 TO TP%
    IF Vb(I) >= maxv THEN LET maxv = Vb(I)
    IF Vb(I) <= minv THEN LET minv = Vb(I)
    IF Lb(I) >= maxl THEN LET maxl = Lb(I)
    IF Lb(I) <= minl THEN LET minl = Lb(I)
  NEXT I
END SUB

```

Appendix B

Experimental Data

Air-Water Bubble Column, $U_\ell = 0.00205 \text{ m/s}$

U_g (m/s)	$\bar{\ell}_b$ (m)	σ_ℓ (m)	$\ell_{b,vs}$ (m)	U_b (m/s)	f (1/s)	ϵ_g (-)	\bar{t}_i (1/2500 s)	$(\epsilon_g U_b)/f$ (m)	$0.8467 f \bar{\ell}_b$ (m/s)	$U_b \epsilon_g$ (m/s)
0.00475	0.00762	0.00521	0.01757	0.6555	5.806	0.04544	19.28	0.00513	0.03746	0.02979
0.01065	0.00915	0.00668	0.02089	0.7353	8.319	0.07063	21.32	0.00624	0.06445	0.05193
0.02721	0.01251	0.01198	0.03696	0.9007	15.02	0.1291	22.1	0.00774	0.15909	0.11628
0.04264	0.01812	0.02502	0.09103	1.308	23.17	0.1974	21.76	0.01114	0.35546	0.2582
0.07374	0.02337	0.04929	0.3318	1.291	27.38	0.2644	24.86	0.01247	0.54176	0.34134
0.10483	0.03005	0.04979	0.1953	1.671	26.86	0.297	27.91	0.01848	0.68338	0.49629
0.1457	0.03906	0.06301	0.2589	1.857	31.56	0.3309	26.6	0.01947	1.04371	0.61448
0.20853	0.02759	0.04224	0.1463	1.87	35.06	0.3728	26.14	0.01988	0.81899	0.69714
0.26761	0.02949	0.05536	0.2336	1.791	39.44	0.4298	27.18	0.01952	0.98475	0.76977
0.35399	0.022	0.04645	0.332	2.029	42.83	0.4754	27.86	0.02252	0.79778	0.96459
0.45674	0.02528	0.04367	0.1974	1.862	54.56	0.5129	23.05	0.0175	1.16779	0.95502
0.56815	0.02367	0.03402	0.1431	2.224	56.39	0.587	25.84	0.02315	1.13009	1.30549
0.71933	0.02442	0.03748	0.176	2.516	62.67	0.6068	24.14	0.02436	1.29574	1.52671
0.90676	0.02714	0.04995	0.3392	2.503	71.06	0.7067	24.77	0.02489	1.63285	1.76887
0.98687	0.02802	0.05333	0.382	2.671	67	0.705	26.29	0.02811	1.58948	1.88306
1.32965	0.02772	0.04763	0.3658	2.915	72.39	0.8047	26.6	0.0324	1.69896	2.3457
1.89948	0.03303	0.05199	0.2398	2.751	59.06	0.8628	35.8	0.04019	1.65164	2.37356
2.33254	0.04083	0.07004	0.3033	2.548	44.5	0.9216	52.14	0.05277	1.53834	2.34824
2.43572	0.06542	0.2064	2.167	2.578	36.94	0.9086	62.18	0.06341	2.04607	2.34237
2.67123	0.05771	0.1335	0.7067	2.325	31.77789	0.9453	65.52925	0.06916	1.5527	2.19782
2.9371	0.05483	0.1169	0.6059	2.812	28.91556	0.9229	66.69	0.08975	1.34234	2.59519
3.62151	0.07394	0.2666	2.45	2.389	22.17	0.933	104.7	0.10054	1.3879	2.22894
5.30169	0.2668	0.8495	4.879	2.896	5.816	0.8574	183.6	0.42693	1.31378	2.48303
6.81641	0.7543	1.696	6.563	2.84	--	0.8119	--	--	--	2.3058

Air-Water Bubble Column, $U_\ell = 0.00615$ m/s

U_g (m/s)	$\bar{\ell}_b$ (m)	σ_ℓ (m)	$\ell_{b,vs}$ (m)	U_b (m/s)	f (1/s)	ε_g (-)	\bar{t}_i (1/2500 s)	$(\varepsilon_g U_b)/f$ (m)	$0.8467 f \bar{\ell}_b$ (m/s)	$U_b \varepsilon_g$ (m/s)
0.00472	0.00651	0.00331	0.01111	0.6201	4.883	0.03482	18	0.00442	0.02691	0.02159
0.01065	0.00802	0.00477	0.01493	0.7512	8.903	0.06463	18.15	0.00545	0.06045	0.04855
0.04003	0.01264	0.01613	0.06632	1.01	25.21	0.1771	17.29	0.0071	0.26979	0.17887
0.07045	0.013	0.01218	0.03737	1.346	30.5	0.2362	19.32	0.01042	0.3357	0.31793
0.11876	0.02311	0.03211	0.1015	1.384	31.89	0.3075	24.33	0.01335	0.62397	0.42558
0.1474	0.01971	0.02783	0.1058	1.855	37.72	0.3373	22.6	0.01659	0.62946	0.62569
0.21253	0.03876	0.05647	0.1796	1.858	35.56	0.4023	27.86	0.02102	1.16697	0.74747
0.28281	0.02391	0.04038	0.183	1.605	41.89	0.4111	23.89	0.01575	0.84801	0.65982
0.3327	0.0256	0.03896	0.1642	1.832	37.5	0.4735	31.4	0.02313	0.8128	0.86745
0.46782	0.02742	0.05491	0.3769	1.989	53.56	0.5621	26.13	0.02087	1.24343	1.11802
0.5847	0.02353	0.03697	0.1928	2.32	60.06	0.6159	25.11	0.02379	1.19652	1.42889
0.69503	0.02544	0.03545	0.1404	2.435	62	0.6266	25.23	0.02461	1.33543	1.52577
1.00411	0.02494	0.04995	0.3634	2.458	69.67	0.7103	25.45	0.02506	1.47114	1.74592
1.24977	0.026	0.04485	0.2815	3.098	70.89136	0.8169	29.6	0.0357	1.56056	2.53076
1.8499	0.03001	0.04091	0.1735	2.994	59.33	0.8584	35.39	0.04332	1.50748	2.57005
2.13386	0.04109	0.07178	0.3479	2.52045	42.94	0.9028	53.71	0.05299	1.49385	2.27547
2.38282	0.04415	0.08983	0.4168	2.015	31.44	0.9384	58.56546	0.06014	1.17524	1.89088
2.56142	0.0615	0.1222	0.5276	2.177	28.52	0.9293	65.065	0.07094	1.48504	2.02309
2.93642	0.05556	0.1366	0.9146	3.03	24.14501	0.914	65.11	0.1147	1.1358	2.76942
3.73525	0.07743	0.17	0.8155	2.637	18.59	0.9186	122.4	0.1303	1.21871	2.42235
5.20656	0.1384	0.3998	2.462	2.631	8.877	0.8795	246.12349	0.26067	1.0402	2.31396
6.70199	0.06464	0.1356	0.4803	1.44	--	0.8474	--	--	--	1.22026

Air-Water Bubble Column, $U_\ell = 0.0184$ m/s

U_g (m/s)	$\bar{\ell}_b$ (m)	σ_ℓ (m)	$\ell_{b,vs}$ (m)	U_b (m/s)	f (1/s)	ε_g (-)	\bar{t}_i (1/2500 s)	$(\varepsilon_g U_b)/f$ (m)	$0.8467 f \bar{\ell}_b$ (m/s)	$U_b \varepsilon_g$ (m/s)
0.00389	0.00693	0.00739	0.04317	0.6705	5.05	0.03172	15.67	0.00421	0.02963	0.02127
0.01065	0.00618	0.0026	0.00868	0.5987	9.848	0.06233	15.96	0.00379	0.05153	0.03732
0.02777	0.00875	0.01012	0.04954	0.8683	19.06	0.1161	15	0.00529	0.1412	0.10081
0.04017	0.01112	0.01072	0.034	1.127	26.75	0.1696	15.97	0.00715	0.25185	0.19114
0.0691	0.01596	0.02148	0.08389	1.484	35.5	0.2463	17.19	0.0103	0.4797	0.36551
0.10737	0.02574	0.06312	0.4873	1.474	34.39	0.3093	22.56	0.01326	0.74947	0.45591
0.15413	0.02797	0.05979	0.3345	1.703	38.83	0.3376	21.22	0.01481	0.91954	0.57493
0.19938	0.02105	0.03528	0.1903	1.723	34.11	0.3645	26.67	0.01841	0.60792	0.62803
0.2816	0.02661	0.04822	0.2222	1.853	43.56	0.4683	26.27	0.01992	0.9814	0.86776
0.33099	0.02912	0.05747	0.4082	1.793	47.72	0.4722	25.06	0.01774	1.17653	0.84665
0.43677	0.02804	0.04025	0.1639	1.891	48.44	0.5545	28.35	0.02165	1.14999	1.04856
0.56729	0.02529	0.0331	0.1348	2.082	58	0.5801	25.74	0.02082	1.24191	1.20777
0.70881	0.02393	0.03482	0.1653	2.245	61	0.6049	24.44	0.02226	1.2359	1.358
0.95398	0.03052	0.04772	0.2195	2.595	66.06	0.732	27.43	0.02875	1.70701	1.89954
1.17164	0.0313	0.0444	0.1746	2.975	68.52368	0.806	31.07	0.03499	1.81592	2.39785
1.43716	0.03939	0.0723	0.4616	3.209	64.06685	0.8632	37.35	0.04324	2.13664	2.77001
1.42943	0.02987	0.04681	0.2128	3.128	65.45961	0.8352	34.4	0.03991	1.65547	2.61251
1.80536	0.03601	0.05532	0.2207	3.233	56.28	0.8548	37.01	0.0491	1.71589	2.76357
2.14691	0.04761	0.1018	0.7504	3.262	53.67	0.877	40.58	0.0533	2.16343	2.86077
2.83703	0.05592	0.1015	0.4317	2.736	39.61	0.9274	58.6	0.06406	1.87536	2.53737
3.50466	0.06331	0.1259	0.5733	2.761	25.71	0.9451	91.29	0.10149	1.37812	2.60942
5.10025	0.1518	0.4699	2.888	2.49	10.75	0.9088	210.6	0.2105	1.38163	2.26291
6.01724	0.2917	1.257	8.998	1.971	5.611	0.8712	278.82334	0.30603	1.38576	1.71714

Air-Water Bubble Column, $U_\ell = 0.04554$ m/s

U_g (m/s)	$\bar{\ell}_b$ (m)	σ_ℓ (m)	$\ell_{b,vs}$ (m)	U_b (m/s)	f (1/s)	ε_g ($\frac{m}{s}$)	τ_i (1/2500 s)	$(\varepsilon_g U_b)/f$ (m)	$0.8467 f \bar{\ell}_b$ (m/s)	$U_b \varepsilon_g$ (m/s)
0.00213	0.00363	0.00369	0.01969	0.4747	2.75	0.01513	13.53	0.00261	0.00845	0.00718
0.00593	0.00337	0.00216	0.00723	0.4805	6.025	0.03417	13.75	0.00273	0.01719	0.01642
0.01541	0.0045	0.00413	0.01563	0.6142	12.13	0.07606	15.93	0.00385	0.04622	0.04672
0.02256	0.00701	0.01307	0.07062	0.6894	11.28	0.08866	19.27	0.00542	0.06695	0.06112
0.03955	0.01823	0.02249	0.07897	1.041	17.22	0.1421	20.94	0.00859	0.26579	0.14793
0.05649	0.01529	0.0218	0.08289	1.184	24.46	0.2102	21.32	0.01017	0.31665	0.24888
0.07884	0.02428	0.03411	0.1133	1.282	25.63	0.2301	22.72	0.01151	0.52688	0.29499
0.11312	0.02482	0.03922	0.1518	1.499	28.05	0.2644	23.11	0.01413	0.58945	0.39634
0.14738	0.02903	0.05633	0.2371	1.73	30.78	0.2912	23.08	0.01637	0.75653	0.50378
0.18234	0.03149	0.08199	0.6186	1.611	34.78	0.3285	24.17	0.01522	0.92729	0.52921
0.2385	0.03134	0.07767	0.5255	1.873	33.72	0.3912	29.02	0.02173	0.89474	0.73272
0.30031	0.02293	0.04032	0.1942	1.795	45	0.4305	24.15	0.01717	0.87363	0.77275
0.36385	0.02748	0.05654	0.2919	1.943	45.11	0.4673	24.97	0.02013	1.04955	0.90796
0.50749	0.02639	0.05402	0.4236	2.231	56.94	0.555	24.11	0.02175	1.27224	1.23821
0.6605	0.02444	0.0354	0.156	2.6	64.11	0.6618	25.61	0.02684	1.3266	1.72068
0.91975	0.02442	0.03491	0.1382	2.945	69.44	0.7482	26.92	0.03173	1.43571	2.20345
1.17947	0.04609	0.1119	0.662	3.291	68.24513	0.8359	37.68	0.04031	2.66312	2.75095
1.78882	0.03628	0.1025	1.055	2.975	54.39	0.8648	40.55	0.0473	1.6707	2.57278
2.12959	0.04371	0.08951	0.5153	3.126	49.5	0.8938	47.79	0.05644	1.83189	2.79402
2.8324	0.06007	0.1272	0.5828	2.766	32.78	0.9212	71.32	0.07773	1.66717	2.54804
3.54375	0.07035	0.1721	1.134	2.968	23	0.9391	101.8	0.12118	1.36995	2.78725
4.82895	0.2224	0.8004	6.102	2.8	11.42061	0.8287	161.1	0.20317	2.15049	2.32036
6.03064	0.05213	0.09117	0.3041	2.664	--	0.8872	--	--	--	2.3635

Air-Water Bubble Column, $U_\ell = 0.06375$ m/s

U_g (m/s)	$\bar{\ell}_b$ (m)	σ_ℓ (m)	$\ell_{b,vs}$ (m)	U_b (m/s)	f (1/s)	ε_g (-)	\bar{t}_i (1/2500 s)	$(\varepsilon_g U_b)/f$ (m)	$0.8467 f \bar{\ell}_b$ (m/s)	$U_b \varepsilon_g$ (m/s)
0.00426	0.00317	0.00227	0.00979	0.4592	4.125	0.02326	13.87	0.00259	0.01107	0.01068
0.01039	0.00515	0.00634	0.02481	0.5623	8.821	0.06004	17.36	0.00383	0.03846	0.03376
0.02623	0.00669	0.01069	0.05601	0.745	14.58	0.1055	18.22	0.00539	0.08258	0.0786
0.03779	0.01966	0.02832	0.1162	0.9828	19.27	0.1695	22.6	0.00864	0.32076	0.16658
0.07083	0.02233	0.0347	0.1264	1.496	30.56	0.2436	19.57	0.01192	0.57777	0.36443
0.10217	0.02957	0.0465	0.1643	1.587	31.06	0.2937	23.86	0.01501	0.77762	0.4661
0.13463	0.0244	0.04471	0.2019	1.925	33.94	0.3094	23.07	0.01755	0.70116	0.5956
0.19336	0.02856	0.05142	0.2472	2.084	39.28	0.3742	24.09	0.01985	0.94982	0.77983
0.24236	0.02591	0.04531	0.1794	1.823	48.17	0.4315	22.56	0.01633	1.05671	0.78662
0.28297	0.02347	0.03668	0.1449	2.105	47.5	0.412	21.05	0.01826	0.94389	0.86726
0.39829	0.02217	0.03655	0.1925	2.096	52.5	0.5246	24.91	0.02094	0.98546	1.09956
0.47824	0.02598	0.078	0.9961	2.585	59.05292	0.5573	22.41	0.0244	1.29895	1.44062
0.56613	0.02883	0.04568	0.1777	2.509	63.09192	0.6219	23.42	0.02473	1.54004	1.56035
0.72304	0.02607	0.05083	0.3933	2.895	69.49861	0.6865	22.77	0.0286	1.53402	1.98742
0.86606	0.03165	0.07504	0.7586	3.132	69.06	0.8195	29.74	0.03717	1.8506	2.56667
1.04504	0.02959	0.06624	0.6957	2.939	73.44	0.7666	25.62	0.03068	1.83988	2.25304
1.40042	0.03115	0.05265	0.2598	3.059	72.17	0.8139	28	0.0345	1.90339	2.48972
1.75253	0.04262	0.08875	0.6311	3.071	63.17	0.8564	33.19	0.04163	2.27949	2.63
2.11649	0.04462	0.07782	0.3462	3.483	54.44	0.8963	39.82	0.05734	2.05665	3.12181
2.80472	0.0428	0.09458	0.4579	2.553	37.33	0.8974	59.21	0.06137	1.35274	2.29106
3.49585	0.0999	0.2621	1.505	2.998	23.96	0.9252	101.1	0.11577	2.02658	2.77375
4.80319	0.1881	0.5547	3.062	2.373	6.677	0.862	247.09295	0.30635	1.06337	2.04553
5.9435	0.0861	0.2264	0.9313	1.634	7.233	0.9529	355.34957	0.21527	0.52727	1.55704

Air-Water Bubble Column, $U_\ell = 0.0729$ m/s

U_g (m/s)	$\bar{\ell}_b$ (m)	σ_ℓ (m)	$\ell_{b,vs}$ (m)	U_b (m/s)	f (1/s)	ε_g (-)	\bar{t}_i (1/2500 s)	$(\varepsilon_g U_b)/f$ (m)	$0.8467 f \bar{\ell}_b$ (m/s)	$U_b \varepsilon_g$ (m/s)
0.00211	0.00297	0.00125	0.00405	0.4609	2.383	0.02254	17.24698	0.00436	0.00599	0.01039
0.00584	0.00364	0.0028	0.01035	0.5174	4.467	0.02559	14.46	0.00296	0.01377	0.01324
0.01512	0.0054	0.0067	0.02958	0.59	10.04	0.07033	17.51	0.00413	0.0459	0.04149
0.02202	0.00637	0.01193	0.06081	0.5957	10.59	0.08384	20.42	0.00472	0.05711	0.04994
0.03849	0.0191	0.02231	0.06414	1.027	17.97	0.1428	19.92	0.00816	0.2906	0.14666
0.05499	0.01857	0.02523	0.09489	1.268	22.26	0.1785	19.82	0.01017	0.34999	0.22634
0.07675	0.02706	0.04362	0.2024	1.553	24	0.1977	20.61	0.01279	0.54986	0.30703
0.10924	0.02626	0.03346	0.09983	1.432	27.14	0.2372	21.93	0.01252	0.60342	0.33967
0.13801	0.03555	0.05914	0.2132	1.639	36.28	0.3337	22.35	0.01508	1.09199	0.54693
0.16696	0.02709	0.03867	0.1389	1.925	35.89	0.3671	26.02	0.01969	0.82318	0.70667
0.22384	0.02568	0.05378	0.3181	1.811	45.06	0.3892	22.2	0.01564	0.97971	0.70484
0.28081	0.02546	0.04323	0.1675	2.052	47.94	0.4432	23.55	0.01897	1.0334	0.90945
0.342	0.02794	0.06167	0.4442	2.187	47.06	0.4712	24.92	0.0219	1.11325	1.03051
0.47292	0.02519	0.04237	0.2394	2.454	56.11	0.5763	25.65	0.0252	1.19669	1.41424
0.59314	0.02569	0.04305	0.2143	2.873	63.2312	0.6864	22.69	0.03119	1.37533	1.97203
0.82361	0.03549	0.06193	0.2837	3.024	69.11	0.8029	28.63	0.03513	2.07663	2.42797
1.41242	0.02757	0.04497	0.2265	3.052	76.56	0.7921	25.81	0.03158	1.78711	2.41749
1.75758	0.0343	0.05615	0.303	3.072	71.94	0.8319	28.93	0.03552	2.08919	2.5556
2.10461	0.04129	0.08307	0.4343	3.1	53.22	0.8865	40.97	0.05164	1.86051	2.74815
2.79077	0.04972	0.1278	1.044	2.544	38.5	0.9261	62.38	0.06119	1.62071	2.356
3.43333	0.07662	0.1462	0.5709	3.296	21.3	0.9202	108.3	0.14239	1.38177	3.03298
4.6733	0.1912	0.5625	3.34	3.298	6.951	0.8844	310.5	0.41962	1.12525	2.91675
5.77162	0.04592	0.1318	0.8535	1.683	--	0.9248	--	--	--	1.55644

Air-Water Bubble Column, $U_\ell = 0.100$ m/s

U_g (m/s)	$\bar{\ell}_b$ (m)	σ_ℓ (m)	$\ell_{b,vs}$ (m)	U_b (m/s)	f (1/s)	ε_g (-)	\bar{t}_i (1/2500 s)	$(\varepsilon_g U_b)/f$ (m)	$0.8467 f \bar{\ell}_b$ (m/s)	$U_b \varepsilon_g$ (m/s)
0.00206	0.00286	0.00167	0.00524	0.5204	2.975	0.01985	21.64	0.00347	0.0072	0.01033
0.00562	0.00303	0.00213	0.00855	0.5132	4.392	0.02001	11.86	0.00234	0.01127	0.01027
0.01445	0.0044	0.00477	0.01938	0.5743	9.375	0.05292	14.01	0.00324	0.03493	0.03039
0.02089	0.00542	0.00874	0.04397	0.6826	12.58	0.08073	15.64	0.00438	0.05773	0.05511
0.036	0.01694	0.02386	0.09129	1.246	23.04	0.1514	16.34	0.00819	0.33045	0.18864
0.0517	0.01524	0.01673	0.05049	1.374	30.19	0.1741	14.45	0.00792	0.38955	0.23921
0.0725	0.01732	0.02554	0.08995	1.275	37.17	0.2242	14.87	0.00769	0.54507	0.28586
0.10321	0.01608	0.02609	0.1219	1.608	41.78	0.2506	14.52	0.00964	0.56881	0.40296
0.13346	0.01556	0.0255	0.117	1.545	49.39	0.279	14.23	0.00873	0.65067	0.43106
0.16415	0.02118	0.05021	0.3178	1.782	55.78	0.3185	14.52	0.01018	1.00027	0.56757
0.21168	0.02079	0.03513	0.1756	1.986	55.83	0.4084	18.33	0.01453	0.98273	0.81108
0.2664	0.02855	0.05648	0.3071	2.196	55.22	0.4457	19.86	0.01772	1.3348	0.97876
0.32293	0.03005	0.05726	0.2701	2.218	62.61	0.4871	19.01	0.01726	1.59294	1.08039
0.43702	0.02628	0.05354	0.348	2.298	65.94	0.5635	21.26	0.01964	1.46719	1.29492
0.55077	0.02424	0.03979	0.2447	3.103	70.75	0.6874	21.8	0.03015	1.45206	2.133
1.03887	0.02611	0.03702	0.1577	2.809	78.94	0.7445	23.36	0.02649	1.74508	2.0913
1.03887	0.02411	0.0312	0.1177	2.836	77.94	0.7371	23.4	0.02682	1.591	2.09042
1.38453	0.0274	0.04362	0.2296	3.013	76.94	0.7975	26.27	0.03123	1.78491	2.40287
1.71377	0.03843	0.06771	0.3239	3.429	68.89	0.8608	31.38	0.04285	2.2415	2.95168
2.06302	0.04389	0.1192	1.208	3.459	62.94	0.8769	34.47	0.04819	2.33886	3.0332
2.72139	0.07212	0.1802	1.086	2.939	39.33	0.9328	60.05	0.06971	2.40155	2.7415
3.33471	0.1062	0.3935	2.714	3.19	19.03	0.9414	121.9	0.15781	1.7111	3.00307
4.51333	0.458	1.193	4.673	3.04	4.952	0.8339	419.5	0.51193	1.92025	2.53506
5.56299	0.03861	0.1193	0.6603	1.548	--	0.7836	--	--	--	1.21301

Air-Water Bubble Column, $U_\ell = 0.155 \text{ m/s}$

U_g (m/s)	\bar{z}_b (m)	σ_ℓ (m)	$\ell_{b,vs}$ (m)	U_b (m/s)	f (1/s)	ε_g (-)	t_i^- (1/2500 s)	$(\varepsilon_g U_b)/f$ (m)	$0.8467 f \bar{\ell}_b$ (m/s)	$U_b \varepsilon_g$ (m/s)
0.00181	0.0022	0.00065	0.00262	0.5842	6.017	0.04015	6.711	0.0039	0.01121	0.00712
0.00503	0.00238	0.00082	0.003	0.5592	6.242	0.01981	7.877	0.00177	0.01258	0.01108
0.01322	0.00249	0.00098	0.00341	0.5911	12.04	0.03978	8.331	0.00195	0.02538	0.02351
0.01895	0.00268	0.00109	0.00369	0.6133	19.42	0.06953	8.92	0.0022	0.04407	0.04264
0.03427	0.0027	0.00108	0.00361	0.5636	26.25	0.1076	10.22	0.00231	0.06001	0.06064
0.0484	0.00288	0.00121	0.00404	0.5892	36.28	0.157	10.82	0.00255	0.08847	0.0925
0.06667	0.00311	0.00145	0.00463	0.6384	43.06	0.1906	11.22	0.00283	0.11338	0.12168
0.09313	0.00417	0.00534	0.05291	1.034	66.11	0.2599	9.682	0.00406	0.23341	0.26874
0.11962	0.00554	0.01334	0.1314	1.255	80.61	0.3127	9.62	0.00487	0.3781	0.39244
0.14407	0.0045	0.00683	0.06208	1.332	85.78	0.3313	9.579	0.00514	0.32682	0.44129
0.18777	0.00587	0.01093	0.08535	1.459	87.78	0.397	11.29	0.0066	0.43626	0.57922
0.29625	0.02651	0.04241	0.1607	2.44	72.61	0.4622	15.9	0.01553	1.62974	1.12777
0.36493	0.02867	0.04954	0.1929	2.298	70.5	0.4609	16.36	0.01502	1.71131	1.05915
0.50771	0.02427	0.04494	0.265	2.378	75.33	0.5322	17.32	0.0168	1.54793	1.26557
0.67811	0.03083	0.05211	0.2801	2.823	80.83	0.6342	19.32	0.02215	2.10988	1.79035
0.99686	0.03461	0.06673	0.6183	3.131	90.83	0.7605	20.9	0.02622	2.6616	2.38113
1.32935	0.03227	0.06159	0.398	3.149	85.72	0.8067	23.57	0.02963	2.34204	2.5403
1.65508	0.0346	0.06354	0.3687	3.173	76.94	0.8533	27.18	0.03519	2.25393	2.70752
1.96715	0.04377	0.08486	0.3938	3.063	57.67	0.8962	37.87	0.0476	2.13717	2.74506
2.58229	0.107	0.3073	2.149	3.306	28.88	0.952	60.44359	0.10898	2.61634	3.14731
3.18779	0.1045	0.4277	3.534	3.176	22.73	0.9366	93.77	0.13087	2.01107	2.97464
4.28314	0.04795	0.09727	0.3433	1.491	10.46	0.9219	219	0.13141	0.42465	1.37455

Air-Water Bubble Column, $U_\ell = 0.219 \text{ m/s}$

U_g (m/s)	$\bar{\ell}_b$ (m)	σ_ℓ (m)	$\ell_{b,vs}$ (m)	U_b (m/s)	f (1/s)	ε_g (-)	\bar{t}_i (1/2500 s)	$(\varepsilon_g U_b)/f$ (m)	$0.8467 f \bar{\ell}_b$ (m/s)	$U_b \varepsilon_g$ (m/s)
0.00359	0.00218	0.00074	0.0028	0.7534	2.025	0.0042	5.296	0.00156	0.00374	0.00316
0.01305	0.00236	0.00099	0.00362	0.7599	6.404	0.01604	6.369	0.0019	0.0128	0.01219
0.02552	0.0027	0.00158	0.00706	0.7332	11.43	0.03399	7.459	0.00218	0.02613	0.02492
0.03744	0.00333	0.00249	0.00952	0.8547	21.81	0.07701	8.875	0.00302	0.06149	0.06582
0.06522	0.00406	0.005	0.02709	1.048	39.56	0.1404	9.003	0.00372	0.13599	0.14714
0.09318	0.00484	0.00526	0.02595	1.171	50.89	0.1851	9.022	0.00426	0.20854	0.21675
0.12847	0.00836	0.01096	0.06123	1.428	74.28	0.2667	9.161	0.00513	0.52576	0.38085
0.18168	0.00863	0.00936	0.0408	1.725	100.2	0.3325	8.374	0.00572	0.73213	0.57356
0.24938	0.01406	0.0221	0.09897	2.395	131.9	0.4256	8.313	0.00773	1.57016	1.01931
0.30124	0.01492	0.02358	0.1111	2.596	137.4	0.4562	8.639	0.00862	1.73567	1.1843
0.4731	0.02419	0.04537	0.2169	3.102	137.1	0.5512	10.1	0.01247	2.80793	1.70982
0.60762	0.02517	0.04727	0.2672	3.122	133.2	0.6237	11.18	0.01462	2.83857	1.94719
0.8116	0.02978	0.04901	0.2787	3.442	122.28412	0.712	15.04	0.02004	3.08324	2.4507
1.0713	0.03208	0.05342	0.2618	3.42	109.4	0.779	18.16	0.02435	2.97142	2.66418
1.45683	0.03718	0.06105	0.2799	3.497	91.83	0.8529	23.35	0.03248	2.89072	2.98259
1.27421	0.03318	0.0459	0.1627	3.742	99.4429	0.8157	18.6	0.03069	2.79359	3.05235
1.56895	0.03967	0.06269	0.2302	3.644	90	0.8787	24.03	0.03558	3.02285	3.20198
1.83485	0.04238	0.09571	0.7157	3.41	78.78	0.9124	28.57	0.03949	2.82676	3.11128
2.39325	0.04126	0.08145	0.343	3.204	60.22	0.9437	39.13	0.05021	2.10369	3.02361
2.91134	0.03943	0.1021	0.5527	2.091	37.1	0.9675	64.79	0.05453	1.23855	2.02304
5.50396	0.02464	0.06887	0.3807	1.745	1.475	-5.312	165.30641	--	0.03077	-9.26944

U_g (m/s)	0.005	0.008	0.012	U_ℓ (m/s)	0.023	0.032	0.050	0.070	0.100
					σ_t/\bar{k}_t				
0.00205	0.75975	0.80561	0.87043		1.09278	1.29169	1.61792	1.77062	1.84266
0.00615	0.71268	0.74718	0.79836		0.97257	1.11986	1.3586	1.54476	1.86457
0.0184	0.63969	0.67858	0.71764		0.83842	0.93266	1.41007	1.78595	1.92614
0.04554	0.73225	0.78982	0.87529		1.24119	1.41111	1.7714	2.01131	2.15505
0.06232	0.84786	0.96614	1.10428		1.53697	1.69116	1.90104	2.07819	2.24969
0.07135	0.82426	0.93664	1.00785		1.63957	1.71264	1.96649	2.10337	2.28744
0.10002	0.75818	0.84784	0.94224		1.39592	1.44137	1.59476	2.1663	2.37142
0.155	0.56607	0.56757	0.56948		0.57245	0.62569	0.60668	0.64299	0.72357
0.2186	0.50285	0.5183	0.53629		0.61739	0.79039	1.01667	1.14124	1.05959

1.5 mm Glass Beads Three-Phase Fluidized Bed, $U_\ell = 0.0154$ m/s

U_g (m/s)	f (1/s)	ε_g (-)	\bar{t}_i (1/2500 s)	$\bar{\ell}_b$ (m)	σ_ℓ (m)	$\ell_{b,vs}$ (m)	U_b (m/s)	$(\varepsilon_g U_b)/f$ (m)	$U_b \varepsilon_g$ (m/s)	$0.8467 f \bar{\ell}_b$ (m/s)
0.01524	3.05	0.1384	113.5	0.04207	0.04	0.1369	0.6964	0.0316	0.09638	0.10864
0.02225	3.592	0.1848	129.1	0.04565	0.03606	0.09677	0.6722	0.03458	0.12422	0.13883
0.03922	4.142	0.2343	142	0.06397	0.09139	0.6337	0.8562	0.04843	0.20061	0.22434
0.05648	4.75	0.28	147.4	0.06913	0.06927	0.2087	0.8462	0.04988	0.23694	0.27802
0.07881	5.222	0.2905	139.1	0.06835	0.07377	0.2245	0.9404	0.05231	0.27319	0.3022
0.11281	6.071	0.3248	133.6	0.08363	0.1391	0.726	0.98	0.05243	0.3183	0.42987
0.14775	6.944	0.3506	126.1	0.07567	0.1151	0.3625	1.124	0.05675	0.39407	0.44488
0.18167	7.727	0.3875	125.3	0.07536	0.09832	0.3035	1.207	0.06053	0.46771	0.49302
0.23848	9.863	0.4206	106.1	0.06331	0.09371	0.3112	1.147	0.04891	0.48243	0.52868
0.30281	12.17	0.4632	94.8	0.05847	0.09863	0.345	1.441	0.05485	0.66747	0.60247
0.36699	13.89	0.4854	86.92	0.06219	0.1396	0.6852	1.279	0.0447	0.62083	0.73137
0.51897	17.2	0.5481	79.03	0.04864	0.1256	0.6273	1.452	0.04627	0.79584	0.70833
0.69506	23.5	0.6298	66.3	0.05709	0.2192	1.53	1.769	0.04741	1.11412	1.1359
1.02418	32.33	0.6852	52.05	0.0372	0.09466	0.7681	2.158	0.04574	1.47866	1.01827
1.32236	35.72	0.7744	53.86	0.02765	0.05168	0.2645	2.254	0.04887	1.7455	0.83622
1.58918	39.33	0.8073	50.39	0.02677	0.04929	0.2755	2.694	0.0553	2.17487	0.89142
1.77326	35.83	0.8498	50.13928	0.04478	0.1295	1.135	2.382	0.0565	2.02422	1.35845
2.86366	27.94	0.8628	60.16713	0.037	0.07234	0.359	1.944	0.06003	1.67728	0.87527
3.64211	23.96	0.8958	93.04	0.06718	0.1327	0.5483	2.54	0.09496	2.27533	1.36282
5.20124	11.13	0.9548	214.2	0.07453	0.1655	0.697	1.817	0.15587	1.73487	0.70233

1.5 mm Glass Beads Three-Phase Fluidized Bed, $U_\ell = 0.0184$ m/s

U_g (m/s)	f (1/s)	ε_g (-)	τ_i (1/2500 s)	$\bar{\ell}_b$ (m)	σ_ℓ (m)	$\ell_{b,vs}$ (m)	U_b (m/s)	$(\varepsilon_g U_b)/f$ (m)	$U_b \varepsilon_g$ (m/s)	$0.8467 f \bar{\ell}_b$ (m/s)
0.00211	1.15	0.03215	69.88	0.01902	0.0104	0.02948	0.4875	0.01363	0.01567	0.01852
0.00585	1.983	0.07293	91.86	0.02646	0.01925	0.05687	0.6133	0.02256	0.04473	0.04442
0.01518	3.058	0.1259	102.9	0.03371	0.02281	0.06701	0.5969	0.02457	0.07515	0.08728
0.02228	3.408	0.1705	125.1	0.05092	0.04412	0.1402	0.7359	0.03682	0.12547	0.14693
0.03925	4.092	0.2211	135	0.05797	0.05135	0.1494	0.8402	0.0454	0.18577	0.20084
0.05614	4.385	0.2554	145.8	0.07151	0.06209	0.1772	0.9023	0.05255	0.23045	0.26549
0.07888	5.232	0.2919	139.2	0.07098	0.07424	0.2224	0.895	0.04993	0.26125	0.31442
0.1123	5.292	0.3235	152.4	0.09454	0.1081	0.3905	0.8973	0.05485	0.29028	0.42359
0.1459	6.628	0.338	127.3	0.08669	0.1015	0.3134	1.065	0.05431	0.35997	0.48648
0.18094	7.246	0.3792	130.5	0.08564	0.09736	0.2559	1.15	0.06018	0.43608	0.5254
0.23799	9.981	0.4238	105.8	0.07977	0.1196	0.5005	1.38	0.0586	0.58484	0.6741
0.3037	11.89	0.4634	97.08	0.07711	0.1392	0.5421	1.377	0.05367	0.6381	0.77626
0.36921	13.97	0.4887	86.86	0.08099	0.1689	0.7445	1.694	0.05926	0.82786	0.95794
0.52477	19.03	0.5681	75.39	0.06267	0.1369	0.5419	1.598	0.0477	0.90782	1.00974
0.71357	26.24	0.6094	57.59	0.04692	0.1206	0.5959	2.129	0.04944	1.29741	1.0424
1.08423	35.72	0.6665	46.93	0.0202	0.02403	0.08535	2.469	0.04607	1.64559	0.61091
1.36537	40.78	0.8035	48.48	0.04012	0.1505	1.614	2.627	0.05176	2.11079	1.38523
1.61506	40.5	0.8327	51	0.03696	0.07837	0.5206	2.633	0.05414	2.1925	1.26736
2.21511	39.28	0.8182	51.81	0.03716	0.09463	0.5466	2.242	0.0467	1.8344	1.23583
3.01871	36.17	0.8556	61.43	0.04954	0.1581	1.377	2.236	0.05289	1.91312	1.51711
3.84454	25.63	0.9203	90.79	0.07872	0.2278	1.418	2.469	0.08865	2.27222	1.70823
5.85934	8.123	0.9079	257.6	0.1884	0.5616	2.708	2.384	0.26646	2.16443	1.29572

1.5 mm Glass Beads Three-Phase Fluidized Bed, $U_\ell = 0.0273$ m/s

U_g (m/s)	f (1/s)	ε_g (-)	\bar{t}_i (1/2500 s)	$\bar{\ell}_b$ (m)	σ_ℓ (m)	$\ell_{b,vs}$ (m)	U_b (m/s)	$(\varepsilon_g U_b)/f$ (m)	$U_b \varepsilon_g$ (m/s)	$0.8467 f \bar{\ell}_b$ (m/s)
0.00209	1.467	0.03556	57.72	0.01379	0.00778	0.02283	0.4522	0.01096	0.01608	0.01713
0.00581	1.483	0.04945	82.8	0.02244	0.01479	0.04394	0.5598	0.01867	0.02768	0.02818
0.01508	2.492	0.08825	88.48	0.03031	0.02441	0.07386	0.7416	0.02626	0.06545	0.06395
0.02202	2.85	0.1098	96.26	0.0372	0.03599	0.119	0.7819	0.03012	0.08585	0.08976
0.03859	3.658	0.155	106	0.04813	0.05018	0.1793	0.835	0.03538	0.12943	0.14906
0.05528	4.577	0.1843	100.4	0.04614	0.05552	0.2101	0.8139	0.03277	0.15	0.1788
0.07755	5.473	0.2184	99.47	0.04525	0.05119	0.1672	1.054	0.04206	0.23019	0.20968
0.11068	7.71	0.2679	87.43	0.05748	0.08511	0.3481	1.15	0.03996	0.30809	0.37522
0.14304	8.733	0.3105	90.32	0.04981	0.0632	0.199	1.378	0.04899	0.42787	0.36829
0.18214	8	0.3274	102.1	0.0719	0.09126	0.2658	1.154	0.04723	0.37782	0.487
0.23522	12.83	0.4043	78.56	0.06127	0.08592	0.2631	1.358	0.04279	0.54904	0.66556
0.30027	14.28	0.3846	67.48	0.06076	0.1687	1.186	1.832	0.04934	0.70459	0.73461
0.35908	18.63	0.4651	61.64	0.04243	0.08545	0.3737	1.553	0.03877	0.7223	0.66927
0.50236	23.96	0.5422	55.15	0.04044	0.08294	0.3554	1.805	0.04085	0.97867	0.82037
0.67799	29.33	0.5878	49.44	0.03325	0.06647	0.3216	1.889	0.03786	1.11035	0.82569
0.97828	40.5	0.7038	42.99	0.0266	0.05134	0.3184	2.546	0.04424	1.79187	0.91211
1.19756	43.61	0.7905	44.88	0.03806	0.08963	0.5996	3.012	0.0546	2.38099	1.40529
1.42843	46.33	0.8176	41.97	0.03217	0.05342	0.2272	2.687	0.04742	2.19689	1.2619
2.15294	44.28	0.8212	46.42	0.03436	0.08361	0.5717	2.407	0.04464	1.97663	1.28817
2.83134	34.44	0.8973	63.96	0.04944	0.1313	0.9864	2.419	0.06302	2.17057	1.44163
3.601	23.21	0.9387	102	0.05072	0.09211	0.363	2.184	0.08833	2.05012	0.99671
5.09655	11.39	0.9462	233.7	0.1035	0.28	1.501	2.111	0.17537	1.99743	0.99811

1.5 mm Glass Beads Three-Phase Fluidized Bed, $U_\ell = 0.04554$ m/s

U_g (m/s)	f (1/s)	ε_g (-)	τ_i^- (1/2500 s)	\bar{z}_b (m)	σ_ℓ (m)	$\ell_{b,vs}$ (m)	U_b (m/s)	$(\varepsilon_g U_b)/f$ (m)	$U_b \varepsilon_g$ (m/s)	$0.8467 f \bar{z}_b$ (m/s)
0.00208	2.683	0.0339	28.68	0.01189	0.01075	0.03944	0.5541	0.007	0.01878	0.02701
0.00575	2.475	0.03619	37.49	0.01591	0.01292	0.04649	0.7743	0.01132	0.02802	0.03334
0.01493	3.217	0.06568	51.46	0.02347	0.02031	0.05853	0.8504	0.01736	0.05585	0.06393
0.02196	3.9	0.08725	55.99	0.02857	0.03072	0.1054	0.9008	0.02015	0.07859	0.09434
0.03838	5.549	0.1285	58.43	0.03602	0.04885	0.2131	1.015	0.0235	0.13043	0.16923
0.05484	6.155	0.1488	60.44	0.03609	0.05728	0.2929	1.172	0.02833	0.17439	0.18807
0.07672	8.127	0.1905	58.75	0.03941	0.05156	0.1846	1.16	0.02719	0.22098	0.27117
0.10979	9.315	0.224	60.35	0.05005	0.07932	0.3346	1.681	0.04042	0.37654	0.39473
0.14192	12.31	0.2401	48.69	0.03505	0.05903	0.2214	1.469	0.02865	0.35271	0.36531
0.1736	14.39	0.3156	54.29	0.04728	0.08241	0.3208	1.445	0.03169	0.45604	0.57604
0.2314	16.76	0.3238	47.86	0.05307	0.08581	0.307	1.662	0.03211	0.53816	0.75307
0.2938	23.37	0.4003	43.01	0.0319	0.05209	0.1959	1.572	0.02693	0.62927	0.63119
0.36168	22.75	0.4456	48.42	0.03716	0.06485	0.2407	1.899	0.0372	0.84619	0.71576
0.48709	31.83	0.535	41.87	0.02361	0.03591	0.1505	1.863	0.03131	0.99671	0.63628
0.62357	42.28	0.5974	35.06	0.02456	0.03923	0.1921	2.18	0.0308	1.30233	0.87918
0.87901	53.67	0.7441	34.98	0.03064	0.05732	0.3095	2.854	0.03957	2.12366	1.3923
1.10998	67	0.8128	29.96	0.02689	0.04145	0.1966	2.831	0.03434	2.30104	1.52538
1.76706	56.39	0.8119	35.47	0.03236	0.0728	0.5819	3.076	0.04429	2.4974	1.54498
2.12229	49.78	0.8697	43.56	0.03849	0.09379	0.6681	2.977	0.05201	2.5891	1.62224
2.84498	41.5	0.9107	53.31	0.05467	0.1119	0.7493	2.773	0.06085	2.52537	1.92092
3.55834	22.79	0.9449	103.4	0.08934	0.1909	0.8179	2.589	0.10734	2.44635	1.72386

1.5 mm Glass Beads Three-Phase Fluidized Bed, $U_\ell = 0.0638$ m/s

U_g (m/s)	f (1/s)	ε_g (-)	τ_i (1/2500 s)	$\bar{\ell}_b$ (m)	σ_ℓ (m)	$\ell_{b,vs}$ (m)	U_b (m/s)	$(\varepsilon_g U_b)/f$ (m)	$U_b \varepsilon_g$ (m/s)	$0.8467 f \bar{\ell}_b$ (m/s)
0.00207	3.533	0.02787	20.94	0.00459	0.00345	0.01095	0.5265	0.00415	0.01467	0.01373
0.00573	4.816	0.03939	20.71	0.00581	0.0073	0.02964	0.6306	0.00516	0.02484	0.02369
0.015	5.583	0.06549	29.4	0.00914	0.01418	0.07647	0.7546	0.00885	0.04942	0.0432
0.02184	7.667	0.09387	29.99	0.02349	0.03055	0.1343	1.124	0.01376	0.10551	0.15248
0.03799	7.879	0.1239	39.22	0.03262	0.09098	0.8308	1.079	0.01697	0.13369	0.2176
0.05441	8.617	0.1314	37.83	0.02897	0.04298	0.2127	1.232	0.01879	0.16188	0.21136
0.07574	10.96	0.166	38.51	0.02994	0.03471	0.1032	1.327	0.0201	0.22028	0.27783
0.10756	13.59	0.2138	39.68	0.03658	0.04805	0.1555	1.401	0.02204	0.29953	0.4209
0.14009	13.74	0.2491	45.2	0.04355	0.07262	0.3086	1.679	0.03044	0.41824	0.50663
0.17019	17.33	0.3057	43.89	0.03073	0.04349	0.1628	1.446	0.02551	0.44204	0.45089
0.22113	19.89	0.3098	39.19	0.03094	0.04992	0.1935	1.668	0.02598	0.51675	0.52104
0.27814	25.54	0.3877	38.28	0.02508	0.04053	0.1587	1.514	0.02298	0.58698	0.54233
0.33566	28.78	0.432	37.12	0.02671	0.04298	0.1783	1.791	0.02688	0.77371	0.65084
0.47665	34.06	0.4649	33.79	0.03242	0.06053	0.2823	1.931	0.02636	0.89772	0.93491
0.62021	59.11	0.6024	25.3	0.01952	0.02493	0.08839	2.512	0.0256	1.51323	0.97691
0.845	74.56	0.7545	25.53	0.02352	0.0398	0.2303	3.026	0.03062	2.28312	1.48476
1.39225	70.39	0.7802	27.68	0.02768	0.04004	0.1634	3.249	0.03601	2.53487	1.64964
1.73276	71.78	0.7839	26.81	0.02587	0.07285	0.7917	2.982	0.03257	2.33759	1.57222
2.08088	57.78	0.8463	37.04	0.03931	0.07677	0.3932	3.234	0.04737	2.73693	1.92306
2.7234	38	0.9239	61.43	0.05687	0.1203	0.5505	3.115	0.07574	2.87795	1.8297
3.41605	21.37	0.9229	108.5	0.09748	0.2304	1.001	3.41	0.14727	3.14709	1.76373
4.64092	8.267	0.9084	253.5	0.1735	0.8658	5.491	2.179	0.23943	1.9794	1.21439
5.72492	29.47	0.8293	--	0.03457	0.08502	0.4021	1.033	0.02907	0.85667	0.86257

1.5 mm Glass Beads Three-Phase Fluidized Bed, $U_\ell = 0.0729$ m/s

U_g (m/s)	f (1/s)	ε_g (-)	τ_i^- (1/2500 s)	\bar{z}_b (m)	σ_ℓ (m)	$\ell_{b,vs}$ (m)	U_b (m/s)	$(\varepsilon_g U_b)/f$ (m)	$U_b \varepsilon_g$ (m/s)	$0.8467 f \bar{z}_b$ (m/s)
0.00205	1.833	0.01315	18.44	0.0034	0.00197	0.00599	0.461	0.00331	0.00606	0.00528
0.00567	4.575	0.03085	16.83	0.00473	0.00472	0.01884	0.6119	0.00413	0.01888	0.01832
0.01474	8.937	0.06438	17.77	0.00718	0.01149	0.05716	0.8206	0.00591	0.05283	0.05433
0.02151	9.033	0.09172	25.4	0.01042	0.01812	0.09616	0.8559	0.00869	0.0785	0.07969
0.03788	10.42	0.1272	31.12	0.02835	0.03553	0.1232	1.176	0.01436	0.14959	0.25011
0.05453	10.49	0.1351	32.45	0.02887	0.03981	0.1528	1.309	0.01686	0.17685	0.25641
0.07499	12.56	0.1734	33.9	0.03027	0.04244	0.1584	1.286	0.01775	0.22299	0.3219
0.10676	15.78	0.2157	35.12	0.02582	0.04218	0.176	1.317	0.018	0.28408	0.34497
0.13768	16.55	0.2739	40.84	0.04012	0.0966	0.572	1.715	0.02838	0.46974	0.56217
0.16421	21.42	0.3112	36.44	0.02917	0.0458	0.1781	1.641	0.02384	0.51068	0.52902
0.21262	24	0.3572	37.01	0.04048	0.07689	0.3077	1.729	0.02573	0.6176	0.82255
0.26813	31.22	0.3794	30.46	0.02426	0.03747	0.1462	1.904	0.02314	0.72238	0.64126
0.32374	31.67	0.4103	32.34	0.02293	0.03688	0.141	2.051	0.02657	0.84153	0.61484
0.44872	44.11	0.523	29.58	0.02567	0.03991	0.1792	2.183	0.02588	1.14171	0.95868
0.56277	70.67	0.6504	23.06	0.02242	0.03794	0.2581	2.438	0.02244	1.58568	1.34148
0.77114	71.33	0.7776	26.8	0.02373	0.03528	0.1527	2.813	0.03067	2.18739	1.43312
1.39225	78.28	0.7716	24.28	0.02551	0.04253	0.2904	2.904	0.02862	2.24073	1.69073
1.73764	66.83	0.8411	30.93	0.02969	0.06151	0.4294	3.172	0.03992	2.66797	1.67994
2.07529	56.94	0.8711	37.45	0.04117	0.0969	0.667	3.076	0.04706	2.6795	1.98477
2.73768	34.78	0.9179	65.1	0.05683	0.1509	1.107	2.854	0.07532	2.61969	1.67348
3.3976	19.1	0.9094	118.3	0.09916	0.2591	1.632	2.986	0.14217	2.71547	1.60355
4.62907	6.385	0.8223	341.8	0.1894	0.5878	3.217	2.906	0.37425	2.3896	1.02389
5.70143	26.4	0.855	--	0.05958	0.1918	1.241	1.627	0.05269	1.39109	1.33173

1.5 mm Glass Beads Three-Phase Fluidized Bed, $U_\ell = 0.100$ m/s

U_g (m/s)	f (1/s)	ε_g (-)	\bar{t}_i (1/2500 s)	$\bar{\ell}_b$ (m)	σ_ℓ (m)	$\ell_{b,vs}$ (m)	U_b (m/s)	$(\varepsilon_g U_b)/f$ (m)	$U_b \varepsilon_g$ (m/s)	$0.8467 f \bar{\ell}_b$ (m/s)
0.002	2.85	0.01737	12.3	0.003	0.0016	0.00537	0.4981	0.00304	0.00865	0.00724
0.00555	4.5	0.02568	14.31	0.00377	0.00643	0.06181	0.5582	0.00319	0.01433	0.01436
0.01418	10.8	0.06038	14.09	0.0044	0.00555	0.02897	0.7375	0.00412	0.04453	0.04023
0.0206	12.19	0.08471	17.52	0.00731	0.01283	0.06074	0.853	0.00593	0.07226	0.07545
0.03512	16.06	0.1135	17.68	0.01587	0.02325	0.1126	1.152	0.00814	0.13075	0.21579
0.04976	19.78	0.1519	19.1	0.0237	0.04348	0.2702	1.461	0.01122	0.22193	0.39691
0.07038	28.62	0.1677	14.62	0.01739	0.03206	0.1544	1.442	0.00845	0.24182	0.42139
0.09831	33.22	0.2287	16.92	0.02389	0.03403	0.1277	1.88	0.01294	0.42996	0.67194
0.12796	38.11	0.3022	19.44	0.03129	0.05371	0.2176	2.002	0.01588	0.605	1.00962
0.15948	38	0.3105	20.51	0.02849	0.05199	0.2385	1.823	0.0149	0.56604	0.91662
0.2029	41.06	0.3587	21.44	0.02683	0.05055	0.2501	1.694	0.0148	0.60764	0.93272
0.2576	49.61	0.3873	19.24	0.02458	0.03561	0.1404	2.18	0.01702	0.84431	1.03244
0.30864	49.22	0.4625	23.22	0.02246	0.03116	0.1168	1.966	0.01847	0.90928	0.93597
0.42135	64.06	0.5353	20.8	0.02428	0.04425	0.271	2.368	0.01979	1.26759	1.31689
0.53204	79.83	0.6534	20.19	0.02231	0.03027	0.1395	2.792	0.02285	1.82429	1.50792
1.02428	91.39	0.7208	19.79	0.02654	0.04004	0.2004	3.152	0.02486	2.27196	2.05358
1.37658	79.61	0.789	24.74	0.03547	0.0561	0.2348	3.163	0.03135	2.49561	2.39079
1.73099	72.61	0.8461	29.6	0.03427	0.05146	0.2041	3.409	0.03972	2.88435	2.1068
2.02975	62.61	0.8786	34.62	0.04391	0.1158	1.131	3.326	0.04667	2.92222	2.32766
2.6659	27.52	0.9211	71.8663	0.06559	0.1673	0.8294	3.477	0.11638	3.20266	1.52826
3.30122	20.87	0.9296	130.77994	0.097	0.2297	1.12	3.061	0.13634	2.84551	1.71398
4.48088	5.133	0.8624	410.3	0.2319	0.6949	3.194	2.996	0.50336	2.58375	1.00782

1.5 mm Glass Beads Three-Phase Fluidized Bed, $U_g = 0.155$ m/s

U_g (m/s)	f (1/s)	ε_g (-)	\bar{t}_i (1/2500 s)	\bar{t}_b (m)	σ_ℓ (m)	$\ell_{b,vs}$ (m)	U_b (m/s)	$(\varepsilon_g U_b)/f$ (m)	$U_b \varepsilon_g$ (m/s)	$0.8467 f \bar{t}_b$ (m/s)
0.00179	2.5	0.01023	11.3	0.00256	0.00085	0.00311	0.5328	0.00218	0.00545	0.00542
0.00495	5.458	0.01879	8.428	0.00229	0.00076	0.00293	0.5161	0.00178	0.0097	0.01058
0.01303	11.83	0.04368	9.315	0.00241	0.0008	0.00299	0.5311	0.00196	0.0232	0.02414
0.01884	18.58	0.07144	9.784	0.00267	0.00099	0.00346	0.5771	0.00222	0.04123	0.042
0.03299	27.33	0.1175	10.94	0.00292	0.00124	0.00403	0.6274	0.0027	0.07372	0.06757
0.04681	33.38	0.1558	11.58	0.00312	0.00141	0.00468	0.6032	0.00282	0.09398	0.08818
0.06454	52.67	0.2195	10.57	0.00343	0.00181	0.00566	0.7798	0.00325	0.17117	0.15296
0.09259	86.56	0.2367	6.676	0.00386	0.00279	0.01102	1.358	0.00371	0.32144	0.28289
0.14534	76.56	0.2622	8.505	0.01538	0.02382	0.1054	2.118	0.00725	0.55534	0.99694
0.17692	87.67	0.3261	9.478	0.01898	0.03052	0.1714	2.232	0.0083	0.72786	1.40883
0.23518	104	0.3634	8.814	0.01595	0.02205	0.08237	2.427	0.00848	0.88197	1.40445
0.35145	99.5	0.417	10.37	0.02067	0.03164	0.1176	2.488	0.01043	1.0375	1.74131
0.3629	89.33	0.4817	13.24	0.02631	0.04808	0.2223	2.531	0.01365	1.21918	1.9899
0.505	85.61	0.5312	15.44	0.03	0.05225	0.2368	2.599	0.01613	1.38059	2.17449
0.67438	75.28	0.5349	17.82	0.0269	0.04118	0.1749	2.833	0.02013	1.51537	1.71453
0.98629	85.22	0.7674	22.19	0.03434	0.04949	0.2214	3.26	0.02936	2.50172	2.47773
1.3125	87.33	0.7918	22.82	0.03346	0.0455	0.1611	3.264	0.02959	2.58444	2.47401
1.62222	76.22	0.8516	27.76	0.0418	0.07438	0.3148	3.348	0.03741	2.85116	2.69748
1.92024	62.94	0.8706	34.57	0.0439	0.09316	0.5602	3.266	0.04518	2.84338	2.3394
2.48466	33.29	0.9359	66.19	0.06354	0.1273	0.4933	3.134	0.08811	2.93311	1.79091
3.0718	18.67	0.9338	128.2	0.1562	0.3759	1.654	3.341	0.1671	3.11983	2.4691

1.5 mm Glass Beads Three-Phase Fluidized Bed.

U_g (m/s)	U_L (m/s)					σ_t/\bar{f}_i	σ_t/\bar{f}_i
	0.0025	0.0031	0.0050	0.012	0.020	0.030	0.050
0.0184	0.63685	0.62532	0.595	0.68479	0.73647	0.7806	0.91607
0.0273	0.8394	0.78816	0.66125	0.76208	0.83132	0.93763	1.15717
0.0455	1.01355	0.99191	0.93492	1.00533	1.10518	1.21207	1.35057
0.06376	0.97463	0.99862	1.07514	1.22077	1.33575	1.38074	1.42911
0.0729	0.72032	0.75093	0.85417	1.09463	1.33947	1.457	1.55787
0.1	0.668	0.6603	0.83454	0.97135	1.39615	1.48761	1.71778
0.155	0.68423	0.6603	0.56675	0.53025	0.57849	0.60745	0.63453

4.5 mm Glass Beads Three-Phase Fluidized Bed, $U_\ell = 0.0364$ m/s

U_g (m/s)	f (1/s)	ε_g (-)	τ_i (1/2500 s)	\bar{z}_b (m)	σ_ℓ (m)	$\ell_{b,vs}$ (m)	U_b (m/s)	$(\varepsilon_g U_b)/f$ (m)	$U_b \varepsilon_g$ (m/s)	$0.8467 f \bar{z}_b$ (m/s)
0.00313	2.133	0.02584	30.46	0.00768	0.00578	0.01546	0.5058	0.00613	0.01307	0.01387
0.00578	3.5	0.0439	31.3	0.00797	0.00754	0.02351	0.5748	0.00721	0.02523	0.02362
0.01086	4.667	0.05657	30.3	0.00952	0.01041	0.03408	0.6174	0.00748	0.03493	0.03762
0.01504	6.083	0.07946	32.64	0.01242	0.01621	0.05262	0.7315	0.00956	0.05812	0.06397
0.0219	8.349	0.1048	31.23	0.00898	0.01107	0.03892	0.6829	0.00857	0.07157	0.06348
0.0388	10.8	0.1473	34.61	0.0063	0.01207	0.07696	0.5546	0.00756	0.08169	0.05761
0.05513	14.25	0.1897	33.3	0.00908	0.02265	0.1558	0.7926	0.01055	0.15036	0.10955
0.07735	15.67	0.2823	45.16	0.03908	0.06404	0.1951	1.197	0.02156	0.33791	0.51848
0.11038	16.18	0.3601	55.68	0.0383	0.0533	0.1543	1.121	0.02495	0.40367	0.52467
0.14266	17.53	0.3946	56.19	0.04437	0.06961	0.2246	1.083	0.02438	0.42735	0.65854
0.17633	18.33	0.4362	59.23	0.044	0.09617	0.4757	1.397	0.03324	0.60937	0.68285
0.23206	20.19	0.4764	59.06	0.03316	0.05658	0.1953	1.385	0.03268	0.65981	0.56684
0.34678	21.83	0.5435	61.62	0.04646	0.07559	0.2559	1.233	0.0307	0.67014	0.85871
0.35808	24.95	0.5638	56.06	0.04429	0.08574	0.3296	1.493	0.03374	0.84175	0.9356
0.50234	28.14	0.6401	56.5	0.04578	0.1162	0.6659	1.933	0.04397	1.23731	1.09072
0.65057	41.83	0.6956	40.64	0.02968	0.09085	0.6584	2.091	0.03477	1.4545	1.05115
0.91532	59.5	0.7449	30.83	0.02222	0.04105	0.2132	2.817	0.03527	2.09838	1.11937
1.17217	52.83	0.8164	37.87	0.03241	0.07679	0.6059	3.15	0.04868	2.57166	1.44968
1.77314	52.28	0.7981	37.59	0.02803	0.04462	0.2169	3.18	0.04855	2.53796	1.24071
2.12959	47.78	0.8734	45.33	0.02931	0.04775	0.2393	3.391	0.06199	2.9617	1.1857
2.82485	27.57	0.8876	80.09	0.05405	0.1202	0.5994	2.922	0.09407	2.59357	1.26167
3.50506	16.58	0.907	135.8	0.1108	0.3395	2.065	2.531	0.13846	2.29562	1.55538
4.82111	6.65	0.8961	338.8	0.2663	0.6898	3.056	2.338	0.31505	2.09508	1.49936

4.5 mm Glass Beads Three-Phase Fluidized Bed, $U_\ell = 0.0455$ m/s

U_g (m/s)	f (1/s)	ε_g (-)	\bar{t}_i (1/2500 s)	$\bar{\ell}_b$ (m)	σ_ℓ (m)	$\ell_{b,vs}$ (m)	U_b (m/s)	$(\varepsilon_g U_b)/f$ (m)	$U_b \varepsilon_g$ (m/s)	$0.8467 f \bar{\ell}_b$ (m/s)
0.00312	4.217	0.03655	19.93	0.00457	0.00429	0.01618	0.412	0.00357	0.01506	0.01632
0.00573	5.183	0.04541	22.37	0.00461	0.00439	0.01604	0.4552	0.00399	0.02067	0.02023
0.01078	5.991	0.0592	24.37	0.0054	0.00615	0.02536	0.4757	0.0047	0.02816	0.02739
0.01496	7.046	0.06994	24.17	0.0059	0.0085	0.03408	0.5231	0.00519	0.03659	0.0352
0.02185	9.968	0.09961	24.78	0.00723	0.01465	0.09675	0.6524	0.00652	0.06499	0.06102
0.03828	11.98	0.1549	31.86	0.00866	0.01927	0.1039	0.7204	0.00931	0.11159	0.08784
0.05554	12.87	0.2101	40.79	0.0437	0.09928	0.5939	1.211	0.01977	0.25443	0.47618
0.07615	14.78	0.2744	46.52	0.03493	0.04512	0.1343	0.8696	0.01614	0.23862	0.4371
0.1092	14.06	0.3105	54.96	0.03574	0.0483	0.1602	1.144	0.02526	0.35521	0.42545
0.14188	19.11	0.3769	49.07	0.05452	0.1234	0.6384	1.306	0.02576	0.49223	0.88212
0.17722	18.81	0.383	50.67	0.04793	0.1032	0.4556	1.285	0.02616	0.49216	0.76332
0.23194	20.41	0.4374	53.17	0.02348	0.03997	0.1452	1.4	0.03	0.61236	0.40575
0.34402	28.28	0.5079	44.43	0.02708	0.06301	0.3017	1.582	0.02841	0.8035	0.6484
0.34896	25.81	0.5243	50.35	0.036	0.07811	0.3031	1.668	0.03388	0.87453	0.78669
0.49913	30	0.5982	49.38	0.02571	0.05564	0.3041	1.823	0.03635	1.09052	0.65303
0.63668	41.11	0.6939	41.75	0.02197	0.05128	0.3175	2.059	0.03475	1.42874	0.7647
0.91127	56.17	0.7585	33.61	0.02324	0.04884	0.3492	2.845	0.03842	2.15793	1.10523
1.1196	49.28	0.8411	42.37	0.03009	0.05658	0.3021	2.898	0.04946	2.43751	1.25547
1.78228	47.72	0.814	42.29	0.0332	0.06432	0.4047	3.006	0.05128	2.44688	1.34138
2.12319	49.39	0.8466	43.06	0.0359	0.0585	0.2117	2.782	0.04769	2.35524	1.50123
2.80013	28.57	0.9006	76.93	0.07377	0.2146	1.314	2.568	0.08095	2.31274	1.78444
3.47445	17.39	0.9416	145.4	0.08033	0.2152	1.867	2.453	0.13282	2.30974	1.18274
4.72949	6.633	0.8631	326.7	0.08578	0.209	1.178	2.244	0.29199	1.9368	0.48174

4.5 mm Glass Beads Three-Phase Fluidized Bed, $U_\ell = 0.0546$ m/s

U_g (m/s)	f (1/s)	ε_g (-)	\bar{t}_i (1/2500 s)	$\bar{\ell}_b$ (m)	σ_ℓ (m)	$\ell_{b,vs}$ (m)	U_b (m/s)	$(\varepsilon_g U_b)/f$ (m)	$U_b \varepsilon_g$ (m/s)	$0.8467 f \bar{\ell}_b$ (m/s)
0.00311	4.517	0.03374	18.74	0.00382	0.00248	0.00743	0.3982	0.00297	0.01344	0.01461
0.00572	5.233	0.03957	18.24	0.00347	0.0032	0.01229	0.4017	0.00304	0.0159	0.01537
0.01075	7.222	0.0567	19.96	0.00459	0.00445	0.01498	0.4615	0.00362	0.02617	0.02807
0.01489	8.936	0.0738	20.98	0.00478	0.00556	0.02042	0.5256	0.00434	0.03879	0.03616
0.02184	11.43	0.09358	19.76	0.00535	0.00742	0.03536	0.6429	0.00526	0.06016	0.05177
0.03808	16.54	0.1546	24.18	0.00802	0.02191	0.1574	0.7808	0.0073	0.12071	0.11231
0.05414	17.28	0.1879	26.35	0.00746	0.01408	0.07432	0.778	0.00846	0.14619	0.10914
0.07674	14	0.2648	47.39	0.03467	0.05221	0.1872	1.221	0.02309	0.32332	0.41096
0.1095	14.56	0.306	52.69	0.05058	0.06442	0.1867	1.121	0.02356	0.34303	0.62352
0.14189	16.73	0.3646	54.05	0.04399	0.06462	0.1963	1.235	0.02691	0.45028	0.62311
0.17446	17.57	0.3751	53.2	0.03979	0.07933	0.3355	1.474	0.03147	0.5529	0.59191
0.22902	18.2	0.4347	59.66	0.0781	0.1365	0.557	1.603	0.03829	0.69682	1.20347
0.34224	22.38	0.4681	51.76	0.04033	0.08528	0.3911	1.752	0.03664	0.82011	0.76419
0.34544	28.39	0.572	49.94	0.04173	0.1137	0.5652	1.934	0.03897	1.10625	1.00306
0.48014	38.17	0.5879	38.02	0.02661	0.05801	0.3215	2.113	0.03254	1.24223	0.85996
0.62063	53.94	0.649	29.86	0.02385	0.0427	0.2285	2.429	0.02923	1.57642	1.08921
0.87013	63.11	0.757	29.91	0.02208	0.03721	0.1914	2.685	0.03221	2.03255	1.1798
1.41227	59.67	0.7971	32.88	0.0279	0.04901	0.2552	3.183	0.04252	2.53717	1.40952
1.76761	49.11	0.817	41.09	0.02863	0.05236	0.3284	2.937	0.04886	2.39953	1.19043
2.10484	41	0.8706	53	0.03583	0.07626	0.3768	3.22	0.06837	2.80333	1.24378
2.77664	27.14	0.9154	83.64	0.09691	0.3241	2.933	3.124	0.10537	2.85971	2.22685
3.45449	17.13	0.8982	130.4	0.09762	0.2166	1.017	2.728	0.14304	2.45029	1.41582
4.70361	5.517	0.8258	372.8	0.3051	1.039	6.763	2.428	0.36343	2.00504	1.42514

4.5 mm Glass Beads Three-Phase Fluidized Bed, $U_g = 0.0638$ m/s

U_g (m/s)	f (1/s)	ε_g (-)	τ_i (1/2500 s)	$\bar{\ell}_b$ (m)	σ_ℓ (m)	$\ell_{b,vs}$ (m)	U_b (m/s)	$(\varepsilon_g U_b)/f$ (m)	$U_b \varepsilon_g$ (m/s)	$0.8467 f \bar{\ell}_b$ (m/s)
0.00305	3.592	0.02206	15.03	0.00296	0.00159	0.00495	0.3843	0.00236	0.00848	0.009
0.00563	5.275	0.03428	16.22	0.00328	0.00207	0.00643	0.411	0.00267	0.01409	0.01465
0.01067	8.309	0.0545	16.34	0.00357	0.00331	0.01453	0.4935	0.00324	0.0269	0.02511
0.01474	9.293	0.06163	16.45	0.00364	0.00469	0.03111	0.5149	0.00341	0.03173	0.02864
0.02156	14.25	0.1085	18.05	0.00612	0.01251	0.07245	0.6268	0.00477	0.06801	0.07384
0.0376	15.89	0.1261	20.56	0.00666	0.01625	0.1144	0.7175	0.00569	0.09048	0.0896
0.0536	18.08	0.1964	26.63	0.01017	0.02709	0.1448	0.8669	0.00942	0.17026	0.15568
0.07481	15.28	0.2088	34.23	0.03613	0.05561	0.181	1.292	0.01766	0.26977	0.46742
0.10703	17.63	0.2974	41.95	0.03289	0.05096	0.1656	1.174	0.0198	0.34915	0.49094
0.13871	20.04	0.3235	40.2	0.02625	0.03687	0.1158	1.597	0.02578	0.51663	0.44539
0.17052	19	0.3603	47.36	0.04145	0.06907	0.2359	1.31	0.02484	0.47199	0.66679
0.22113	23	0.3929	42.27	0.02893	0.05924	0.3138	1.549	0.02646	0.6086	0.56336
0.33045	30.44	0.4504	36.32	0.03616	0.07502	0.3389	1.767	0.02615	0.79586	0.93193
0.33718	31.39	0.5204	41.13	0.05403	0.1137	0.4431	2.089	0.03463	1.08712	1.43595
0.4626	36.56	0.5487	37.42	0.02334	0.0411	0.1692	2.116	0.03176	1.16105	0.72247
0.60675	55.89	0.6575	29.12	0.02574	0.05497	0.3481	2.565	0.03018	1.68649	1.21802
0.83839	56.44	0.7704	33.93	0.03088	0.0629	0.362	2.925	0.03993	2.25342	1.47563
1.40022	66.28	0.7645	28.73	0.03176	0.06183	0.3783	2.826	0.0326	2.16048	1.78228
1.74752	53.83	0.8253	37.55	0.03462	0.0822	0.6369	3.093	0.04742	2.55265	1.57784
2.10432	41.94	0.8852	52.45	0.05136	0.1108	0.5873	2.935	0.06195	2.59806	1.82375
2.77598	24.17	0.9141	93.84	0.1108	0.3216	1.87	3.282	0.12412	3.00008	2.2674
3.42651	16.58	0.9364	136.8	0.144	0.5294	4.787	2.907	0.16418	2.72211	2.02143
4.63179	6.033	0.8593	354.9	0.2192	0.661	3.31	2.546	0.36264	2.18778	1.11966

4.5 mm Glass Beads Three-Phase Fluidized Bed, $U_\ell = 0.0729$ m/s

U_g (m/s)	f (1/s)	ε_g (-)	\bar{t}_i (1/2500 s)	$\bar{\ell}_b$ (m)	σ_ℓ (m)	$\ell_{b,vs}$ (m)	U_b (m/s)	$(\varepsilon_g U_b)/f$ (m)	$U_b \varepsilon_g$ (m/s)	$0.8467 f \bar{\ell}_b$ (m/s)
0.00304	3.933	0.02235	14.18	0.00268	0.00126	0.00399	0.4184	0.00238	0.00935	0.00892
0.00563	5.508	0.03085	14.47	0.003	0.00305	0.01687	0.446	0.0025	0.01376	0.01399
0.0107	8.631	0.0471	13.65	0.00309	0.00283	0.01653	0.4751	0.00259	0.02238	0.02258
0.01463	10.89	0.06454	15.32	0.00335	0.00323	0.01533	0.4975	0.00295	0.03211	0.03089
0.0214	14.63	0.08997	15.29	0.0046	0.00837	0.05284	0.6491	0.00399	0.0584	0.05698
0.03723	18.03	0.1344	19.28	0.00588	0.01205	0.07163	0.7746	0.00577	0.10411	0.08976
0.0532	22.06	0.1724	19.97	0.00681	0.01423	0.08042	0.8714	0.00681	0.15023	0.12719
0.07514	17.83	0.2175	30.28	0.05366	0.2044	1.588	1.451	0.0177	0.31559	0.81005
0.1042	20.83	0.2498	29.8	0.0237	0.03302	0.1243	1.424	0.01708	0.35572	0.41797
0.13538	20.83	0.2855	34.22	0.02451	0.04797	0.2007	1.554	0.0213	0.44367	0.43226
0.16646	24.24	0.3497	35.9	0.03569	0.07874	0.4218	1.494	0.02155	0.52245	0.73247
0.21168	29.39	0.4192	35.25	0.02997	0.05939	0.2566	1.987	0.02834	0.83295	0.74576
0.31217	31.72	0.441	34.29	0.02965	0.05628	0.2301	1.83	0.02544	0.80703	0.79629
0.32234	38.33	0.4927	31.89	0.02451	0.06124	0.3624	1.916	0.02463	0.94401	0.79542
0.44057	43.67	0.5928	33.57	0.02521	0.04599	0.2268	2.033	0.0276	1.20516	0.93211
0.56052	61.56	0.6607	26.56	0.02393	0.04856	0.3353	2.573	0.02762	1.69998	1.24725
1.02723	59.78	0.7199	29.76	0.02604	0.03975	0.194	2.825	0.03402	2.03372	1.31798
1.40022	58.89	0.7827	33.45	0.02643	0.04434	0.2032	2.764	0.03674	2.16338	1.31781
1.74256	48.67	0.8465	43.47	0.04918	0.09836	0.5231	3.3	0.0574	2.79345	2.02657
2.0811	42.56	0.8834	51.32	0.04935	0.09815	0.4316	2.947	0.06117	2.60338	1.77828
2.73082	24.1	0.9344	96.25	0.06401	0.1084	0.4854	2.857	0.11077	2.66958	1.3061
3.38051	15.06	0.909	150.5	0.1272	0.248	0.9756	2.999	0.18102	2.72609	1.6219
4.6192	6.641	0.8759	326.6	0.2232	1.014	7.656	2.411	0.31799	2.11179	1.25499

4.5 mm Glass Beads Three-Phase Fluidized Bed, $U_t = 0.100$ m/s

U_g (m/s)	f (1/s)	ε_g (-)	\bar{t}_i (1/2500 s)	$\bar{\ell}_b$ (m)	σ_{ℓ} (m)	$\ell_{b,vs}$ (m)	U_b (m/s)	$(\varepsilon_g U_b)/f$ (m)	$U_b \varepsilon_g$ (m/s)	$0.8467 f \bar{\ell}_b$ (m/s)
0.00288	4.392	0.02182	13.93	0.00247	0.00108	0.00352	0.4649	0.00231	0.01014	0.00918
0.00531	5.817	0.02702	11.11	0.00261	0.00123	0.00403	0.457	0.00212	0.01235	0.01285
0.00998	10.2	0.04482	10.76	0.00275	0.00193	0.00893	0.5426	0.00238	0.02432	0.02375
0.01376	12.37	0.05694	11.89	0.00287	0.00344	0.02976	0.5581	0.00257	0.03178	0.03006
0.02004	20.03	0.1059	13.32	0.00425	0.0083	0.06203	0.609	0.00322	0.06449	0.07207
0.03481	23.33	0.1364	14.16	0.00429	0.00689	0.04706	0.8527	0.00499	0.11631	0.08474
0.05083	29.04	0.151	13.49	0.00374	0.00597	0.04602	0.7902	0.00411	0.11932	0.09196
0.06749	29.5	0.1757	14.85	0.01512	0.0372	0.2213	1.681	0.01001	0.29535	0.37765
0.0993	33.94	0.2228	16.45	0.02027	0.03409	0.1289	1.975	0.01296	0.44003	0.58248
0.12387	36.06	0.2579	17.58	0.01696	0.03199	0.198	1.95	0.01395	0.50291	0.5178
0.15152	37.78	0.299	19.46	0.02453	0.08318	0.6436	1.892	0.01497	0.56571	0.78464
0.19475	41.72	0.3479	20.48	0.02353	0.04478	0.1947	1.948	0.01624	0.67771	0.83115
0.28573	43.83	0.4365	24.58	0.02837	0.04956	0.2086	2.035	0.02027	0.88828	1.05279
0.36784	39.61	0.4329	26.63	0.03385	0.06515	0.3272	2.13	0.02328	0.92208	1.13521
0.51873	52.5	0.5162	24.25	0.02589	0.04469	0.2017	2.33	0.02291	1.20275	1.15081
0.6911	59.06	0.6135	25.77	0.02386	0.03257	0.1337	2.483	0.02579	1.52332	1.1931
1.02418	65.44	0.7393	28.05	0.03153	0.05816	0.3127	2.821	0.03187	2.08557	1.74695
1.37292	63.78	0.7918	30.43	0.02646	0.04153	0.1665	2.765	0.03433	2.18933	1.42885
1.70432	50.56	0.8749	43.14	0.04456	0.1013	0.9602	3.01	0.05209	2.63345	1.9075
2.03005	42.11	0.8869	52.36	0.0542	0.1459	1.067	3.352	0.0706	2.97289	1.9324
2.66524	21.88	0.9403	106.8	0.1036	0.2162	0.9104	3.071	0.13198	2.88766	1.9192
3.26863	11.27	0.8964	196.8	0.1635	0.4196	2.202	3.017	0.23997	2.70444	1.56011
4.38139	4.5	0.8087	459.8	0.1538	0.5725	2.894	1.772	0.31845	1.43302	0.58598

4.5 mm Glass Beads Three-Phase Fluidized Bed, $U_\ell = 0.128$ m/s

U_g (m/s)	f (1/s)	ε_g (-)	\bar{t}_i (1/2500 s)	\bar{z}_b (m)	σ_ℓ (m)	$\ell_{b,vs}$ (m)	U_b (m/s)	$(\varepsilon_g U_b)/f$ (m)	$U_b \varepsilon_g$ (m/s)	$0.8467 f \bar{z}_b$ (m/s)
0.00277	4.667	0.01769	10.03	0.00236	0.0009	0.00312	0.5059	0.00192	0.00895	0.00933
0.00512	7.25	0.02971	10.11	0.00242	0.00106	0.00364	0.5168	0.00212	0.01535	0.01485
0.00969	10.76	0.04095	9.41	0.00235	0.00084	0.00299	0.5399	0.00205	0.02211	0.02141
0.0132	16.22	0.06516	9.695	0.00276	0.0018	0.00738	0.5732	0.0023	0.03735	0.0379
0.01934	22.88	0.08799	9.643	0.00277	0.00135	0.00444	0.6431	0.00247	0.05659	0.05366
0.03373	34.83	0.1352	9.953	0.0034	0.00484	0.03614	0.8131	0.00316	0.10993	0.10026
0.04783	39.28	0.163	10.47	0.00318	0.00378	0.03204	0.7638	0.00317	0.1245	0.10576
0.06718	55	0.217	10.14	0.00389	0.006	0.05123	0.9988	0.00394	0.21674	0.18114
0.09437	61.22	0.2478	10.22	0.0042	0.0066	0.05356	1.228	0.00497	0.3043	0.2177
0.14342	44.94	0.2749	15.42	0.03408	0.09134	0.6607	2.205	0.01349	0.60615	1.29672
0.17725	43.28	0.2862	16.8	0.02585	0.04109	0.1315	2.119	0.01401	0.60646	0.94724
0.23268	50.33	0.3314	16.6	0.02326	0.04638	0.222	2.282	0.01503	0.75625	0.99117
0.34499	56.28	0.461	20.24	0.03082	0.06245	0.2652	2.25	0.01843	1.03725	1.46859
0.36682	64.94	0.4527	17.5	0.02244	0.04194	0.1969	2.488	0.01734	1.12632	1.23381
0.51593	61.78	0.5184	20.84	0.02628	0.0453	0.2245	2.584	0.02168	1.33955	1.37463
0.68352	68.94	0.6245	22.54	0.02643	0.04031	0.1977	2.692	0.02439	1.68115	1.5427
1.00217	69.72	0.7345	26.23	0.03191	0.05582	0.4115	2.991	0.03151	2.19689	1.88363
1.33655	64.5	0.8166	31.44	0.035	0.06083	0.2908	2.863	0.03625	2.33793	1.91135
1.66815	52.22	0.8875	42.39	0.03898	0.07052	0.3235	2.982	0.05068	2.64653	1.72342
1.97797	42.83	0.8895	52.78	0.06673	0.1987	1.758	3.142	0.06525	2.79481	2.41981
2.57957	20.67	0.9215	111.1	0.09737	0.2723	1.603	2.805	0.12505	2.58481	1.70403
3.15283	12.78	0.9439	164.7	0.1129	0.313	1.749	2.658	0.19631	2.50889	1.22162
4.22758	14.69	0.9336	--	0.06683	0.1691	0.7174	2.187	0.13899	2.04178	0.8312

4.5 mm Glass Beads Three-Phase Fluidized Bed, $U_\ell = 0.155$ m/s

U_g (m/s)	f (1/s)	ε_g (-)	τ_i (1/2500 s)	\bar{z}_b (m)	σ_ℓ (m)	$\ell_{b,vs}$ (m)	U_b (m/s)	$(\varepsilon_g U_b)/f$ (m)	$U_b \varepsilon_g$ (m/s)	$0.8467 f \bar{z}_b$ (m/s)
0.00311	2.842	0.01038	9.261	0.00223	0.00081	0.00287	0.499	0.00182	0.00518	0.00537
0.00572	4.275	0.01465	8.376	0.00233	0.00103	0.00358	0.5423	0.00186	0.00794	0.00843
0.01095	8.272	0.03068	9.26	0.00235	0.00111	0.00359	0.5346	0.00198	0.0164	0.01646
0.015	11.7	0.04345	9.19	0.00262	0.00169	0.00645	0.6016	0.00223	0.02614	0.02595
0.0219	17.08	0.06818	9.646	0.00265	0.00131	0.00463	0.588	0.00235	0.04009	0.03832
0.03859	24.88	0.0993	10.02	0.00306	0.00327	0.02341	0.6991	0.00279	0.06942	0.06446
0.05513	40.11	0.1484	9.141	0.00334	0.00291	0.013	0.8349	0.00309	0.1239	0.11343
0.07715	40	0.1748	10.9	0.00427	0.01002	0.101	0.8393	0.00367	0.14671	0.14461
0.1101	48.67	0.1969	10.36	0.00437	0.01015	0.09579	0.9984	0.00404	0.19658	0.18008
0.14266	63.06	0.2727	11.21	0.00597	0.01418	0.1083	1.321	0.00571	0.36024	0.31874
0.17869	68.61	0.2904	10.37	0.00683	0.01984	0.1821	1.386	0.00587	0.40249	0.39675
0.23579	64.94	0.3412	13.19	0.02066	0.0409	0.1919	2.066	0.01085	0.70492	1.13594
0.35426	70.39	0.3698	13.29	0.02103	0.03814	0.2332	2.396	0.01259	0.88604	1.25332
0.36385	71.61	0.4374	14.74	0.02027	0.03647	0.1838	2.363	0.01443	1.03358	1.22897
0.44629	72.5	0.4754	16.48	0.02719	0.06254	0.3274	2.498	0.01638	1.18755	1.66901
0.68352	73.44	0.6654	22.33	0.03164	0.0577	0.3029	2.623	0.02377	1.74534	1.96735
1.00207	77.22	0.7502	23.53	0.03181	0.04825	0.1881	2.997	0.02912	2.24835	2.07973
1.3328	65.28	0.8421	32.05	0.04106	0.07186	0.3423	3.099	0.03998	2.60967	2.2694
1.6553	53	0.8821	41.58	0.04701	0.1148	0.9193	2.998	0.0499	2.64454	2.1095
1.96311	44.56	0.8932	49.98	0.06366	0.1607	1.291	3.065	0.06144	2.73766	2.40173
2.54929	23.7	0.9389	95.71	0.08061	0.3128	2.517	2.631	0.10423	2.47025	1.61752
3.15243	16.98	0.928	144.1	0.06674	0.1348	0.5158	2.397	0.131	2.22442	0.95948
4.21861	10.74	0.9183	220.7	0.07414	0.2987	2.678	1.623	0.13877	1.4904	0.67417

4.5 mm Glass Beads Three-Phase Fluidized Bed, $U_\ell = 0.218$ m/s

U_g (m/s)	f (1/s)	ε_g (-)	τ_i (1/2500 s)	$\bar{\ell}_b$ (m)	σ_ℓ (m)	$\ell_{b,vs}$ (m)	U_b (m/s)	$(\varepsilon_g U_b)/f$ (m)	$U_b \varepsilon_g$ (m/s)	$0.8467 f \bar{\ell}_b$ (m/s)
0.00306	3.75	0.01125	7.637	0.00204	0.00064	0.00247	0.5485	0.00165	0.00617	0.00648
0.00565	5.5	0.01709	7.91	0.00218	0.00072	0.0027	0.5557	0.00173	0.0095	0.01015
0.01067	9.436	0.03088	8.21	0.00226	0.00079	0.0029	0.5793	0.0019	0.01789	0.01806
0.01474	11.27	0.03545	7.854	0.00248	0.00188	0.01245	0.6333	0.00199	0.02245	0.02366
0.02151	15.74	0.05419	8.618	0.00267	0.0014	0.00512	0.6706	0.00231	0.03634	0.03558
0.03779	24.19	0.08295	8.316	0.00278	0.00188	0.00907	0.7182	0.00246	0.05957	0.05694
0.05413	32.56	0.107	8.049	0.00278	0.00132	0.00424	0.8157	0.00268	0.08728	0.07664
0.07734	39.89	0.1376	8.493	0.00397	0.00646	0.05355	0.9577	0.0033	0.13178	0.13408
0.10865	58.44	0.2034	8.676	0.00415	0.00607	0.07288	1.143	0.00398	0.23249	0.20534
0.14188	70.72	0.242	8.648	0.0047	0.00757	0.05172	1.278	0.00437	0.30928	0.28142
0.17141	81.56	0.2603	7.858	0.00468	0.0061	0.03571	1.413	0.00451	0.3678	0.32317
0.23081	94.28	0.3249	8.184	0.00551	0.01147	0.08275	1.557	0.00537	0.50587	0.43983
0.34229	84.83	0.3693	10.73	0.0217	0.0506	0.3051	2.359	0.01027	0.87118	1.55855
0.35427	90.61	0.4277	11.61	0.01917	0.03177	0.1393	2.505	0.01182	1.07139	1.47065
0.43133	94.39	0.4915	12.54	0.02181	0.03758	0.1596	2.793	0.01454	1.37276	1.74299
0.65545	90.61	0.6326	17.67	0.02381	0.0321	0.1353	2.767	0.01932	1.7504	1.82662
0.95722	92.11	0.7449	20.15	0.02978	0.04663	0.2143	3.094	0.02502	2.30472	2.32244
1.28979	80.78	0.8208	25.21	0.03935	0.07665	0.4889	3.149	0.032	2.5847	2.69129
1.58026	60.39	0.8796	36.46	0.04429	0.08407	0.4737	3.376	0.04917	2.96953	2.26456
1.87173	42	0.9155	53.51	0.06081	0.1018	0.3689	2.986	0.06509	2.73368	2.1624
2.43963	21.81	0.9289	106.1	0.108	0.217	0.9075	3.163	0.13471	2.93811	1.99431
2.97679	14.11	0.8807	143.5	0.1534	0.4367	2.117	2.847	0.1777	2.50735	1.83259
3.9429	52.29	0.9295	--	0.0235	0.04683	0.2146	1.941	0.0345	1.80416	1.0404

4.5 mm Glass Beads Three-Phase Fluidized Bed.

U_g (m/s)	U_ℓ (m/s)						
	0.0035	0.0050	0.0080	0.012	0.020	0.030	0.040
	$\sigma_t/\bar{\epsilon}_i$						
0.0364	0.94059	0.87405	0.84012	0.86642	1.01325	1.12159	1.21328
0.0455	0.81288	0.83849	0.90506	1.00791	1.19163	1.37716	1.46422
0.0546	0.84993	0.87667	0.8967	0.9515	1.23568	1.42616	1.62394
0.0638	0.76796	0.83753	0.90127	0.97252	1.29119	1.46835	1.64185
0.0729	0.82572	0.94318	0.91615	0.85012	1.30143	1.46652	1.67357
0.1	0.7542	0.83638	0.74949	0.82052	1.28326	1.47697	1.70511
0.128	0.74208	0.66829	0.64284	0.68503	0.65109	0.9587	1.16334
0.155	0.61055	0.62498	0.66177	0.68236	0.65137	0.71018	0.77967
0.218	0.57679	0.55415	0.56374	0.58648	0.61541	0.60734	0.61394

1.2 mm Steel Shot Three-Phase Fluidized Bed, $U_\ell = 0.0364$ m/s

U_g (m/s)	f (1/s)	ε_g (-)	τ_i^- (1/2500 s)	\bar{x}_b (m)	σ_ℓ (m)	$\ell_{b,vs}$ (m)	U_b (m/s)	$(\varepsilon_g U_b)/f$ (m)	$U_b \varepsilon_g$ (m/s)	$0.8467 f \bar{\ell}_b$ (m/s)
0.00298	1.433	0.01539	26.81	0.00644	0.00676	0.0207	0.4697	0.00504	0.00723	0.00781
0.00549	2.075	0.02356	28.4	0.00594	0.00579	0.01546	0.5993	0.0068	0.01412	0.01044
0.01033	4.025	0.05018	31.17	0.00781	0.0117	0.04377	0.5502	0.00686	0.02761	0.02662
0.0144	5.253	0.06627	31.48	0.00692	0.01038	0.03829	0.6587	0.00831	0.04365	0.03078
0.02102	7.246	0.1001	34.69	0.00678	0.01139	0.05445	0.537	0.00742	0.05375	0.04159
0.03701	10.5	0.1457	34.64	0.00712	0.0107	0.03594	0.7031	0.00976	0.10244	0.0633
0.05146	9.556	0.1471	38.41	0.03057	0.07127	0.4426	1.252	0.01927	0.18417	0.24733
0.0735	11	0.1878	42.61	0.02721	0.04011	0.1365	1.412	0.02411	0.26517	0.25342
0.10515	12.97	0.2429	46.82	0.01442	0.0213	0.08482	1.068	0.02	0.25942	0.15835
0.1366	15.03	0.2942	48.94	0.02047	0.03737	0.1898	1.239	0.02425	0.36451	0.26049
0.16884	16.67	0.347	51.79	0.01968	0.04462	0.2586	0.9409	0.01959	0.32649	0.27776
0.22157	20.37	0.3719	45.66	0.01058	0.01409	0.05009	1.334	0.02436	0.49611	0.18247
0.28264	25.21	0.4416	44.79	0.00856	0.01584	0.09552	0.9356	0.01639	0.41316	0.18271
0.3435	28	0.4558	40.26	0.01374	0.02649	0.11	1.461	0.02378	0.66592	0.32573
0.48431	32.94	0.4932	36.22	0.01337	0.03292	0.186	1.693	0.02535	0.83499	0.37288
0.63924	35.83	0.5626	38.82	0.02502	0.0652	0.309	1.883	0.02957	1.05938	0.75901
0.89181	50.39	0.6609	31.38	0.01258	0.02019	0.08289	1.547	0.02029	1.02241	0.53671
1.1747	47.5	0.6853	35.48	0.01839	0.04129	0.2232	1.902	0.02744	1.30344	0.73958
1.41325	46.5	0.808	43.91	0.04066	0.1475	1.031	1.973	0.03428	1.59418	1.60078
1.97627	48.33	0.7351	34.11	0.01811	0.0496	0.3777	1.679	0.02554	1.23423	0.74105
2.62937	39.33	0.8181	54.47	0.02981	0.06992	0.353	1.677	0.03488	1.37195	0.99266
3.29095	32.17	0.8509	62.6	0.02168	0.05642	0.3295	1.751	0.04631	1.48993	0.5905
4.6733	6.162	0.8013	317.1	0.08498	0.2743	1.598	1.582	0.20572	1.26766	0.44335

1.2 mm Steel Shot Three-Phase Fluidized Bed, $U_\ell = 0.0455 \text{ m/s}$

U_g (m/s)	f (1/s)	ε_g (-)	τ_i (1/2500 s)	$\bar{\ell}_b$ (m)	σ_ℓ (m)	$\ell_{b,vs}$ (m)	U_b (m/s)	$(\varepsilon_g U_b)/f$ (m)	$U_b \varepsilon_g$ (m/s)	$0.8467 f \bar{\ell}_b$ (m/s)
0.00297	1.5	0.01333	22.22	0.0055	0.00696	0.02559	0.4493	0.00399	0.00599	0.00699
0.00547	2.583	0.02831	27.51	0.0062	0.00702	0.02294	0.5487	0.00601	0.01553	0.01356
0.01029	4.025	0.03741	23.27	0.00577	0.00796	0.0337	0.6348	0.0059	0.02375	0.01966
0.0144	4.771	0.05378	28.17	0.00793	0.01166	0.04567	0.642	0.00724	0.03453	0.03203
0.02102	7.348	0.08357	28.54	0.00805	0.01397	0.06009	0.6381	0.00726	0.05333	0.05008
0.03657	9.519	0.1254	32.98	0.00824	0.01549	0.06779	0.8243	0.01086	0.10337	0.06641
0.05239	12.12	0.1545	31.78	0.00571	0.01331	0.08442	0.6191	0.00789	0.09565	0.05859
0.07364	12.38	0.1872	37.78	0.02093	0.03426	0.1597	1.199	0.01813	0.22445	0.21938
0.1051	14.36	0.2134	37	0.02319	0.05649	0.3293	1.101	0.01636	0.23495	0.28195
0.13622	15.7	0.2434	38.55	0.02006	0.03701	0.1516	1.229	0.01905	0.29914	0.26665
0.16799	18.43	0.2831	38.17	0.02131	0.04404	0.1979	1.083	0.01664	0.3066	0.33252
0.22043	19.89	0.3371	42.41	0.00866	0.01731	0.1064	1.01	0.01712	0.34047	0.14584
0.28439	24.62	0.4197	42.24	0.01764	0.06333	0.4796	1.143	0.01948	0.47972	0.3677
0.34789	27.52	0.4256	38.34	0.01669	0.03308	0.1281	1.387	0.02145	0.59031	0.38888
0.46965	35.67	0.4607	32.56	0.01677	0.02947	0.1138	1.342	0.01733	0.61826	0.50646
0.60675	40.44	0.5044	30.96	0.01064	0.01863	0.0907	1.653	0.02062	0.83377	0.36431
0.87079	48.22	0.6562	31.9	0.02034	0.04073	0.1659	1.836	0.02499	1.20478	0.83041
1.09888	47.33	0.7481	39.25	0.02492	0.06591	0.4188	2.141	0.03384	1.60168	0.99861
1.64548	46.28	0.7459	38.94	0.01484	0.0335	0.1773	1.872	0.03017	1.39632	0.58149
1.97627	43.17	0.764	44.01	0.02289	0.03806	0.3794	1.749	0.03095	1.33624	0.83664
2.61674	35.57	0.8237	56.53	0.02488	0.05771	0.2497	2.019	0.04675	1.66305	0.74928
3.29679	29.08	0.8718	71.36	0.02286	0.06437	0.4661	1.607	0.04818	1.40098	0.56284
4.62797	3.308	0.6612	474.2	0.2302	0.8289	4.343	1.527	0.30522	1.00965	0.64474

1.2 mm Steel Shot Three-Phase Fluidized Bed, $U_\ell = 0.0546$ m/s

U_g (m/s)	f (1/s)	ε_g (-)	τ_i (1/2500 s)	$\bar{\ell}_b$ (m)	σ_ℓ (m)	$\ell_{b,vs}$ (m)	U_b (m/s)	$(\varepsilon_g U_b)/f$ (m)	$U_b \varepsilon_g$ (m/s)	$0.8467 f \bar{\ell}_b$ (m/s)
0.00297	2.308	0.01657	18.04	0.00647	0.00783	0.0294	0.7403	0.00531	0.01227	0.01264
0.00548	3.042	0.02674	22.05	0.00697	0.00917	0.03198	0.6384	0.00561	0.01707	0.01795
0.01031	5.121	0.0469	22.9	0.00713	0.01091	0.04562	0.7355	0.00674	0.03449	0.03091
0.01423	6.436	0.05594	21.75	0.00651	0.00762	0.02422	0.8087	0.00703	0.04524	0.03547
0.02087	8.895	0.09253	26.07	0.00753	0.01254	0.05164	0.6743	0.00701	0.06239	0.05671
0.03648	11.87	0.1264	26.57	0.00751	0.01374	0.05817	0.7163	0.00763	0.09054	0.07547
0.05226	12.02	0.1496	31.1	0.00684	0.01195	0.05811	0.6546	0.00815	0.09793	0.06961
0.07212	13.21	0.1911	36.17	0.02782	0.05269	0.2262	1.16	0.01678	0.22168	0.31115
0.10412	14.39	0.2211	38.18	0.0215	0.0446	0.1921	1.174	0.01804	0.25957	0.26195
0.13195	16.52	0.251	38.01	0.01698	0.02692	0.09865	1.231	0.0187	0.30898	0.2375
0.16382	17.23	0.2987	43.09	0.02156	0.04313	0.1855	1.049	0.01819	0.31334	0.31452
0.22301	20.04	0.3309	41.24	0.01896	0.02936	0.09324	1.422	0.02348	0.47054	0.3217
0.27113	26.33	0.3862	36.38	0.02904	0.0569	0.2089	1.358	0.01992	0.52446	0.64738
0.32951	28.05	0.4185	37.28	0.02849	0.1077	0.8486	1.494	0.02229	0.62524	0.67661
0.44509	31	0.4675	35.93	0.02179	0.05233	0.3447	1.678	0.02531	0.78447	0.57191
0.58227	38.89	0.5676	36.52	0.01564	0.02594	0.09876	1.304	0.01903	0.74015	0.51498
0.80874	43.22	0.6696	38.06	0.02923	0.08814	0.4936	1.622	0.02513	1.08609	1.06961
1.31468	45.22	0.6226	34.41	0.01661	0.04066	0.2709	1.736	0.0239	1.08083	0.63593
1.63316	46.78	0.7487	40.78	0.02182	0.0837	0.8173	1.54	0.02465	1.153	0.86423
1.96147	42.28	0.7578	42.77	0.03227	0.0746	0.3692	1.497	0.02683	1.13443	1.15517
2.5968	35.57	0.8167	56.88	0.01923	0.03023	0.08842	1.272	0.02921	1.03884	0.57913
3.21984	26.59	0.8643	75.25	0.02491	0.07246	0.4572	1.585	0.05152	1.36992	0.5608
4.63734	2.008	0.5008	639.7	0.1581	0.3722	1.459	1.442	0.35964	0.72215	0.26879

1.2 mm Steel Shot Three-Phase Fluidized Bed, $U_\ell = 0.0638$ m/s

U_g (m/s)	f (1/s)	ε_g (-)	\bar{t}_i (1/2500 s)	$\bar{\ell}_b$ (m)	σ_ℓ (m)	$\ell_{b,vs}$ (m)	U_b (m/s)	$(\varepsilon_g U_b)/f$ (m)	$U_b \varepsilon_g$ (m/s)	$0.8467 f \bar{\ell}_b$ (m/s)
0.00296	2.958	0.02179	18.3	0.0059	0.00855	0.0427	0.6433	0.00474	0.01402	0.01478
0.00546	4.042	0.02997	18.53	0.0068	0.01129	0.04951	0.6758	0.00501	0.02025	0.02327
0.01026	5.581	0.03964	17.75	0.0049	0.00551	0.01834	0.6859	0.00487	0.02719	0.02315
0.01417	7.097	0.05245	18.45	0.00645	0.00989	0.0451	0.8772	0.00648	0.04601	0.03876
0.02068	9.556	0.07424	19.45	0.00516	0.01035	0.07781	0.7171	0.00557	0.05324	0.04175
0.03631	11.27	0.1121	25.08	0.008	0.01399	0.06735	0.7231	0.00719	0.08106	0.07634
0.05201	11.93	0.131	27.52	0.0056	0.00921	0.04255	0.6636	0.00729	0.08693	0.05656
0.07277	12.48	0.1899	38.22	0.02648	0.04308	0.1589	1.608	0.02447	0.30536	0.2798
0.10403	15.79	0.2335	37.12	0.02599	0.05251	0.251	1.23	0.01819	0.28721	0.34746
0.13456	14.39	0.2559	44.3	0.03094	0.07483	0.3161	1.27	0.02258	0.32499	0.37696
0.16224	17.3	0.2909	41.84	0.02417	0.06626	0.4563	1.504	0.02529	0.43751	0.35403
0.2134	20.3	0.3001	36.68	0.01774	0.03495	0.1511	1.386	0.02049	0.41594	0.3049
0.27094	24.29	0.3863	39.67	0.01717	0.02716	0.0996	1.18	0.01877	0.45583	0.35311
0.31562	29.44	0.4606	38.09	0.01589	0.0344	0.1941	1.78	0.02785	0.81987	0.39607
0.4317	29.67	0.4351	36.5	0.03978	0.1614	1.139	1.87	0.02742	0.81364	0.9993
0.54572	40.5	0.5607	33.68	0.02863	0.08688	0.4649	1.805	0.02499	1.01206	0.98172
0.97541	38.83	0.5395	34.54	0.01578	0.0272	0.1303	1.618	0.02248	0.87291	0.51878
1.31468	41.39	0.6709	40.79	0.01439	0.0269	0.1181	1.641	0.0266	1.10095	0.50428
1.62509	42.61	0.6864	41.45	0.02643	0.103	0.8306	1.945	0.03133	1.33505	0.9535
1.95179	47.89	0.7591	39.36	0.02688	0.09178	0.5897	1.386	0.02197	1.05211	1.0899
2.5841	35.14	0.7985	51.46	0.03175	0.09319	0.4445	1.368	0.03109	1.09235	0.94462
3.22644	22.79	0.8986	107.5	0.03576	0.08052	0.3248	1.675	0.06604	1.50516	0.69001
4.54758	1.692	0.4818	509.9	0.1552	0.5187	2.178	2.116	0.60253	1.01949	0.22233

1.2 mm Steel Shot Three-Phase Fluidized Bed, $U_\ell = 0.0729$ m/s

U_g (m/s)	f (1/s)	ε_g (-)	\bar{t}_i (1/2500 s)	$\bar{\ell}_b$ (m)	σ_ℓ (m)	$\ell_{b,vs}$ (m)	U_b (m/s)	$(\varepsilon_g U_b)/f$ (m)	$U_b \varepsilon_g$ (m/s)	$0.8467 f \bar{\ell}_b$ (m/s)
0.00293	3.492	0.01978	14.21	0.00477	0.00535	0.01838	0.7523	0.00426	0.01488	0.0141
0.00543	4.64	0.02959	15.8	0.00539	0.00521	0.01571	0.6837	0.00436	0.02023	0.02117
0.01028	5.646	0.04067	18.07	0.00563	0.00613	0.02006	0.7551	0.00544	0.03071	0.02691
0.01407	7.742	0.06338	20.5	0.00748	0.01133	0.0466	0.8122	0.00665	0.05148	0.04903
0.02063	8.619	0.0703	20.46	0.00785	0.01487	0.0709	0.8137	0.00664	0.0572	0.05728
0.03598	11.06	0.0947	21.58	0.00578	0.00912	0.03945	0.7309	0.00626	0.06922	0.05412
0.05106	10.18	0.1178	28.88	0.01949	0.02114	0.06154	1.493	0.01728	0.17588	0.16799
0.07123	13.9	0.1683	30.22	0.02273	0.03841	0.1484	1.661	0.02011	0.27955	0.2675
0.09933	14.03	0.2033	36.03	0.02196	0.03598	0.1394	1.249	0.0181	0.25392	0.26086
0.12909	15.52	0.2437	39.02	0.01832	0.03142	0.1481	1.191	0.0187	0.29025	0.24073
0.15898	18.56	0.2667	35.66	0.02385	0.04318	0.1749	1.457	0.02094	0.38858	0.37478
0.21026	22.38	0.3076	33.72	0.02236	0.05842	0.419	1.824	0.02507	0.56106	0.42369
0.25955	24.71	0.3609	37.68	0.01907	0.04491	0.228	1.261	0.01842	0.45509	0.39897
0.31197	26.81	0.3822	35.35	0.01572	0.02605	0.1221	1.495	0.02131	0.57139	0.35683
0.43035	34.61	0.4672	33.65	0.0258	0.05486	0.2524	1.588	0.02144	0.74191	0.75602
0.54572	43.11	0.5977	34.62	0.01135	0.01957	0.08672	1.493	0.0207	0.89237	0.41427
0.96333	38.5	0.5636	36.38	0.01406	0.02431	0.09879	1.577	0.02309	0.8888	0.45831
1.31293	46.5	0.6586	35.15	0.01656	0.02973	0.1229	1.672	0.02368	1.10118	0.65197
1.66337	46	0.7134	36.03	0.02165	0.03771	0.1253	1.346	0.02087	0.96024	0.8432
2.00205	40.5	0.777	48.25	0.04424	0.1131	0.4939	1.791	0.03436	1.39161	1.51699
2.69391	31.53	0.8456	72.76	0.03331	0.109	0.6756	1.878	0.05037	1.58804	0.88922
3.54223	9.034	0.8852	265.9	0.06897	0.3959	3.773	1.485	0.14551	1.31452	0.52754
4.53516	1.058	0.3847	1028	0.5003	1.353	4.571	2.149	0.7814	0.82672	0.44816

1.2 mm Steel Shot Three-Phase Fluidized Bed, $U_\ell = 0.100$ m/s

U_g (m/s)	f (1/s)	ε_g (-)	\bar{t}_i (1/2500 s)	$\bar{\ell}_b$ (m)	σ_ℓ (m)	$\ell_{b,vs}$ (m)	U_b (m/s)	$(\varepsilon_g U_b)/f$ (m)	$U_b \varepsilon_g$ (m/s)	$0.8467 f \bar{\ell}_b$ (m/s)
0.00287	2.483	0.01023	10.57	0.00428	0.00405	0.01379	0.868	0.00358	0.00888	0.009
0.0053	3.992	0.01758	10.77	0.00384	0.00289	0.00805	0.882	0.00391	0.01561	0.01298
0.00996	5.656	0.02735	12.17	0.00532	0.00735	0.03238	1.027	0.00497	0.02809	0.02548
0.01376	5.948	0.03308	14.35	0.00622	0.00921	0.03635	0.8585	0.00477	0.0284	0.03132
0.02012	8.116	0.05215	16.53	0.00632	0.01172	0.0683	0.8563	0.0055	0.04466	0.04343
0.03509	10.48	0.081	19.47	0.00479	0.00679	0.02711	0.7536	0.00582	0.06104	0.0425
0.0492	11.23	0.1106	24.75	0.00877	0.01584	0.06942	0.9116	0.00898	0.10082	0.08339
0.06625	13.51	0.129	23.73	0.0295	0.05702	0.2372	1.456	0.0139	0.18782	0.33743
0.09245	15.61	0.164	26.23	0.01699	0.02779	0.1343	1.687	0.01772	0.27667	0.22455
0.12143	17.87	0.1962	27.08	0.02398	0.03488	0.1147	1.704	0.01871	0.33432	0.36282
0.14537	19.67	0.2566	32.27	0.02958	0.06232	0.2502	1.951	0.02545	0.50063	0.49262
0.19112	24.25	0.2705	27.91	0.02731	0.0568	0.3107	2.04	0.02276	0.55182	0.56072
0.28397	18.7	0.2795	37.14	0.03042	0.06134	0.3168	1.681	0.02513	0.46984	0.48163
0.34512	18.63	0.3058	40.91	0.02588	0.05754	0.2695	1.873	0.03074	0.57276	0.40822
0.48669	28.94	0.3882	33.47	0.01855	0.04159	0.2197	1.528	0.0205	0.59317	0.45452
0.65117	34.22	0.4588	33.3	0.01908	0.0305	0.1045	1.489	0.01996	0.68315	0.5528
0.95168	41.44	0.5551	33.38	0.02257	0.04827	0.2303	1.964	0.02631	1.09022	0.79189
1.27632	49.11	0.6502	33.41	0.02212	0.03092	0.1432	1.835	0.02429	1.19312	0.91975
1.5791	45.78	0.7626	41.64	0.02109	0.04168	0.2044	1.653	0.02754	1.26058	0.81746
1.88345	45.89	0.7726	39.25	0.02024	0.05901	0.3671	1.469	0.02473	1.13495	0.7864
2.47763	28.07	0.8698	84.07	0.03001	0.08435	0.4704	1.43	0.04431	1.24381	0.71322
3.12798	8.483	0.8634	272	0.07631	0.07723	0.3146	1.411	0.14361	1.21826	0.54808
4.65132	3.167	0.7653	623.4	0.3168	1.14	6.678	2.719	0.65704	2.08085	0.84947

1.2 mm Steel Shot Three-Phase Fluidized Bed, $U_\ell = 0.155$ m/s

U_g (m/s)	f (1/s)	ε_g (-)	τ_i (1/2500 s)	$\bar{\ell}_b$ (m)	σ_ℓ (m)	$\ell_{b,vs}$ (m)	U_b (m/s)	$(\varepsilon_g U_b)/f$ (m)	$U_b \varepsilon_g$ (m/s)	$0.8467 f \bar{\ell}_b$ (m/s)
0.00294	2.983	0.00611	5.123	0.00339	0.00259	0.00815	1.359	0.00278	0.0083	0.00856
0.00543	5.505	0.01108	5.028	0.00305	0.00256	0.00877	1.207	0.00243	0.01337	0.01422
0.01021	6.813	0.01812	6.594	0.0034	0.00297	0.00966	1.144	0.00304	0.02073	0.01961
0.01417	10.02	0.02564	6.39	0.00308	0.00266	0.00861	1.325	0.00339	0.03397	0.02613
0.02068	11.95	0.03893	8.105	0.00457	0.00686	0.02914	1.273	0.00415	0.04956	0.04624
0.03639	13.6	0.06155	11.45	0.00545	0.0073	0.03017	1.092	0.00494	0.06721	0.06275
0.05201	17.18	0.08112	12.01	0.00492	0.00678	0.02658	1.135	0.00536	0.09207	0.07157
0.07277	17.93	0.08896	12.51	0.00536	0.00671	0.02126	1.039	0.00516	0.09243	0.08137
0.10313	31.14	0.162	12.5	0.01738	0.02381	0.08627	2.054	0.01069	0.33275	0.45823
0.13399	28.56	0.1849	16.18	0.02733	0.04499	0.1873	2.221	0.01438	0.41066	0.66086
0.16485	33.39	0.1854	13.92	0.02227	0.0432	0.216	1.963	0.0109	0.36394	0.62958
0.21683	38.56	0.2236	14.45	0.02181	0.03402	0.1299	2.242	0.013	0.50131	0.71204
0.2753	48.94	0.3105	15.52	0.01765	0.02594	0.1028	1.99	0.01263	0.6179	0.73134
0.33304	52.89	0.3479	16.34	0.01679	0.02231	0.08587	2.399	0.01578	0.83461	0.75186
0.46965	63.56	0.4114	16.08	0.01906	0.03773	0.2249	2.101	0.0136	0.86435	1.0257
0.62021	78.56	0.5282	16.81	0.01508	0.01738	0.06062	2.49	0.01674	1.31522	1.00303
0.91707	79.06	0.674	20.79	0.02604	0.08179	0.79	2.742	0.02338	1.84811	1.74305
1.22516	69.89	0.7939	27.89	0.02184	0.03851	0.1678	2.545	0.02891	2.02048	1.29235
1.53253	62.94	0.8506	33.26	0.0287	0.0526	0.271	2.557	0.03456	2.17498	1.5294
1.84425	42.94	0.9039	52.3	0.04336	0.1194	0.7083	2.758	0.05806	2.49296	1.57639
2.45122	17.7	0.8798	123.4	0.06426	0.1794	1.089	2.451	0.12183	2.15639	0.963
3.03324	7.988	0.8768	289.5	0.153	0.4687	2.592	2.643	0.29011	2.31738	1.03477

1.2 mm Steel Shot Three-Phase Fluidized Bed, $U_\ell = 0.200$ m/s

U_g (m/s)	f (1/s)	ε_g (-)	τ_1^- (1/2500 s)	$\bar{\ell}_b$ (m)	σ_ℓ (m)	$\ell_{b,vs}$ (m)	U_b (m/s)	$(\varepsilon_g U_b)/f$ (m)	$U_b \varepsilon_g$ (m/s)	$0.8467 f \bar{\ell}_b$ (m/s)
0.00293	3.542	0.00531	3.764	0.00252	0.00129	0.00406	1.338	0.00201	0.0071	0.00756
0.0054	5.874	0.00874	3.74	0.0025	0.00127	0.00392	1.428	0.00212	0.01248	0.01243
0.01014	9.833	0.01459	3.693	0.00266	0.00152	0.00471	1.435	0.00213	0.02094	0.02215
0.014	16.67	0.02552	3.806	0.00276	0.00167	0.0051	1.542	0.00236	0.03935	0.03895
0.02039	26.57	0.0363	3.416	0.00285	0.00209	0.00741	1.668	0.00228	0.06055	0.06411
0.0358	33	0.04878	3.736	0.00286	0.00211	0.00678	1.601	0.00237	0.0781	0.07991
0.05106	44.5	0.08049	4.454	0.00319	0.00286	0.01056	1.622	0.00293	0.13055	0.12019
0.07144	51.61	0.105	5.202	0.00354	0.00358	0.01279	1.596	0.00325	0.16758	0.15469
0.10196	60.17	0.1502	6.186	0.00434	0.00639	0.03067	1.444	0.0036	0.21689	0.2211
0.13305	65.06	0.196	7.682	0.01468	0.01868	0.08049	2.801	0.00844	0.549	0.80864
0.16298	60.83	0.2107	8.439	0.01415	0.01739	0.06538	2.595	0.00899	0.54677	0.72876
0.2134	62.72	0.2381	9.714	0.01622	0.02575	0.1145	2.778	0.01055	0.66144	0.86133
0.2715	65.39	0.2703	10.13	0.01567	0.01864	0.06502	2.476	0.01023	0.66926	0.86755
0.32928	72.17	0.3396	11.51	0.01778	0.02286	0.09164	2.428	0.01143	0.82455	1.08643
0.46436	90.67	0.4638	12.52	0.02192	0.04773	0.3439	2.937	0.01502	1.36218	1.68274
0.61337	107.1	0.573	13.41	0.02054	0.03025	0.1207	2.832	0.01515	1.62274	1.86253
0.92042	115.6	0.7261	15.92	0.01917	0.02967	0.1431	2.748	0.01726	1.99532	1.87626
1.23779	93.72	0.8381	22.25	0.0258	0.0607	0.4375	2.673	0.0239	2.24024	2.04722
1.54501	72.67	0.8967	28.84	0.03154	0.07339	0.4407	2.722	0.03359	2.44082	1.94057
1.85048	54.94	0.9206	40.31	0.03863	0.09703	0.5224	2.697	0.04519	2.48286	1.79691
2.45052	14.89	0.9474	160	0.09066	0.3127	1.914	2.626	0.16708	2.48787	1.14294
2.98266	5.325	0.905	447.1	0.1525	0.5637	3.394	1.576	0.26785	1.42628	0.68755
4.40079	1.6	0.7537	1143	0.1897	0.1052	0.2467	1.319	0.62133	0.99413	0.25698

1.2 mm Steel Shot Three-Phase Fluidized Bed, $U_\ell = 0.311$ m/s

U_g (m/s)	f (1/s)	ε_g (-)	\bar{t}_i (1/2500 s)	$\bar{\ell}_b$ (m)	σ_ℓ (m)	$\ell_{b,vs}$ (m)	U_b (m/s)	$(\varepsilon_g U_b)/f$ (m)	$U_b \varepsilon_g$ (m/s)	$0.8467 f \bar{\ell}_b$ (m/s)
0.00297	4.15	0.00678	4.087	0.00213	0.00077	0.00272	1.096	0.00179	0.00743	0.00748
0.0055	5.862	0.01023	4.373	0.00228	0.00124	0.00421	1.113	0.00194	0.01139	0.01132
0.0103	8.254	0.01423	4.334	0.00222	0.00098	0.00338	1.138	0.00196	0.01619	0.01551
0.01423	11.87	0.0202	4.271	0.00229	0.00098	0.00322	1.243	0.00212	0.02511	0.02301
0.02072	18.17	0.02527	3.494	0.00259	0.00141	0.00464	1.561	0.00217	0.03945	0.03984
0.03606	33.06	0.04429	3.326	0.00271	0.00136	0.00426	1.721	0.00231	0.07622	0.07586
0.05142	54.28	0.06591	3.066	0.00259	0.00151	0.00614	1.825	0.00222	0.12029	0.11903
0.07193	73.39	0.08376	2.902	0.00265	0.0015	0.00485	1.932	0.0022	0.16182	0.16466
0.10238	92.5	0.1244	3.211	0.00315	0.00324	0.01616	1.886	0.00254	0.23462	0.2467
0.13187	110.8	0.1749	3.818	0.00314	0.004	0.02502	1.919	0.00303	0.33563	0.29457
0.16046	105.9	0.1803	4.109	0.00319	0.00443	0.02476	1.801	0.00307	0.32472	0.28602
0.21104	135.4	0.2697	5.074	0.00369	0.00686	0.0445	1.757	0.0035	0.47386	0.42302
0.26679	128.7	0.282	5.734	0.0036	0.00579	0.03602	1.615	0.00354	0.45543	0.39228
0.32423	134.5	0.361	6.837	0.00392	0.006	0.04298	1.631	0.00438	0.58879	0.4464
0.46512	135.2	0.4851	8.798	0.00679	0.01573	0.09657	1.504	0.0054	0.72959	0.77725
0.61858	142.9	0.6936	12.15	0.02586	0.04226	0.1838	3.774	0.01832	2.61765	3.12877
0.91813	116.2	0.8062	17.73	0.02404	0.045	0.2546	3.084	0.0214	2.48632	2.36512
1.21074	87.89	0.8742	25.31	0.03694	0.08356	0.508	3.051	0.03035	2.66718	2.74884
1.4818	55.11	0.9314	42.35	0.03538	0.1095	0.9921	2.433	0.04112	2.2661	1.65082
1.77464	29.58	0.9556	68.28	0.03813	0.112	0.6696	1.852	0.05983	1.76977	0.95494
2.29617	21.94	0.9578	112.1	0.02016	0.0922	0.9101	1.195	0.05217	1.14457	0.37449
3.20103	13.56	0.9306	169.7	0.1523	0.5651	4.175	2.972	0.20396	2.76574	1.74853
4.33518	1.467	0.648	1157	0.2202	0.00543	0.01515	1.969	0.86974	1.27591	0.2735

1.2 mm Steel Shot Three-Phase Fluidized Bed, $U_\ell = 0.404$ m/s

U_g (m/s)	f (1/s)	ε_g (-)	\bar{t}_i (1/2500 s)	$\bar{\ell}_b$ (m)	σ_ℓ (m)	$\ell_{b,vs}$ (m)	U_b (m/s)	$(\varepsilon_g U_b)/f$ (m)	$U_b \varepsilon_g$ (m/s)	$0.8467 f \bar{\ell}_b$ (m/s)
0.00297	2.117	0.0033	3.917	0.00193	0.00059	0.00229	0.9704	0.00151	0.0032	0.00346
0.00548	3.633	0.00654	4.485	0.00207	0.0006	0.00243	0.9723	0.00175	0.00636	0.00637
0.01023	6.593	0.01159	4.396	0.00218	0.00082	0.00285	1.037	0.00182	0.01202	0.01217
0.01413	10.1	0.01822	4.516	0.00233	0.00089	0.00305	1.13	0.00204	0.02059	0.01992
0.02067	12.96	0.0255	4.91	0.00239	0.00106	0.00355	1.054	0.00207	0.02688	0.02622
0.03581	25.19	0.04545	4.497	0.00281	0.0014	0.00432	1.363	0.00246	0.06195	0.05993
0.05118	30.83	0.06042	4.895	0.00274	0.00127	0.00413	1.309	0.00257	0.07909	0.07152
0.07144	51.28	0.0832	3.988	0.0029	0.00161	0.00555	1.641	0.00266	0.13653	0.12591
0.10148	85	0.1353	4.034	0.00317	0.00388	0.02908	1.841	0.00293	0.24909	0.22813
0.13042	106.6	0.1612	3.749	0.00292	0.00249	0.01265	1.843	0.00279	0.29709	0.26354
0.16046	134.4	0.1999	3.561	0.00307	0.00346	0.02031	1.896	0.00282	0.37901	0.34934
0.21012	152.8	0.2625	4.344	0.00353	0.00546	0.05302	1.843	0.00317	0.48379	0.45668
0.26727	170.4	0.3861	5.432	0.00386	0.008	0.08728	1.864	0.00422	0.71969	0.55689
0.32342	174.7	0.4712	6.251	0.00434	0.01005	0.09641	1.717	0.00463	0.80905	0.64194
0.44948	165.2	0.5733	8.643	0.00583	0.01322	0.1056	1.585	0.0055	0.90868	0.81544
0.64098	152.1	0.7387	11.92	0.02676	0.04234	0.1813	3.861	0.01875	2.85212	3.4461
0.94732	128.2	0.7978	15.5	0.03114	0.04954	0.2165	3.739	0.02327	2.98297	3.38002
1.27301	125.5	0.8107	16.08	0.03231	0.06252	0.3566	3.547	0.02291	2.87555	3.43315
1.5715	127.2	0.8125	15.9	0.02912	0.05149	0.2228	3.557	0.02272	2.89006	3.13611
1.87798	129.4	0.8328	15.44	0.02363	0.0416	0.219	3.667	0.0236	3.05388	2.58887
2.44355	130.7	0.8562	15.89	0.0285	0.08728	0.8678	4.193	0.02747	3.59005	3.15379
2.98197	74.44	0.9139	30.75	0.03819	0.1042	0.7202	4.002	0.04913	3.65743	2.40696

U_g (m/s)	U_ℓ (m/s)			$\sigma_t/\bar{\epsilon}_t$	U_ℓ (m/s)	0.012	0.020	0.030	0.040
	0.0035	0.0050	0.0080						
0.0364	0.88054	0.92033	0.95198	1.01924	1.09218	1.21546	1.29445		
0.0455	0.87475	0.91712	1.01073	1.09548	1.16334	1.31136	1.39516		
0.0546	0.93819	0.96677	1.02381	1.12223	1.32339	1.45824	1.51548		
0.0638	0.99685	1.06633	1.13206	1.23607	1.38189	1.44007	1.51306		
0.0729	1.00943	1.05551	1.09705	1.22184	1.41674	1.45756	1.51366		
0.1	1.00377	1.08128	1.15434	1.25233	1.3607	1.52922	1.6276		
0.155	0.87763	0.90263	1.09136	1.2168	1.44661	1.57065	1.58189		
0.2	0.66007	0.67659	0.68796	0.7756	0.83639	1.05433	1.26339		
0.311	0.59532	0.67797	0.61847	0.55004	0.55947	0.6471	0.69587		
0.404	0.53196	0.52853	0.54475	0.54364	0.54469	0.5545	0.5741		

Appendix C

Data Validation

In order to validate the experimental data in this work, a material balance on gas passing a cross-section of the column can be written either as

$$U_g A_c = f_T \frac{\pi}{6} d_b^3 \quad (C1)$$

or as

$$U_g = U_b \varepsilon_g \quad (C2)$$

where f_T is the total bubble frequency based on the column cross-section, assuming that the system contains only spherical bubbles having uniform size and rising at a uniform velocity, U_b .

With a conductivity probe, only those bubbles having their center points within a circle of diameter equal to the bubble diameter can be detected. Hence, assuming the bubbles are uniformly distributed across the column cross-section,

$$f_T = f A_c / \left(\frac{\pi}{4} d_b^2 \right) \quad (C3)$$

The relationship between bubble diameter and measured average bubble chord length for spherical bubbles can be correlated by the following equation (Weimer et al., 1985):

$$d_b = \frac{4}{\pi} \bar{\ell}_b \quad (C4)$$

Substituting Equations (C3) and (C4) into Equation (C1) and rearranging, one obtains

$$U_g = \frac{8}{3\pi} f \bar{\ell}_b \quad (C5)$$

It should be noted that the above equation applies exactly only to systems of uniform spherical bubbles which are distributed evenly across the column cross-sectional area and are not impeded by any wall effect.

Figures C1 and C2, respectively, present the local experimental data of $U_b \varepsilon_g$ and $\frac{8}{3\pi} f \bar{\ell}_b$ with respect to the superficial gas velocity, U_g , in the air-water bubble column.

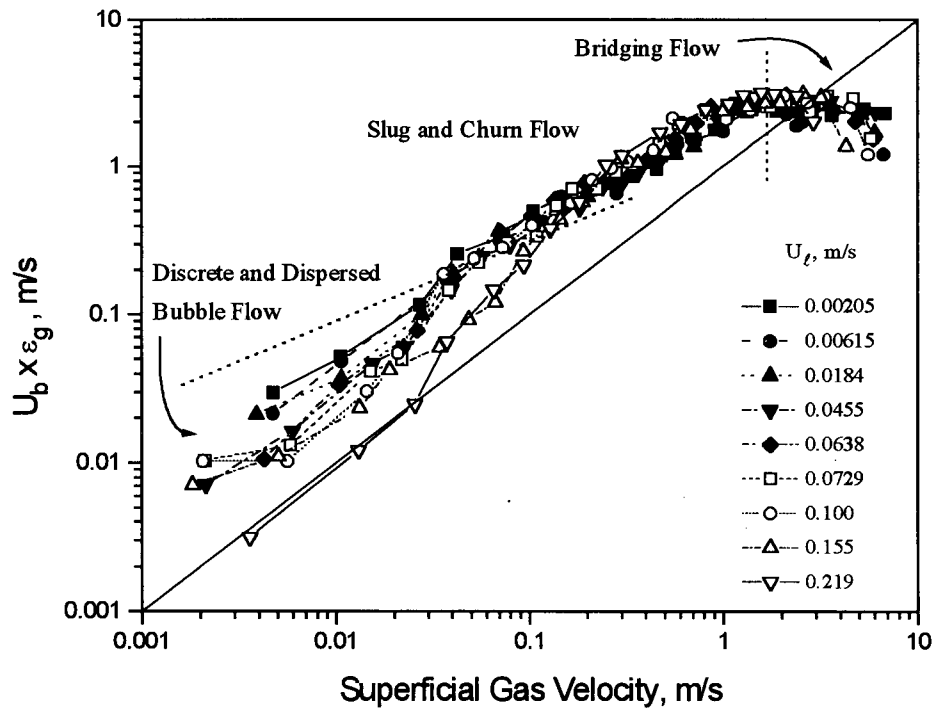


Figure C1. Variation of $U_b \varepsilon_g$ with superficial gas velocity at different liquid velocities for air-water bubble column.

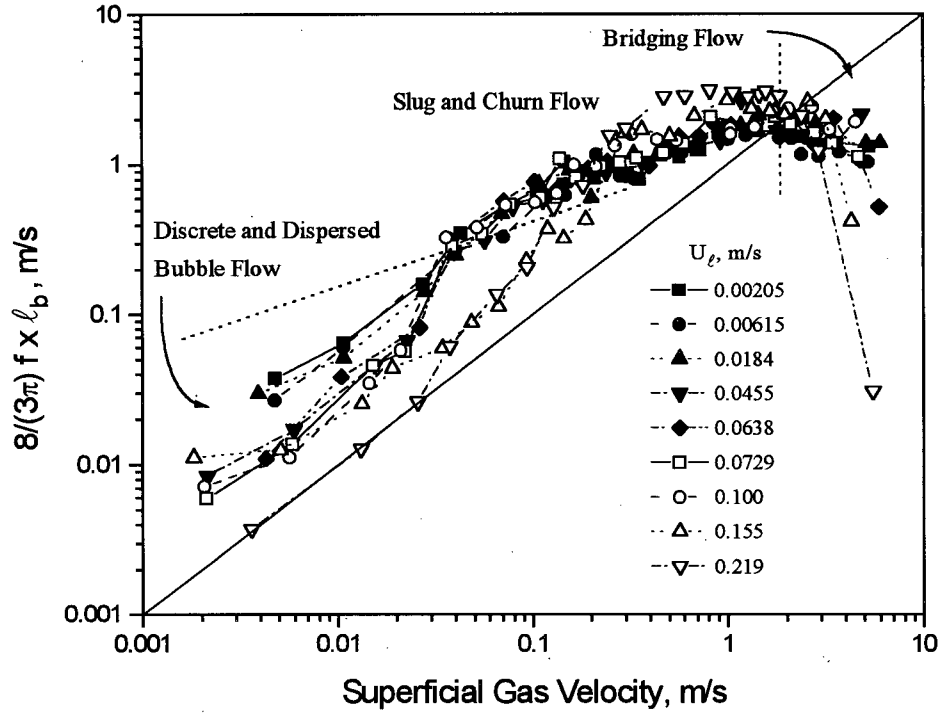


Figure C2. Variation of $\frac{8}{3\pi} f \bar{\ell}_b$ with superficial gas velocity at different liquid velocities for air-water bubble column.

It is seen that most experimental results for $U_b \epsilon_g$ and $\frac{8}{3\pi} f \bar{\ell}_b$ measured at the center of the column are greater than the superficial gas velocity, indicating non-uniform distribution of the gas phase. As the superficial liquid velocity is increased, both $U_b \epsilon_g$ and $\frac{8}{3\pi} f \bar{\ell}_b$ decrease and approach the value of U_g in the discrete and dispersed bubble flow regimes. At very high liquid velocity, $U_l = 0.219$ m/s, and low gas velocity, $U_g \leq 0.025$ m/s, both $U_b \epsilon_g$ and $\frac{8}{3\pi} f \bar{\ell}_b$ are equal to the value of U_g , which results from the uniform distribution of spherical gas bubbles in the dispersed bubble flow regime. It is also seen that both $U_b \epsilon_g$ and $\frac{8}{3\pi} f \bar{\ell}_b$ increase with increasing

superficial gas velocity in the slug and churn flow regimes, but decrease in the bridging flow regime.

Similar results were obtained for the three-phase fluidized beds tested in this work as shown in Figures C3 to C8. The results are all consistent with the observed uniformities in bubble characteristics in the discrete and dispersed bubble flow regimes, and the observed non-uniformities in the other regimes.

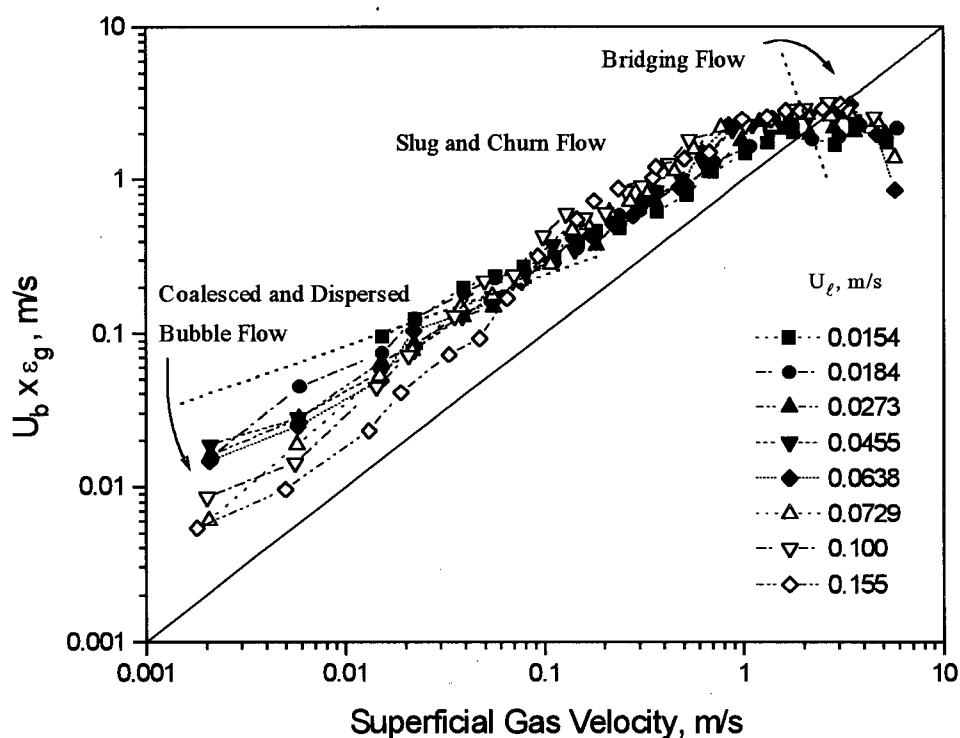


Figure C3. Variation of $U_b \epsilon_g$ with superficial gas velocity at different liquid velocities for 1.5 mm glass bead three-phase fluidized bed.

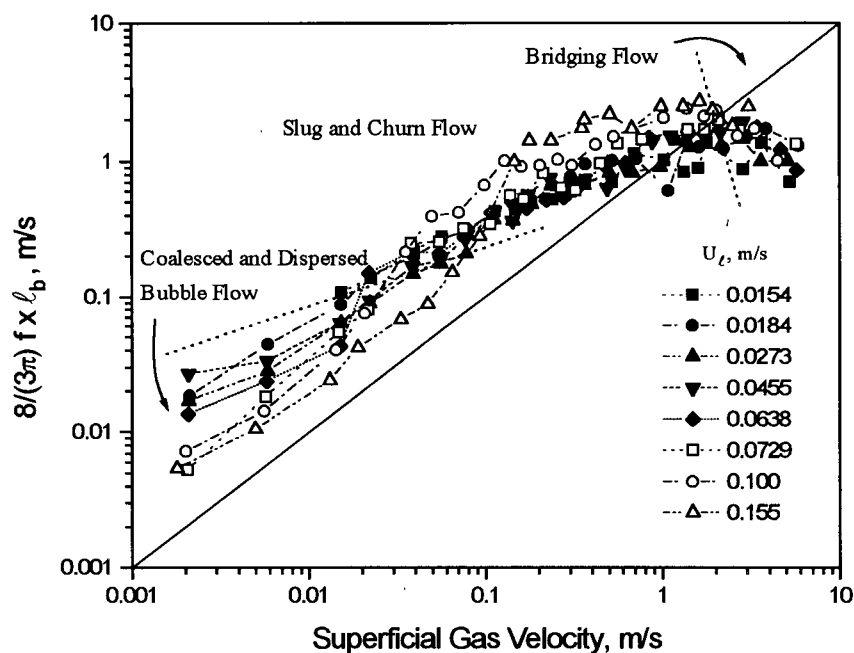


Figure C4. Variation of $\frac{8}{3\pi} f \bar{l}_b$ with superficial gas velocity at different liquid velocities for 1.5 mm glass bead three-phase fluidized bed.

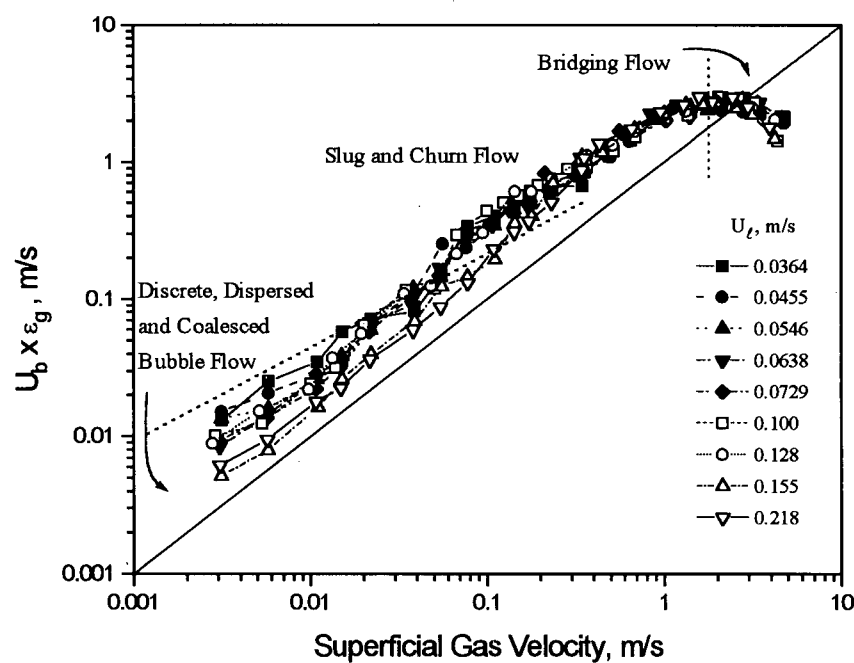


Figure C5. Variation of $U_b \epsilon_g$ with superficial gas velocity at different liquid velocities for 4.5 mm glass bead three-phase fluidized bed.

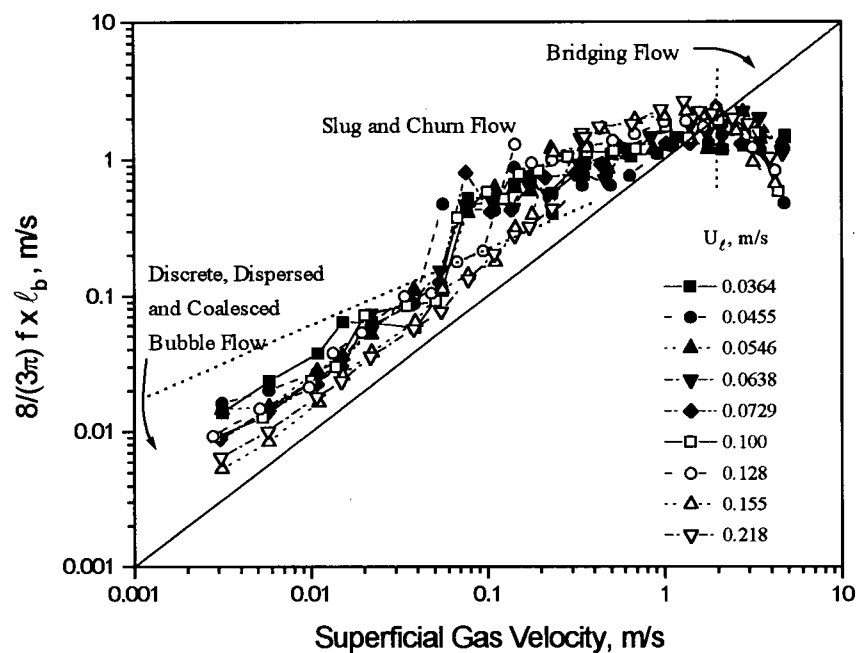


Figure C6. Variation of $\frac{8}{3\pi} f \bar{\ell}_b$ with superficial gas velocity at different liquid velocities for 4.5 mm glass bead three-phase fluidized bed.

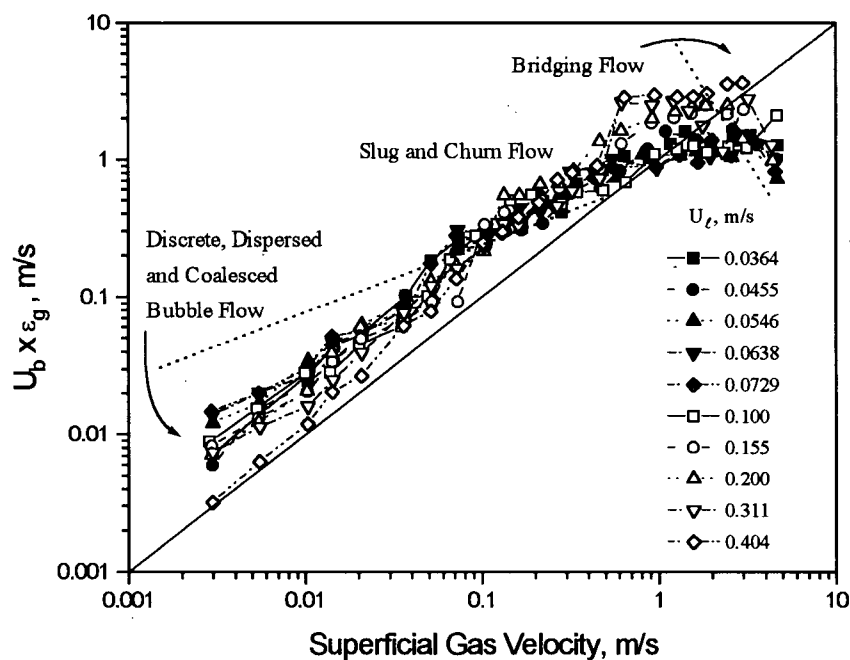


Figure C7. Variation of $U_b \varepsilon_g$ with superficial gas velocity at different liquid velocities for 1.2 mm steel shot three-phase fluidized bed.

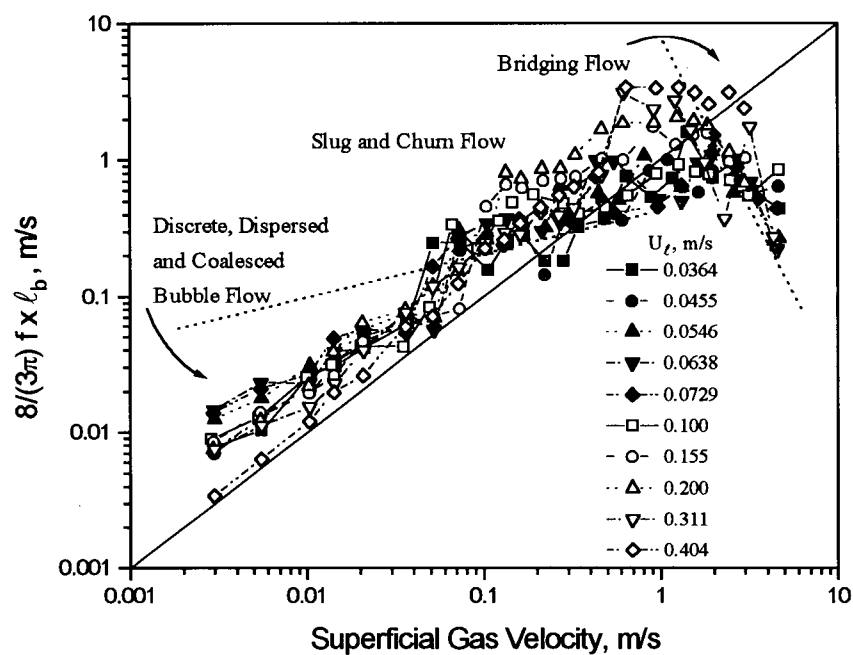


Figure C8. Variation of $\frac{8}{3\pi} f \bar{l}_b$ with superficial gas velocity at different liquid velocities for 1.2 mm steel shot three-phase fluidized bed.